# Examination of myocardial electrophysiology using novel panoramic optical mapping techniques

by

Andrew James Allan

BSc MRes

Submitted in fulfilment of the requirements for the Degree

of Doctor of Philosophy

to

Institute of Cardiovascular & Medical Sciences

College of Medical, Veterinary and Life Sciences

University of Glasgow

2016

# Abstract

Optical mapping of voltage signals has revolutionised the field and study of cardiac electrophysiology by providing the means to visualise changes in electrical activity at a high temporal and spatial resolution from the cellular to the whole heart level under both normal and disease conditions. The aim of this thesis was to develop a novel method of panoramic optical mapping using a single camera and to study myocardial electrophysiology in isolated Langendorff-perfused rabbit hearts. First, proper procedures for selection, filtering and analysis of the optical data recorded from the panoramic optical mapping system were established. This work was followed by extensive characterisation of the electrical activity across the epicardial surface of the preparation investigating time and heart dependent effects.

In an initial study, features of epicardial electrophysiology were examined as the temperature of the heart was reduced below physiological values. This manoeuvre was chosen to mimic the temperatures experienced during various levels of hypothermia *in vivo*, a condition known to promote arrhythmias. The facility for panoramic optical mapping allowed the extent of changes in conduction timing and pattern of ventricular activation and repolarisation to be assessed.

In the main experimental section, changes in epicardial electrical activity were assessed under various pacing conditions in both normal hearts and in a rabbit model of chronic MI. In these experiments, there was significant changes in the pattern of electrical activation corresponding with the changes in pacing regime. These experiments demonstrated a negative correlation between activation time and APD, which was not maintained during ventricular pacing. This suggests that activation pattern is not the sole determinant of action potential duration in intact hearts. Lastly, a realistic 3D computational model of the rabbit left ventricle was developed to simulate the passive and active mechanical properties of the heart. The aim of this model was to infer further information from the experimental optical mapping studies. In future, it would be feasible to gain insight into the electrical and mechanical performance of the heart by simulating experimental pacing conditions in the model.

# Table of Contents

# List of Tables

# List of Figures

# List of Equations

# Acknowledgements

This research has been one of the most challenging and enjoyable times of my life, and I am extremely grateful to all those who have been a part of it. This study was funded by the British Heart Foundation, and I am thankful for their generosity.

I would like to thank my wife Jennifer Allan for her love, patience, support and above all understanding throughout the course of my PhD. I would like to dedicate my thesis to my wife and to my son Alexander Allan who was born during the final year of my PhD.

I cannot express enough my appreciation to my supervisors Francis Burton and Xiaoyu Luo for their continued support, advice and guidance throughout my PhD.

I cannot thank enough both Aileen Rankin and Michael Dunne for the technical support and above all for putting up with my moaning and occasional coarse language when experiments did not go quite as planned. I would like to thank Julie from the mechanical workshop and Nosrat from the bioelectronics workshop for their hard work, without which my experiments would not have been possible.

Lastly, I would like to thank my parents, Malcolm and Nancy, for the unrelenting support and positivity.

# Author's Declaration

The coronary artery ligation procedure for producing the chronic MI rabbit model was carried out by Mr Michael Dunne and Mrs Aileen Rankin at the Glasgow Cardiovascular Research Centre. All the work contained in this thesis was undertaken by me. Mrs Aileen Rankin assisted me in the optical mapping experiments. The removal of the heart from the rabbit was carried out by either Mr Michael Dunne or Mrs Aileen Rankin. The material has not been submitted previously for any other degree.

## Publications

Dietrichs E.S., McGlynn K., **Allan A.**, Burton F.L., Tveita T., Smith G.L. (*In Preparation)*. **Assessment of cardiac electrophysiology during hypothermia and rewarming in isolated Langendorff perfused rabbit hearts.**

Gao H., **Allan A.**, McComb C., Luo X., & Berry C. (2014). **Left ventricular strain and its pattern estimated from cine CMR and validation with DENSE**. *Physics in Medicine and Biology.59 (13), 3637.*

## Abstracts and posters

**Allan A.**, Smith G.L., Burton F.L. (2014). **Correlation between ventricular repolarisation patterns and T-wave generation in isolated rabbit hearts using panoramic imaging**. Abstract – 58th Biophysical Society Meeting, San Francisco, California. *Biophysical Journal 2014; 106(2) 631a*

**Allan A.**, Smith G.L., Burton F.L. (2013). **Panoramic imaging of isolated rabbit hearts using a single camera system**. Abstract – 40th International Congress on Electrocardiology, Glasgow, Scotland. *Journal of Electrocardiology* 2013; 4:e32.

Dietrichs E.S., **Allan A.**, Burton F.L., Tveita T., Smith G.L. (2013). **Measurements of ventricular activation and repolarisation during deep hypothermia and rewarming using panoramic optical mapping of isolated Langendorff perfused rabbit hearts**. Abstract - 40th International Congress on Electrocardiology, Glasgow, Scotland. *Journal of Electrocardiology* 2013; 4:e36

**Allan A.**, Smith G.L., Burton F.L., (2012). **Panoramic imaging of isolated rabbit hearts using a single camera**. Abstract - Annual Meeting of the German Biophysical Society (P169).

# Definitions/Abbreviations

| | |
|---|---|
| $\Delta F$ | Change In Fluorescence |
| ACE | Angiotensin-Converting Enzyme |
| ADC | Analogue-To-Digital Converter |
| AP | Action Potential |
| APD | Action Potential Duration |
| $APD_{50}$ | Action Potential Duration at 50% Repolarisation |
| $APD_{75}$ | Action Potential Duration at 75% Repolarisation |
| $APD_{90}$ | Action Potential Duration at 90% Repolarisation |
| ARB | Angiotensin II-Receptor Blockers |
| AV | Atrio-Ventricular |
| BDM | 2,3-Butanedione Monoxime |
| BiV | Bi-Ventricular |
| $[Ca^{2+}]_e$ | Extracellular Calcium Concentration |
| $[Ca^{2+}]_i$ | Intracellular Calcium Concentration |
| $Ca^{2+}{}_T$ | Intracellular Calcium Transient |
| CCD | Charge-Coupled Device |
| CF | Coronary Flow |
| CHD | Coronary Heart Disease |

| | |
|---|---|
| CICR | Calcium-Induced Calcium Release |
| CMOS | Complementary Metal Oxide Semiconductor |
| CRT | Cardiac Resynchronisation Therapy |
| CT | Computed Tomography |
| CV | Conduction Velocity |
| Cx43 | Connexin 43 |
| Cyto D | Cytochalasin D |
| DAD | Delayed Afterdepolarisations |
| DMSO | Dimethyl Sulphoxide |
| DTI | Diffusion Tensor Imaging |
| EAD | Early Afterdepolarisations |
| E-C | Excitation-Contraction |
| ECG | Electrocardiogram |
| $E_M$ | Membrane Potential |
| EM | Electron Multiplying |
| E-M | Electro-Mechanical |
| EMCCD | Electron Multiplying Charge Coupled Device |
| EMD | Electro-Mechanical Delay |
| EP | Epicardial Pacing |

| | |
|---|---|
| FE | Finite Element |
| FPS | Frames Per Second |
| IB | Immersed Boundary |
| $I_{CaL}$ | L-Type Calcium Current |
| $I_{CaT}$ | T-Type Calcium Current |
| $I_f$ | Pacemaker Current |
| $I_{K1}$ | Inward Rectifier Potassium Current |
| $I_{KATP}$ | ATP-Sensitive Potassium Current |
| $I_{Kr}$ | Rapid Delayed Rectifier Potassium Current |
| $I_{Ks}$ | Slow Delayed Rectifier Potassium Current |
| $I_{Na}$ | Sodium current |
| $I_{to}$ | Transient Outward Potassium Current |
| I-V | Current-To-Voltage |
| $[K^+]_e$ | Extracellular Potassium Concentration |
| LA | Left Atrium |
| LED | Light Emitting Diode |
| LV | Left Ventricle |
| LVD | Left Ventricular Dysfunction |
| LVSD | Left ventricular Systolic Dysfunction |

| | |
|---|---|
| $[Mg^{2+}]_e$ | Extracellular Magnesium Concentration |
| MRI | Magnetic Resonance Imaging |
| NCX | Sodium-Calcium Exchanger |
| NHE | Sodium-Hydrogen Exchanger |
| PDA | Photodiode Array |
| POI | Points Of Interest |
| QE | Quantum Efficiency |
| RA | Right Atrium |
| ROI | Region Of Interest |
| RV | Right Ventricle |
| RVOT | Right Ventricle Outflow Tract |
| RyR | Ryanodine Receptors |
| SA | Sino-Atrial |
| SCD | Sudden Cardiac Death |
| SERCA | Sarco-Endoplasmic Reticulum $Ca^{2+}$-ATPase |
| SIFT | Scale-Invariant Feature Transform |
| SNR | Signal-To-Noise Ratio |
| SR | Sarcoplasmic Reticulum |
| SURF | Speeded-Up Robust Features |

| | |
|---|---|
| $TAct_M$ | Activation Time |
| TH | Tungsten-Halogen |
| $TRepol_{50}$ | 50% Repolarisation |
| $TRepol_{75}$ | 75% Repolarisation |
| $TRepol_{90}$ | 90% Repolarisation |
| VF | Ventricular Fibrillation |
| $V_m$ | Transmembrane Potential |
| VSD | Voltage-Sensitive Dyes |
| VT | Ventricular Tachycardia |

# Chapter 1: Introduction

## Aims

The aim of this introduction is to provide an overview of basic cardiac electrophysiology and the background of isolated heart preparations. Furthermore, an in depth introduction into the genesis, mechanisms, developments and methods of cardiac optical mapping will be given.

# Cardiac electrophysiology

## Cardiac action potential

Cardiac excitation requires the generation of the cardiac action potential (AP), which can be defined as the dynamic change in membrane potential ($V_m$) generated through the complex interplay between many different ion channels and transporters. The cardiac AP can be split into two types: pacemaker AP's, generated by the pacemaker cells present within the sino-atrial (SA) and atrio-ventricular (AV) nodes, which display automaticity; and non-pacemaker AP's, generated in the atrial, ventricular and Purkinje myocytes triggered through propagating currents. The AP is divided into five distinct phases (0-4, see Figure 1.1a), with a summary of the key underlying ionic currents involved shown in Figure 1.1b (Ruan et al., 2009).

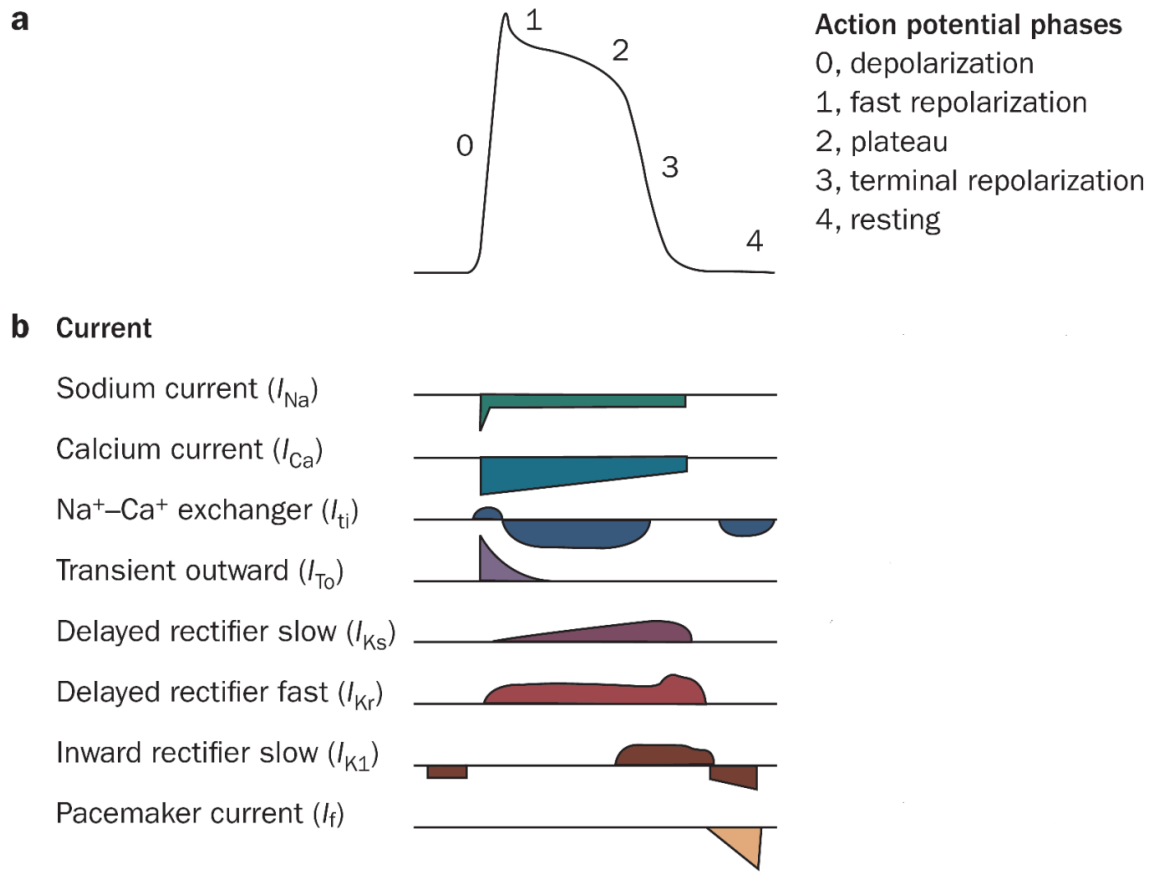


**Figure 1.1 Ventricular action potential**
**(a) Phases of ventricular action potential**
**(b) Major sarcolemmal ionic currents.**

## Excitation-contraction coupling

Effective function of the cardiac muscle occurs through the process of excitation-contraction (E-C) coupling (Figure 1.2). The cardiomyocyte is depolarised with the arrival of the AP down the transverse tubule (T-tubule), resulting in the activation of the voltage-sensitive L-type calcium ($Ca^{2+}$) channels. The subsequent influx of $Ca^{2+}$ via the L-type $Ca^{2+}$ current, contributing to the plateau of the AP, activates nearby ryanodine receptors (RyRs) bound to the sarcoplasmic reticulum (SR), triggering further release of larger amounts of $Ca^{2+}$ from the SR store. This process is known as calcium-induced calcium release (CICR). The resulting rise in intracellular $[Ca^{2+}]_i$ allows $Ca^{2+}$ to bind to the myofilament protein troponin C, leading to crossbridge formation and contraction of the cell. During the relaxation phase $Ca^{2+}$ is returned to the SR via the sarco-endoplasmic reticulum $Ca^{2+}$-ATPase (SERCA) pump, at the expense of ATP, and extruded from the cell across the surface sarcolemma via the sodium-calcium exchanger (NCX). This fall in intracellular $Ca^{2+}$ allows the dissociation of $Ca^{2+}$ from troponin and relaxation of the cardiomyocyte.

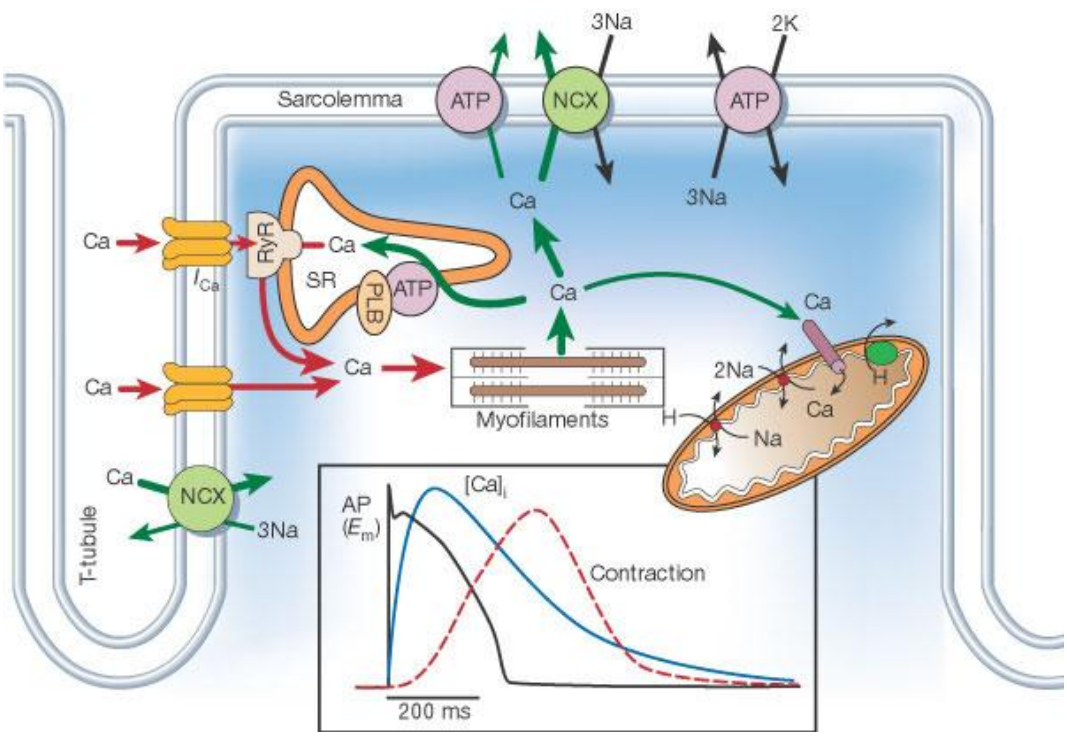


**Figure 1.2 Excitation-contraction coupling within the ventricular myocyte**

**Schematic representation of $Ca^{2+}$ transport in ventricular myocytes, with inset showing the time course of an action potential (black line), $Ca^{2+}$ transient (blue line) and contraction (red dashed line) (Bers, 2002).**

Events at the cellular level are translated to the whole heart in a sequence determined partly by the specialised conduction system. The initial electrical event that triggers each heart beat originates within the SA node (Figure 1.3). From the SA node, electrical impulses propagate through the atria to the AV node, which delays the transmission of excitation to the ventricles long enough to allow atrial contraction to precede ventricular contraction. Propagation proceeds down the bundle of His and to the left and right bundle branches, along the Purkinje fibres, whose distribution within the ventricles determines the final spread of excitation. Adjacent cardiomyocytes within the ventricular myocardium are excited by conduction from cell to cell via intercalated disc complexes made up of gap junctions that permit the transfer of molecules and ions between cells. Through this sequence of electrical events the subsequent mechanical contraction during the cardiac cycle is determined.

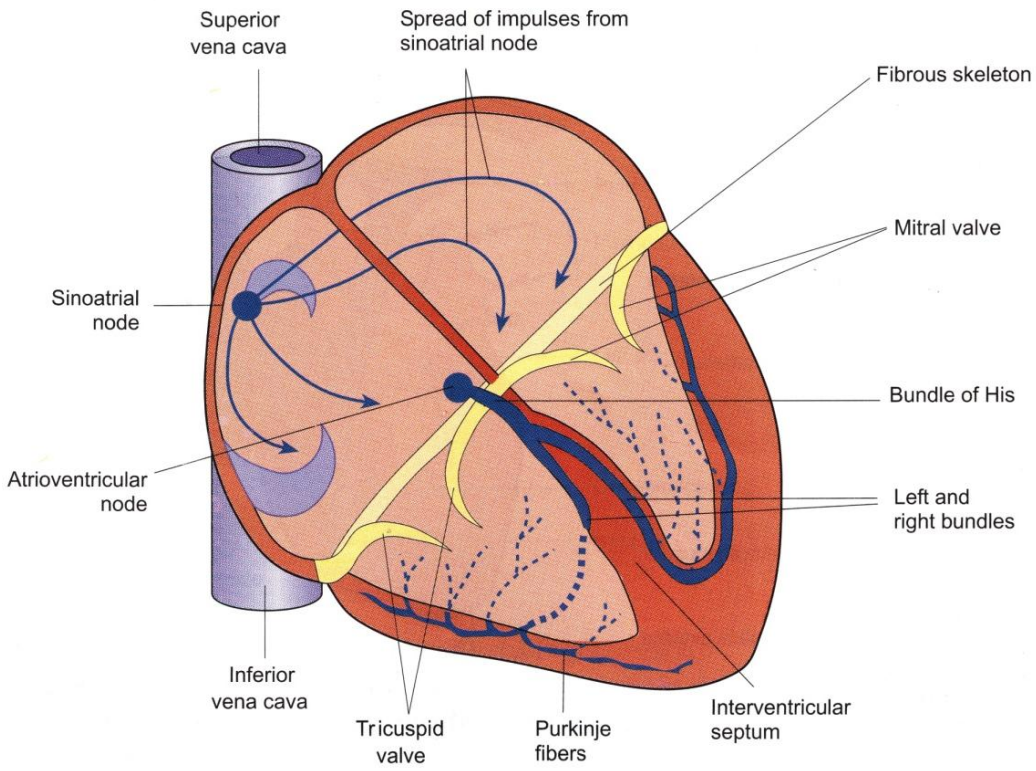


**Figure 1.3 Schematic of gross heart anatomy of specialised conduction system (Pocock and Richards, 2004)**

## Cardiac cycle

The heart is responsible for the continuous circulation of blood flow throughout the body, allowing the transport of oxygen, nutrients (glucose, amino acids and fatty acids), hormones (insulin, adrenaline and noradrenalin) and the removal of waste (carbon dioxide, urea and lactic acid) to and from the various tissues. It is organized as four distinct chambers: the right atria (RA), left atria (LA), right ventricle (RV) and the left ventricle (LV) (Figure 1.4). During the normal cardiac cycle deoxygenated blood collects in the RA, entering via the superior and inferior vena cava, and is pumped across the tricuspid valve and into the RV, whereupon it is pumped across the pulmonary valve travelling along the pulmonary artery to the lungs to allow the exchange of carbon dioxide for oxygen. At the same time, oxygenated blood collects in the LA until it is pumped across the mitral valve into the LV, whereupon it is pumped via the aortic valve and into the aorta.

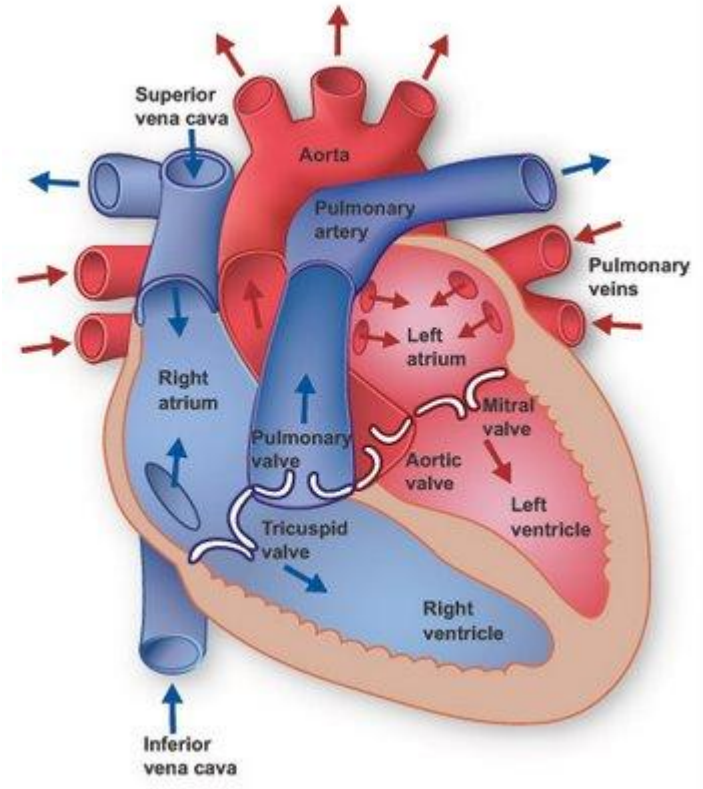


**Figure 1.4 Gross anatomy of chambers and valves of the heart (Pocock et al., 2013)**

## Myocardial infarction

### Acute myocardial infarction

Acute myocardial infarction (MI) remains a leading cause of morbidity and mortality worldwide. Myocardial infarction occurs when myocardial ischemia, a diminished blood supply to the heart, exceeds a critical threshold and overwhelms myocardial cellular repair mechanisms designed to maintain normal operating function and homeostasis. Ischemia at this critical threshold level for an extended time results in irreversible myocardial cell damage or death.

Typically, critical myocardial ischemia occurs because of increased myocardial metabolic demand and decreased delivery of oxygen and nutrients to the myocardium via the coronary circulation. A disruption in the supply of myocardial oxygen and nutrients occurs when a thrombus is superimposed on an ulcerated or unstable atherosclerotic plaque and results in coronary occlusion (Cotran et al., 1999). In addition, a high-grade (>75%) fixed coronary artery stenosis caused by atherosclerosis or a dynamic stenosis associated with coronary vasospasm can also limit the supply of oxygen and nutrients to precipitate an MI. Conditions associated with increased myocardial metabolic demand include extremes of physical exertion, severe hypertension (including forms of hypertrophic obstructive cardiomyopathy), and severe aortic valve stenosis. Other cardiac valvular pathologies and low cardiac output states associated with a decreased mean aortic pressure, which is the prime component of coronary perfusion pressure, can also precipitate MI.

Myocardial infarction can be subcategorized on the basis of anatomic, morphologic, and diagnostic clinical information. From an anatomic or morphologic standpoint, the two types of MI are transmural and nontransmural. A transmural MI is characterized by ischemic necrosis of the full thickness of the affected muscle segment(s), extending from the endocardium through the myocardium to the epicardium. A nontransmural MI is defined as an area of ischemic necrosis that does not extend through the full thickness of myocardial wall segment(s). In a nontransmural MI, the area of ischemic necrosis is limited to the endocardium or to the endocardium and myocardium. It is the endocardial

and subendocardial zones of the myocardial wall segment that are the least perfused regions of the heart and the most vulnerable to conditions of ischemia.

### Remodelling and development of chronic myocardial infarction

The acute loss of myocardium results in an abrupt increase in loading conditions that induces a unique pattern of remodelling involving the infarcted border zone and remote non-infarcted myocardium. Myocyte necrosis and the resultant increase in load trigger a cascade of biochemical intracellular signalling processes that initiates and subsequently modulates reparative changes, which include dilatation, hypertrophy, and the formation of a discrete collagen scar. Ventricular remodelling may continue for weeks or months until the distending forces are counterbalanced by the tensile strength of the collagen scar. This balance is determined by the size, location, and transmurality of the infarct, the extent of myocardial stunning, the patency of the infarct-related artery, and local tropic factors (Warren et al., 1988; Pfeffer and Braunwald, 1990).

Myocardial infarction results in the migration of macrophages, monocytes, and neutrophils into the infarct zone; this initiates intracellular signalling and neurohormonal activation, which localizes the inflammatory response. Changes in circulatory hemodynamics are determined primarily by the magnitude of myocyte loss, the stimulation of the sympathetic nervous system and renin-angiotensin-aldosterone system, and the release of natriuretic peptides.

Post infarction remodelling has been arbitrarily divided into an early phase (within 72 hours) and a late phase (beyond 72 hours). The early phase involves expansion of the infarct zone, which may result in early ventricular rupture or aneurysm formation (Erlebacher et al., 1984). Late remodelling involves the left ventricle globally and is associated with time-dependent dilatation, the distortion of ventricular shape, and mural hypertrophy. The failure to normalize increased wall stresses results in progressive dilatation, recruitment of border zone myocardium into the scar, and deterioration in contractile function (White et al., 1987; Pfeffer and Braunwald, 1990).

In this thesis, chronic MI in the context of the rabbit model used is defined as 8 weeks post coronary artery ligation, where longitudinal data from our group has

shown no change in morphology of the infarct or changes in electrophysiology of the heart after 8-weeks post MI.

## Heart failure

Heart failure is a complex clinical syndrome of symptoms and signs that suggest the efficiency of the heart as a pump is impaired. It is caused by dysfunction of the heart due to muscle damage (systolic or diastolic dysfunction), valvular dysfunction, arrhythmias or other rare causes. Some patients have heart failure due to left ventricular systolic dysfunction (LVSD) which is associated with a reduced left ventricular ejection fraction. Others have heart failure with a preserved ejection fraction (HFPEF). Most of the evidence on treatment is for heart failure due to LVSD. Acute heart failure can present as new-onset heart failure in people without known cardiac dysfunction, or as acute decompensation of chronic heart failure. The most common cause of heart failure in the UK is coronary artery disease, and many patients have had a myocardial infarction in the past (Petersen et al., 2002).

Acute heart failure is a common cause of admission to hospital (over 67,000 admissions in England and Wales per year) and is the leading cause of hospital admission in people 65 years or older in the UK. Heart failure has a poor prognosis: 30–40% of patients diagnosed with heart failure die within a year – but thereafter the mortality is less than 10% per year (Hobbs et al., 2007; Cowie et al., 2000).

### Dyssynchronous heart failure

Heart failure most often occurs as the result of the loss of normal functioning of the ventricles of the heart. Under normal conditions, the ventricles should pump at the same time and in synchronisation with the atria. If the contractions lack synchrony, either within or between the ventricles, or between the atria and ventricles, the heart becomes less efficient as a pump. Dyssynchronous heart failure can present in the following ways (Bax et al., 2004):

1) Atrioventricular (AV) dyssynchrony – irregular difference in timing between atrial and ventricular contractions

2) Interventricular dyssynchrony – difference in timing between the RV and LV

3) Systolic intraventricular dyssynchrony – abnormal activation and contraction of segments of the LV wall

## Electrophysiological changes in heart failure

### Action potential characteristics

In a study of patients with end-stage heart failure undergoing cardiac transplantation, ventricular myocytes were isolated and stimulated at a frequency of 0.5Hz. Measurements of $APD_{90}$ showed significant prolongation in these cells in comparison to cells isolated from normal donor hearts (Beuckelmann et al., 1992). APD prolongation has been confirmed in multicellular human ventricular preparations, but the difference between normal and failing ventricles was only significant at low stimulation rates (0.33Hz) and was not observed at physiological rates (1Hz) (Gwathmey et al., 1987). Comparable APD prolongation at low stimulation rates was observed in isolated myocytes from canine hearts that had undergone chronic rapid pacing to induce dilated cardiomyopathy and heart failure (Nuss et al., 1999; Kääb et al., 1996). In a combined pressure and volume overload model of heart failure in rabbit, intrinsic APD was found to be unchanged in comparison to normal myocytes (Wiegerinck et al., 2008).

### Prolongation in APD and arrhythmogenesis

It is conceivable that prolongation of APD in heart failure could be protective against re-entrant arrhythmias by the maintenance of relatively longer refractory periods and hence a smaller excitable gap, in effect contributing to a less arrhythmogenic *substrate*. However, the prolongation in APD may be pro-arrhythmic in terms of *trigger*, by increasing the propensity for after-depolarisations and triggered activity. In isolated mid-myocardial cells from canine hearts of pacing-induced heart failure, there was a prolongation in APD and increased propensity for early afterdepolarisations (EADs) (Li et al., 2002). The changes observed in APD has been reproduced in the prolongation of QT interval in heart failure patients as well as being linked to the increased risk of arrhythmias (Vrtovec et al., 2003). In ventricular trabeculae of failing human

and rabbit hearts, there was an increased occurrence of delayed afterdepolarisations (DADs) and triggered activity when compared to normal ventricular trabeculae in the presence of superfusion solution modified to contain low potassium, magnesium and noradrenalin (Vermeulen et al., 1994).

### Effects of heart failure on repolarising currents

In heart failure, the prolongation in intrinsic APD has been attributed principally to alterations in the density of repolarising potassium ($K^+$) currents. In humans and animals with heart failure, a decline in functional density of the transient outward $K^+$ current ($I_{to}$) has been observed (Wettwer et al., 1994; Kääb et al., 1996; Beuckelmann et al., 1993). In isolated mid-myocardial cells from canine hearts that have undergone rapid pacing there was a marked increase in the plateau potential, a decrease in the size of the AP notch and APD prolongation, consistent with a reduction in $I_{to}$ (Kääb et al., 1996). Furthermore, the blockade of $I_{to}$ pharmacologically in normal cells generates similar effects.

Conversely, the association between changes in $I_{to}$ and APD are balanced by the influence of the changes in plateau potential on the magnitude of L-type $Ca^{2+}$ current ($I_{CaL}$). Depending on the interaction between other ionic currents, a decrease in $I_{to}$ may result in attenuation or prolongation in the ventricular AP, where these effects may also be species-dependent (Greenstein et al., 2000). In heart failure in the human and in a pacing-induced canine model, a decrease in the inward rectifier current ($I_{K1}$), which contributes to terminal repolarisation, has also been observed (Kääb et al., 1996; Beuckelmann et al., 1993). The blockade of $I_{k1}$ generates spontaneous activity and EADs in isolated failing myocytes, which suggests that the downregulation of $I_{k1}$ could lead to instability in the repolarisation phase of the AP in failing hearts. Furthermore, in a canine model of tachycardia-induced heart failure the presence of EADs and APD prolongation was reported alongside a decrease in the density of the slow component of the delayed rectifier $K^+$ current ($I_{Ks}$) (Li et al., 2002).

### Calcium cycling in heart failure

In failing hearts, abnormalities in $Ca^{2+}$ cycling have been consistently demonstrated. For instance, in both isolated cells (Beuckelmann et al., 1992)

and ventricular muscle (Gwathmey et al., 1987) from humans with end-stage heart failure, reduced amplitude of intracellular $Ca^{2+}$ transients ($Ca^{2+}_T$), prolongation in $Ca^{2+}$ decay and increased levels of diastolic $Ca^{2+}$. These alterations in $Ca^{2+}$ have been correlated with functional abnormalities in $Ca^{2+}$ handling proteins and their associated regulatory proteins (Houser et al., 2000). Abnormal $Ca^{2+}$ cycling plays a central role in the development of contractile dysfunction as well as a potential role in ventricular arrhythmogenesis within heart failure, due to the coupling that exists between $[Ca^{2+}]_i$ and membrane potential ($V_m$) in cardiomyocytes. For instance, in a combined pressure and volume overload model of heart failure in rabbit, alterations in $Ca^{2+}_T$ were directly linked with the development of DADs during beta-adrenergic stimulation (Antonius Baartscheer et al., 2003).

### L-type calcium current

The L-type $Ca^{2+}$ current ($ICa_L$) acts as the trigger for SR $Ca^{2+}$ release, whereby alterations in the magnitude of $ICa_L$ influence the amount of $Ca^{2+}$ released. In some experimental models of heart failure, a decrease in $ICa_L$ has been observed which would tend to shorten APD, however, in others there is no change in $ICa_L$ (Richard et al., 1998). In contrast, a rise in the single-channel open probability of L-type calcium channels has been reported in human heart failure, which may contribute to the prolongation in APD (Schröder et al., 1998).

### Sarcoplasmic reticulum calcium release

During heart failure, affects on the SR $Ca^{2+}$ release channel (RyR), results in an elevated propensity for diastolic $Ca^{2+}$ leak and to the generation of propagating spontaneous $Ca^{2+}$ waves, that have been implicated in the development of DADs (Ai et al., 2005). Dyssynchronous SR $Ca^{2+}$ release has been suggested as a likely mechanism underlying the abnormal $Ca^{2+}_T$ from models of heart failure following an MI (Litwin et al., 2000).

### Calcium reuptake to the sarcoplasmic reticulum

There is evidence to suggest that there is a decrease in the activity of the SR $Ca^{2+}$ reuptake ATPase (SERCA 2a) during heart failure (Schmidt et al., 1998; O'Rourke et al., 1999). It has also been suggested that the impaired function of

SERCA may lead to an increase in the proportion of cytosolic $Ca^{2+}$ being removed via the $Na^{+}$-$Ca^{2+}$ exchanger (NCX). Since transport via NCX is electrogenic, this may lead to prolongation in APD and electrical instability during repolarisation.

### Intracellular sodium in heart failure

Through the actions of NCX, intracellular sodium concentration ($[Na^{+}]_i$) and calcium concentration ($[Ca^{2+}]_i$) are closely linked. In addition, $[Na^{+}]_i$ is linked to intracellular pH via the $Na^{+}$-$H^{+}$ exchanger (NHE). In rabbit experimental models of heart failure, elevated activity of NHE has been reported (A Baartscheer et al., 2003). Consequently, these changes have been implicated in alterations in $Ca^{2+}$ cycling and $Ca^{2+}$ mediated afterdepolarisations in isolated myocytes from failing hearts as a result of elevated $[Na^{+}]_i$.

### Changes in electrical coupling in heart failure

As discussed in Chapter 3, the degree of electrotonic coupling that exists between myocytes within the cardiac syncytium modulates the degree of electrophysiological heterogeneity. The electrotonic coupling between cells leads to a reduction in APD and has the effect of homogenising electrical activity between cells (Joyner et al., 1991). In ventricular myocardium electrotonic coupling is mediated primarily by connexin 43 (Cx43) gap junctional proteins. In both human and experimental models of hearts failure a reduction in Cx43 expression has been observed (Peters et al., 1993).

Therefore, increased electrophysiological heterogeneity in heart failure may arise from either heterogeneous changes in cellular AP characteristics, $Ca^{2+}$ cycling or from the reduction in electrotonic coupling between cells.

The aim of the work described in this chapter is to examine the effect of different forms of ventricular pacing protocols on the activation pattern and action potential duration in isolated rabbit hearts in order to simulate the clinical ventricular stimulation regimens. The primary question to address is whether biventricular pacing results in a physiological pattern of epicardial activation times and action potential durations?

## Sudden cardiac death in heart failure

Heart failure is a common condition in western society with an associated high mortality rate (McMurray and Stewart, 2000). It is a complex and diverse clinical syndrome where patients are exposed to competing risks of sudden cardiac death or death from progressive pump failure (Packer, 1985). To prevent the occurrence of arrhythmic sudden cardiac death (SCD) constitutes a particular obstacle because accurate risk prediction is difficult in such a vast and heterogeneous population (Gehi et al., 2005).

In many cases, the exact causes of sudden cardiac deaths are difficult to classify as they are typically unexpected and so are often unwitnessed. The prevalence of SCD in heart failure comes mainly from clinical trials and observational studies, in which the definition of SCD is arbitrary and pragmatic (Myerburg and Castellanos, 2006). The accepted definition is death from a cardiac cause, which is sudden and unexpected, in the absence of progressive cardiac deterioration, either within one hour of cardiac symptoms, in bed during sleep or within 24 hours of last being alive (Greenberg et al., 2004). Based on these definitions of endpoint classification for SCD, as much as 50% of total mortality in heart failure is due to SCD (Group and others, 1999).

A number of different underlying pathologies, including ventricular arrhythmias, acute cardiogenic shock, tamponade and acute pulmonary embolism, may result in sudden cardiac death. There is a debate over the relative importance of arrhythmic or vascular events as causes of SCD in heart failure (Cleland et al., 1999). Data regarding the specific aetiology of SCD are difficult to gather, but where they are available, recordings from monitored episodes of SCD show that the cause is ventricular arrhythmia in around 85% of cases (Engdahl et al., 2002). Therefore, it is reasonable to assume that the majority of the SCD in heart failure is arrhythmic in nature.

The main substrate for the development of ventricular arrhythmias in the heart is left ventricular (LV) remodelling, which includes varying degrees of scar formation, chamber dilatation and hypertrophy, depending on the aetiology of heart failure (Burton et al., 2000). Electrophysiological changes have been shown to accompany LV remodelling in humans and animal models (Janse, 2004).

In man, pharmacological attenuation of LV remodelling is associated with a reduction in mortality (Pfeffer et al., 1992). Coronary heart disease (CHD) is among the most common causes of heart failure (McMurray and Pfeffer, 2005) and patients with heart failure and CHD remain at risk of acute myocardial ischemia and myocardial infarction (MI), either of which may trigger ventricular arrhythmias. Autopsy studies suggest that acute coronary events are implicated in around 50% of sudden deaths in heart failure patients (Uretsky et al., 2000). Optimal pharmacological therapy for low ejection heart failure now includes a renin-angiotensin-aldosterone system blockade (McMurray et al., 2003), often with multiple agents and in addition to diuretic therapy, in patients who commonly have impaired renal function (Hillege et al., 2006). These combinations may precipitate electrolyte abnormalities, particularly abnormalities of serum potassium, which can predispose patients to ventricular arrhythmias.

## Ventricular arrhythmias

### Ventricular Tachycardia

Ventricular tachycardia (VT) is a condition that affects the heart, causing an irregular rapid heart rate. In general, VT is caused by abnormal electrical circuits originating from diseased areas of the ventricular myocardium. This can result in a rapid heartbeat, preventing effective ventricular refill and impaired cardiac output. VT has various forms of classification, however, in general it can be classified as the presence of three or more beats in a row on a ECG that originate from the ventricle at a rate of >100 beats per minute.

### Ventricular Fibrillation

Ventricular fibrillation (VF) is a cardiac arrhythmia in which the electrical activity of the ventricles is rapid, chaotic and uncoordinated. This renders the ventricles unable to contract synchronously and results in the immediate loss of cardiac output and death, unless corrective measures are undertaken. Although in humans VF can be precipitated by a wide variety of conditions, ranging from electric shocks to drug overdoses, it is usually seen in the context of coronary artery disease. In an ECG, VF can be identified by chaotic irregular deflections of

varying amplitude with no identifiable P waves, QRS complexes or T waves with a beat rate between 150 and 500.

## Mechanisms of ventricular arrhythmias

Normal electrical conduction in the heart involves an AP originating from the sino-atrial (SA) node, conducted through the atria via the atrio-ventricular (AV) node down through the Purkinje fibres and then to the ventricles. Abnormality in the properties of ionic currents can lead to abnormal impulse generation and/or propagation that lead to electrical disorder in the ventricles.

Three main mechanisms of ventricular tachyarrhythmias are:

1) Automaticity

2) Triggered activity

3) Re-entry

In the case of re-entrant arrhythmias, the first and second mechanisms are potential triggers for the arrhythmia, while re-entry itself maintains the arrhythmia.

### Automaticity

Automaticity is a normal feature in the cells in the sino-atrial node. In this case, the electrical behaviour is determined by the expression of channel proteins, including the pacemaker current ($I_f$), the T-type $Ca^{2+}$ current ($I_{CaT}$), and deactivation of delayed rectifier potassium current ($I_{Kr}$ or $I_{Ks}$). Under normal conditions in the ventricle and atria, $I_f$ is absent or its activation voltage is too negative. However, Carmeliet et al. demonstrated that ß-adrenergic stimulation in Purkinje fibres shifts the activation kinetics of $I_f$ to a less negative activation potential thus enhancing the diastolic repolarisation (Carmeliet and Vereecke, 2002). Under these circumstances, Purkinje fibres may be the source of arrhythmic triggers.

### Triggered activity

There are two types of triggered activity; early afterdepolarisations (EADs) and delayed afterdepolarisations (DADs). The membrane potential at the onset differentiates between these two types of triggered activity; EADs occur during phase 2 and phase 3 of AP, whereas DADs occur immediately after the membrane potential has returned to the baseline (phase 4). These triggering events (EADs and DADs) are most commonly observed during plasma electrolyte imbalances (low $[K^+]_e$, $[Ca^{2+}]_e$, $[Mg^{2+}]_e$ and pH) and they are more common in heart failure (Pogwizd et al., 2001). Delayed after-depolarisations are caused by spontaneous release of $Ca^{2+}$ from the sarcoplasmic reticulum (SR) of cardiac muscle during diastole (Pogwizd et al., 2001), the raised intracellular $Ca^{2+}$ is extruded mainly by the electrogenic $Na^+/Ca^{2+}$ exchanger and the subsequent inward current can depolarise the cardiac cell sufficiently to activate $I_{Na}$ and generate a subsequent arrhythmic action potential. These events occur when the SR $Ca^{2+}$ content is higher than normal or when the SR $Ca^{2+}$ release channel is sensitised to cytoplasmic $Ca^{2+}$.

The mechanism of EADs is less well defined. A common cause of EADs is prolongation of the APD and the extension of the plateau phase sufficiently to allow reactivation of inward currents $I_{CaL}$ (Pogwizd et al., 2001). Prolongation of APD can be due to bradycardia or inhibition of repolarising currents (e.g. $I_{Kr}$).

### Re-entry

Botting et al. stated that of the three main mechanisms, only re-entry has been demonstrated as the arrhythmogenic mechanism during acute ischemia (Botting et al., 1985). However, in most of the cases, re-entry is triggered by an ectopic impulse in the context of an abnormal dispersion of refractoriness between the normal and ischemic myocardium. Experimental studies with animal models have demonstrated that lethal arrhythmias occur most frequently 4-7 minutes post occlusion due to re-entrant mechanisms (Steven M Pogwizd and Corr, 1987; Kuo et al., 1983; SCHERLAG et al., 1974; Elieser Kaplinsky et al., 1979; ELIESER Kaplinsky et al., 1979; Fleet et al., 1994). Acute regional myocardial ischemia in canine right ventricular wedge preparations results in heterogeneous loss of the transient outward potassium current ($I_{to}$)-mediated AP dome across the ischemic

border leading to phase 2 re-entry which is capable of initiating VF by producing R-on-T extra systoles (Yan et al., 2004).

During acute myocardial ischemia, shortening of repolarisation by ATP-regulated potassium channel openers ($I_{KATP}$) has been reported to increase the susceptibility of the heart towards re-entry and fibrillation (Uchida et al., 1999; Padrini et al., 1992; Coromilas et al., 2002). The substrate for initiation and maintenance of ventricular arrhythmia during acute ischemia has been extensively studied in porcine and canine hearts. Janse et al. showed that during coronary artery occlusion in isolated perfused hearts, the "focal" mechanism occurs at the normal side of the ischemic border and the macro- and micro-reentry in ischemic myocardium are responsible for the very early ischemic arrhythmias (Janse et al., 1980). A study by Pogwizd et al. reported that during early ischemia in canine hearts, the initiation and maintenance of ventricular arrhythmia is due to both intramural re-entry and non-reentrant mechanisms. In both these studies, the arrhythmic event is preceded by ventricular premature beats (VPBs) (STEVEN M Pogwizd and Corr, 1987).

Chou et al. have demonstrated that during the sub-acute phase of myocardial infarction, the dynamic properties of the action potential and $Ca^{2+}$ cycling are heterogeneously altered in the peri-infarct zone which may promote ventricular premature beats and increase the incidence of wave breaks during VF (Chou et al., 2007). Several early studies in canine model of acute ischemia concluded that ectopic beats were generated near the infarct borders by automatic foci (Harris et al., 1954; HARRIS, 1950). The authors suggested that these events were triggered by the release of $K^+$ from ischemic cells, but given present knowledge of cardiac electrophysiology, this is unlikely to be the cellular mechanism, currently it is uncertain what circumstances in the peri-infarct zone may make premature electrical events more common.

# Isolated heart preparation

## The isolated mammalian heart preparation according to Langendorff

In 1895, Oskar Langendorff developed a method for the investigation of the isolated heart in which the excised intact heart could be kept alive for prolonged periods of time (Langendorff, 1895). There exist two principal types of Langendorff preparations: the constant flow and the constant pressure model.

The technique involves inserting an aortic cannula into the ascending aorta of the heart and perfusing solution retrogradely down the cannula. Retrograde flow delivered either by a hydrostatic pressure (constant pressure model) or by a peristaltic pump (constant flow model), closes the leaflets of the aortic valve preventing perfusate entering the left ventricle and permitting the flow of perfusate into the coronary arteries via the ostia at the aortic root (Figure 1.5). Following coronary circulation, the perfusate enters the right atrium via the coronary sinus, into the right ventricle and eventually exits out the pulmonary artery. The advantages and disadvantages of both modes of Langendorff perfusion (constant pressure vs. constant flow) is summarised in Table 1.1.

In order to measure cardiac contractile function in Langendorff preparations there are typically two options. First, is to use a force transducer with a hook and thread sutured to the surface of the heart to measure isometric force of contraction (Beckett, 1970). Alternatively, a latex balloon attached to a pressure transducer can be inserted into the cavity of the left ventricle via the left atrium in order to measure isovolumetric ventricular pressure (Güttler et al., 1981). Using this option, it is possible to monitor developed force in the whole ventricle.

**Table 1.1 Advantages and disadvantages of Langendorff perfusion modes**

| Langendorff Perfusion Mode | Advantages | Disadvantages |
|---|---|---|
| Constant Pressure | • Physiological mode<br>• No risk of damaging heart by unintentionally high pressure<br>• Most commonly used method, facilitates comparison with large body of literature | • Heart does only isovolumetric work<br>• Can involve higher cost<br>• Since flow is not constant effective dose is difficult to calculate |
| Constant Flow | • Lower cost<br>• Simple methodology usually employed in compound screening<br>• Facilitates measurement of vascular resistance | • Heart does only isovolumetric work<br>• Non-physiological mode<br>• Risk of massive pressure may cause heart damage |

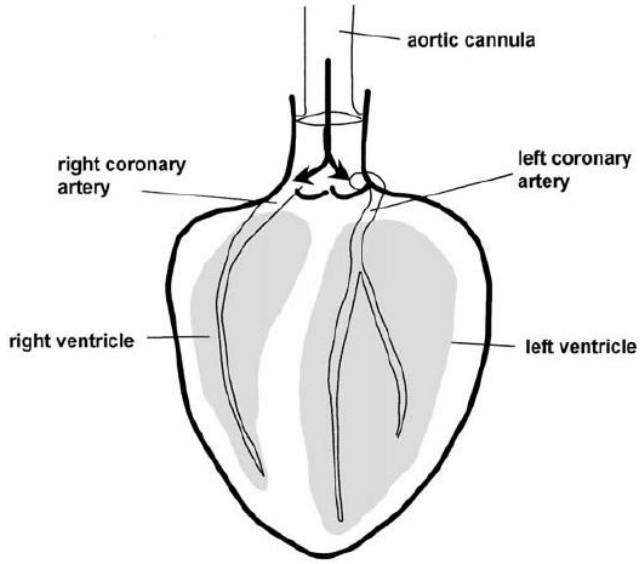


**Figure 1.5 Langendorff method**
Schematic of isolated perfused heart in Langendorff mode (Dhein et al., 2005)

## Constant pressure model

A typical setup for a constant pressure model involves a reservoir (Boyle Marriot bottle) connected to a glass-column heat exchanger and connecting tube (Figure 1.6). The heart is then fixed to the aortic cannula via the connecting tube. Using this setup the heart can be perfused under constant hydrostatic pressure, dictated by the height of the reservoir. During constant pressure perfusion the heart maintains the ability to autoregulate coronary vascular tone, which is an

important consideration when studying the effects of ischemia-reperfusion injury and during changes in workload conditions.

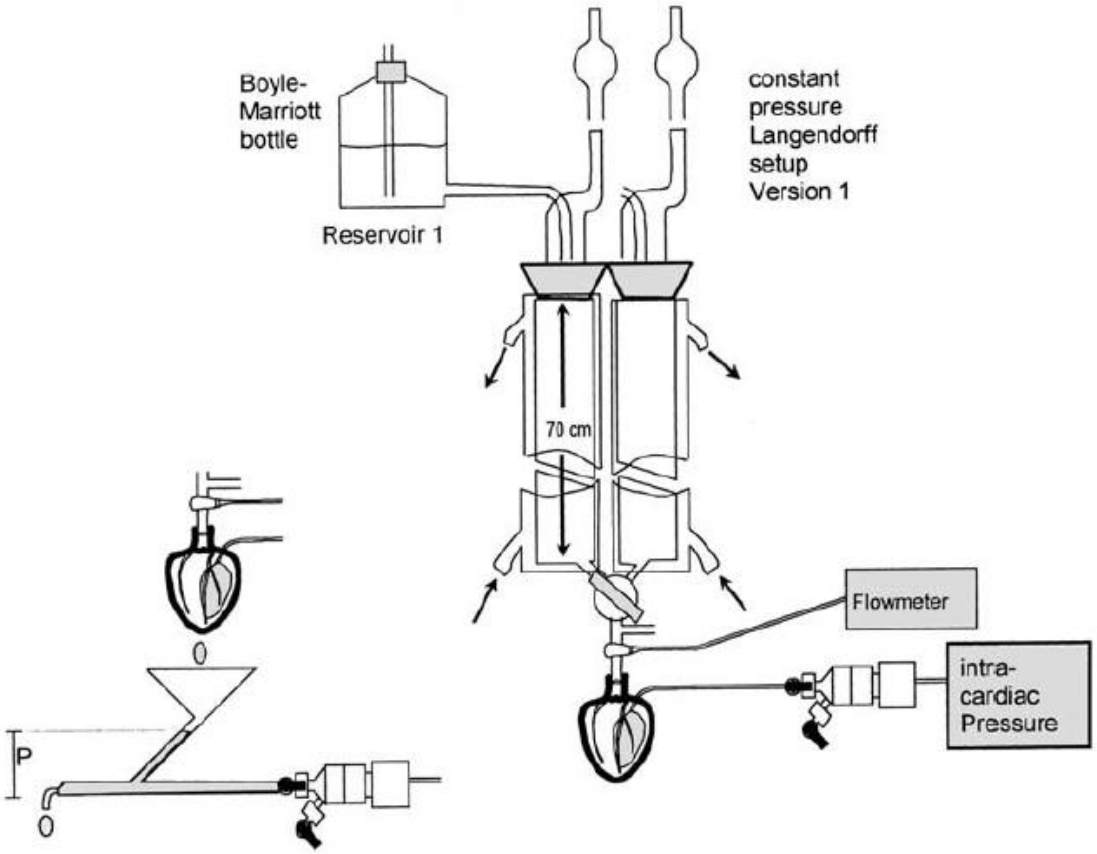


**Figure 1.6 A constant pressure model**
A schematic of a constant pressure Langendorff mode setup (Dhein et al., 2005).

## Constant flow model

A typical constant flow setup involves perfusing the heart via a peristaltic pump at a specified flow rate, via a glass-column heat exchanger and connecting tube (Figure 1.7). Under standard physiological conditions, the coronary flow within the heart can be estimated as a function of heart weight (Döring et al., 1988):

$$CF = 7.43 \times (Heart\ Weight^{0.56})$$

Using an in-line transducer coronary perfusion pressure can also be monitored and used as an index of coronary vascular resistance. Constant flow perfusion allows for precise and reproducible experimental conditions, where coronary pressure can be easily monitored alongside constant flow.

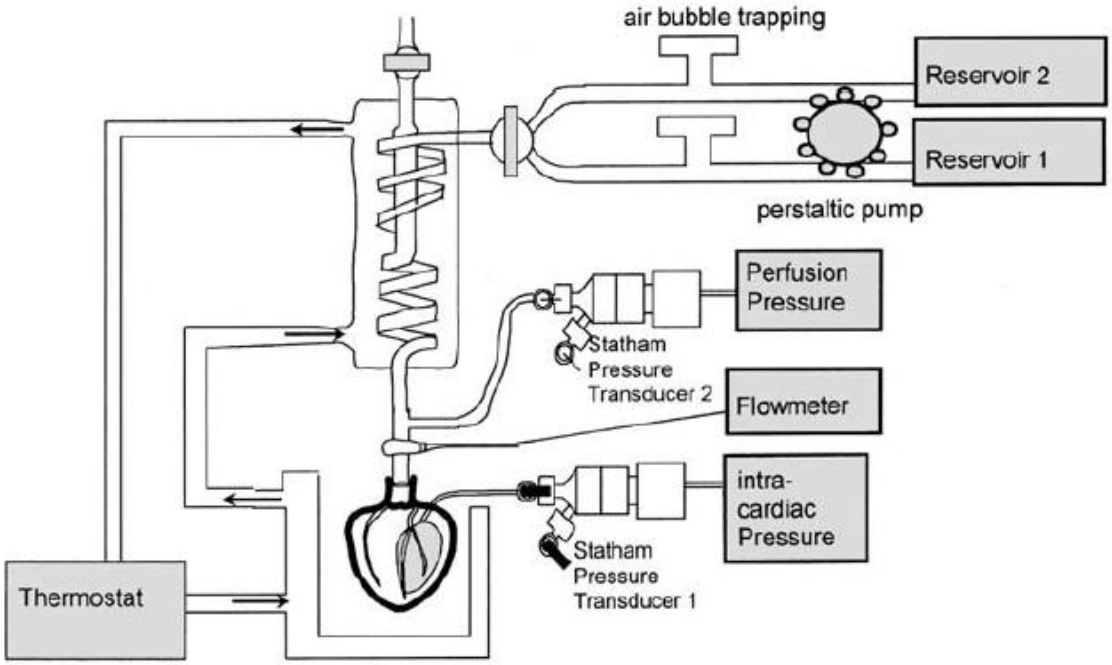


**Figure 1.7 A constant flow model**
A schematic of a constant flow Langendorff mode setup (diagram courtesy of (Dhein et al., 2005))

# Optical mapping

## Background

The majority of what we know now about changes in membrane potential within heart cells is based on measurements made from impaling single cells with glass pipette microelectrodes ('gold standard'). This method of recording membrane potential has the advantage of being able to record at high temporal resolution, in addition to permitting direct recording of intracellular electrical activity in single cells. However, this technique is impractical when trying to make stable recordings of membrane potential from more than one site simultaneously and when studying whole heart preparations. In order to understand the mechanisms

that lead to arrhythmias and loss of normal contractile function within the whole heart, accurate visualisation and mapping of the spread of electrical activity at multiple sites simultaneously across the heart is necessary. Recordings of monophasic action potentials using extracellular contact electrodes was proposed as a possible solution to recording from multiple sites simultaneously. However, these recordings are constrained to the use of a limited number of electrodes (~dozens) due to the technical challenges involved in maintaining adequate contact pressure at all electrodes.

For this reason, attempts were made to develop a technique that could transduce membrane potential to an optical signal that could be recorded non-invasively from multiple sites with sufficient temporal and spatial resolution to resolve normal and abnormal/arrhythmic event sequences. A further advantage of optical methods is apparent when studying mechanisms of defibrillation, which would prevent the recording of signals by conventional methods using electrodes, due to the incompatibility between conventional amplification of millivolt signals and the magnitude of typical defibrillation shocks (tens to hundreds of volts). The first report of this technique was in 1968, where changes in fluorescence associated with membrane potential were recorded from isolated nerve cells from a giant squid axon (Tasaki et al., 1968; Cohen et al., 1968). Although the initial recordings of intrinsic signals obtained from light scattering and bifringence within axons followed the rapid time course of the action potential (AP), they had poor signal-to-noise ratio (SNR). A significant advance was the ability to record extrinsic signals obtained by staining the axons with fluorescent dyes, resulted in significantly improved SNR. Following on from their initial work and in the pursuit of usable signals, Cohen and Salzberg screened over 1,000 dyes as possible probes of membrane potential (Cohen and Salzberg, 1978). Salama and Morad using the voltage-sensitive dye Merocyanine-540 made the first set of successfully recorded optical action potentials in mammalian hearts in 1979 (Morad and Salama, 1979). Following the success of voltage-sensitive dyes, optical mapping has become a widely used tool in experimental cardiac electrophysiology, revolutionising research into our understanding of the mechanisms of cardiac electrical activity at the cellular to whole heart level.

## Fluorescence

Fluorescence is the emission of light (photons) that occurs after the absorption of light, typically of shorter wavelength. The absorption and emission wavelength properties are based on the fluorescent molecule (fluorophore) used. When illuminating a fluorescent compound with an excitation light source, the fluorophore absorbs light energy, resulting in a shift in the energy of the electrons from a ground state ($S_0$) to an excited state ($S_1$ or $S_2$). The probability of absorption depends on the wavelength of excitation light. When the electron energy returns to the ground state, the fluorophore emits a photon of less energy and longer wavelength. The difference in the peaks of the absorption and emission spectra is known as the Stokes-shift (Figure 1.8). The entire process can be best summarised via a Jablonski diagram, as shown in Figure 1.9.

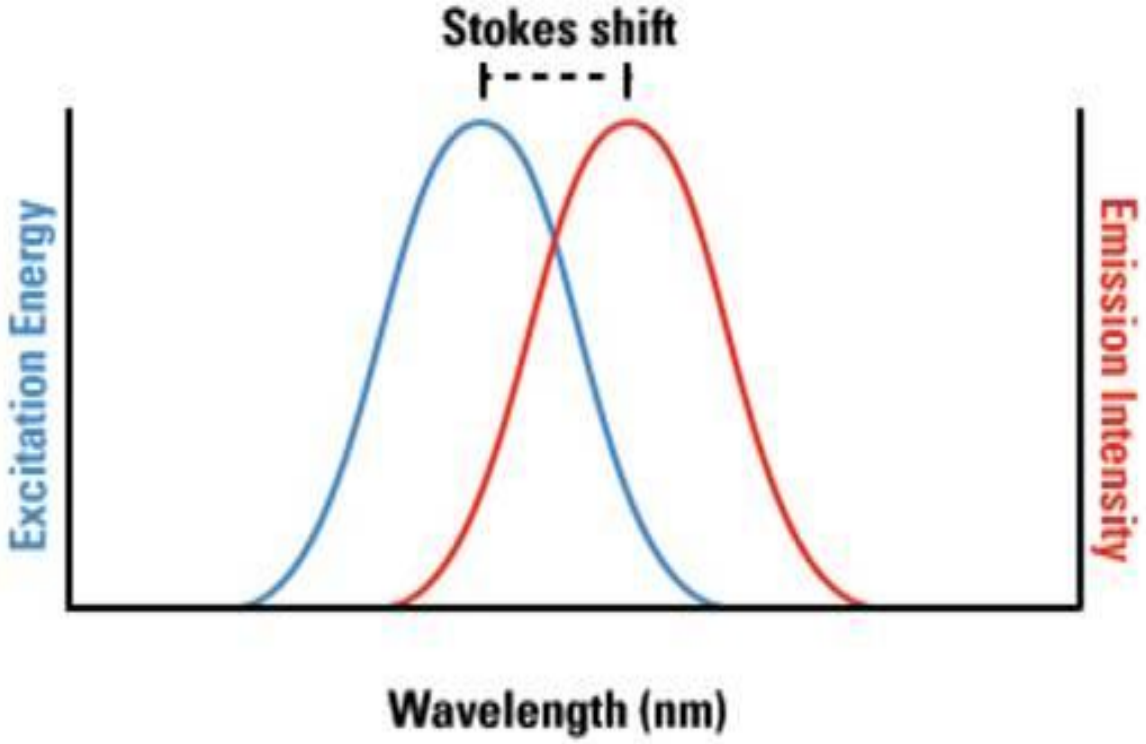


**Figure 1.8 Stokes' shift between the peaks of absorption and emission spectra (courtesy of ThermoFisher Scientific)**

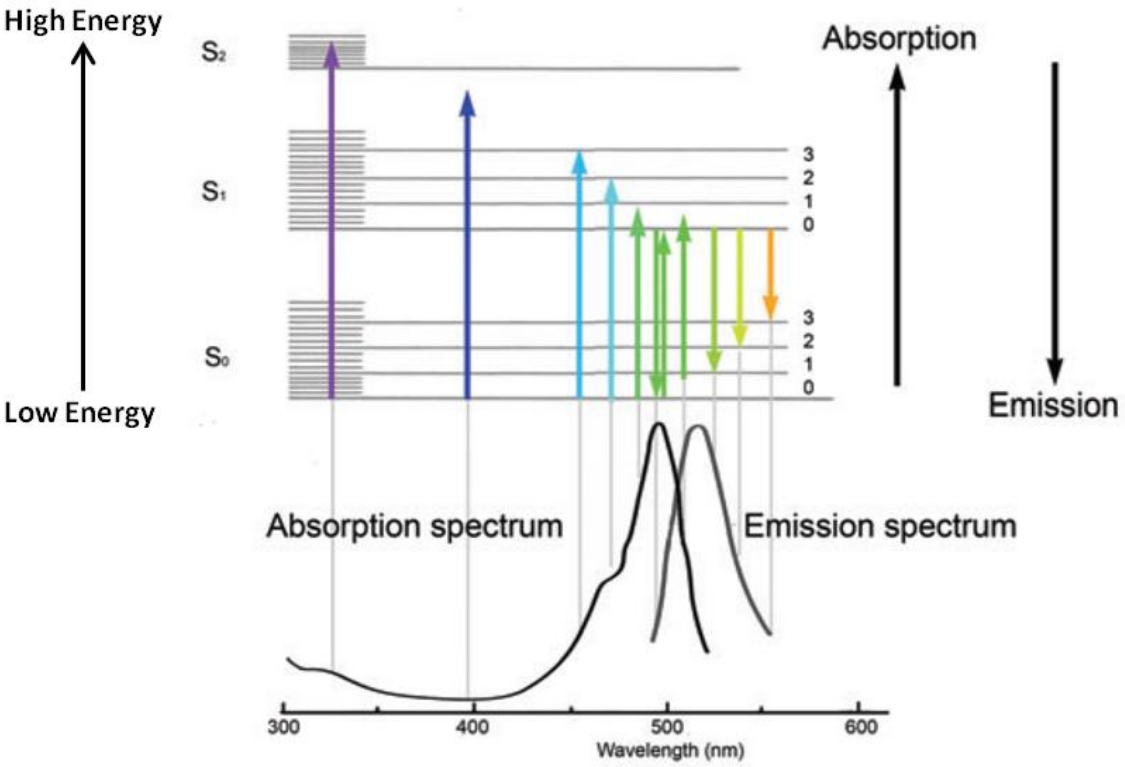


**Figure 1.9 Jablonski diagram**

**This diagram shown the different electrotonic states ($S_0$, $S_1$, and $S_2$) of the fluorophore with its corresponding absorption and emission spectra (courtesy of (Lichtman and Conchello, 2005)).**

## Voltage-sensitive dyes

### Mechanism of action

Voltage-sensitive dyes (VSD) are fluorescent compounds with a high affinity for the plasma membrane of cells which change their fluorescence spectra in response to changes in transmembrane potential, (Loew, 2011). The aminonaphthylethenylpyridinium (ANEP) family of dyes have become popular in studies of electrical activity in both neuronal (Grinvald and Hildesheim, 2004) and cardiac preparations (Salama and Choi, 2000). Among the most common ANEP dyes are di-4-ANEPPS and di-8-ANEPPS which when bound to the cellular membrane exhibit a fairly uniform 10% change in fluorescence intensity per 100mV in cardiac tissue. In general, di-4-ANEPPS is used in short-term experiments (over hours) due to the rapid loading and internalisation of the dye in the cell, whereas di-8-ANEPPS has significantly extended loading times and is retained for longer in the outer leaflet of the plasma membrane.

Consequently, di-4-ANEPPS has become the standard for optical mapping studies of electrical activity in whole heart preparations (Efimov et al., 2004; Loew, 2001). VSD delivery to the whole heart, cardiac tissue or isolated myocytes is typically through bolus injection into the coronary arteries via the perfusion system or direct loading of the dye via the cell culture medium. In the case of di-4-ANEPPS, the dye molecules intercalate themselves into the extracellular side of the cell membrane due to affinity between the pair of hydrocarbons on the dye molecule and the amphiphilic lipid molecules in the membrane surface (Loew, 1996). The chromophore (the part of the molecule that gives it colour) orientates perpendicular to the membrane surface. The action of Di-4-ANEPPS can be best explained by the electrochromic theory, as illustrated in Figure 1.10.

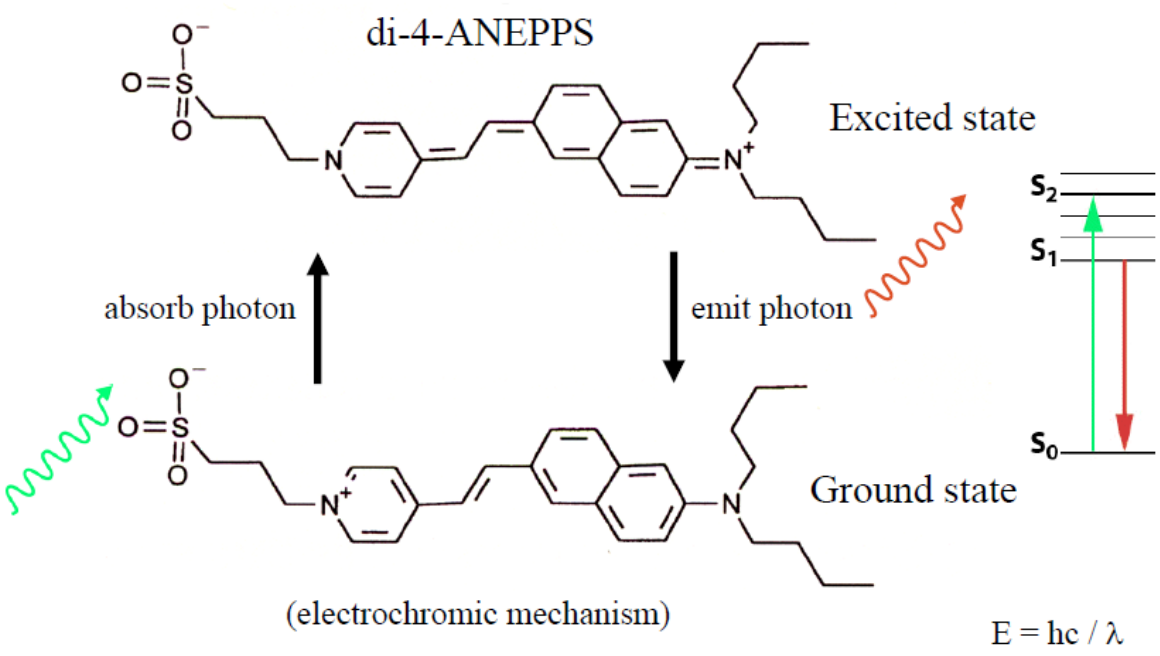


**Figure 1.10 Electrochromic mechanism**

**Illustration of electrochromic mechanism in di-4-ANEPPS dye molecule**

During excitation of the membrane, the dye molecules undergo a charge redistribution whereby causing a shift in the spectrum when membrane potential changes. In this case, the spectrum shifts to shorter wavelength upon membrane depolarisation, as depicted in Figure 1.12 (Loew, 2011).

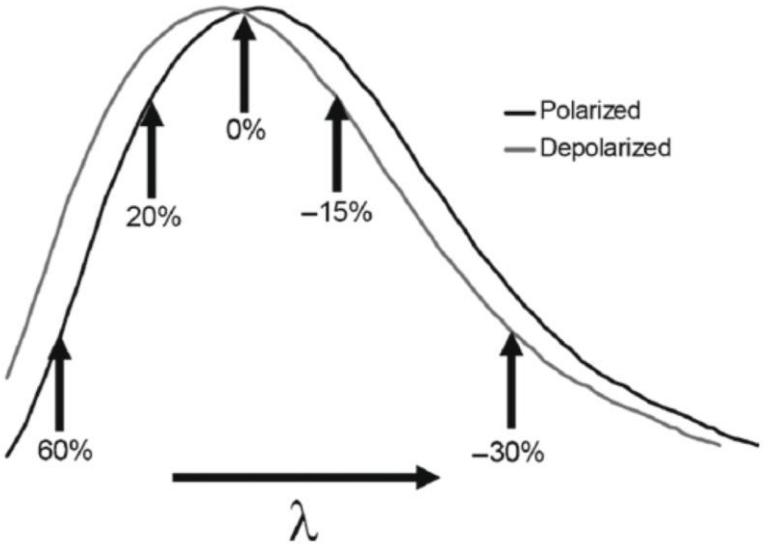


**Figure 1.11 Spectra shift**
**The shift in spectra in response to depolarisation (Loew, 2011)**

For example, during a typical action potential, depolarisation of the cell results in the resting transmembrane potential ($V_m$ = -90mV) rising rapidly toward a less negative voltage ($V_m$ = -40mV and 0mV), during which time the spectra of fluorescence emission shifts to the left, as indicated by the arrows in Figure 1.12. The figure shows a shaded region under each spectra corresponding to the amount of light that passes through the emission filter and is recorded by the photodetector. The emission filter permits the transmittance of light above a certain wavelength signified by the vertical line.

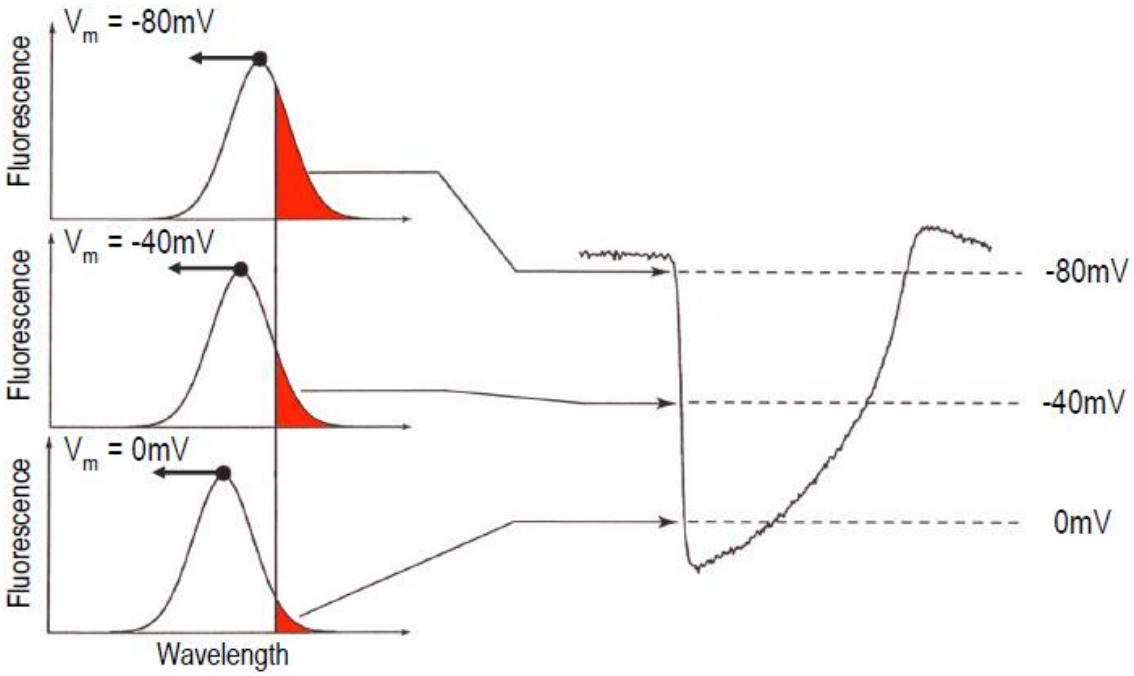


**Figure 1.12 Emission spectra shift**

**Change in emission fluorescent spectra with change in membrane potential, where arrows indicate the direction of shift in spectra with respect to wavelength.**

Di-4-ANEPPS is widely used in cardiac preparations due to its very rapid response times, in the order of microseconds, in reaction to changes in membrane potential. Therefore, even the rapid upstroke (~5-10ms) of a typical cardiac action potential can be reliably and accurately represented by changes in fluorescence. However, ANEPPS dyes tend to have a low dynamic range, where the magnitude of the potential-dependent fluorescent change in di-4-ANEPPS ranges between 2-10% per 100mV. Optical measurements are quantified as a change in fluorescence (ΔF) or as a fractional change in fluorescence (ΔF/F) (ratio between the change in fluorescence and the background fluorescence).

Some of the side effects of voltage-sensitive dyes on cardiac preparations include phototoxicity and coronary vasoconstriction leading to changes in perfusion pressure. Phototoxic effects arise from intense illumination of the preparation, inducing photodynamic damage from the formation of reactive-oxygen intermediates and/or free radicals (Schaffer et al., 1994). However, with careful loading of dye and recording and illumination of the preparation these side effects are generally negligible.

## Illumination

The choice of light source for illuminating the preparation is a key consideration in any optical mapping setup. There are many different light sources currently used within optical mapping systems: tungsten-halogen (TH) lamps, arc lamps, laser and light emitting diodes (LEDs). TH lamps with a power of 100-250W have been the common choice in the past owing to their low cost, low noise, long life and flexibility due to their flat spectrum in the visible range allowing choice of excitation wavelength through use of an excitation filter (Fast, 2005). Arc lamps (typically Xenon or Mercury) also have a flat spectrum in the visible range, but are able to illuminate at higher light intensities. However, arc lamps are more prone to projection of imaging artefacts onto the sample under analysis, which impacts on the spatial uniformity of light, where stable illumination of the preparation requires specialized control electronics (Moe et al., 2005). Lasers can emit light rays at discreet wavelengths (monochromatic) that are almost parallel, such that the laser output can be focused into a high intensity, diffraction-limited spot (Parker, 2002). However, lasers typically suffer from increased noise, shorter lifespan and higher cost. LEDs have become an attractive alternative, particularly within optical mapping studies, due to their low power consumption, reduced imaging artefacts and low cost (Moe et al., 2005). More importantly, LEDs have a narrower spectral output range compared to white light sources, thereby reducing the need for additional optical filtering (excitation and heat filters) whilst giving greater flexibility over laser light by being able to cost-effectively illuminate over a wide range of wavelengths (Lakowicz, 2007).

## Detectors

There are three main types of sensors typically used in heart imaging applications – PDA, CCD and CMOS. One of the main factors determining the function of any camera sensor is its quantum efficiency (QE). Quantum efficiency is dependent on the wavelength of the incident light and describes the capacity of the sensor to absorb the incident photons, as shown in the example in Figure 1.13. Therefore, the quantum efficiency describes the sensitivity of a sensor at different wavelengths of light and the probability (0-100%) of detecting the incident photons. Two other important factors to consider are the temporal and spatial resolution of the detector, defined as the frames per second (fps) and the number of pixels in the detector, respectively.

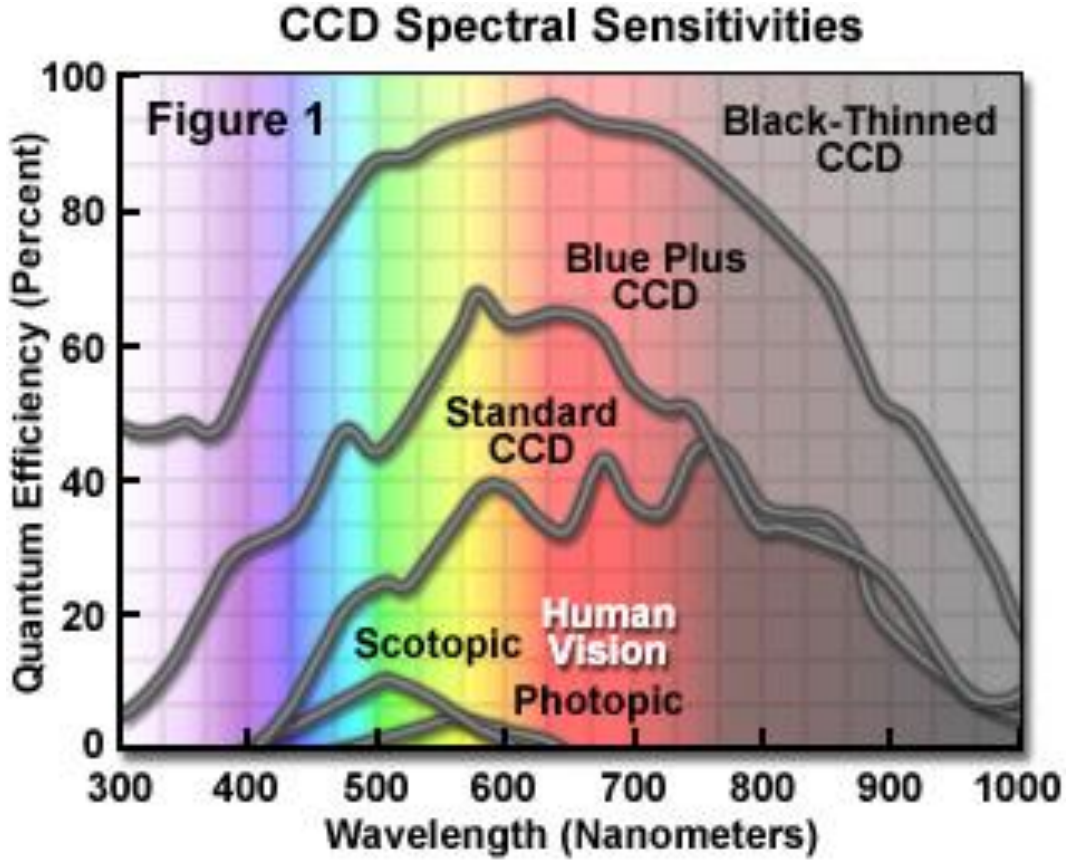


**Figure 1.13 CCD spectral sensitivities**

**An example of how different charge coupled devices (CCD) react across the spectrum in terms of their quantum efficiency (courtesy of Hamamatsu web site).**

**Photodiode array (PDA)**

A PDA consists of a number of single element photodiodes laid side by side to form an array connected through external circuitry. PDA systems were first developed by Centronix and are now widely available through Hamamatsu and WuTech. Photodiodes are semiconductor p-n junctions, typically made of silicon, which transduce incident photons to electrical charge, where the generated current is proportional in strength to the incident light. The photo-generated current is converted to voltage via a current-to-voltage (I/V) converter, where it is passed to a signal conditioner/amplifier. The output is then recorded by a data acquisition system (ADC device) and passed to a computer. Each photodiode detects photons from a different region of the image, which corresponds to the photons emitted from a specific region of the heart. The main advantage of PDA systems is their large dynamic range, high sensitivity and temporal resolution. This is primarily because of the large pixel size (up to $1mm^2$), the continuous generation of photocurrent in response to membrane potential and the parallel readout from the diodes (Entcheva and Bien, 2006; Rosenbaum, 2001). Segment A of Figure 1.14 shows the high intensity limit of the Redshirt Imaging NeuroPDA in comparison to the NeuroCCD which saturates at significantly lower light levels. The QE for photodiodes is also very high (~90% at 600nm, in some cases) (Fast, 2005).

The main disadvantage of PDA systems is their limited spatial resolution (typically 256 pixels or less) and increased dark noise in contrast to their counterparts. Although it is possible to increase the number of photodiodes in an array to increase the spatial resolution this option is both costly and impractical (Entcheva and Bien, 2006). Segment C of Figure 1.14 is right-shifted in comparison to segment D for the NeuroCCD, showing the presence of increased dark noise for the NeuroPDA. In general, PDA systems are used in applications involving moderate to high intensity light levels and small areas of interest, as their noise characteristics decrease and their temporal resolution increases with reduction in sensor area (Parker, 2002). For example, they are widely used in mapping studies considering activation and repolarisation characteristics when investigating small regions on the surface of the heart (Rosenbaum, 2001; Salama and Choi, 2000; Efimov et al., 2004; Qu et al., 2007).

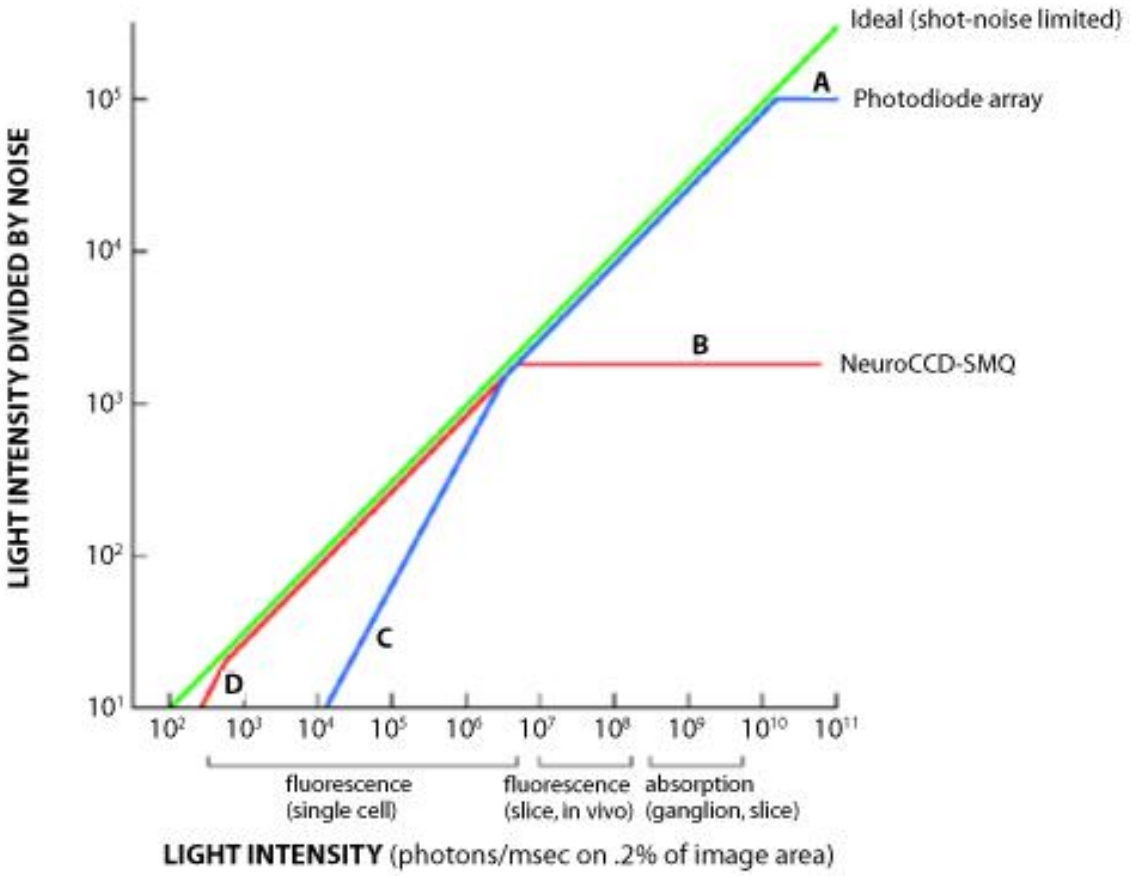


**Figure 1.14 Performance of two RedShirtImaging systems**

**Photodiode array (NeuroPDA – blue line) and a CCD (NeuroCCD – red line). The shot noise limitation is shown alongside the two systems over the range of intensities (green line) (courtesy of RedShirt Imaging website)**

## Charge-coupled device (CCD)

CCD sensors architecture differ from their PDA counterparts in that rather than being comprised of multiple discrete sensors connected through external circuitry they are monolithic sensors fabricated on a single semiconductor wafer. CCD sensors are integrative, collecting light over a period of time (exposure time), whereby charge is stored locally within the CCD elements until being transmitted to an on-chip readout amplifier, sequentially converted to voltage, and digitised. A typical CCD is comprised of a grid of charge registers with the capability to store charge associated with the number of incident photons detected at the charge register over the period of exposure. A CCD is comprised of a sensor and readout zone, where these come in a number of different configurations each with its own advantages and disadvantages. The most basic

type of CCD is a full frame transfer CCD, which uses progressive scan readout (Figure 1.15). The accumulated charge at each pixel is shifted vertically row by row to the serial output register whereby each row of the readout register must be shifted horizontally to readout each pixel. This process is susceptible to smearing caused by incident light on the sensor during the transfer of accumulated charge to the readout register. One possible solution is with a mechanical shutter used to cover the sensor during readout or by carefully controlling the timing of the illumination light source.

An alternative CCD architecture to avoid light smearing is the frame transfer CCD sensor, which is split into two parts (image array and storage array) (Figure 1.15). The image array is the light-sensitive region containing the sites for charge accumulation and the storage array is the region for charge transfer, protected from light using an opaque mask (typically made of aluminium). Using this architecture the accumulated charge is rapidly shifted (in the order of milliseconds) into the storage array for transfer to the serial output register. This minimises the light smearing by allowing charge to accumulate on the image array whilst stored charge can be read out. In addition, faster frame rates than the full frame CCD are possible. The main disadvantage of this type of CCD sensor is the cost due to the increased size of array needed.

Interline CCD's incorporate the charge transfer channels (interline mask) adjacent to each light-sensitive region allowing rapid and efficient shifting of accumulated charge (Figure 1.15). This allows for very rapid frame rates and virtually eliminates image smearing through electronic shuttering. One drawback of this architecture is that the interline mask reduces the overall light sensitive area of the sensor. Typically, these devices compensate for this by using microlens arrays to increase the photodiode fill factor and QE.

A more recent development in sensor technology is the EMCCD (electron multiplying charge-couple device), introduced in the early 2000's by Andor Technology Plc. Unlike a typical CCD, an EMCCD uses a solid state Electron Multiplying (EM) register or gain register prior to amplification by the output amplifier (Figure 1.16). This allows any weak signals to be multiplied before the output amplifier adds any readout noise. In the gain register charge is transferred across a large electric field (between voltage and clocked

electrodes) resulting in impact ionization and the generation of new electrons in a probabilistic fashion (EM gain). The main advantage of an EMCCD sensor is its sensitivity, whereby signals with acceptable SNR can be generated even under imaging conditions involving weak signals.

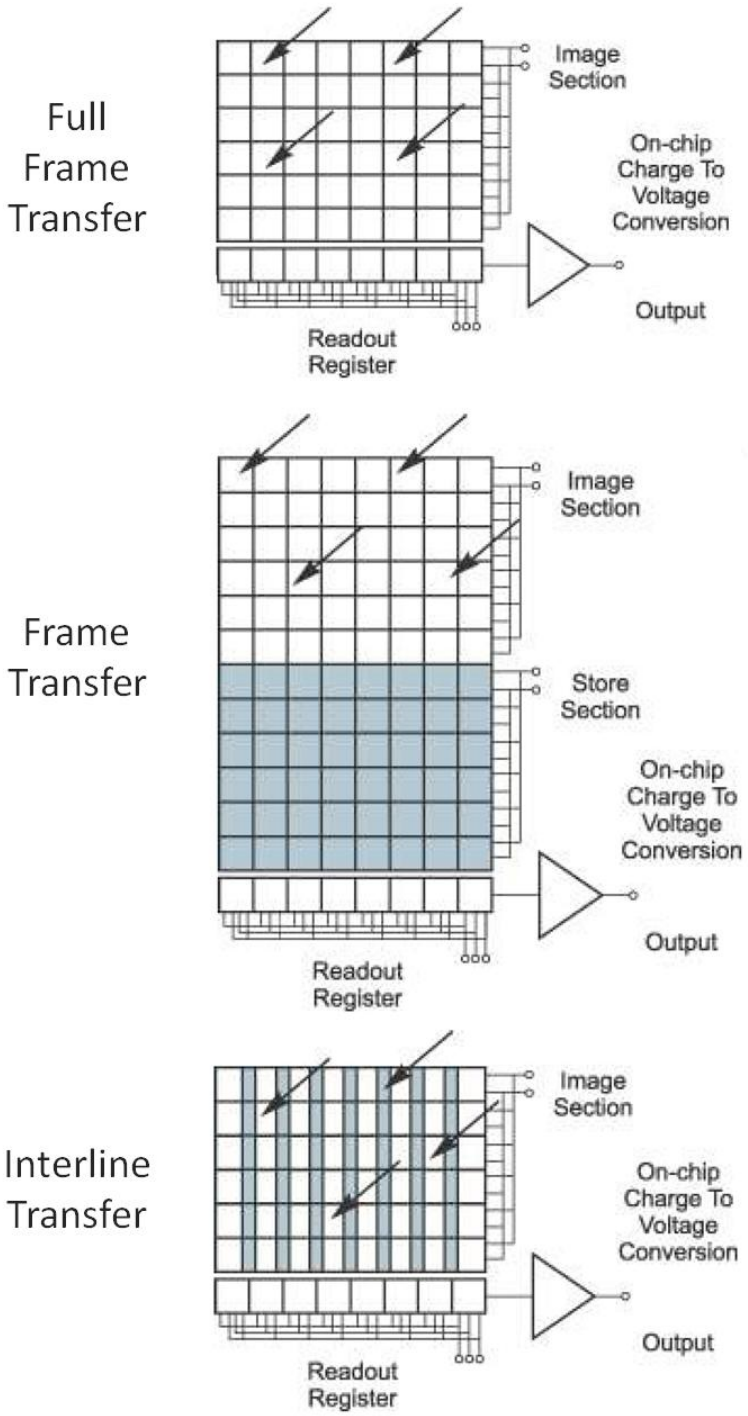


**Figure 1.15 CCD sensor types**

**Different types of CCD sensor (full frame transfer CCD, frame transfer CCD and interline transfer CCD) (courtesy of Andor Technology Plc.).**

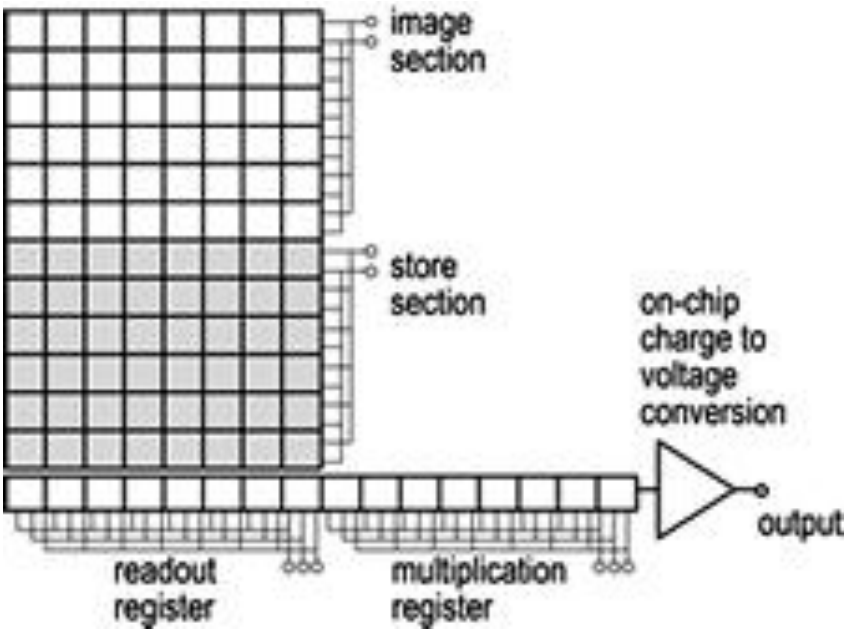


**Figure 1.16 EMCCD architecture**
**(courtesy of Andor Technology Plc.)**

The saturation of CCD systems are limited by the 'full well capacity', which defines the maximal amount of charge that can be accumulated for each CCD pixel element. The QE for some of the best CCD sensors is comparable with PDA-based sensors (~80%). Using back-illumination (back thinning) can give improvements in the QE of the sensor by increasing the amount of light which is captured. In general, CCD sensors are prone to readout noise generated from the on-chip readout amplifier and ADC process. Readout noise can be mitigated through slowing the readout speed of the ADC. However, a more common approach in order to increase SNR in CCD systems is through the process of binning. Binning involves combining charge from neighbouring pixels in a CCD array, where this process is offset with an overall reduction in the spatial resolution. CCD arrays can be manufactured with large numbers of photosensitive elements ($>10^6$), where the pixel size of CCD systems is in the order of micrometers. Therefore, CCD arrays have the capacity to make recordings at significantly higher spatial resolution than their PDA counterparts do. However, this is accompanied by a reduction in the level of temporal resolution that can be achieved. One common measure used to reduce the effects of dark noise within the semiconductor layers of the CCD is by reducing the temperature of the active components. By cooling the camera through thermoelectric or cryogenic refrigeration the generation of thermal energy

within the sensor and associated dark noise can be significantly mitigated (~50% reduction in dark noise for every 5˚C cooling), as shown in Figure 1.17.

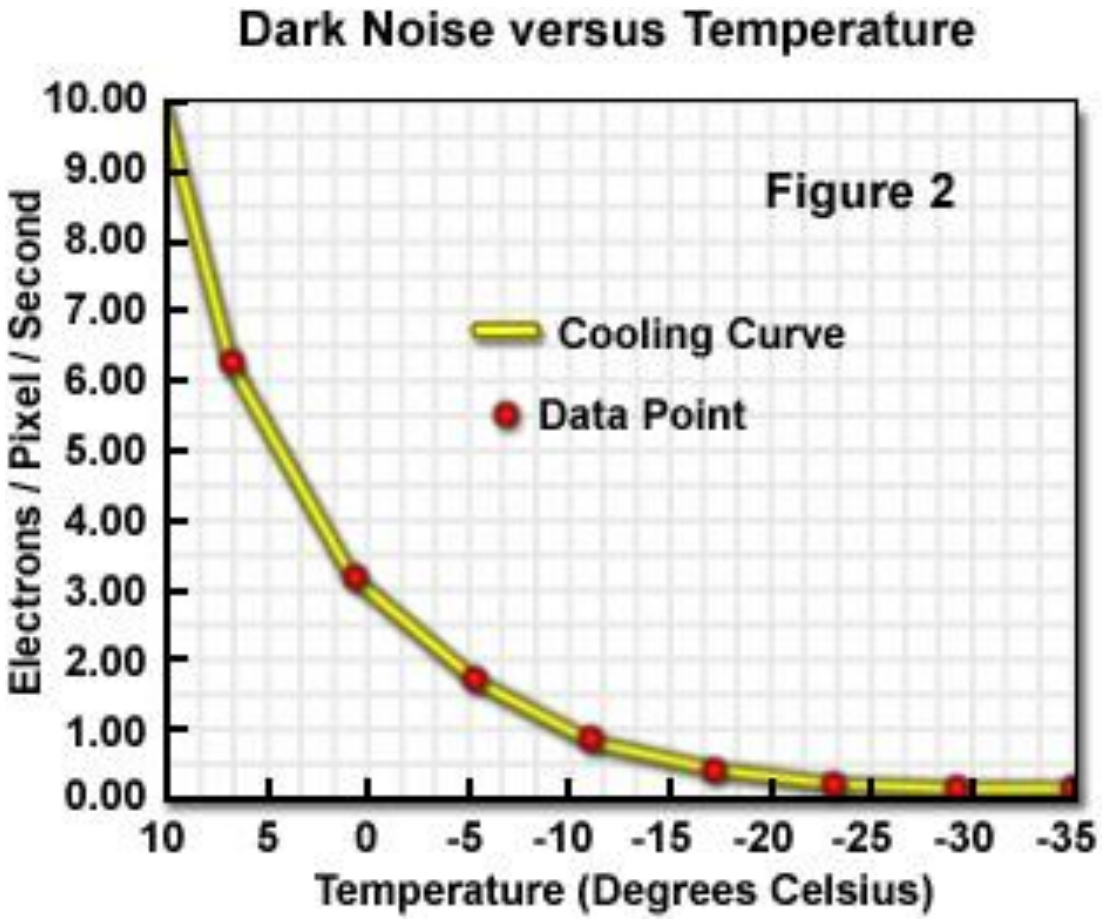


**Figure 1.17 Performance of CCD in relation to temperature**
**Considering dark noise in relation to temperature (courtesy of Olympus).**

### Complementary metal oxide semiconductor (CMOS)

CMOS sensors were invented (1960s) around the same time as the CCD and have a similar mechanism of sensing light (photoelectric effect). However, CMOS sensors differ significantly in that the collected charge within each pixel is converted to a voltage at each pixel site rather than being transferred to a readout register, permitting CMOS cameras to acquire at faster frame rates than conventional CCDs. As a result, each individual pixel has its own readout noise, in contrast to CCD sensors, which use a single readout structure.

## Noise

There are four different types of noise, which can affect an imaging system and the resulting signal to noise ratio (SNR) – Shot (photon) noise, dark noise, read noise and amplification noise.

### Shot noise

Shot noise is present within all optical sensors due to the quantum nature of light, whereby camera sensors can only collect whole numbers of photons. Therefore, there will be random statistical fluctuations when collecting photons from a source over any given period, where it follows a Poisson distribution.

This becomes of particular importance when the signal intensity is low as shot noise is an inherent part of the signal and thus a function of it:

$$Shot\ noise\ = \sqrt{Signal}$$

### Dark noise

Dark (current) noise arises from a build up of thermal energy within the sensor, which generates electrons over time independent of photons falling on the sensor. These additional electrons are then collected by the sensor and counted as signal. Therefore, due to the accumulation of dark current over time careful consideration is needed in preparations involving long exposure times. A common approach is to cool the camera in order to reduce dark noise

### Readout noise

Readout noise occurs because of the analogue to digital converter digitisation process, whereby each camera pixel is subject to readout noise directly proportional to the readout speed. However, this process varies greatly depending on the type of camera sensor used.

### Amplification noise

As part of the readout process, the charge from each pixel is typically converted to voltage and amplified prior to digitisation, resulting in not only the signal

being amplified but the input noise as well. In addition, the amplification process itself can add its own form of additional noise.

## Motion artefacts

One of the key considerations during optical recordings is the approach taken to effectively eliminate or at least minimise motion artefacts that result from whole heart contractility. Specifically, the contraction of the heart results in distortion of the optical signals due to the change in relative position of the heart with respect to the photodetector in time, as shown in the example in Figure 1.18.

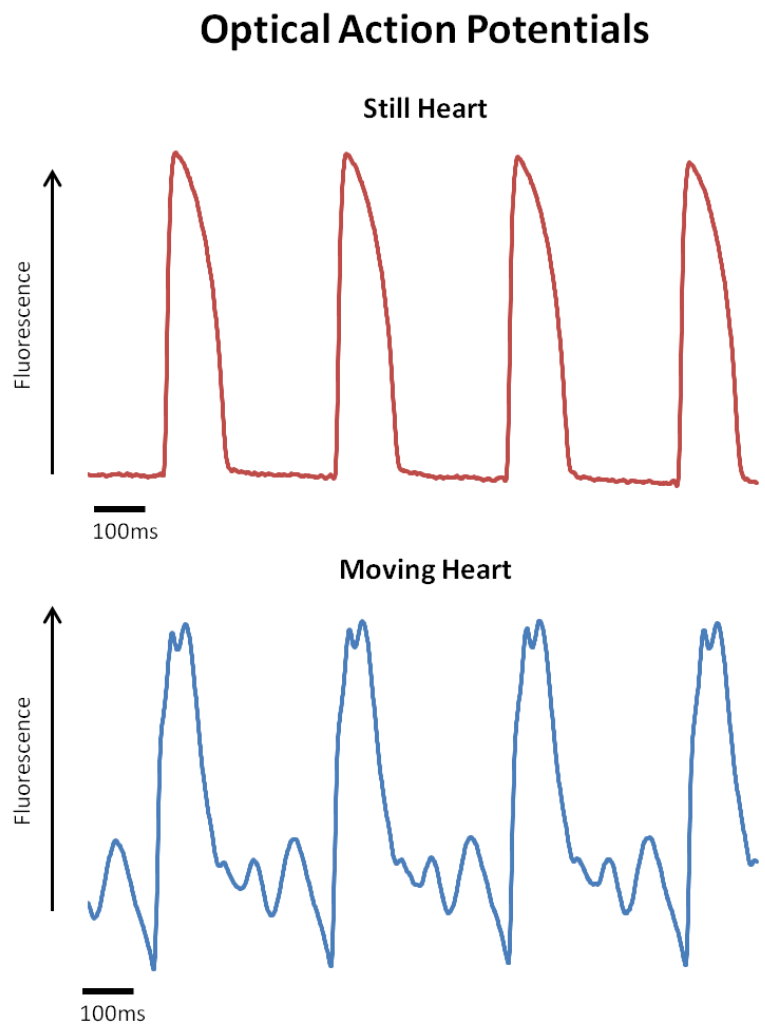


**Figure 1.18 Optical action potentials during contraction**

**Recording of an optical action potentials from both a contracting heart and a motion inhibited heart, showing the severity of distortion in the optical signals when the heart is still moving.**

Currently various methods exist for suppression or attenuation of these motion artefacts: mechanical restraint, reducing or abolishing extracellular calcium $[Ca^{2+}]_e$, use of excitation-contraction (E-C) uncouplers, ratiometry and motion tracking. Each of these is described below.

### Mechanical restraint

Mechanical restraint involves physical restraining the heart typically in the form of pressing the surface of the heart against a Perspex window (Efimov et al., 1994). For the suppression of motion, this approach is acceptable for short intermittent protocols, but less successful for long recordings due to the deterioration in the preparation. In addition, mechanical restraint is susceptible to the development of local ischemia if restraint is maintained for extended periods of time (>10 s) (Kettlewell et al., 2004).

### Reduction in extracellular calcium

Reduction in extracellular $[Ca^{2+}]_e$ was investigated as a possible method for suppression of motion artefacts in Langendorff perfused rabbit hearts measuring monophasic action potentials (MAP) at calcium concentrations of 1.4 and 0.7 mmol $l^{-1}$ (Kettlewell et al., 2004). Kettlewell et al. observed significant prolongation in $MAPD_{90}$ and decreases in conduction velocity with reduction in $[Ca^{2+}]_e$, alongside a decline in left ventricular developed pressure. There results suggest that extracellular calcium below ~1.8 mmol $l^{-1}$ results in marked changes in electrophysiological characteristics.

### Excitation-contraction (E-C) uncouplers

E-C uncouplers are one of the most common approaches used in the field of cardiac optical mapping for suppression of motion. The basis of these compounds is too suppress muscle contraction whilst ideally having no adverse affects on the electrical activity of the heart. Many such compounds are available, with the most common being 2, 3-butanedione monoxime (BDM), cytochalasin D (Cyto D), and more recently blebbistatin.

BDM acts through inhibiting myofibrillar ATPase and has been widely used in heart preparations in the past (Blanchard et al., 1990). However, it has been

shown to be have non-specific effects giving rise to species dependent changes on electrophysiology. In studies of transgenic mice (Baker et al., 2004) and rat (Coulombe et al., 1990; Verrecchia and Hervé, 1997) a prolongation in APD and reduction in conduction velocity at concentrations between 5-15 mmol $l^{-1}$ was observed. In contrast, a shortening of APD in swine (Lee et al., 2001), guinea pig and sheep ventricles (Liu et al., 1993) at 5-20 mmol $l^{-1}$ has been observed. In addition, BDM has been shown to flatten the electrical restitution curve in swine (Lee et al., 2001), canine (Riccio et al., 1999) and rabbit (Kettlewell et al., 2004; Banville and Gray, 2002), and linked with prevented induction of VF and in some cases converted VF to VT in swine ventricle (Lee et al., 2001).

Cytochalasin D acts through inhibiting actin filament polymerisation (Cooper, 1987). Studies in canine ventricle show no effects on repolarisation up to 80 mmol $l^{-1}$ (Wu et al., 1998). In swine ventricle, Lee et al. demonstrated no effects on APD or restitution at 10-40 mmol $l^{-1}$ (Lee et al., 2001). However, in studies of mice there was significant prolongation in APD and membrane hyperpolarisation at 20-80 mmol $l^{-1}$ (Jalife et al., 1998). Furthermore, there is evidence to show prolongation in APD and a reduction in conduction velocity in rabbit (Hayashi et al., 2003; Kettlewell et al., 2004). However, there is a disparity in the findings regarding restitution, where certain reports show an increase in the slope of restitution (Banville and Gray, 2002; Hayashi et al., 2003), whilst others observe a flattening of the restitution curve (Kettlewell et al., 2004). This variation may arise from differences in the pacing protocols used between studies. Lastly, in contrast to BDM, the effects of Cyto D are irreversible, whereby even after prolonged periods of washout the effects of Cyto D persist.

Blebbistatin is a myosin II ATPase inhibitor in the actin detached state (Allingham et al., 2005; Straight et al., 2003). In recent years, blebbistatin has become the most widely used E-C uncoupler in optical mapping studies of cardiac preparations (Fedorov et al., 2007). Blebbistatin has been shown to have minimal effects on ECG parameters and atrial and ventricular electrophysiology compared to other E-C uncouplers (Cyto D and BDM) (Lou et al., 2012; Fedorov et al., 2007). The main disadvantage of blebbistatin is its photosensitivity and phototoxicity. Studies show that both UV and blue light photo-inactivate blebbistatin resulting in toxicity from the production of free radicals damaging

the surrounding cells (Sakamoto et al., 2005; Kolega, 2004). Furthermore, contrary to previous studies recent findings by Ng et al. in rabbit ventricle suggest there are adverse effects to its use in whole heart experiments at 5μM, such as APD prolongation and increases in both the slope of restitution and VF threshold (Brack et al., 2013). As with other E-C uncouplers, it is important to consider these effects when evaluating experimental data.

### Ratiometry

An alternative approach to motion artefact reduction is to apply a ratiometric technique (Kong et al., 2003; Rohr and Kucera, 1998). The ratiometric technique has two common types: excitation ratiometry and emission ratiometry. Excitation ratiometry is accomplished through illuminating sequentially at two different excitation bands and measuring fluorescence at a single emission band. In contrast, emission ratiometry involves illuminating at a single excitation band and measuring at two different emission bands. The benefit of this latter approach is that artefacts due to motion can be attenuated by taking a ratio of the two continuous fluorescence signals (Knisley et al., 2000). Furthermore, it is possible using ratiometry to calibrate the optical signals to measure physical units ($V_m$). However, ratiometry is not a complete solution to the movement problem, where it is only effective at removing motion artefacts when the level of contraction is modest and the pattern of electrical activity relatively homogenous, where problems can be encountered when trying to image moving tissue where there is large pixel-to-pixel variation in AP morphology (Figure 1.19) (Bachtel et al., 2011).

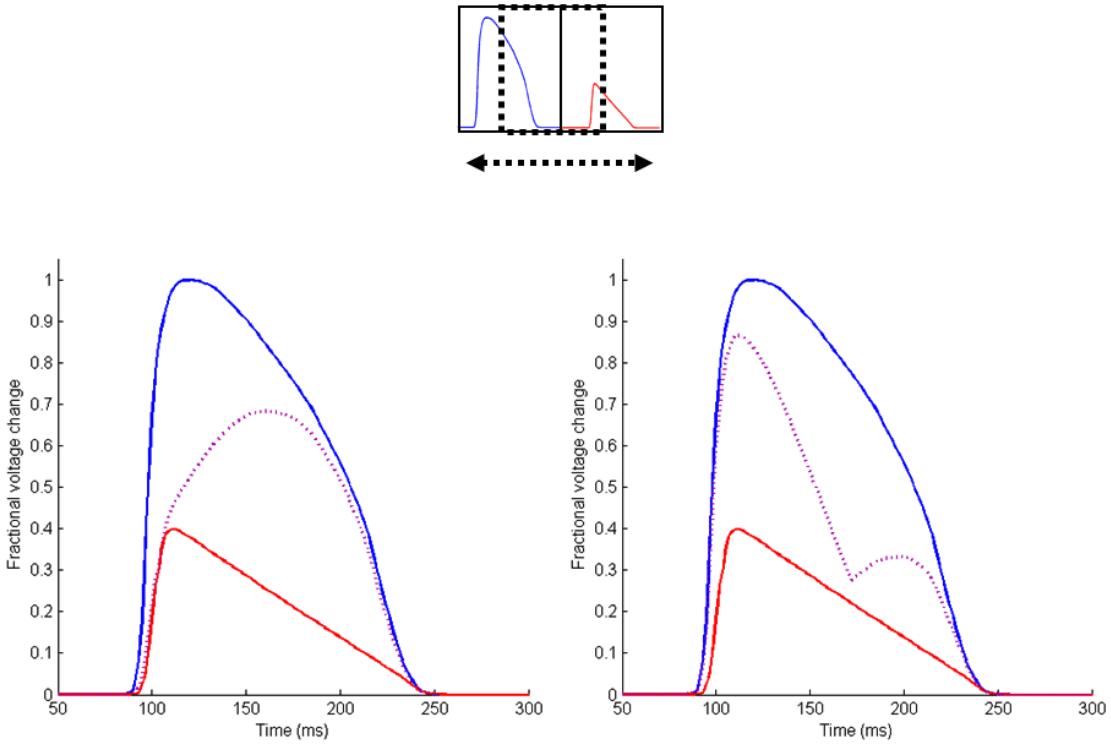


**Figure 1.19 Out of phase ratiometric signals**

**Ratiometry of neighbouring pixels containing different AP shapes (red and blue traces). Left and right panels show two possible resultant AP ratios (dashed purple trace) with different phase relationships between AP and movement timing. (courtesy of Francis Burton).**

## Motion tracking

Ultimately, all the above methods have significant drawbacks. Ideally, the movement of the heart preparation would be tracked in the absence of E-C uncouplers or other means of restraint and the signal reconstructed post acquisition using some form of image registration. The process of image registration is defined as determining a mapping between the spatial coordinates in one image to those in another to achieve biological, anatomical or functional correspondence (Rueckert et al., 1999). The method of image registration determines a transformation mapping from a reference image to a current image, where this procedure can be applied to a sequence of images. Image registration algorithms are composed of three main components:

1) The similarity measure

2) The transformation model

3) The optimisation procedure

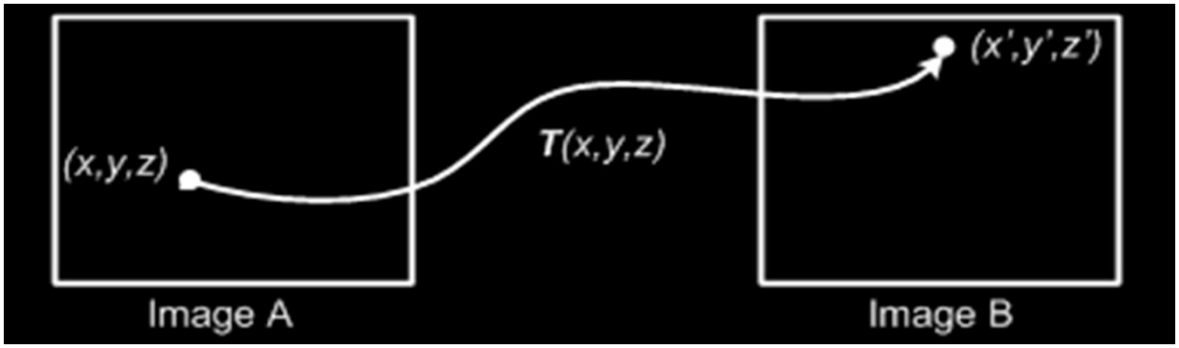


**Figure 1.20 Transformation mapping**
**Mapping of image pixel in image A (reference image) to image B (current image).**

### Similarity measure

The similarity measure can be described as the criteria or metric used to measure the correspondence between a pair of images. This measure can be divided into two types: feature-based or intensity-based approaches.

Feature-based approaches use local point landmarks in images as the criteria to match adjacent image frames in a sequence. Features and landmarks can be identified either manually by selecting ROIs of anatomical or physiological significance or automatically by pin-pointing specific patterns of intensity across an image. Once pairs of landmarks have been set between a pair of images it is possible to infer further correspondence information for the remainder of the image field between the pair of images using interpolation. In recent years, scale-space algorithms have became widely used as a means of feature detection in studies involving MRI imaging, ultrasound, CT and arterial imaging (Cheung and Hamarneh, 2007; Gatta et al., 2011; Moradi et al., 2006). Scale-space methods rely on multi-scale representations of images, typically by convolving with Gaussian kernels with increasing width. Using a scale-space representation permits the detection of information within the images that is invariant to different forms of transformation, such as scaling, translation and rotation, and some cases partial invariance to changes in illumination and affine transformations (ter Haar Romeny, 1999). Using this information a large number of landmarks between images can be generated for the purpose of motion compensation. Two commonly used scale-space methods for feature detection

are Scale-space Invariant Feature Transform (SIFT) (Lowe, 1999) and Speeded-Up Robust Features (SURF) (Bay et al., 2008).

Intensity-based approaches compare intensity patterns between images using a mathematical/statistical criterion. Intensity-based methods differ from feature-based methods in that image similarity is established from global metrics rather than local points of information. Therefore, intensity-based methods benefit from using the whole image information for correspondence, but lack the specificity of geometrical approaches when correspondence between points of interest (POI) is important (i.e. choice of anatomical POI). There exist a variety of measures of similarity, ranging from sum of squared differences and cross correlation coefficients to measures based on optical flow as well as probabilistic approaches such as mutual information (Crum et al., 2004). An important consideration when choosing any intensity-based similarity measure is the correspondence in intensity values between images, where different methods assume either no difference, linear or functional differences. In addition, careful consideration is necessary when registering multi-modal datasets.

**Transformation model**

The transformation mapping is characterised by the type of transformation model used, which exists to map the deformation between images and ultimately defines both how the images are altered in order to minimise the differences between images and interpolate between images when there is no useable information available. Firstly, it is necessary to classify the form of body being deformed in order to choose the correct type of transformation, which best fits, the deformation. Rigid registration identifies correspondence between images by a rigid transformation, which has 6 degrees of freedom. This only incorporates rotation and translation of images. Affine transformations have 12 degrees of freedom incorporating rotation, translation, scaling and shearing. Non-rigid transformations incorporate all non-linear forms of deformation and include large degrees of freedom, easily ranging into hundreds or thousands, dependent on the type of images being registered (Ino et al., 2005). Non-rigid registration is required for accurate compensation of motion within cardiac images, due to the complex deformations, which occur during the cardiac cycle.

Many different models exist for non-rigid types of transformation. One of the most commonly used methods is finite element-based (FE) models for analysing and quantifying deformation in cardiac images (Veress et al., 2005; Pham et al., 2001; McInerney and Terzopoulos, 1995). FE models are implemented by creating a mesh, which is closely representative of the heart. The mesh is then deformed based on the amount of motion within the image data. A similar, common approach is the use of splines, in which various different forms of splines have been used in the past. These include thin-plate splines (Kerwin and Prince, 1998; Amini et al., 1998) and more recently b-splines (Huang et al., 1999; Amini et al., 2001; Allan et al., 2011) for their applicability in cardiac imaging. Splines work in a similar manner to FE models in that they deform an object by manipulating an underlying mesh of control points allowing parameterisation of the transformation.

**Optimisation procedure**

The process of optimisation within the context of image registration refers to the manner in which the transformation is adjusted in order to find as accurate an image transformation as possible by minimising a cost function. The cost function is comprised of the measure of image similarity and typically other additional model constraints (i.e. smoothness constraint). The optimal alignment between images is found by minimising the cost function and numerically solving for the function parameters given a specified tolerance criterion. This procedure can be achieved through standard iterative schemes, such as Quasi-Newton methods, Powell's method, Steepest Gradient Descent and Downhill Simplex Method.

**Application to optical mapping**

Various different image registration methods have been applied in several studies of cardiac optical mapping as a novel alternative to the use of E-C uncouplers with promising results. Using this approach it is possible to make recordings with no adverse effects on the physiological response of the heart, in contrast to all other alternative approaches. In addition, due to the post-acquisition nature of the method it is possible to combine this method with ratiometry to enhance the correction of motion artefacts further.

In one of the first studies applying image registration to optical mapping, Rhode et al. used a mutual information measure in rabbit ventricle to map global motions using affine transformations (rotations, translations, shear and scaling) (Rohde et al., 2005). In this preliminary study, they considered only a small region of interest (ROI) on the epicardial surface, but are able to show a proof-of-concept in correcting for global motions. Mutual information measures have been used widely in medical image registration and have been shown to be accurate in matching images whose intensities values are not linearly related to each other (Crum et al., 2004). Using a similar approach Westergaard et al. used a mutual information measure, but extended the affine transformation model to a non-linear B-spline model in human hearts (Westergaard et al., 2008) in order to correct for motion during both sinus rhythm and VF conditions. Using a cross correlation measure Svrcek et al. considered small ROI's in rats (M Svrcek et al., 2009; M. Svrcek et al., 2009) in an attempt to characterise motion artefacts within optical signals. Their findings suggest that motion artefacts are principally as a result of two factors: a heterogeneous distribution of emission intensity across the epicardial surface due to non-uniform dye staining and contractile motion of the heart surface with respect to the photodetector.

Most of these studies have imaged specific ROI and not studied the motion of the entire epicardial surface of the heart. In contrast, Bourgeois et al. in swine hearts using a cross correlation measure mapped the entire epicardial surface (Bourgeois et al., 2011). In addition, instead of using the intrinsic contrast of the epicardial surface they attached high contrast fiducial markers to the epicardial surface in order to enhance the tracking of the heart surface. Similarly, Seo et al. in rabbits used bead markers on the epicardial surface in order to relate surface deformations to the initiation of arrhythmias (Seo et al., 2010).

More recently, Rodriguez et al. did a comparative study comparing two scale-space based approaches (SIFT and SURF) in whole rat heart images during optical mapping (Rodriguez and Nygren, 2012). Their findings suggest that the SIFT algorithm is more effective at finding landmarks across the epicardial surface with a more even distribution, which would result in better responses when applying the image transformations during registration. Following on from their initial study Rodriguez et al. extended their work to comparing SIFT to the Horn-

Schunck optical flow method, a well-established approach (Horn and Schunck, 1981; Rodriguez and Nygren, 2015). In this study, they found that while the optical flow method offered significant increased computational speed over SIFT, it also produced increased registration errors in comparison to SIFT.

One of the major limiting factors when applying image registration to 2D images is the assumption that the motion of the heart preparation is entirely planar. However, any out of plane motions that occur during these recordings will also be contributing to the overall motion artefact and cannot be corrected for using the current image registration approaches that have been discussed. Another common issue that can arise is the movement of pixels out with the image field of view. In these instances, it is not possible to recover the pixel. A possible solution to both of these issues would be to develop a camera model alongside a multi camera optical mapping setup in order to image the entire surface of the heart. Using this approach, it would be possible to correct for out of plane motion and deal with out of field pixels by having three-dimensional information of the surface of the heart.

## Clinical significance of optical mapping

Optical mapping provides a means to visualise at high temporal and spatial resolution the propagation of electrical activity and how it is altered under numerous physiological and disease conditions. Specifically, optical mapping presents a convenient way to study both the genesis and development of re-entry within the whole heart allowing predictions about arrhythmogenesis to be tested and advances in the design of novel antiarrhythmic therapies.

Hypothermia is a well-established clinical and physiological paradigm, a condition known to promote ventricular arrhythmias and cardiac arrest. In humans, hypothermia induced arrhythmias commonly appear at core temperatures below 28°C, including nodal rhythms, ventricular extra systoles, atrio-ventricular blocks and ventricular fibrillation (VF). The pathophysiology behind development of VF in the hypothermic heart is unknown (Tveita, 2000). Recent experiments have demonstrated hypothermia inducted conduction block and re-entrant VF in canine wedge preparations. In a study of mild hypothermia (30°C) in rabbit hearts, they reported slowed conduction velocity (CV) (Hsieh et

al., 2009), where these circumstances may favour the development of unidirectional block and VF. Optical mapping of rabbit hearts cooled to 17°C have also shown that severe hypothermia can induce spatial alterations in CV, a known predictor of VF (Egorov et al., 2012). It is unclear from previous studies whether electrophysiological changes and arrhythmic risk is directly related to the degree of hypothermia.

Conversely, the apparent beneficial effect of hypothermia, i.e. allowing patients to survive cardiac arrest for a prolonged period, is utilized in aortic arch surgery, where severe hypothermia down to 15°C is used (Di Luozzo and Griepp, 2012). Hypothermia is further induced in comatose survivors of cardiac arrest, where temperatures above 30°C are considered safe (Polderman and Herold, 2009). Although hypothermia is used extensively as a therapeutic intervention and survival is possible after extreme exposure, treatment of arrhythmias during rewarming is still challenging. In Chapter 4 an extensive review of the electrophysiological effects of hypothermia are discussed further. In this chapter, the effects of hypothermia were investigated on characteristics of electrophysiology through the use of the panoramic optical mapping system in Langendorff-perfused isolated rabbit hearts.

Chronic heart failure is one of the most common causes of morbidity and mortality within Western society (Cowie et al., 1997). A significant proportion of patients suffering from chronic heart failure typically suffer from cardiac dyssynchrony, where delays in interventricular and intraventricular electrical activation results in impaired mechanical performance. This is typically observed as a reduction in ejection fraction of ≤35% and conduction delays characterised by a QRS duration ≥120ms (Clark et al., 2008; Khan et al., 2007). Despite significant advances in pharmacological therapies: beta-blockers (Bristow, 2000), angiotensin-converting-enzyme (ACE) inhibitors or angiotensin II-receptor blockers (ARB) (Pitt et al., 2000; Flather et al., 2000; Swedberg and Kjekshus, 1988) and spironolactone (Pitt et al., 1999), there is still a poor prognosis for chronic heart failure patients.

Cardiac resynchronisation therapy (CRT) has emerged as an important therapeutic option for patients with heart failure due to systolic dysfunction and

cardiac dyssynchrony. During a typical CRT procedure, both the right and left ventricle are paced simultaneously to synchronise ventricular contraction; this is commonly known as bi-ventricular pacing (BiV). In large randomised clinical trials, CRT is associated with an improvement in LV function and a reduction in both heart failure mortality and sudden cardiac death (Cleland et al., 2005). Crucially, the mechanisms by which CRT might reduce ventricular arrhythmias in failing hearts are poorly understood. The improvement in LV function seen with CRT in patients is significant, occurs early and is likely to be responsible for the associated mortality benefit. That this improvement in LV function is not recapitulated in experimental models represents a major discrepancy and means that experimental findings cannot be extrapolated to human heart failure (Kass, 2002). For a more in depth account into the clinical background underlying the use of BiV pacing and the implications for patients with heart failure, see Chapter 5. In this chapter, the effects of BiV pacing on epicardial electrophysiology were investigated in both normal rabbit hearts and in a rabbit model of chronic chronic MI using the panoramic optical mapping system.

## Study aims

The main aim of this thesis was to develop of a novel method of panoramic optical mapping using a single camera and to study myocardial electrophysiology in isolated Langendorff-perfused rabbit hearts.

The specific aims of this thesis were to:

1) Generate a robust way to study whole heart electrophysiology under physiological and pathophysiological conditions over a period of hours in the Langendorff perfused rabbit heart using a novel method of panoramic optical mapping.

2) Study the characteristics of epicardial electrophysiology when temperature is reduced below physiological values, to mimic temperatures experienced during hypothermia, using the generated method of panoramic optical mapping.

3) Investigate the effects of different modes of pacing on epicardial electrophysiology in normal hearts and hearts after chronic myocardial infarction. Specifically, to examine the effects on activation and repolarisation sequence and distribution of action potential duration across the epicardial surface of the LV and RV of the heart.

# Chapter 2: General methods

# Langendorff perfusion

## Perfusion system

A perfusion system comprising a glass-column heat-exchanger, connected to a thermostat-controlled water bath and peristaltic pump (Gilson Minipuls peristaltic pump) was used in conjunction with a custom-built Perspex chamber (design discussed in detail below). This allowed delivery of temperature-controlled oxygenated physiological saline to the heart preparation for retrograde perfusion through the aorta (Figure 2.1). Perfusion pressure and temperature were both constantly monitored using inline transducers and calibration of flow was performed regularly. Langendorff perfusion was by constant flow rather than a constant pressure method. Flow rate was kept constant at 30 ml/min, with temperature set at 37°C for the majority of experiments, or at 31°C or 17°C during hypothermia protocols.

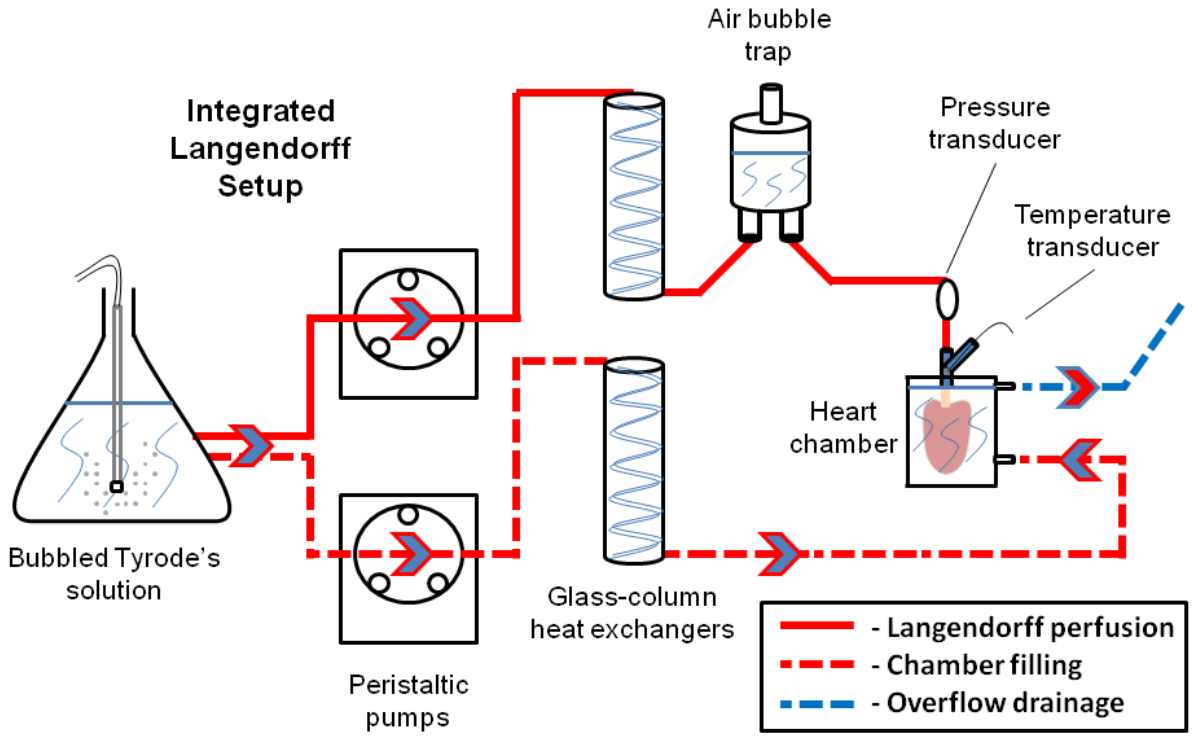


**Figure 2.1 A schematic of the integrated Langendorff system**

## Heart isolation and physiological solution

Adult male New Zealand White rabbits (2.5 – 3.5 kg) were sacrificed with terminal anaesthesia using an intravenous injection of 0.5ml/kg Euthatal (sodium pentobarbitone 200mg/kg, Rhone, Merieux) mixed with 1000 IU of Heparin injected through the left marginal ear vein. The heart was then rapidly excised and immersed in chilled Tyrode's solution, and transferred to a custom-built Perspex rotating chamber to be dissected and the aorta cannulated. During cannulation, the heart was positioned with the anterior surface of the LV in the image plane of the camera system. Once cannulated, the heart was perfused retrogradely through the aorta with oxygenated Tyrode's solution, maintained at a pH of 7.4. The Tyrode's solution was prepared with a composition (in mM) of: $Na^+$ 134.5, $K^+$ 5.0, $Ca^{2+}$ 1.8, $Mg^{2+}$ 1.0, $Cl^-$ 101.8, $SO_4^{2-}$ 1.0, $H_2PO_4^-$ 0.7, $HCO_3^-$ 20, acetate 20 and glucose 25. The solution was then filtered through a 5µm filter (Millipore) before perfusion, and continuously bubbled with gaseous mixture of 95% oxygen ($O^2$) and 5% carbon dioxide ($CO^2$) throughout the experiment to maintain pH.

In order to reduce the effects of motion artefact and inhibit contraction, a excitation-contraction uncoupler was used. In this study, 10µM blebbistatin (Enzo® Life Sciences) was used. Prior to adding the blebbistatin, the solution was warmed to 45°C. Once warmed, blebbistatin could then be added, allowing it to fully dissolve in the solution and minimise the chances of any precipitate forming in the coronary vessels of the heart during the experiments (Swift et al., 2012).

# Panoramic optical mapping system

In this study, a panoramic optical mapping system was developed. This system was then used to record epicardial electrical activity from the whole of the ventricular surface. Functionally, the system is split into two components: the optical mapping setup and the panoramic chamber setup. Successful optical mapping relies on a number of key components:

1) A voltage sensitive dye for staining the heart preparation

2) Optical path, which includes the combination of filters and lenses to filter and focus the emitted light onto the photodetector

3) A photodetector, to measure the emitted fluorescence

## Voltage-sensitive dyes

The voltage-sensitive dye of choice for this study was di-4-ANEPPS (Biotium), which is widely used in studies of cardiac optical mapping. The excitation and emission spectra for di-4-ANEPPS are represented in Figure 2.2. The dye was made up into 1mg/ml stock solution in dimethyl sulphoxide (DMSO) and aliquoted out into vials for storage (Patrick et al., 2007). A bolus of 100µl of di-4-ANEPPS (2mM) was injected slowly into a port proximal to the aortic cannula.

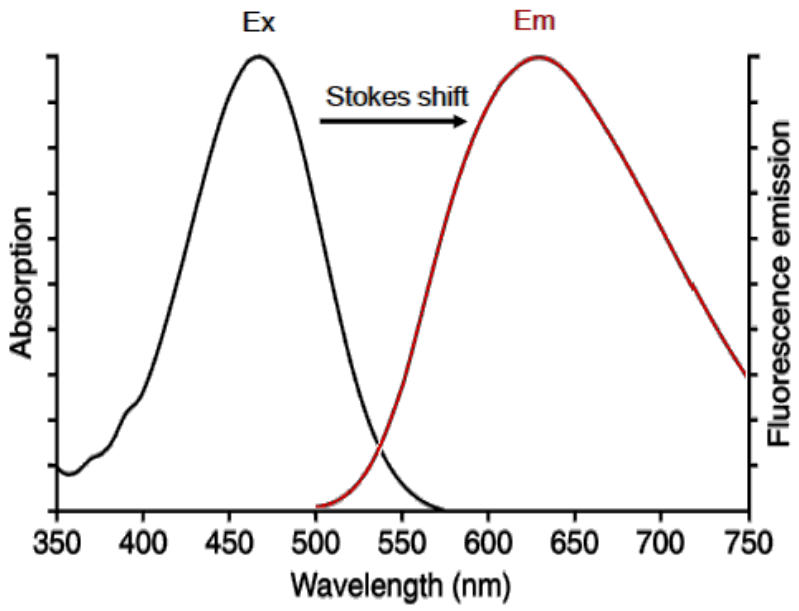


**Figure 2.2 Excitation (Ex) and emission (Em) spectra of di-4-ANEPPS.**

## Illumination, optics and cameras

The preparation was illuminated with an annular array of cyan LEDs (OptoLED, Cairn Research Ltd.) at a wavelength of 480nm. The LEDs illuminated the preparation in synchrony with the camera recordings to reduce the level of light the preparation was exposed to, mitigating the effects of photobleaching of di-4-ANEPPS and photoconversion of blebbistatin (Kolega, 2004; Loew, 2011). The emitted fluorescence was collected and focused through a tandem lens configuration, consisting of a pair of photographic lenses, and split with a dichroic mirror at a wavelength of 630nm. The longer wavelength portion was passed through a long pass filter (665nm wavelength) and was focused onto the CCD chip (Redshirt, Decatur, GA). Signals were recorded at a pixel depth resolution of 14 bit. The fractional change in fluorescence from di-4-ANEPPS on administration of KCL was measured via spectrophotometer in isolated rabbit ventricular cardiomyocytes, where the long wavelength band gave less than 3% change in fluorescence, as shown in Figure 2.3A. The shorter wavelength portion was focused onto a second CCD camera (Dalsa, Coreco Imaging, Canada), which was used to acquire plain images of the preparation at higher resolution. The Redshirt CCD camera was setup to image an array of 80 x 80 pixels with a sampling rate of 1000Hz. The Dalsa CCD camera was setup to acquire single images of the preparation at a higher resolution of 256 x 256 pixels. Camera alignment was achieved through the use of a calibration image grid. A schematic diagram of the panoramic optical mapping system is illustrated in Figure 2.3B.

During the experiment, the heart was rotated to record epicardial membrane potentials from the whole of the ventricular surface. The mapped field was divided into three different views: LV view which consisted mainly of the anterior part of LV with some RV, the LV/RV view which consisted of the postero-lateral parts of the LV and RV and finally the RV view which consisted entirely of the RV. In Figure 2.3C, is an example of three typical images of the heart surface captured by the Dalsa CCD camera from the three viewpoints.

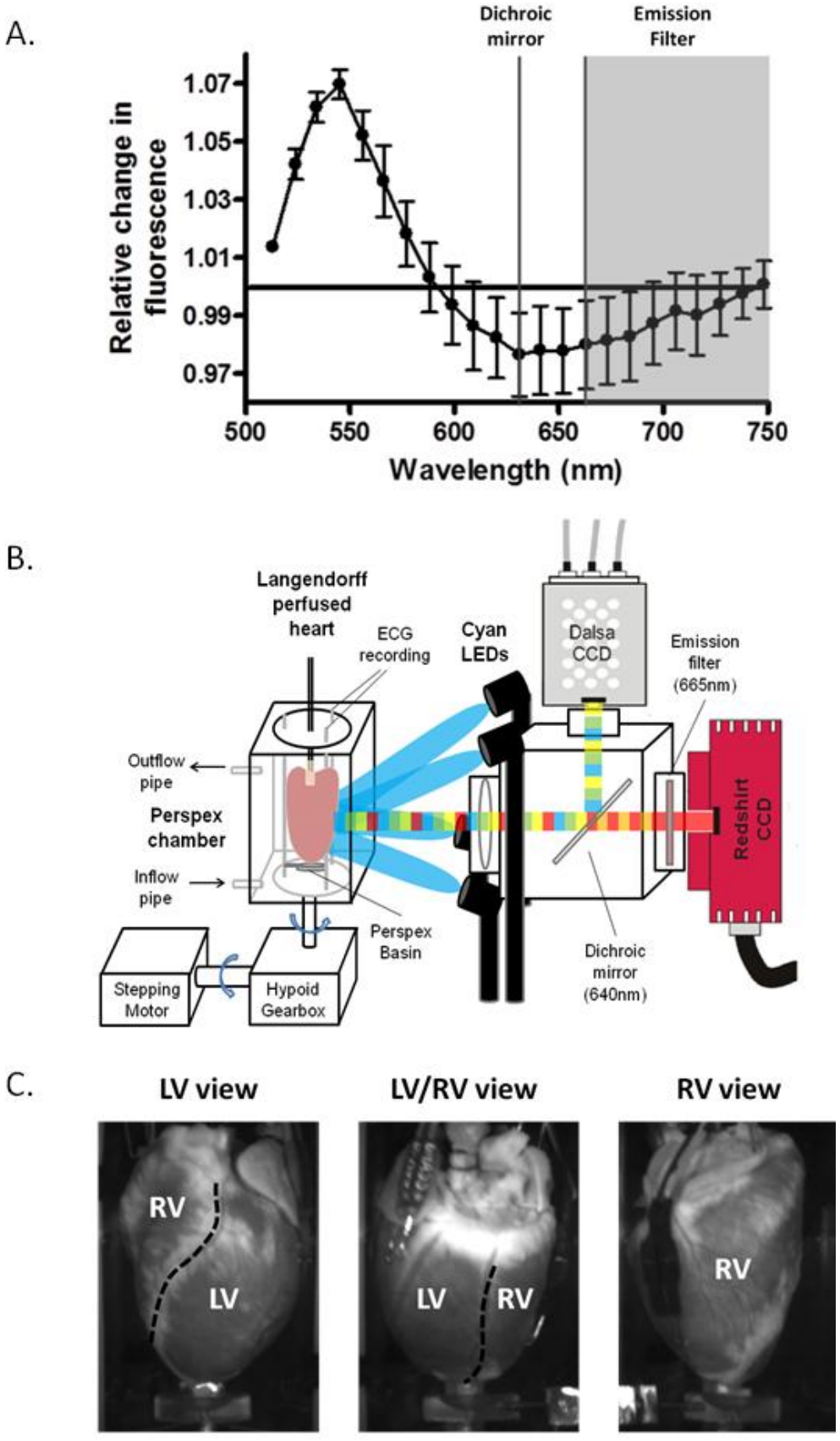


**Figure 2.3 Panoramic optical mapping system**

**A. Fractional change in fluorescence of di-4-ANEPPS on administration of KCL in isolated rabbit ventricular cardiomyocytes (mean ± SE)**

**B. Schematic diagram of the panoramic optical mapping system.**

**C. Images of the epicardial surface of the heart from the three viewpoints.**

## Construction of panoramic chamber and integrated Langendorff

In this system, the heart preparation, inside a custom-built rotating Perspex chamber, was rotated by ±120° from a central position (via stepping motor) and optical data acquired sequentially from each viewpoint using the single Redshirt CCD camera, as discussed above. In addition, the Dalsa CCD camera was used to record short wavelength images of the preparation. After several iterations, the chamber system was constructed with a number of different built in features, custom built by the Institute of Biomedical and Life Sciences (IBLS) mechanical workshop, University of Glasgow (Figure 2.4). The main design included:

1) Outflow and inflow pipe

2) Inlet holes

3) Steel bars

4) Perspex basin

5) Rotating chamber.

The additional apparatus included:

- A hybrid stepping motor
- A hypoid gearbox.

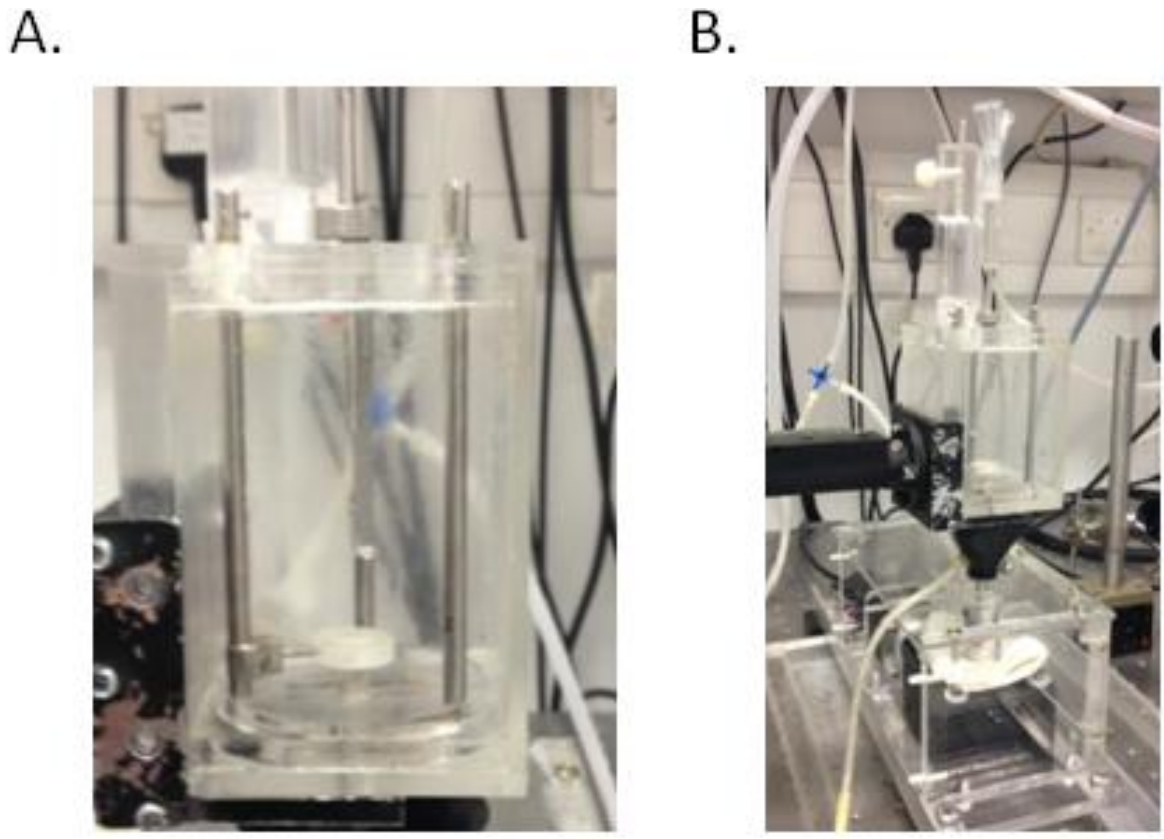


**Figure 2.4 Custom-built Perspex chamber**

**A. Rotating chamber inside the housing chamber.**

**B. The chamber coupled with the stepping motor and gearbox system.**

The outflow pipe allowed excess solution to drain from the chamber. Using a glass-column heat-exchanger, connected to a thermostat-controlled water bath and peristaltic pump (Gilson Minipuls peristaltic pump), the chamber was filled, via the inflow pipe, with temperature controlled Tyrode's solution which surrounded the heart preparation.

The inlet holes on the top of the rotating chamber were used for the insertion of pacing electrodes (Figure 2.5).

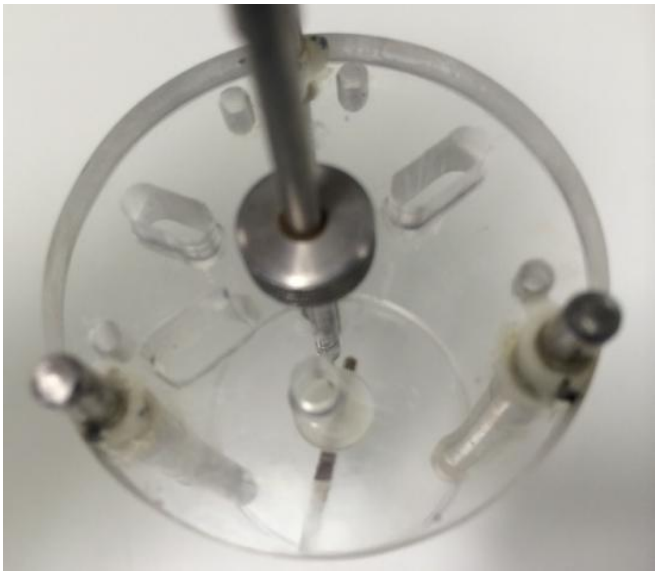

**Figure 2.5 Inlet holes on the top of the chamber**

The two steel bars positioned vertically towards the front of the rotating chamber (anterior surface of the heart) were used as bath electrodes for making ECG recordings, with the cannula used as the third reference electrode (Figure 2.6B). By sliding plastic insulating cuffs over the top of the bars and exposing one at the top (negative electrode – right arm) and one at the bottom (positive electrode – left leg) it was possible to record a pseudo lead-II ECG (+60° relative to the heart)(Figure 2.6A).

A.

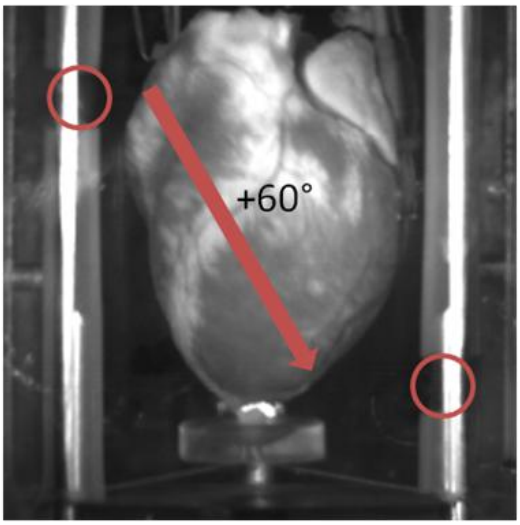


B.

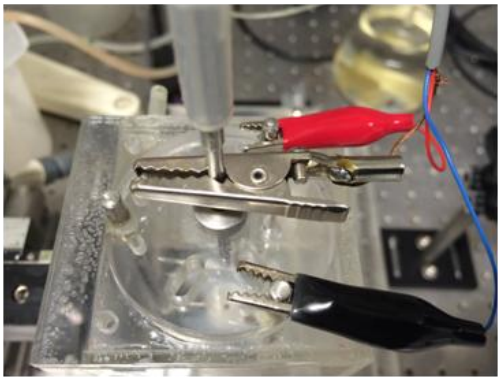

**Figure 2.6 ECG configuration**

**A. Steel bars with exposed regions highlighted in red.**

**B. ECG electrodes attached on the top of the chamber.**

The Perspex basin was used to help support the apex of the heart and keep it centred in the image field of view. A small suture was also threaded through a region of fatty tissue on the apex of the heart and attached to the two front bars of the chamber via a hole in the basin (Figure 2.7). This suture, in addition to the basin, acted as an anchor for the heart during experiments.

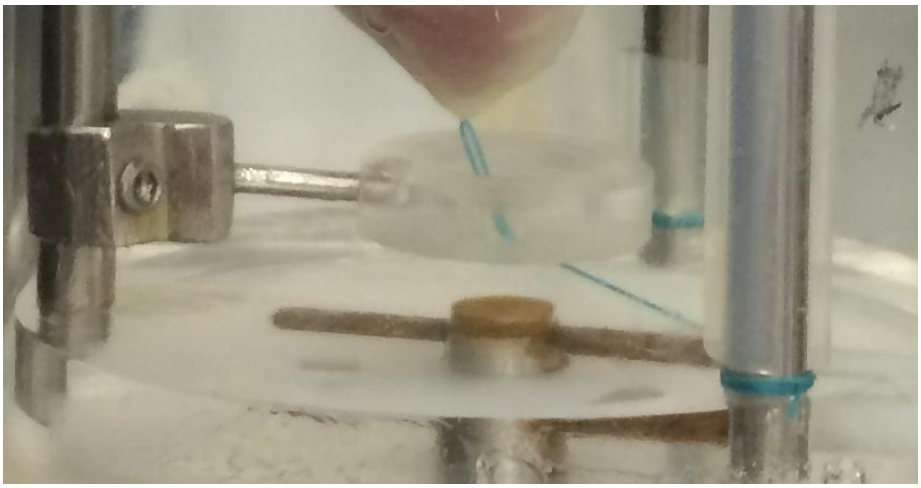

**Figure 2.7 An image of the Perspex basin and apical suture.**

In this study a hybrid bipolar stepping motor (Astrosyn International Technology Ltd.) was chosen to rotate the chamber, with a stepping angle of 1.8° and maximum angular deviation of ±5% per step (0.09° per step) (Figure 2.8A). This motor allowed the chamber to be rotated both clockwise and counter-clockwise. The stepping motor was controlled via an integrated interface-driver circuit (built by the Bioelectronics workshop, University of Glasgow), which could be run in either manual mode or computer mode (Figure 2.8B). In this study, the speed and direction of rotation was controlled via a custom made programme written by Dr Francis Burton (University of Glasgow).

A. B.

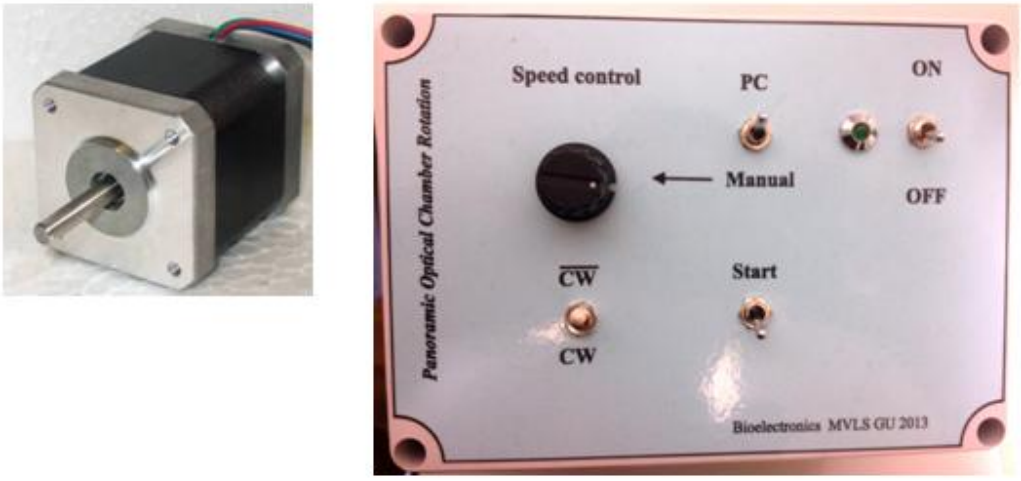


**Figure 2.8 Stepping motor system**

**A. Stepping motor**

**B. Integrated interface-driver circuit**

An important factor in the system was the need for accurate and reproducible rotation of the chamber. So in addition to the stepping motor, a hypoid gearbox (Reliance Precision Ltd.), with a gear ratio of 10, was coupled to the stepping motor (Figure 2.9). With the addition of the gearbox the stepping angle was reduced to 0.18°, with a maximum angular deviation of only 0.009°. Furthermore, this enabled the chamber to be rotated very smoothly, significantly minimising any residual movement of the heart which may have occurred when moving between each viewpoint. Chamber rotations typically took less than 1s.

A. B.

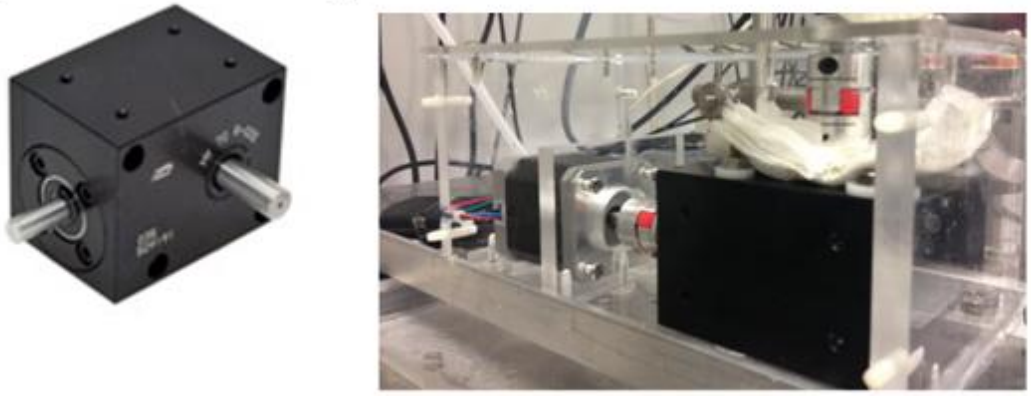

**Figure 2.9 Integrated stepping motor and gearbox system**

**A. Hypoid gearbox**

**B. Coupled stepping motor and gearbox**

### Data acquisition

Control of the Redshirt camera and Redshirt Imaging control box digitiser (DAP820, Redshirt, Decatur, GA) for the acquisition of simultaneous optical and electrical data (pacing and ECG signals) was made using the Redshirt Cardioplex software (RedShirt Imaging, LLC). Using this software the recording parameters could be set, such as the frame rate, pixel array size, duration of recording and the clock pulse triggering of the LEDs.

## Pacing Protocols

In this study three types of pacing method were used to investigate epicardial electrical conduction. The majority of experiments used atrial pacing, with ventricular and bi-ventricular pacing only used in specific protocols. The details of the particular pacing protocols are described in respective chapters.

### Atrial pacing

During atrial pacing a pair of platinum hook electrodes were attached to the right atrium, via one of the inlet holes on the top of the chamber. A constant voltage source (Digitimer DS2A-MKII stimulator) was set to output square pulses of 1ms in width. The stimulus threshold was measured and the voltage set at 5% above the measured threshold to capture the myocardium. The timing of stimulus pulses were controlled using a custom-developed program by Dr Francis Burton (University of Glasgow).

### Ventricular pacing

A custom-made bipolar platinum electrode was made and used for point stimulation on the ventricular epicardial surface. During experiments the ventricular pacing electrode would be secured at the top of the rotating chamber and run down one of the inlet holes on the top, pressing lightly onto the base of the right ventricle.

### Bi-ventricular pacing

Bi-ventricular pacing involved using two pairs of platinum hook electrodes, with one pair attached to the apex of the right ventricle and one pair attached to the base of the left ventricle.

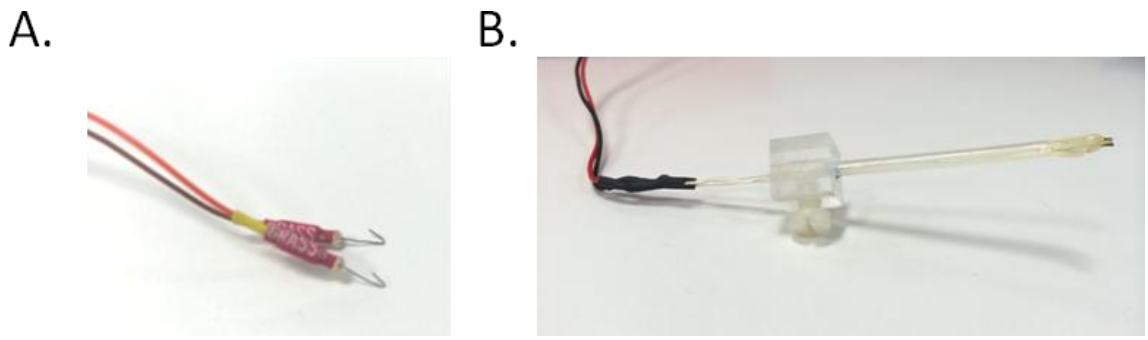


**Figure 2.10 Pacing electrodes**
**A. Platinum hook electrodes**
**B. Custom-made bipolar platinum touch electrodes**

## ECG recording & analysis

### ECG signals recording

In this study, pseudo lead-II ECG recordings were made using the steel bars, as part of the rotating chamber, as bath electrodes. The signals from these electrodes were amplified with an isolated amplifier, custom built by Medical Electronics, University of Glasgow, and were displayed on an oscilloscope (Nicolet Instrument Corporation, Wisconsin, USA) for real time viewing. In synchrony with the optical recordings, ECG signals were recorded using a Redshirt Imaging control box digitiser (DAP820, Redshirt, Decatur, GA). Continuous recordings of ECG signals were made using a laptop computer with a USB compatible digitiser (DI-158U, Dataq Instruments Inc)).

### ECG data analysis

ECG recordings from experiments were analysed using Chart™ 5 Pro (ADInstruments) software. The main ECG parameters that were extracted were RR, PR, QRS and QT intervals. The software functions in a semi-automated way,

whereby the software calculates and assigns a cursor at each relevant time point on each ECG beat, where these may be manually overridden.

### Statistical analysis

All data obtained in the study are expressed as mean ± standard error (SE). Statistical comparisons and significance testing was performed in GraphPad Prism. Comparisons between groups was made with the Student's t-test (paired where appropriate). A two-tailed p-value of less than 0.05 was considered significant. Multiple comparisons were performed using a one-way ANOVA followed by a Tukey-Kramer post-test allowing for multiple comparisons where appropriate. Comparisons between two groups when two dependent variables were being examined were performed using a two-way ANOVA.

# Chapter 3: Panoramic optical mapping: general considerations

## Aims

The work presented in this chapter gives a detailed account of the protocol developed for the robust selection, filtering and analysis of optical data. The primary aim of this chapter was to test the viability of using this protocol with the panoramic optical mapping system for mapping epicardial electrical activity in the isolated rabbit hearts, by investigating time and heart-dependent differences. The results obtained serve as a foundation for subsequent studies utilising this system. The initial experimental work entailed an investigation of the interaction between activation sequence and action potential duration during RA pacing in these hearts.

## Introduction

Regional differences in electrophysiology exist in mammalian ventricular myocardium, but the origin of these differences is unclear. For example, isolated cells from different regions of the heart have different APDs (Main et al., 1998; Bryant et al., 1997; McIntosh et al., 2000), but it is uncertain the extent to which these differences contribute to the regional differences in electrophysiology in the intact ventricles. There are numerous publications to suggest the regional differences in electrophysiology may be associated with the pattern of ventricular activation, i.e. sites in the ventricular myocardium that experience the earliest activation times are associated with longer APD values and sites of later activation with shorter APD values. This effect of activation sequence has been proposed to as a consequence of passive electrotonic interactions between cells that serves to approximately synchronise repolarisation times (Franz et al., 1987). The overall spatial pattern of APD is therefore a combination of these two factors, namely the spatial distribution of intrinsic cellular repolarisation properties (Nerbonne and Kass, 2005) and the electrotonic interactions between cells (Laurita et al., 1996).

One well-known example of spatial differences in myocardial electrophysiology is the trans-epicardial action potential characteristics including APD across the apex-base axis of the ventricle. In a study of rabbit hearts, myocytes isolated from the LV apex were shown to have significantly longer APD than basal myocytes (Cheng et al., 1999). In this study, they also show regional differences

in the density of $I_K$, in particular its two components $I_{Kr}$ and $I_{Ks}$. The dominant component of $I_K$ in apical myocytes was $I_{Kr}$; in contrast, basal myocytes $I_{Ks}$ was the dominant component. Similar findings were reported by Salata et al. who observed a comparable apex-base gradient in the ratio of $I_{Kr}$ to $I_{Ks}$ density (Salata et al., 1996). These differences in cellular electrophysiology were thought to underlie the apex-base differences, but the study did not assess the relative contribution of electrotonic influences discussed above.

In addition to trans-epicardial gradients in electrophysiological properties, there are also inter-ventricular gradients. In a study of canine ventricle epicardium, the magnitude of the $I_{to1}$-current was significantly larger in the RV by comparison to the LV (Di Diego et al., 1996). Similar differences were observed in isolated M cells from the LV and RV, where the density of $I_{to1}$ and $I_{Ks}$ was significantly larger in the RV than LV (Volders et al., 1999). The larger repolarisation currents were associated with a shorter APD observed in isolated RV myocytes when compared to equivalent LV.

The electrotonic interactions between cells, mediated by low-resistance gap junctions, act to spatially average and mask the intrinsic differences between individual cells and in particular attenuate any temporal gradients in repolarisation. Studies using Purkinje fibre preparations and isolated ventricular muscle have shown that depolarising currents applied during the repolarisation phase prolongs APD while repolarising currents shortens APD (Weidmann, 1951; Cranefield and Hoffman, 1958; Vassalle, 1966). An individual cell within the myocardium is subject to electrotonic load from its neighbouring cells, whereby downstream cells that repolarise later generate an inward electrotonic current on their earlier repolarising upstream counterparts, where cells that start to repolarise later are electrically activated later and vice versa. This results in a prolongation in APD in early-activated sites (early repolarising sites) and leads to an observed shortening in APD away from the site of pacing (later repolarising sites). An important factor in the influence of electrotonic currents is the relative coupling resistance between cells, which impacts on the spread of spatial current flow. Joyner et al. suggested that the transmembrane resistance is a dynamic property governed by the current state of transmembrane channels and pumps (Joyner, 1986). In an experimental study, rabbit hearts were

perfused with 20μM of palmitoleic acid, a gap junction uncoupler, to test the effects of reduced intercellular coupling. They observed a significant increase in the dispersion of repolarisation (Dhein et al., 1999). Various experimental studies have shown the electrotonic modulation of repolarisation by the activation sequence in a range of different species (humans, swine, rabbit, rat and many others) and conditions (Franz et al., 1987; Laurita et al., 1996; Yuan et al., 2001; Banville and Gray, 2002; Yue et al., 2005; Chauhan et al., 2006; Hanson et al., 2009; Walton et al., 2013).

Understanding the interaction between the intrinsic cellular repolarisation characteristics and the influence of electrotonic currents within the ventricular myocardium is of central importance to our understanding of cardiac electrophysiology. In this chapter, panoramic imaging of the electrophysiology of the epicardial surface of isolated rabbit hearts was used to examine the interaction between ventricular activation pattern and action potential duration.

# Methods

## Preparation of the rabbit hearts

In this study, 8 New Zealand White rabbits (2.5kg-3.5kg) were used for optical mapping. The rabbits were sacrificed and Langendorff perfused as described in Chapter 2. To suppress motion artefacts the E-C uncoupler blebbistatin (10μM) was added to the perfusate and the preparation stained with voltage-sensitive dye, Di-4-ANEPPS (100μl of 1mg/ml). Hearts were paced via the RA throughout experiments at cycle lengths of 300ms at 37°C. To measure conduction velocity (CV), hearts were paced via the epicardial surface of the RV to assess epicardial conduction without potential artefacts from transmural conduction, using the same cycle length as for RA pacing.

## Data analysis

Optical signals obtained during experiments were carefully selected, filtered and analysed using a custom analysis software package, Optiq, developed by Francis Burton (University of Glasgow). Automated algorithms were used to determine AP characteristics across all sites of the epicardial surface. The section of the trace corresponding to each individual AP for analysis was marked using two cursors, in relation to the stimulus. The automated algorithm was then started, which calculated trace characteristics (e.g. baseline, amplitude and SNR) and AP characteristics for each pixel within the selection. For each analysis approach, the same definitions were used for AP characteristics. Activation time ($TAct_M$) was defined as the time from stimulus to 50% of the upstroke of the AP. Repolarisation time was defined as the time taken to return to baseline. As is standard in this form of analysis, due to the SNR typical of optical AP's, the time at 90% repolarisation ($T_{Repol90}$) was used to calculate the action potential duration at 90% repolarisation ($APD_{90}$). $APD_{90}$ was defined as $TRepol_{90}$ minus $TAct_M$.

In this study, the electrophysiological parameters analysed were: $TAct_M$ (activation time), TRise (rise time), conduction velocity (CV), $APD_{50}$, $APD_{75}$, $APD_{90}$ (action potential duration at 50%, 75%, and 90% repolarisation,

respectively), $TRepol_{50}$, $TRepol_{75}$, $TRepol_{90}$ (time at 50%, 75% and 90% repolarisation, respectively), PR, QRS and QT interval.

The commercial software package, MATLAB (R2013a, The MathWorks Inc., Natick, MA, 2013) was used for further analysis and processing of the data. For calculation of conduction velocity (CV) from RV paced recordings, a custom-written algorithm in MATLAB was used. In this algorithm, epicardial CV was calculated for each pixel, based on its distance from the RV electrode divided by its $TAct_M$. The optical parameters plotted are based on averages across the whole epicardial surface. Typical example contour maps were also processed for individual parameters using custom-written sub-routines in MATLAB. ECG analysis was performed as described in Chapter 2.

# Results

## Selection and filtering of optical signals

Before analysis of optical data sets, selection and masking of data was necessary. Each fluorescent image frame contained foreground pixels (pixels from within the image of the isolated heart) and background pixels (pixels lying outside the area of the image of the heart). Although the signals from the foreground pixels contain voltage information on top of a noisy background, the background pixels will only have noise. Therefore, an important stage of the processing is to remove these background pixels from each image data set. Selection and masking of pixels was performed in two stages.

### First-stage selection

Using a method of automatic segmentation, involving threshold criteria, an initial selection of pixels of the heart preparation was made for the three views. The threshold criterion was based on the signal-to-noise ratio (SNR) of the optical signals at each pixel, where these signals are the fluorescence measured from a single wavelength. In Optiq, SNR was calculated as the peak-peak noise free optical signal divided by the root-mean square value of the noise (Witkowski et al., 2001). The three views of the heart preparation and contour plots of SNR (superimposed over images of heart preparation) over the whole field are shown in Figure 3.1.

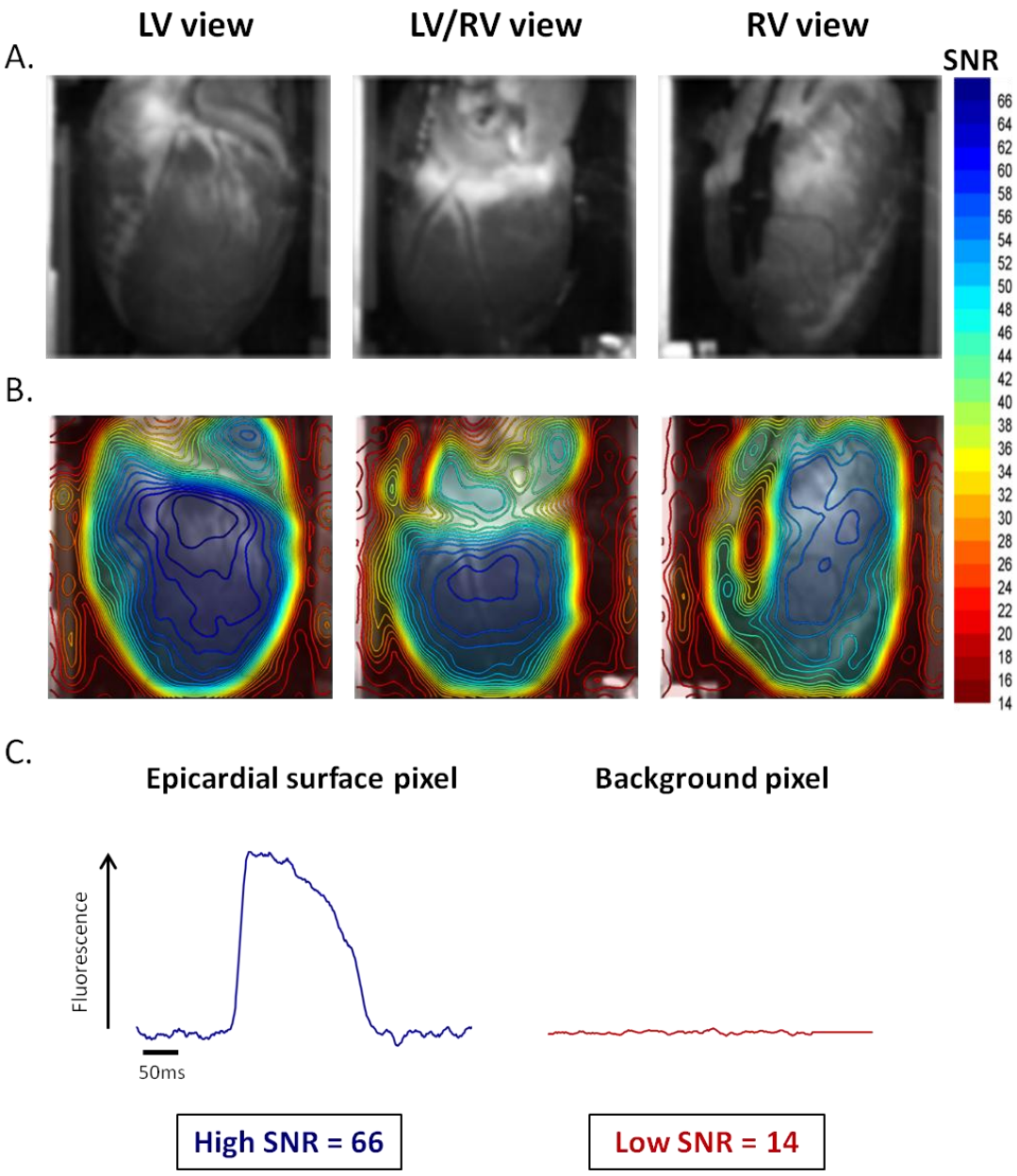


**Figure 3.1 Initial pixel selection procedure**

**A. Images of heart preparation from three views**

**B. Contour plots of SNR (red = low and blue = high, as shown in key)**

**C. Example optical signal from a pixel with a high SNR on the epicardial surface against a background pixel with low SNR.**

The distributions of SNR were summarized as histogram plots, as shown in Figure 3.2. Invariably, the SNR had a bimodal distribution (background and foreground pixels). In this study, the median of each distribution (blue dotted line) was found to be the most appropriate threshold for selection. Typical optical signals across the epicardium for different SNR are given in Figure 3.3, which shows traces from a 3x3 pixel average from a high, mid and low SNR regions.

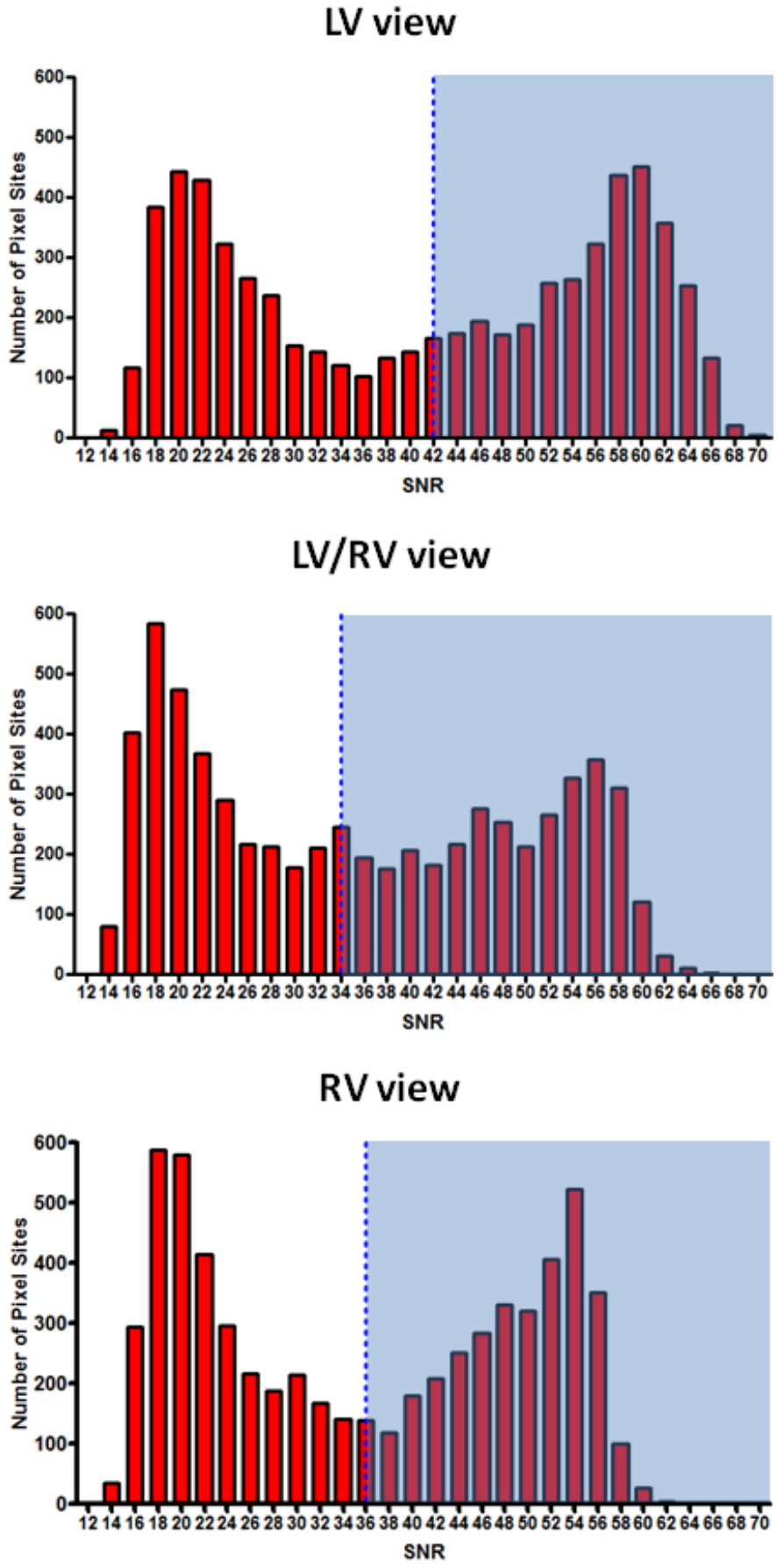


**Figure 3.2 Histograms of signal-to-noise ratio**

**Three views of the heart preparation; the blue dotted line indicates the selection threshold (median) and pixels in distribution highlighted in blue kept for selection.**

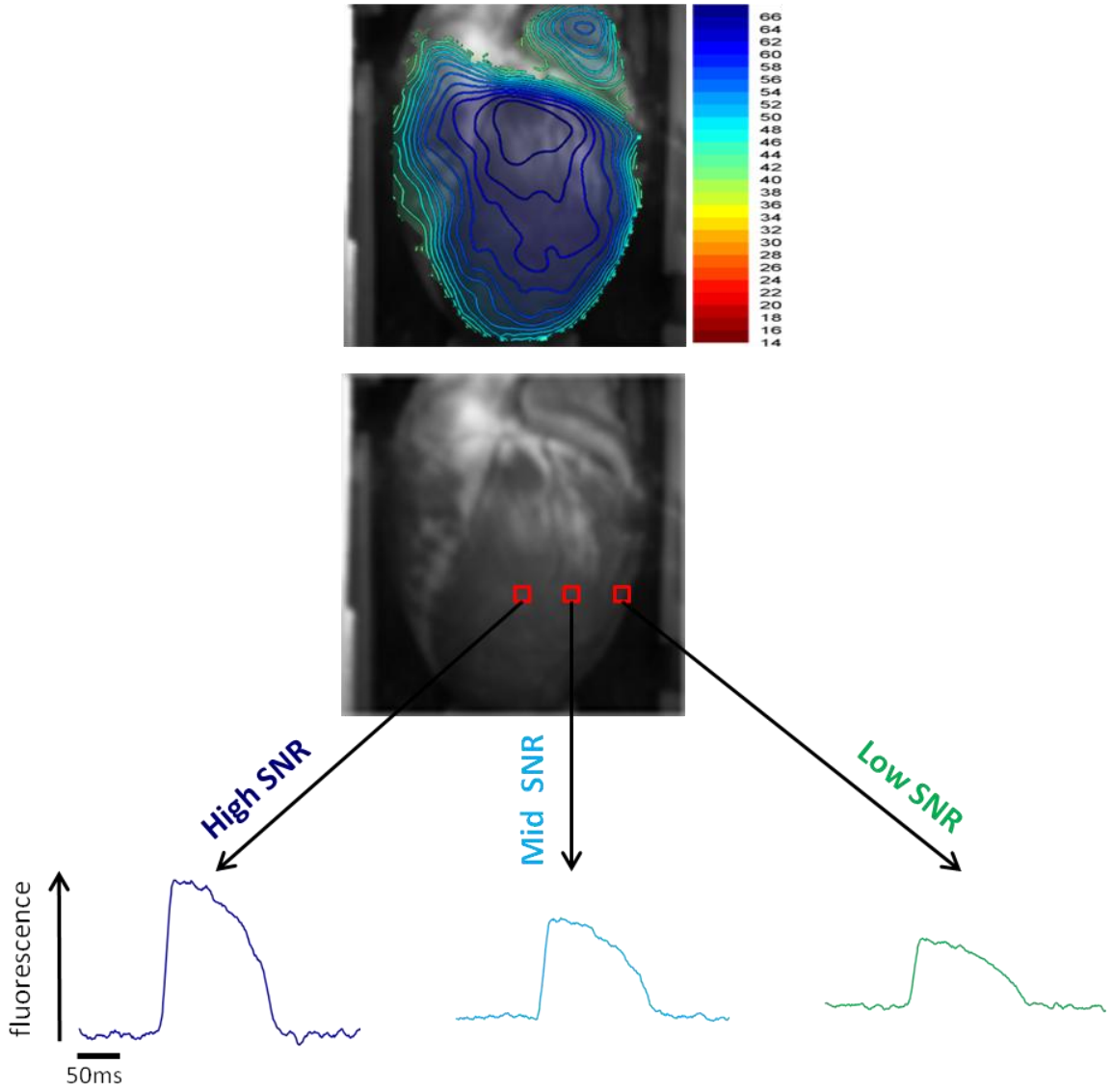


**Figure 3.3 Typical optical AP signals**

**High, mid and low SNR regions over the epicardial surface, where AP signals are based on a 3x3 pixel average.**

The new analysis field are shown in Figure 3.4A after thresholding, with the corresponding initial selection of pixels (superimposed over images of heart preparation) shown in Figure 3.4B. All pixels greater than or equal to the threshold were labelled as 1 s (red) for analysis and all pixels below the threshold were labelled 0 s (blue). Using this method eliminated the majority of background pixels.

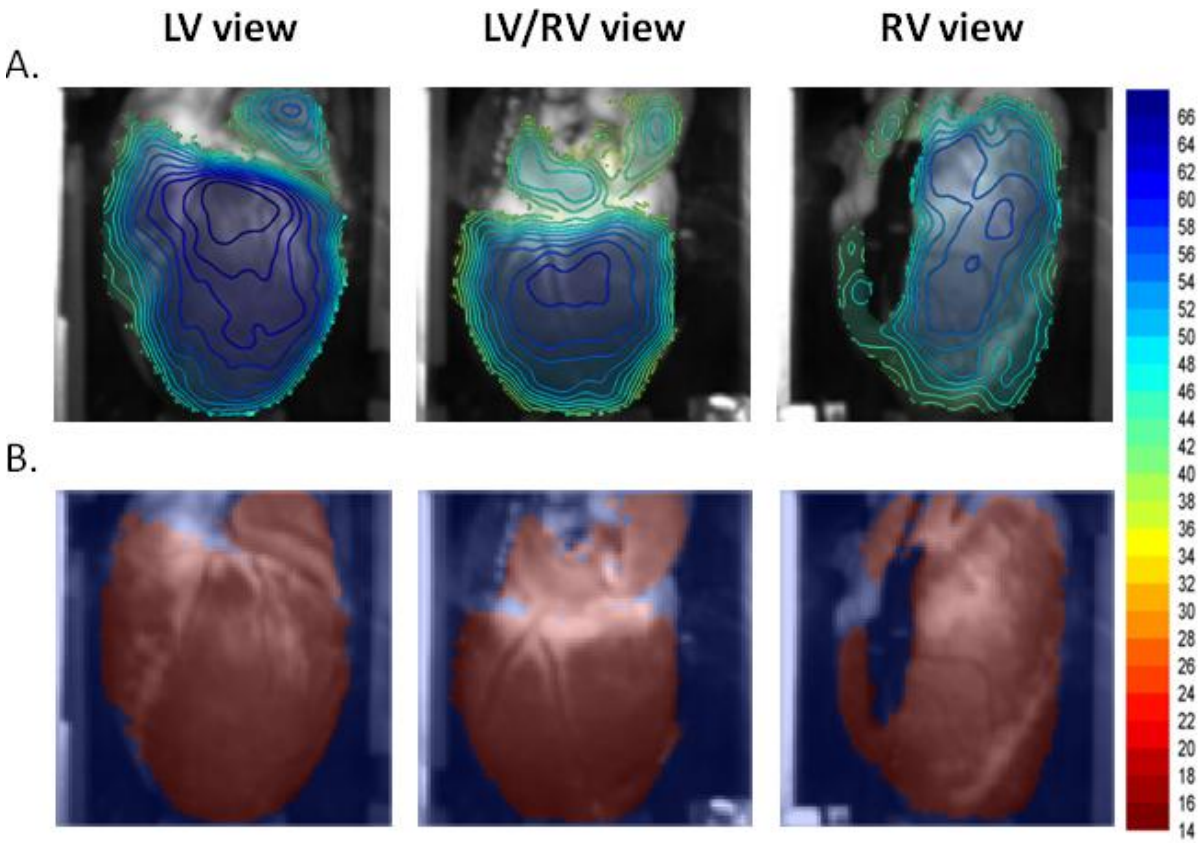


**Figure 3.4 New analysis field after thresholding**

**A. Contour plots of SNR after thresholding**

**B. Initial pixel selections based on median threshold, with red pixels kept for analysis and blue pixels eliminated.**

### Second-stage selection

To ensure no overlap between the three views of the heart preparation and remove areas of poor lighting on the heart preparation at the oblique angles of the epicardial surface, an idealised three-dimensional (3D) anatomical model of the ventricular epicardial surface of the heart was developed.

The epicardial surface was modelled as a semi-prolate spheroid, a widely used geometry in studies of whole heart computational modelling (Figure 3.5A). The model was developed in MATLAB and parameterised using whole heart dimensions (in x, y and z) measured from the heart preparation. Using this model it was possible to map the change in angle of incidence over the epicardial surface of the heart preparation relative to the incident light (Figure 3.5A), where three sample angles are shown in Figure 3.5B.

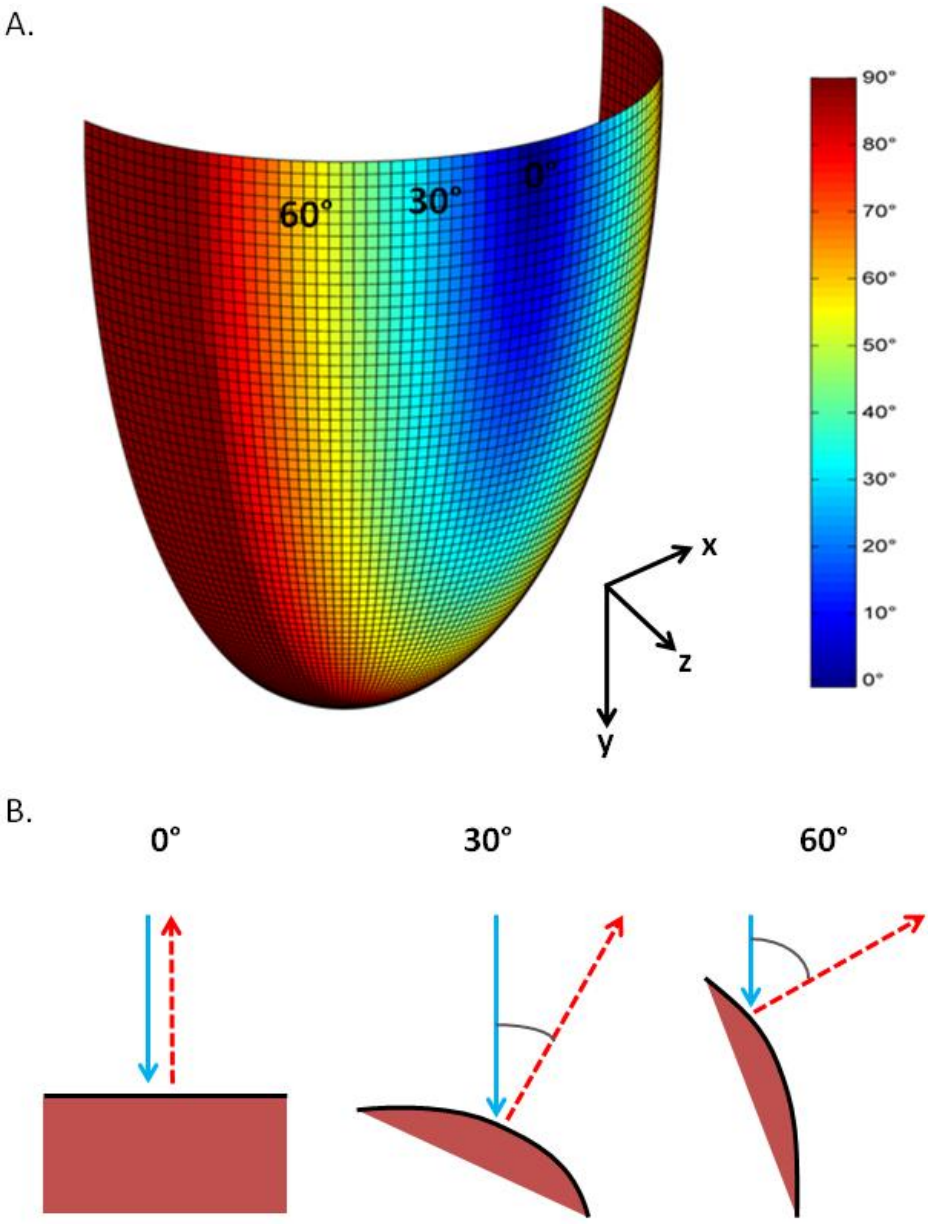


**Figure 3.5 Semi-prolate spheroid model**

**A. Idealised model of the epicardial surface of the heart, with angle of incidence relative to the incident light mapped over the surface.**

**B. An illustration showing three sample angles from the epicardial surface.**

A boundary angle was chosen at ±60°, and a curve fit in the x-y plane to estimate the area of the heart preparation that would lie within this boundary. Based on the curve fit, a sub-routine was written for Optiq to exclude pixels from the initial selection that lay beyond the boundary. The model and exclusion criteria was tested and validated against a marked cylinder object. The cylinder was marked white within the boundary angle and black outside the boundary angle. In Figure 3.6A, the original selection of the cylinder is shown, with both

the white and black regions selected. The exclusion criteria was then applied to the selection in Optiq, with only the white markings remaining selected (Figure 3.6B).

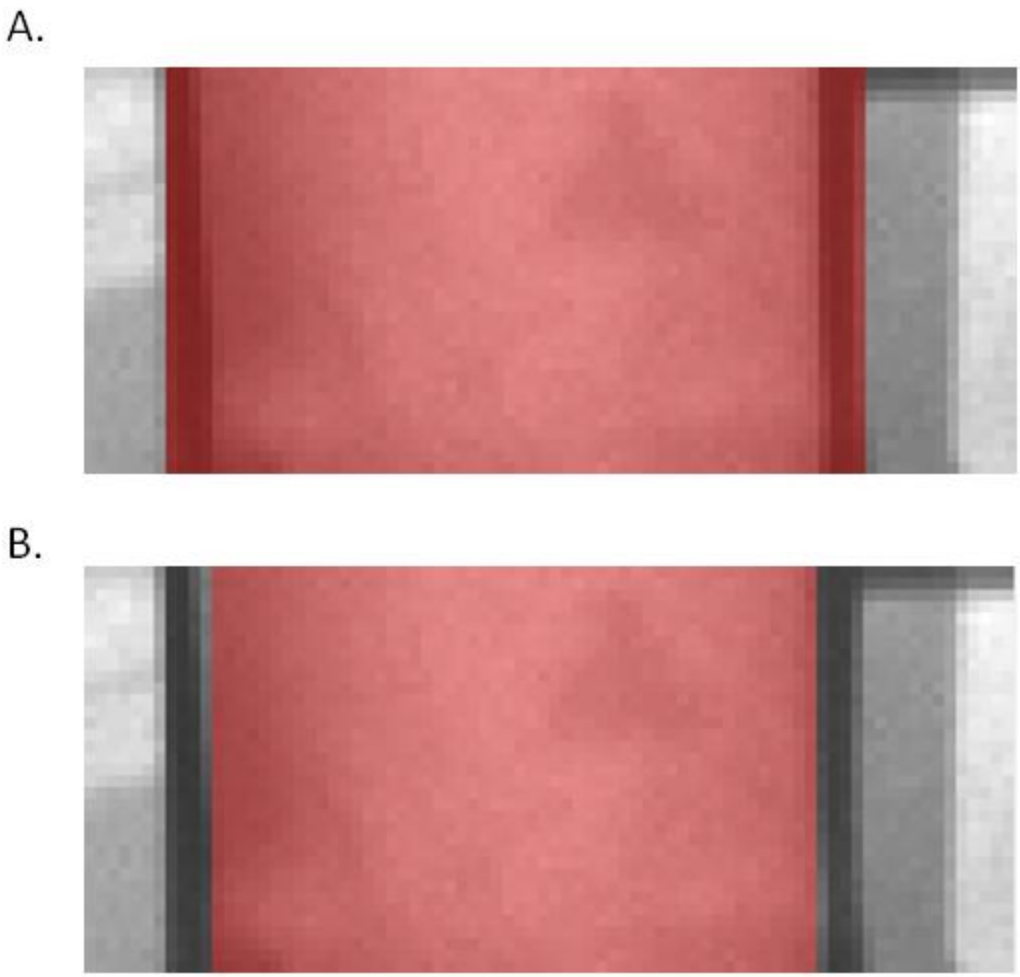


**Figure 3.6 Validation of exclusion criteria**
**A. Original pixel selection of entire cylinder.**
**B. Pixel selection after exclusion criteria is applied.**

A typical experimental example of the exclusion criteria in the heart preparation is demonstrated in Figure 3.7A, where the excluded area is shown in blue. Further manual segmentation by deselecting areas was necessary in order to remove additional artefacts such as pieces of instrumentation (electrodes) and atria from the final selection, as shown in Figure 3.7.

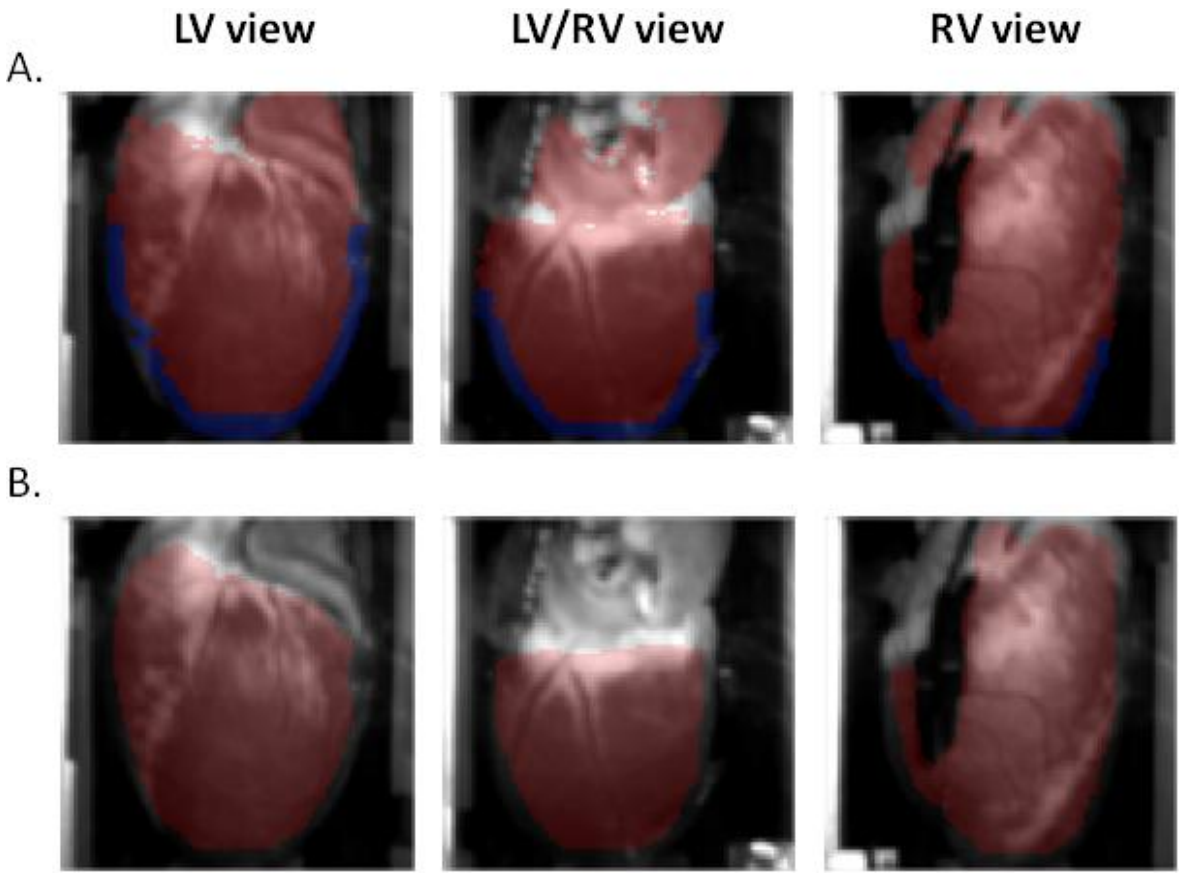


**Figure 3.7 Application of exclusion criteria**

**A. Pixel selection including exclusion criteria with red pixels kept for analysis and blue pixels eliminated.**

**B. Final pixel selection after applying exclusion criteria.**

### Delineation and selection of ventricles

Delineation of the ventricles was carried out in order to assess inter-ventricular differences as well as gaining a more detailed understanding of ventricular electrical behaviour. Using the high-resolution background image as a guide, the pixels that corresponded with the LV and RV were selected. In general, the LV view would be predominantly LV with a small region of RV, the RV view would be predominantly RV with a small region of LV, and finally the LV/RV view would have contributions from both the LV and RV (Figure 3.8). Delineation of the LV and RV views was based on the inter-ventricular septum, which could be easily identified in the background image, as shown by the white dashed line in Figure 3.8A. On the posterior surface of the heart in the LV/RV view, it was more difficult to clearly delineate the LV and RV. However, an appropriate estimation of the location of the LV and RV could be made by identifying the posterior

division of the left descending coronary artery on each heart, based on current literature on patterns of epicardial branching of coronary arteries in rabbit hearts (Lee et al., 2004; Podesser et al., 1997). In general, the septum on the posterior side runs approximately parallel to the posterior division of the left descending coronary artery, as shown by the red dashed line in Figure 3.8A. In addition, each heart was dissected after each experiment where possible in order to check there were no irregular anatomical features and the location of the septum on the posterior view. Figure 3.8B shows the delineation of the selection into LV and RV.

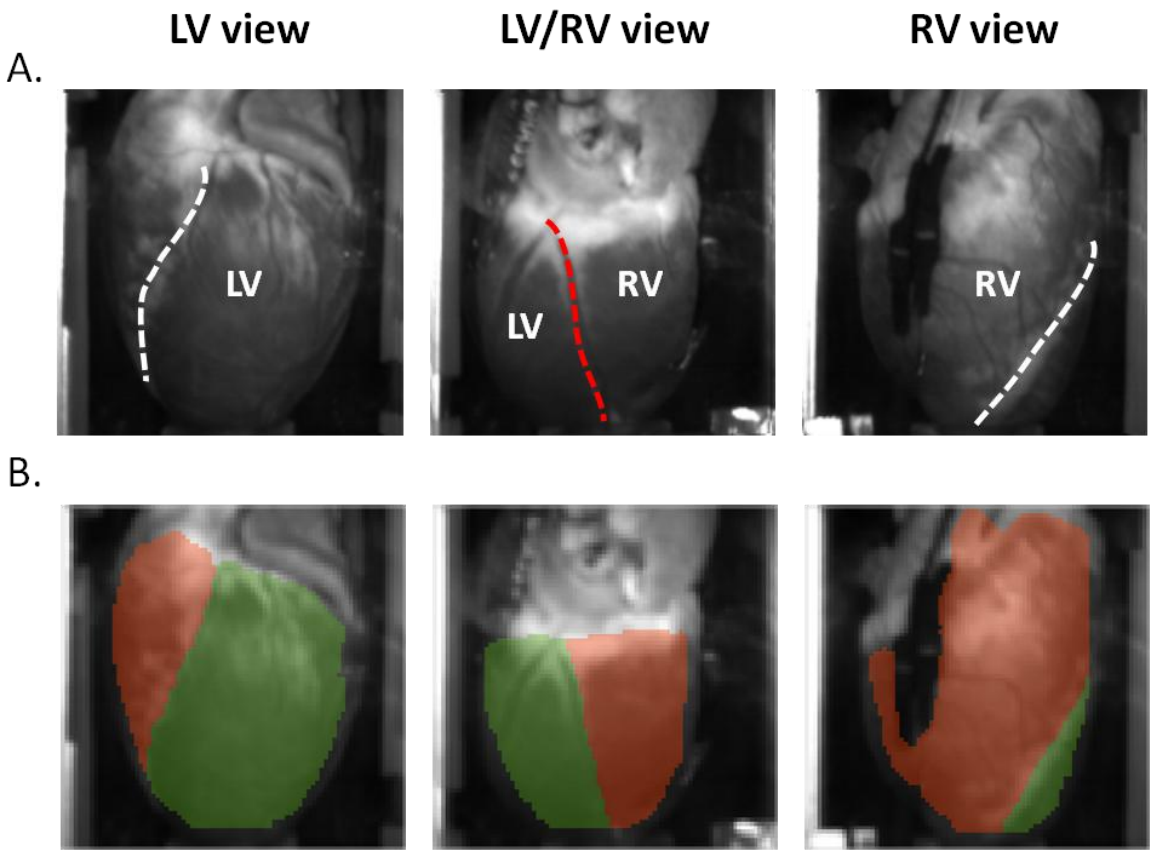


**Figure 3.8 Selection of ventricles**

**A. Images of heart preparation from three views (with inter-ventricular septum shown as dashed white line and posterior division of the left descending coronary artery shown as dashed red line).**

**B. Delineated pixel selection of LV (green) and RV (orange).**

### Digital filtering

Optical signals were spatially filtered using a Gaussian spatial filter, with uniform window size (3 x 3). Temporal filtering was achieved using a $5^{th}$ order Savitzky-Golay polynomial filter with a 21 sample filtering window, which acts as a low-pass smoothing filter. This was chosen to remove unwanted noise whilst preserving the high frequency components of the optical action potential signals through local polynomial regression to determine the smoothed value for each data point.

## Viability of preparation

Maintenance of viability of the heart preparation throughout time course of the experiments was essential to the utility of this technique. In control experiments (n = 7), the stability of the preparation was assessed looking at the change in a number of different analysed parameters over time as well as assessing the relative level of intrinsic heterogeneity between hearts in this control group.

### Stability of signals over time

Optical AP and ECG morphology was assessed over a timescale of 120 minutes. During experiments there was a progressive decrease in the average SNR over time (100.0 ± 6.8 to 84.7 ± 5.8 to 79.6 ± 6.2 to 78.2 ± 8.1 to 67.9 ± 8.0 to 87.3 ± 5.9 to 84.7 ± 8.5 to 79.6 ± 9.3 to 77.7 ± 9.3), shown as a percentage change from baseline in Figure 3.9. From inspecting the AP and ECG signals from the hearts, there were no significant differences that could be observed comparing 0 and 120-minute time points (Figure 3.10). This was confirmed after plotting the analysed optical AP and ECG parameters, which showed no significant changes over time (Figure 3.11 and Table 3.1). In addition, there were no major alterations in the overall pattern of electrical events, evidenced by the isochronal contour maps comparing 0 and 120 minute time points for activation time ($TAct_M$), $APD_{90}$ and repolarisation time ($TRepol_{90}$), as shown in Figure 3.12, Figure 3.13 and Figure 3.14, respectively.

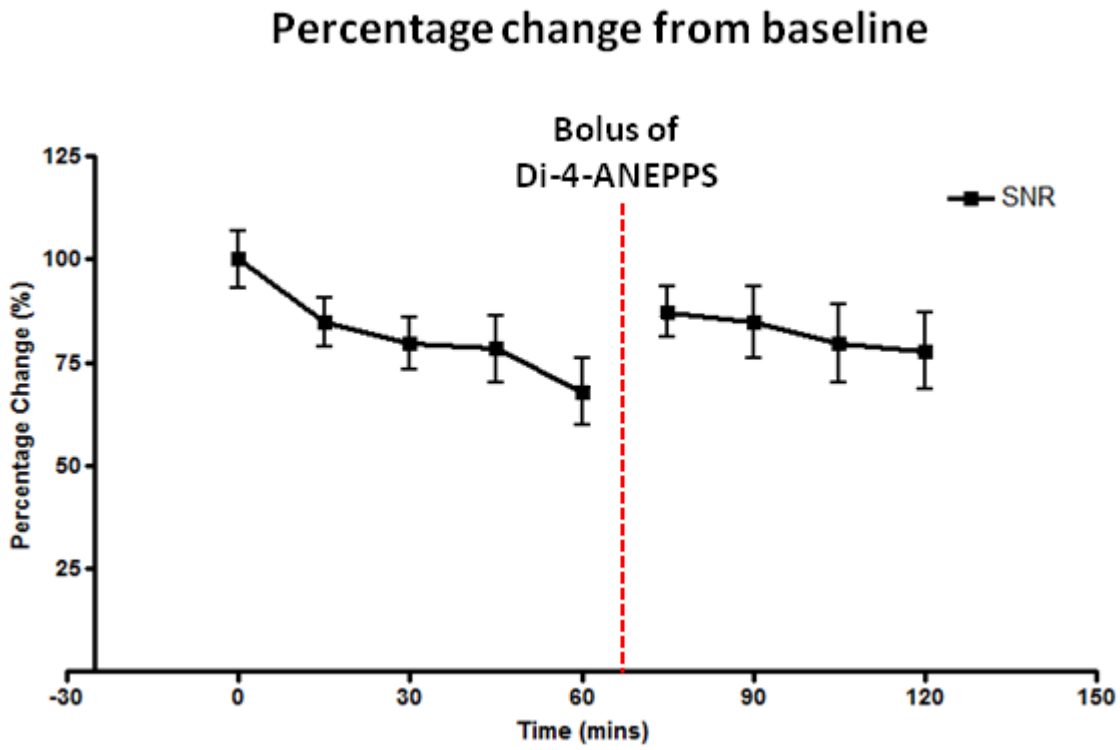


**Figure 3.9 Signal-to-noise over time**

**Percentage change in SNR of preparation over time, with supplementary dye loading shown as dashed red line in time course.**

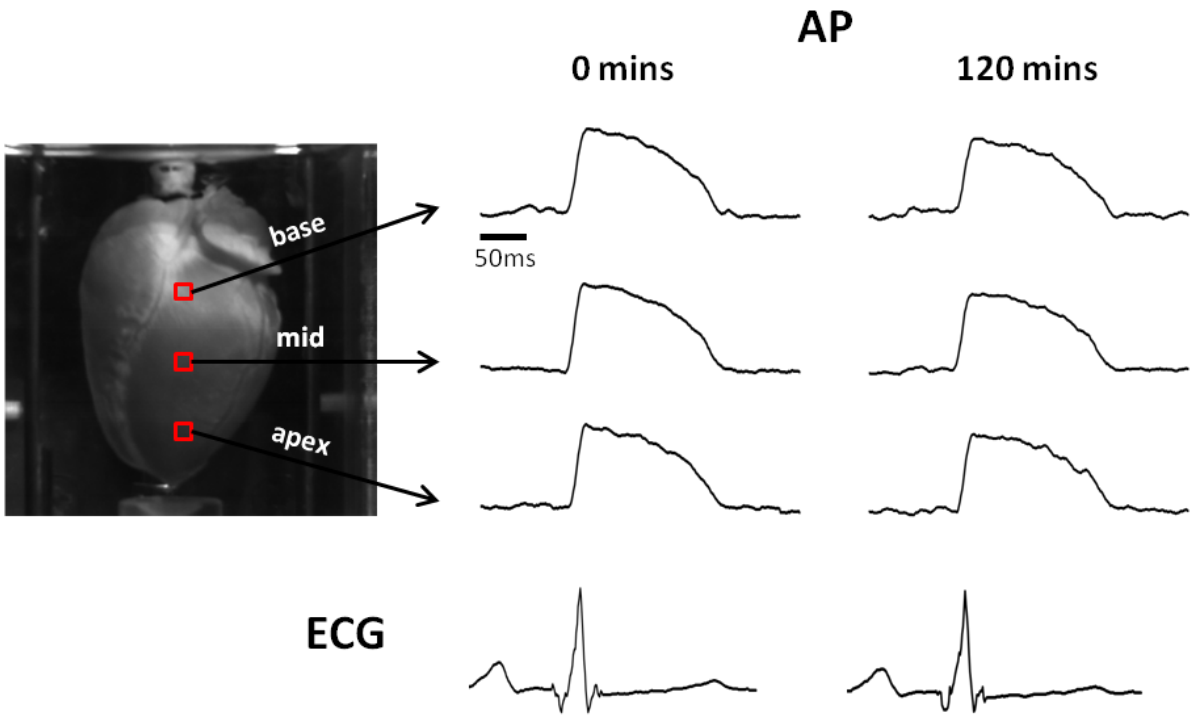


**Figure 3.10 Representative AP and ECG signals**

**A typical example of APs and ECG across the epicardium at 0 and 120 minutes from the experiments.**

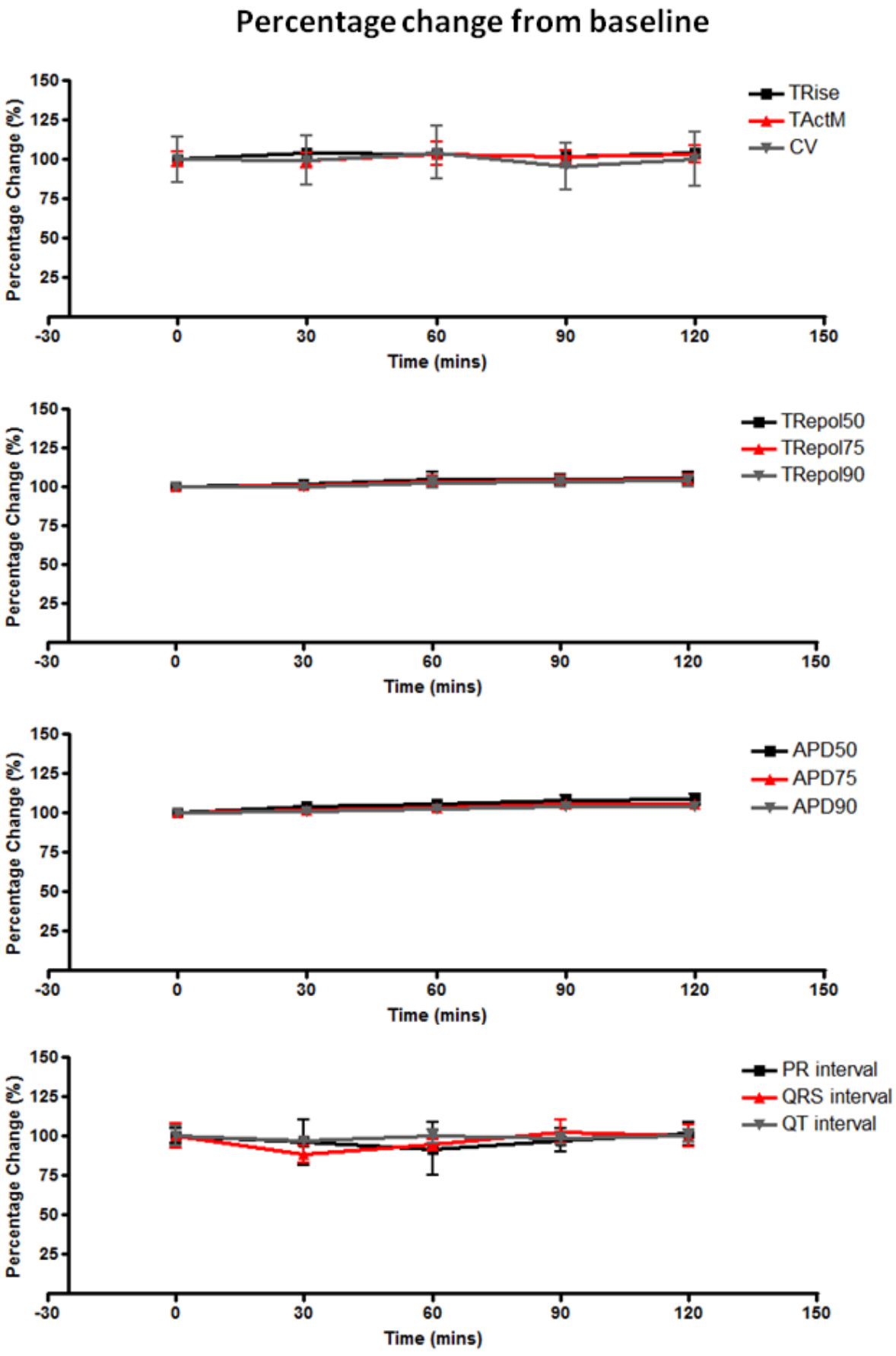


**Figure 3.11 Change in AP and ECG parameters**

**Percentage change (%) from baseline of optical AP and ECG parameters over time course of experiment.**

**Table 3.1 Summary of absolute values for each parameter at each time point (values in ms)**

| | Time (mins) | | | | |
|---|---|---|---|---|---|
| **Parameter (mean ± SE)** | **0** | **30** | **60** | **90** | **120** |
| TRise | 17.2±0.3 | 17.8±0.3 | 17.8±0.4 | 17.5±0.3 | 17.9±0.2 |
| TActM | 105.4±4.8 | 104.9±4.7 | 109.2±8.2 | 107.1±4.6 | 108.7±5.6 |
| CV | 47.7±6.9 | 49.8±8.1 | 47.8±8.1 | 45.5±7.1 | 47.8±8.1 |
| TRepol50 | 214.8±5.2 | 219±6.2 | 225.3±9.9 | 224.8±8 | 227.3±8.9 |
| TRepol75 | 249±5.1 | 251.5±6.2 | 257.9±9.8 | 258.7±8.7 | 260.5±9.2 |
| TRepol90 | 275.7±5.4 | 276.8±6.2 | 283.1±9.7 | 284.7±9.1 | 286.1±9.4 |
| APD50 | 109.5±1.6 | 114±1.9 | 116±3.4 | 117.8±3.7 | 118.6±4 |
| APD75 | 143.7±2.1 | 146.6±2 | 148.7±3.4 | 151.5±4.6 | 151.8±4.4 |
| APD90 | 170.3±2.5 | 171.9±2 | 174±3.3 | 177.5±5 | 177.4±4.6 |
| PR interval | 73±3.5 | 70±10 | 67±11.2 | 71±5.3 | 74±5.5 |
| QRS duration | 35±2.8 | 31±1.7 | 33±1 | 36±2.8 | 35±2.5 |
| QT interval | 183±11.7 | 178±3.8 | 183±8 | 180±6.5 | 183±6.9 |

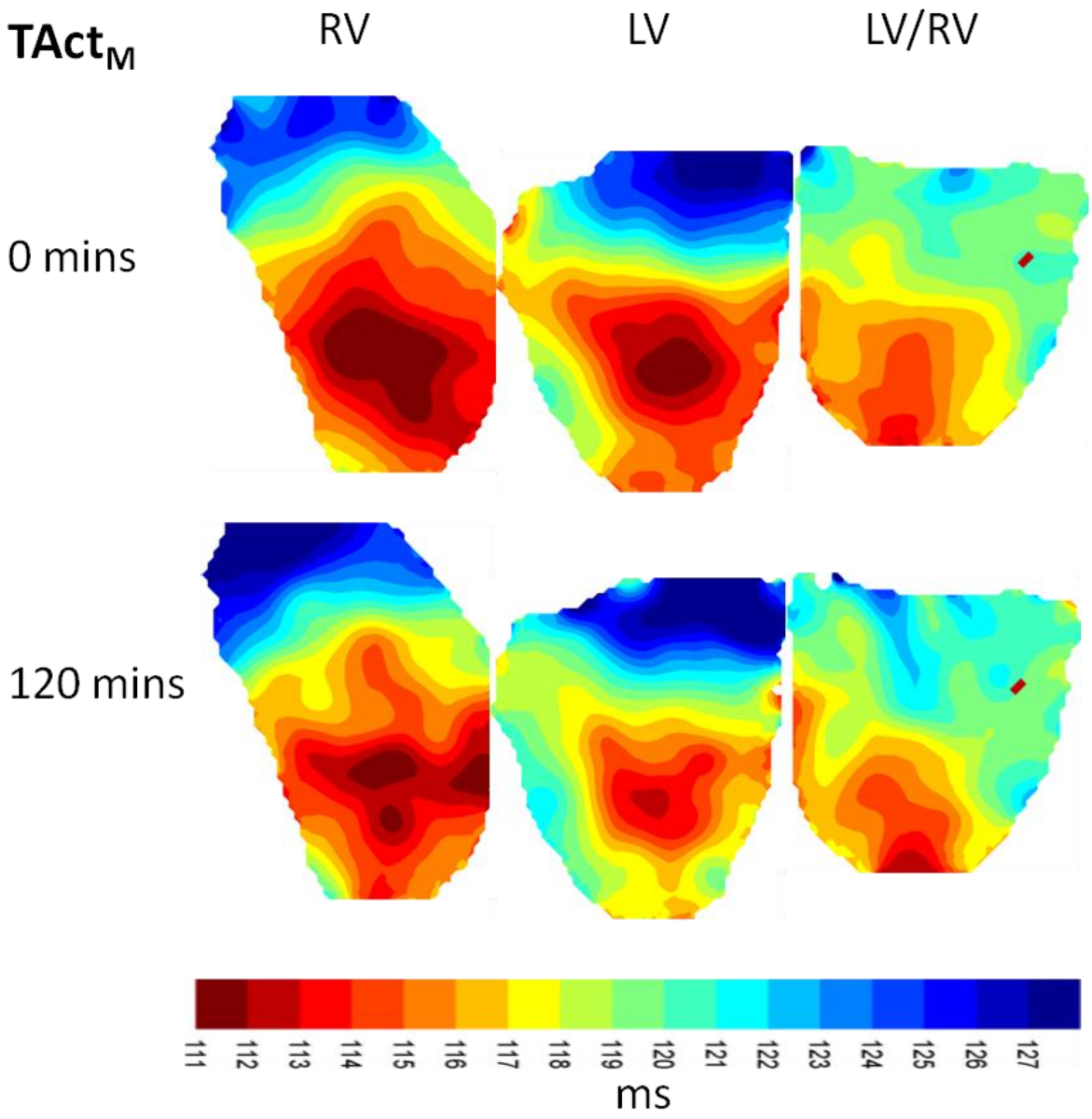


**Figure 3.12 Contour maps of activation time**

**Isochronal contour map of activation time ($TAct_M$) from recordings at 0 and 120 minutes during experiments.**

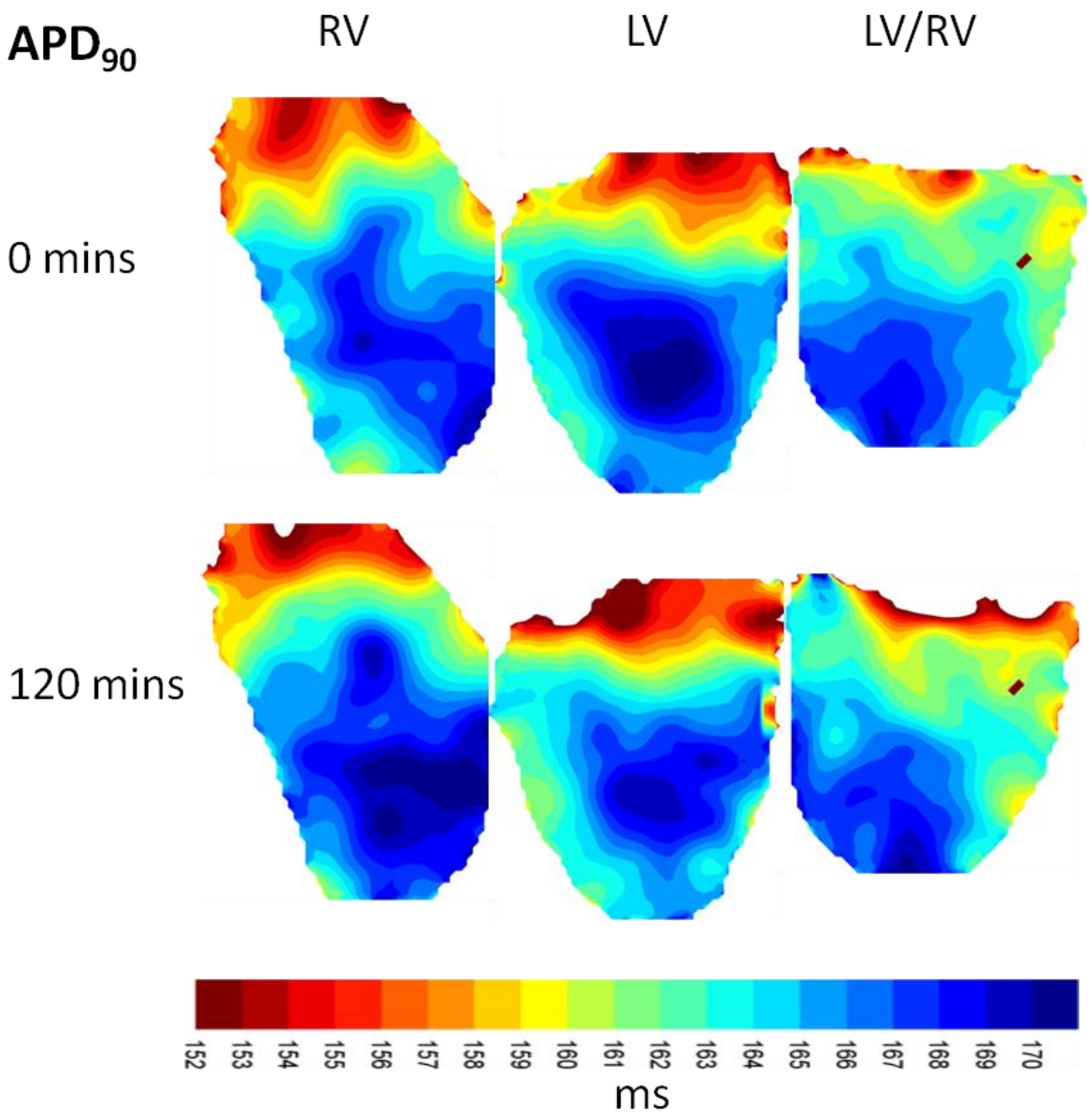


**Figure 3.13 Contour maps of action potential duration**

**Isochronal contour map of $APD_{90}$ from recordings at 0 and 120 minutes during experiments.**

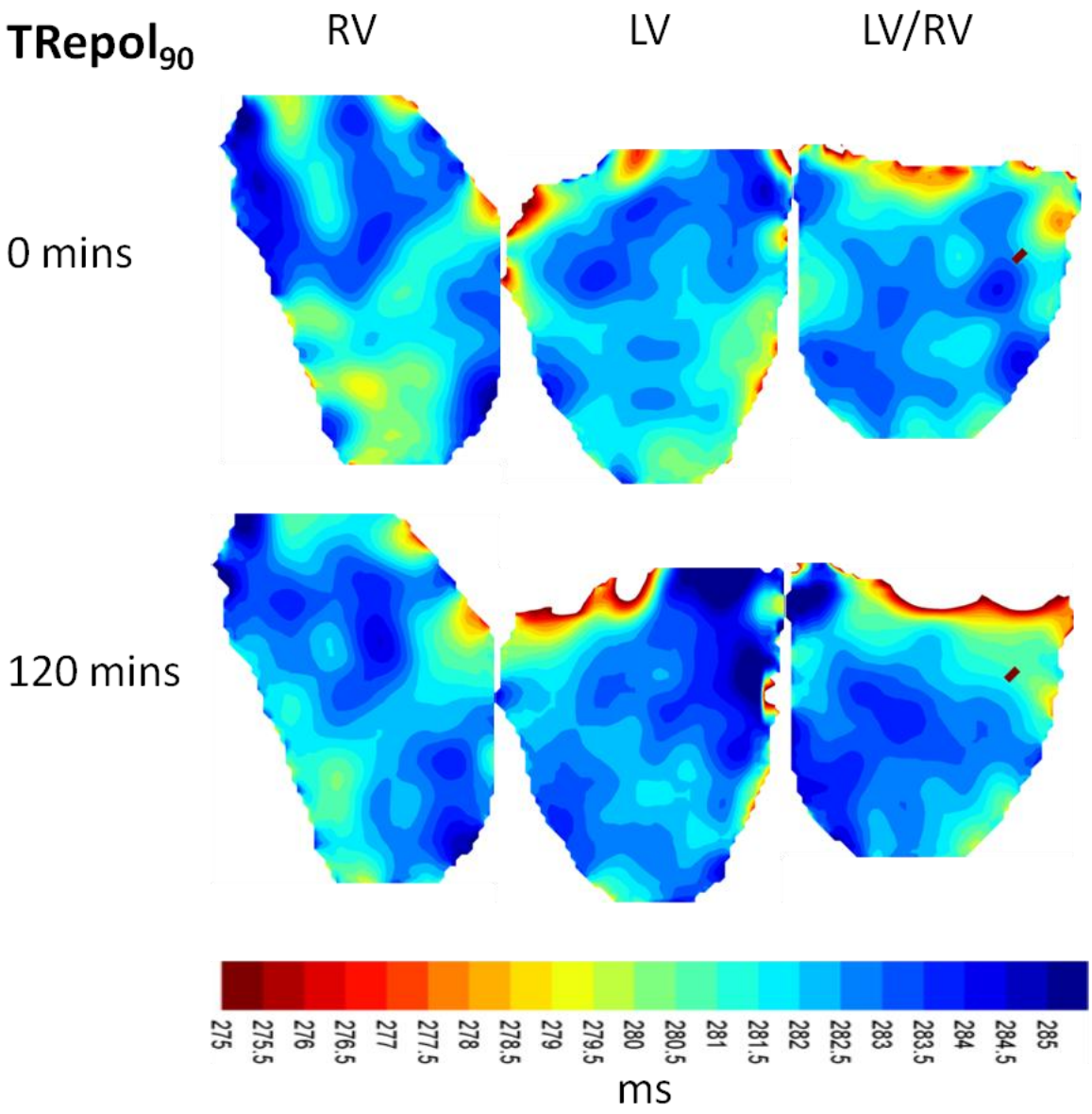


**Figure 3.14 Contour maps of repolarisation time**

**Isochronal contour map of repolarisation time ($TRepol_{90}$) from recordings at 0 and 120 minutes during experiments.**

**Heterogeneity of activation time and action potential duration**

In this set of experiments the earliest activation time on epicardial surface varied significantly between hearts on both the LV and RV, as summarised in Table 3.2 and Table 3.3, respectively. In general, epicardial breakthrough (time of earliest electrical activation on the epicardial surface) occurred synchronously in both ventricles, though in some cases RV breakthrough preceded LV breakthrough.

There were small variations in the range of activation times between hearts on the LV and RV, as summarised in Table 3.2 and Table 3.3, respectively. However, neither the inter-heart or interventricular differences observed were found to be statistically significant ($p>0.05$). In general, the overall distributions of activation times were similar between hearts as shown in Figure 3.15.

**Table 3.2 Summary of AP characteristics in the LV**

| LV | Heart-1 | Heart-2 | Heart-3 | Heart-4 | Heart-5 | Heart-6 | Heart-7 | Mean±SE |
|---|---|---|---|---|---|---|---|---|
| TActM | | | | | | | | |
| Median | 123.0 | 100.0 | 89.0 | 94.0 | 101 | 123 | 117 | 106.7 ± 5.3 |
| 5th Percentile | 116.0 | 96.0 | 81.0 | 88.0 | 97 | 113 | 112 | 100.4 ± 5.1 |
| 95th Percentile | 132.0 | 105.0 | 96.0 | 101.0 | 109.35 | 129 | 123 | 113.6 ± 5.4 |
| Range | 16.0 | 9.0 | 15.0 | 13.0 | 12.3 | 16.0 | 11.0 | 13.2 ± 1 |
| APD90 | | | | | | | | |
| Median | 160.0 | 169.0 | 171.0 | 193.0 | 172 | 161 | 165 | 170.1 ± 4.2 |
| 5th Percentile | 147.0 | 155.0 | 153.4 | 173.0 | 156 | 151 | 156 | 155.9 ± 3.1 |
| 95th Percentile | 169.0 | 177.0 | 181.0 | 201.0 | 179 | 170 | 171 | 178.3 ± 4.2 |
| Range | 22.0 | 22.0 | 27.6 | 28.0 | 23.0 | 19.0 | 15.0 | 22.4 ± 1.7 |
| TRepol90 | | | | | | | | |
| Median | 284.0 | 269.0 | 259.0 | 287.0 | 274 | 284 | 282 | 277 ± 3.8 |
| 5th Percentile | 274.0 | 258.0 | 249.0 | 272.0 | 261 | 277 | 276 | 266.7 ± 4.1 |
| 95th Percentile | 288.0 | 275.0 | 265.0 | 292.0 | 280 | 286 | 285 | 281.6 ± 3.5 |
| Range | 14.0 | 17.0 | 16.0 | 20.0 | 19.0 | 9.0 | 9.0 | 14.9 ± 1.7 |

**Table 3.3 Summary of AP characteristics in the RV**

| RV | Heart-1 | Heart-2 | Heart-3 | Heart-4 | Heart-5 | Heart-6 | Heart-7 | Mean±SE |
|---|---|---|---|---|---|---|---|---|
| TActM | | | | | | | | |
| Median | 127.0 | 101.0 | 90.0 | 95.0 | 104 | 112 | 117 | 106.6 ± 4.9 |
| 5th Percentile | 119.0 | 93.0 | 82.0 | 88.0 | 95 | 104 | 111 | 98.9 ± 5 |
| 95th Percentile | 136.0 | 112.0 | 97.0 | 103.0 | 116 | 124 | 128 | 116.6 ± 5.2 |
| Range | 17.0 | 19.0 | 15.0 | 15.0 | 21.0 | 20.0 | 17.0 | 17.7 ± 0.9 |
| APD90 | | | | | | | | |
| Median | 154.0 | 168.0 | 171.0 | 188.0 | 167 | 171 | 164 | 169 ± 3.9 |
| 5th Percentile | 139.0 | 155.0 | 158.0 | 168.0 | 150 | 159 | 153 | 154.6 ± 3.4 |
| 95th Percentile | 165.0 | 181.0 | 186.0 | 199.0 | 175 | 178 | 170 | 179.1 ± 4.2 |
| Range | 26.0 | 26.0 | 28.0 | 31.0 | 25.0 | 19.0 | 17.0 | 24.6 ± 1.9 |
| TRepol90 | | | | | | | | |
| Median | 281.0 | 270.0 | 261.0 | 283.0 | 271 | 283 | 282 | 275.9 ± 3.3 |
| 5th Percentile | 261.3 | 260.0 | 252.0 | 267.0 | 257 | 276 | 275.6 | 264.1 ± 3.5 |
| 95th Percentile | 288.0 | 278.0 | 271.0 | 292.0 | 278 | 287 | 285 | 282.7 ± 2.8 |
| Range | 26.7 | 18.0 | 19.0 | 25.0 | 21.0 | 11.0 | 9.4 | 18.6 ± 2.5 |

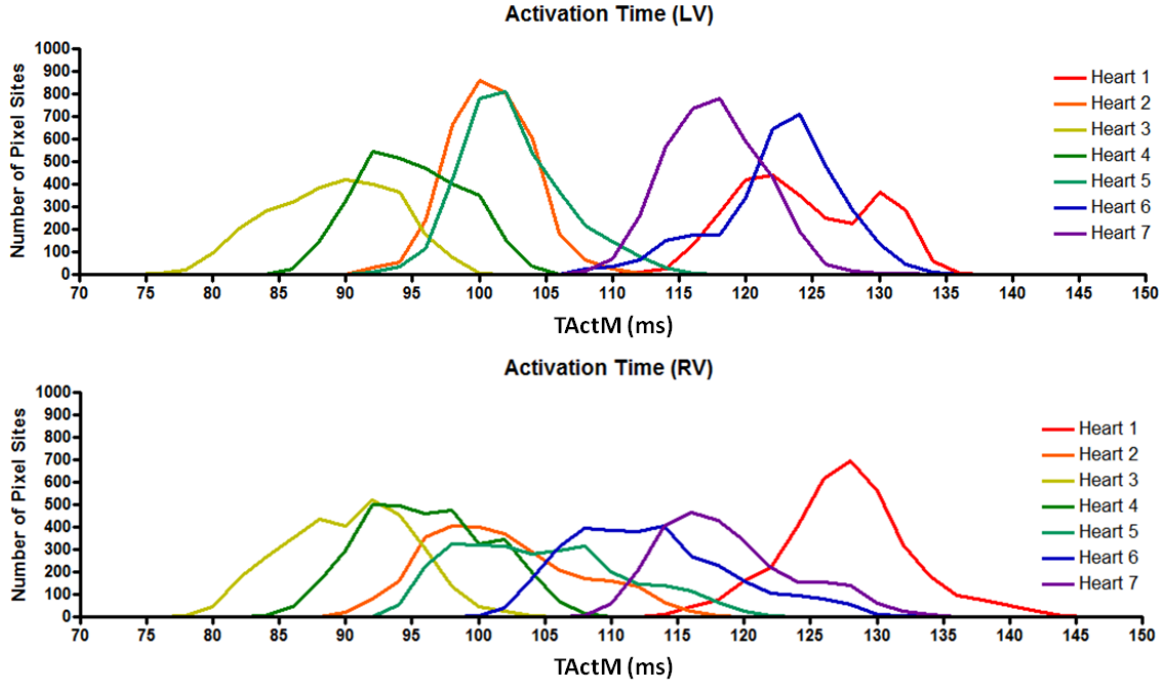


**Figure 3.15 Distribution of activation times (TActM) for the LV and RV.**

The range of APD times were consistent between hearts on both the LV and RV, as summarised in Table 3.2 and Table 3.3, where there were no statistical differences. In general, there was a good overall qualitative agreement between

distributions of repolarisation times between hearts, however, Heart-6 and Heart-7 showed smaller ranges in repolarisation time by comparison to the other hearts in the group. This was reflected in the narrow distributions for Heart-6 and 7 for repolarisation time, as shown in Figure 3.17.

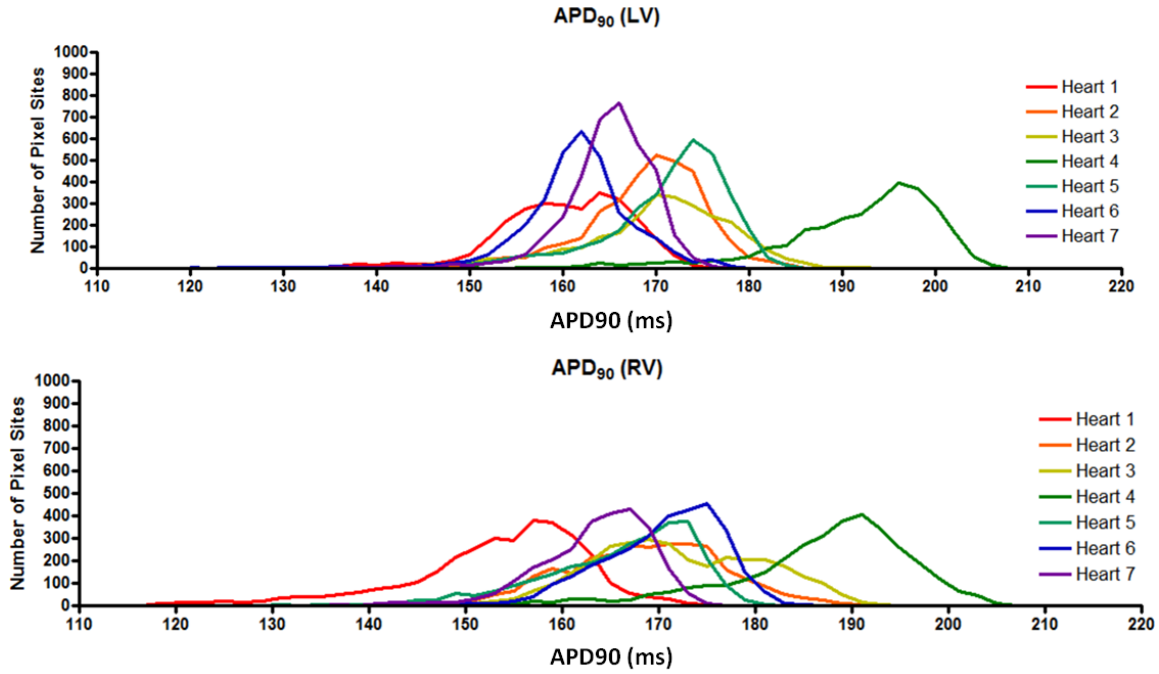


**Figure 3.16 Distribution of APD90 for the LV and RV.**

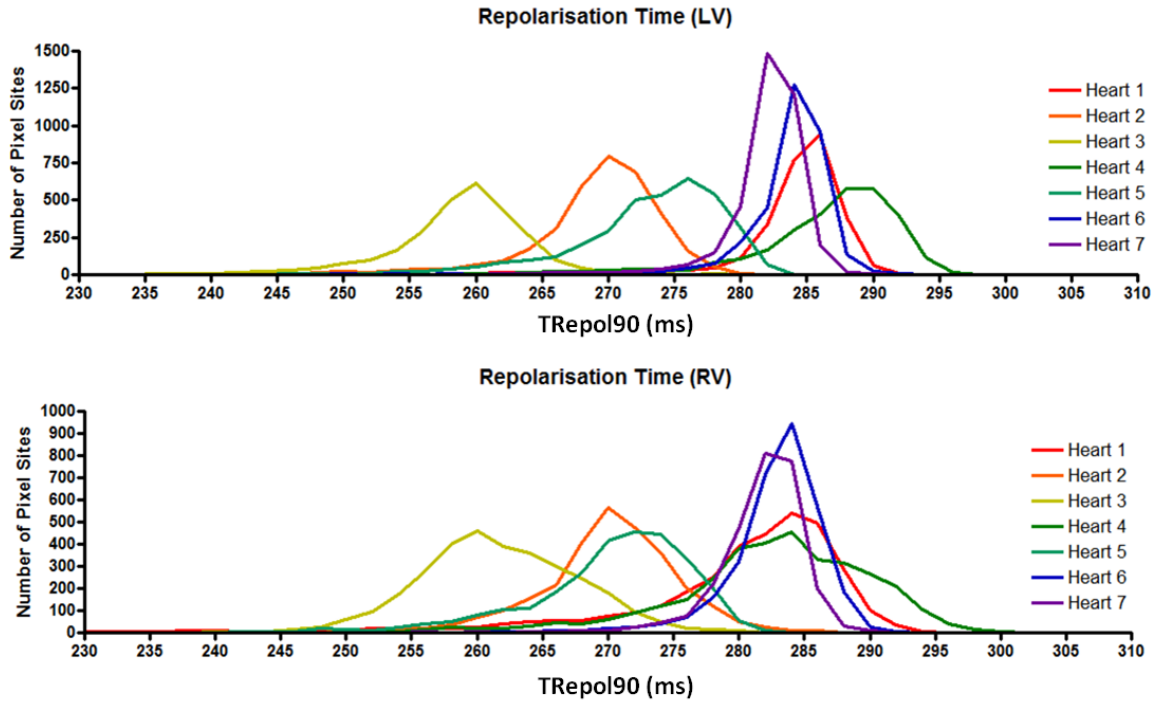


**Figure 3.17 Distribution of repolarisation times (TRepol90) for the LV and RV.**

There was a inverse relationship between APD and activation time across the LV and RV with an average slope of -1.29 ± 0.09 (R=0.54) and -1.04 ± 0.07 (R=0.49), respectively. The slope of the relationship across the LV was significantly different than RV ($P<0.05$), with a mean difference of -0.25 ± 0.09.

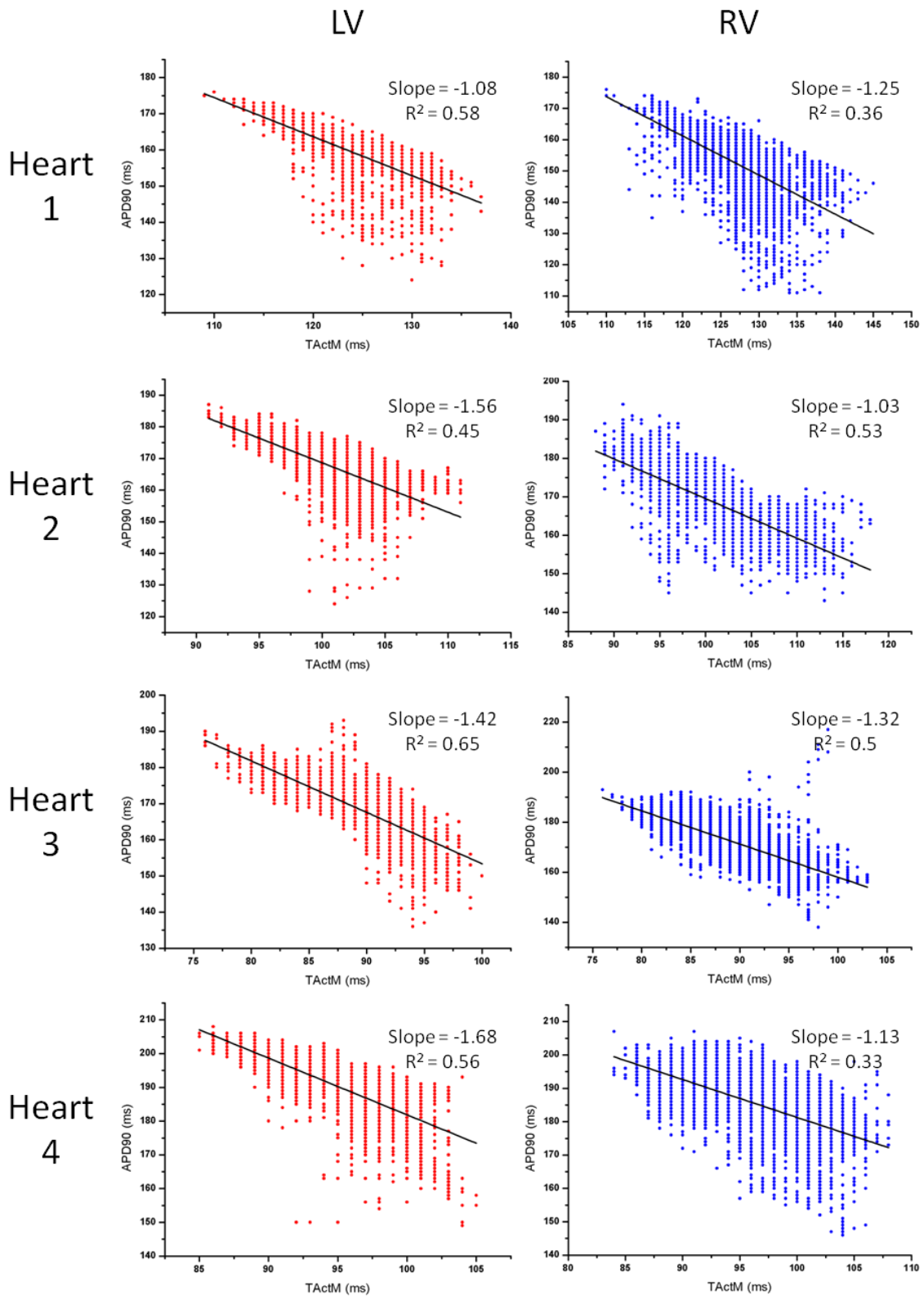
LV
RV
Heart 1
Slope = -1.08
R² = 0.58
Slope = -1.25
R² = 0.36
Heart 2
Slope = -1.56
R² = 0.45
Slope = -1.03
R² = 0.53
Heart 3
Slope = -1.42
R² = 0.65
Slope = -1.32
R² = 0.5
Heart 4
Slope = -1.68
R² = 0.56
Slope = -1.13
R² = 0.33
APD90 (ms)
TActM (ms)

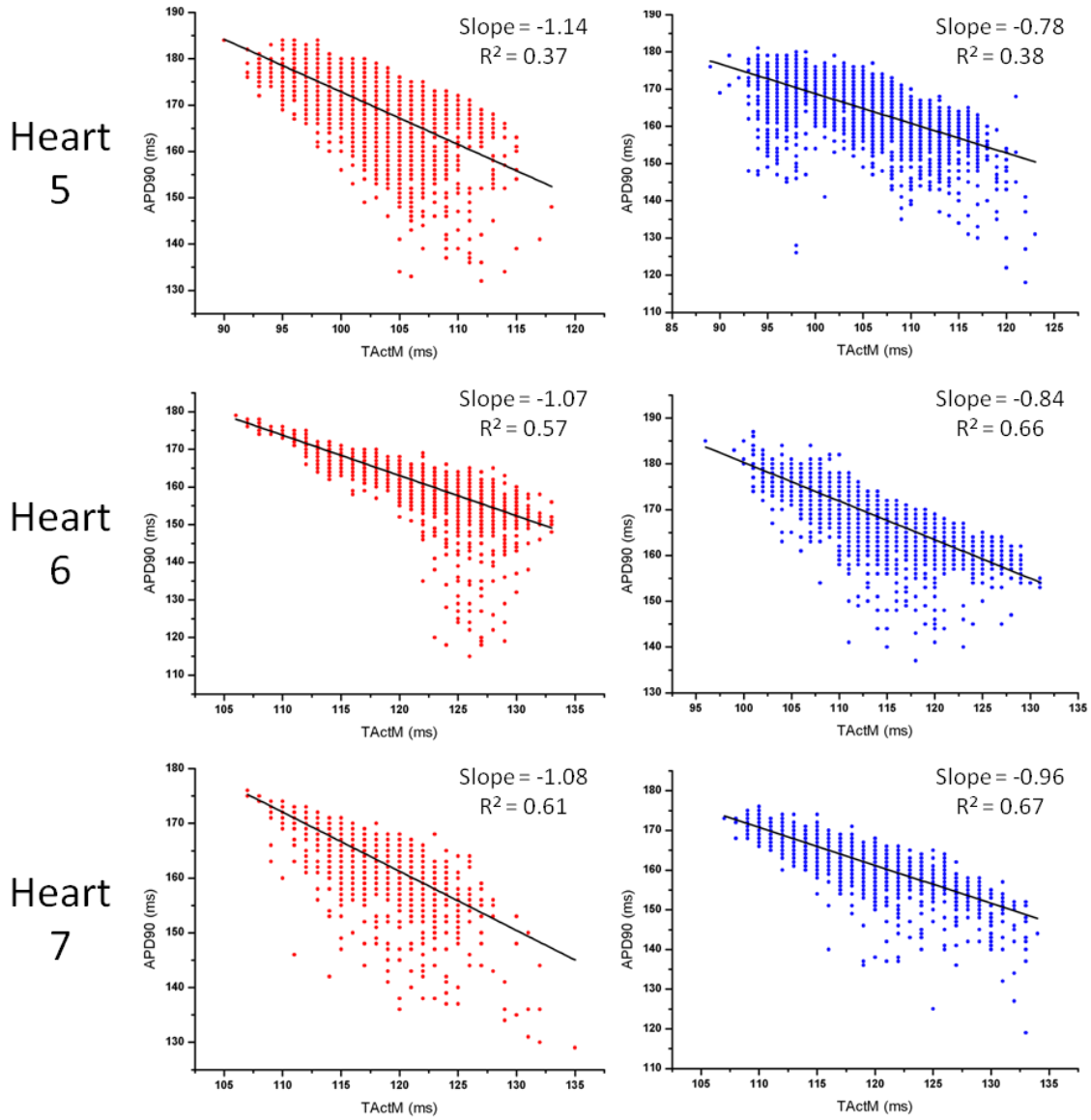


**Figure 3.18 Relationship between APD and activation time ($TAct_M$)**

**Inverse relationship between APD and activation time in each heart in both the LV and RV.**

# Discussion

This chapter describes the protocol developed for the robust selection, filtering and analysis of optical data from the isolated rabbit heart. The protocol was used to investigate the stability of the heart preparation over a 2-hour period using the panoramic optical mapping system to map epicardial electrical activity. Inter-heart variability in ventricular activation time and APD was also examined. Finally, the relationship between activation sequence and action potential duration was investigated in both LV and RV fields during RA pacing.

## Selection and viability of preparation

The protocol for selection, filtering and analysis of optical data was able to reproducibly delineate, filter and analyse optical signals based on a multi-faceted criteria approach.

The time-dependent feature of the experimental results indicated that, despite progressive decrease in SNR (partially restored by further bolus injections of Di-4-ANEPPS), there were no significant changes in optical AP or ECG morphology (Figure 3.11). In addition, there were no significant alterations in the overall pattern of electrical events (Figure 3.12). The experiments were stable over a 2-hour window; all subsequent studies were kept within this timescale, with supplementary dye loading at ~60-minute intervals.

The heterogeneity present between hearts was most prominent in the differences found between the times of earliest activation. These findings are comparable with previous studies, a value of 83±3ms (mean ± SE) was previously reported for the isolated rabbit heart preparation (Walker et al., 2007). The major determinant of the time between RA pacing and the earliest activation on the epicardial surface is conduction through the A-V node. In previous studies (Nisbet, 2008; Nisbet et al., 2014) isolated A-V node conduction times were reported to be 60-70ms, while separate studies on endo-epicardial conduction times for the LV were reported to be 12-13ms at 300ms pacing cycle length (Walker et al., 2007). This suggests that biological variation in A-V nodal conduction time is the predominant cause of the variation in total conduction time. However, the variation in total conduction time reported in the current

study appears to be greater than that previously reported. The cause of this larger variation is not known. There did not appear to be any change over time in the relationship in the heart-to-heart variation, which suggests that improvements in experimental technique were not a factor. Another contributing experimental variable may be temperature; imprecise control over experimental temperatures may generate a variation in total conduction time. In these experiments, a water-jacketed reservoir above the aortic cannula and in-line temperature transducer was used to monitor and maintain physiological temperature in both the perfusate and surrounding bath fluid at all times, as discussed in depth in Chapter-2. Thus it is unlikely that variation seen arises from improper temperature control. The E-C uncoupler blebbistatin was used in all of these experiments in order to record optical action potentials in the absence of significant motion artefacts. Blebbistatin has been shown to have minimal effects on the heart's electrical activity, including ECG parameters (Fedorov et al., 2007; Lou et al., 2012). However, to my knowledge there is no published data on the specific effects on A-V nodal conduction. In summary, the specialised rig and Langendorff perfusion system, used to panoramically map the electrical activity across the heart, provides a stable platform to study short-term (within 2hrs) changes in epicardial electrophysiology. The heart-to-heart variation in epicardial activation time appears to be dominated by changes on overall conduction time suggesting variation in A-V nodal conduction.

## Coupling between APD and activation time

The coupling between activation and repolarisation generated a negative gradient in APD along the activation path, where earlier activation times corresponded with longer action potential durations and later activation times corresponded with shorter action potentials durations (Figure 3.18). This inverse relationship was consistent with values reported in previous experimental studies using RA pacing or during sinus rhythm (Toyoshima and Burgess, 1978; Hanson et al., 2009; Myles et al., 2010; Osaka et al., 1987; Yue et al., 2005). The strong association between the activation sequence and the APD supports the idea of electrotonic current flow as the main determinant of the spatial and temporal pattern of APD. The electrotonic interactions between cells, mediated by low-resistance gap junctions, act to spatially average and mask the intrinsic differences between individual cells and in particular attenuate any temporal

gradients in repolarisation. Studies using Purkinje fibre preparations and isolated ventricular muscle have shown that depolarising currents applied during the repolarisation phase prolongs APD while repolarising currents shortens APD (Weidmann, 1951; Cranefield and Hoffman, 1958; Vassalle, 1966). Moreover, this suggests that the distinct intrinsic repolarisation characteristics of isolated myocytes between apex-base and LV-RV play a lesser role in the overall pattern of APD across the epicardial surface. Subsequently, this association implies that through the modulation of APD by the activation sequence, dispersion in repolarisation would be predominately dictated by the current activation sequence.

Between the LV and RV, there was a significant difference in the slope of the inverse relationship. Electrotonic interactions are a dynamic property affected by tissue geometry and coupling resistance along the path of conduction. The left and right ventricles are structurally heterogeneous, each with distinct regional differences in shape, wall thickness and fibre angle. Therefore, this may contribute to the difference seen between the LV and RV in terms of the electrotonic interaction between APD and activation time.

## Future Directions

In Chapter 5, this technique is used to study the correlation between APD and activation time in more detail by investigating the effects of alternatives forms of pacing on this relationship, and to the effects of different activation sequences on the overall dispersion of repolarisation across the epicardial surface. Epicardial activation was further studied in a rabbit model of chronic MI.

## Conclusion

While the range of epicardial activation times and the pattern of epicardial activation was consistent across a range of isolated rabbit heart preparations, the differences between hearts with respect to earliest activation time was suggestive of variations in A-V nodal conduction as a result of both intrinsic physiological variation between rabbits and potentially a consequence of the experimental procedure although no single experimental variable was identified. The main finding from this study was an inverse relationship between APD and activation time, which manifested in the apex to base axis of the epicardial surface of both LV and RV. Therefore, suggesting that the activation sequence and subsequent electronic interaction is the main determinant of the spatial and temporal distribution of APD across the epicardial surface.

# Chapter 4: Measurements of ventricular activation and repolarisation during hypothermia

## Aims

The aim of this study was to examine the changes in features of epicardial electrophysiology as the temperature of a heart is reduced below physiological values. This manoeuvre was chosen to mimic the temperatures experienced during various levels of hypothermia, a condition known to promote arrhythmias. The facility for panoramic optical mapping allowed the extent of changes in conduction timing and pattern of ventricular activation to be assessed.

## Introduction

Hypothermia can be defined as the fall in core temperature to <35°C and be broadly classified into two categories: mild-therapeutic (31-35°C) and severe (<28°C) (Mallet, 2002; Reuler, 1978). The effects of hypothermia on the cardiovascular system have been of interest for over 60 years, since the pioneering work by Bigelow *et al*. which examined the clinical applications during intracardiac surgery (Bigelow et al., 1950). In particular, severe hypothermic temperatures (15°C) have been utilised in patients during aortic arch surgery for improved cerebral protection (Di Luozzo and Griepp, 2012). In more recent years, therapeutic hypothermia has been used in the clinic for the treatment of patients who have survived a cardiac arrest due to VF, owing to the improved survival and neurological outcomes in patients (Arrich et al., 2007; Bernard et al., 2002).

Hypothermia, from an electrophysiological standpoint, can be characterised by a number of well known effects at both a whole heart and cellular level. At the cellular level there is prolongation in APD, owing to the susceptibility of a number of ionic currents to temperature – $I_{to}$, $I_{Kr}$, $I_{Ca,L}$ and $I_{NCX}$ (Bjørnstad et al., 1995; Sprung et al., 1994, 1995; Bjørnstad et al., 1994; Marshall et al., 2002; Suleiman and Chapman, 1990; Liu et al., 1991; Gambassi et al., 1994; Mortensen et al., 1993). In addition, there is enhanced dispersion of repolarisation (Glukhov et al., 2012; Piktel et al., 2011; Hsieh et al., 2009; Salama et al., 1998), the presence of APD alternans (Glukhov et al., 2012; Hsieh et al., 2009; Egorov et al., 2012) and slowing in conduction velocity (CV), attributed to gap junction remodelling (heterogeneous downregulation and lateralization of Cx43) (Fedorov

et al., 2008, 2005; Hsieh et al., 2011). In particular, enhanced heterogeneities of repolarisation, induced by hypothermia, are associated with increased susceptibility to arrhythmias and re-entrant excitation, further amplified in the presence of slowed conduction. With the growing use of both therapeutic and severe hypothermic temperatures in the clinical setting, it is important to gain insight into its effects on cardiac electrophysiology.

To assess the effects of changes in temperature, temperatures relevant to mild-therapeutic hypothermia (31°C) and severe hypothermia (17°C) were used.

# Methods

## Preparation of the rabbit hearts

In these experiments a total of 8 New Zealand White rabbits (2.5kg-3.5kg) were used for optical mapping. The rabbits were sacrificed and the hearts Langendorff perfused as described in Chapter 2. To suppress motion artefacts the E-C uncoupler blebbistatin (10μM) was added to the perfusate and the preparation stained with voltage-sensitive dye, Di-4-ANEPPS (100μl of 1mg/ml). Hearts were paced via the RA throughout experiments at cycle lengths of 300ms, 450ms and 1700ms for 37°C, 31°C and 17°C, respectively. The definition of the cycle length for pacing at each temperature was based on a subset of pilot experimental animals (n=4) where the typical sinus rate at each temperature was measured, as shown in Figure 4.1. Restitution is defined as the relationship between APD and the preceding diastolic interval (DI). Under normal circumstances, APD does not vary at a constant cycle length. However, as cycle length changes the relationship between DI and APD varies. For example at significantly high heart rates there is a dramatic shortening in APD in proportion to DI (steep restitution curve – slope >1). However, at slower heart rates (shallow restitution curve – slope <1) such as during hypothermia APD tends to stabilise at one value with changes in DI being the predominant factor.

To measure conduction velocity, hearts were paced via the epicardial surface of the RV to assess epicardial conduction without potential artefacts from transmural conduction, using the same cycle lengths as for RA pacing.

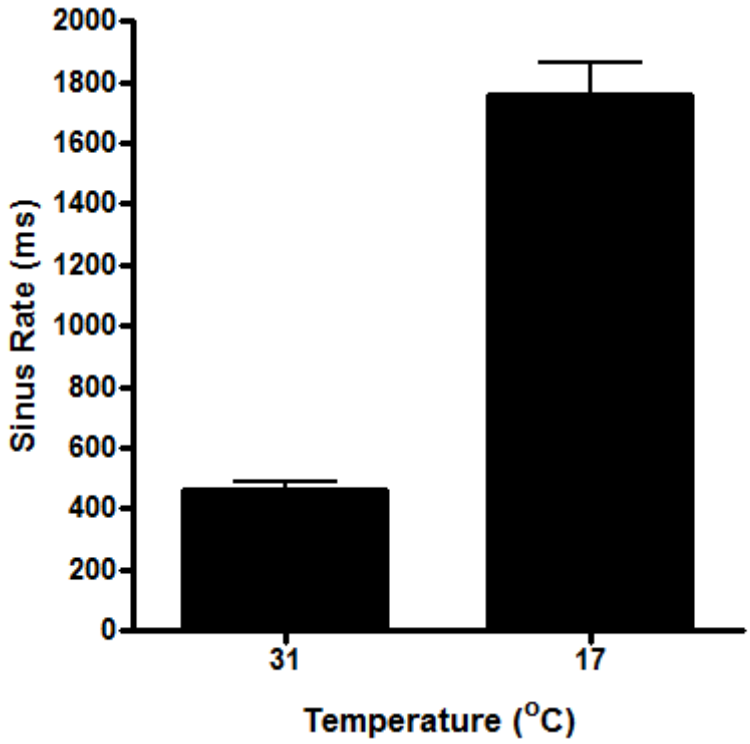


**Figure 4.1 Sinus rate at hypothermic temperatures**

**Sinus rate measured at each hypothermic temperature in a pilot animal group (n=4), where values are represented as mean ± SD.**

## Hypothermia protocol

The temperatures used in this study were chosen to reflect normothermia (37°C), moderate-therapeutic hypothermia (31°C) and severe hypothermia (17°C). A constant perfusion rate of 30ml/min was used throughout experiments, in order to study electrophysiology under the same conditions at different temperatures. Hypothermia was induced by perfusing the heart with temperature controlled Tyrode's solution, via a water bath coupled glass column heat exchanger. Cooling from baseline (37°C) was achieved by gradual reduction of the temperature in the water bath in order to avoid rapid cooling contractures (Bers et al., 1989). The protocol is summarised in (Figure 4.2), where it took ~30 minutes between recordings to gradually cool the preparation. Normothermic control hearts, as discussed in detail in Chapter 3, underwent time matched recordings at 37°C.

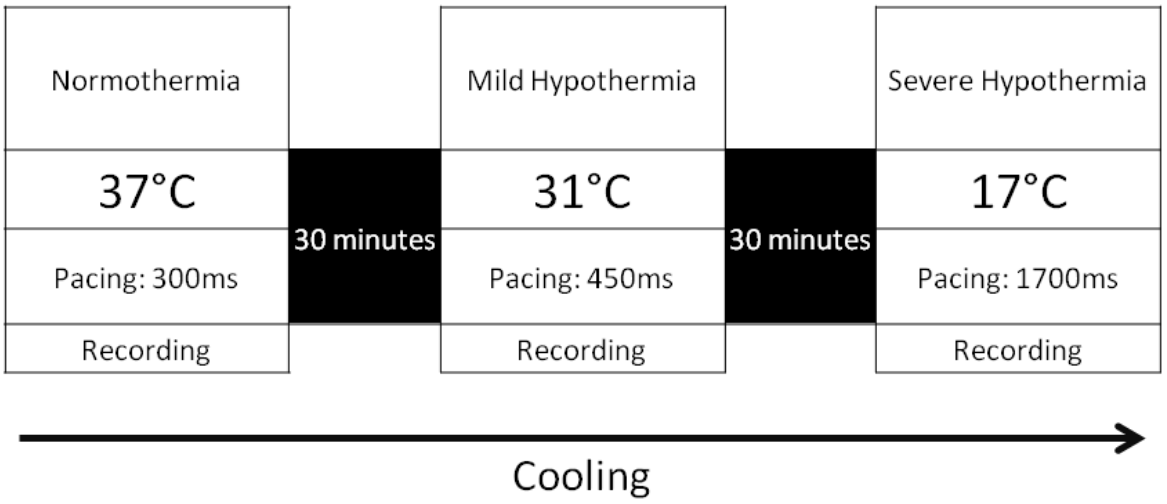


**Figure 4.2 Protocol for hypothermia experiments**

## Data analysis

Optical data and ECG analysis was performed as described in Chapter 3. In this study the electrophysiological parameters analysed were: $TAct_M$ (activation time), CV (conduction velocity), and $APD_{50}$,$APD_{75}$,$APD_{90}$ (action potential duration at 50%, 75%, and 90% repolarisation, respectively), PR, QRS and QT interval. Each of these parameters were plotted as this mean across the epicardial surface unless stated otherwise. For calculation of CV from RV paced recordings a custom-written algorithm in MATLAB was used. In this algorithm epicardial CV was calculated for each pixel, based on its distance from the RV electrode divided by its $TAct_M$. When analysing apex, mid and base differences from the LV and RV views, 10 areas were selected from each view (3 - apex, 4 - mid and 3 – base) covering a 3x3 pixel region with an equal distance between them, as shown in the example in Figure 4.3. An average value was calculated for the apex, mid and base for the LV and RV, taking the three areas at the apex, the four at mid and three at the base. The data values contained in the remainder of results were based on averaged values over the three views of the heart.

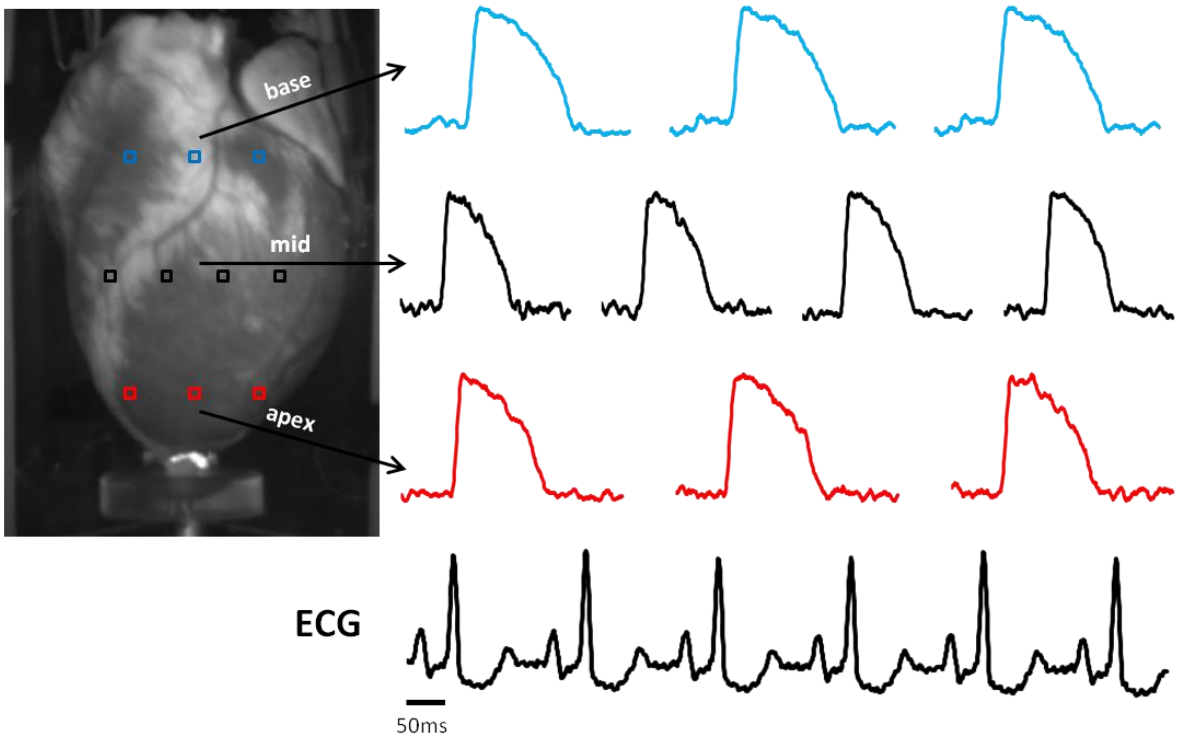


**Figure 4.3 Pixel selection for regional differences**

**Example of 3x3 pixel selections on one view of the heart for analysing the apex, mid and base differences. Optical AP traces recorded from marked regions and corresponding pseudo-ECG.**

## Statistics

Data are expressed as mean ± SEM. Panoramic and ECG data were compared by Student's t-test (paired where appropriate) and apex to base data assessed by two-way ANOVA for repeated measurements, followed, if the F-value exceeded the threshold for significance, by Tukey's test comparing individual groups.

# Results

## Prolongation of repolarisation

Compared to 37˚C, APD ($APD_{50}$, $APD_{75}$ and $APD_{90}$) was significantly prolonged during cooling of the heart (P<0.001) (Figure 4.4). Specifically, $APD_{50}$ during cooling was prolonged from 115.2 ± 1.7 to 183.16 ± 2.8 to 316.03 ± 19.5 (in ms) (P<0.001), respectively, though to lesser degree than $APD_{75}$ and $APD_{90}$ when cooling from 31˚C to 17˚C. $APD_{75}$ during cooling was prolonged from 148.72 ± 2.0 to 216.2 ± 2.4 to 390.5 ± 20.0 (in ms) (P<0.001) and $APD_{90}$ from 172.8 ± 2.3 to 240.2 ± 2.7 to 419.7 ± 20.6 (in ms) (P<0.001).

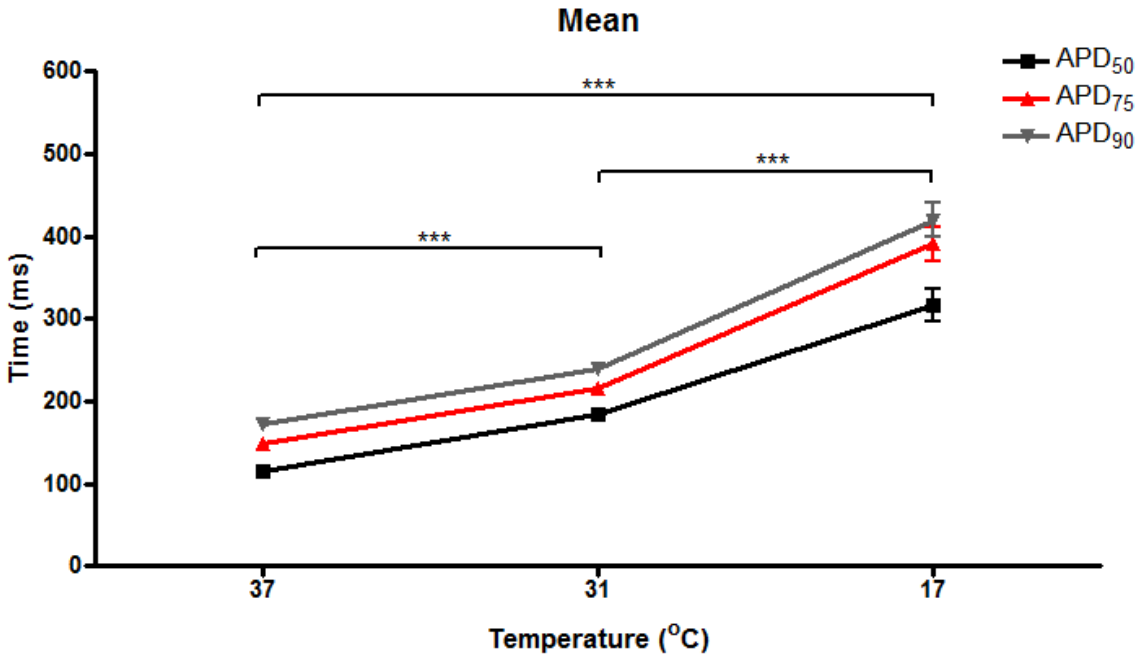


**Figure 4.4 Mean APD**

**Plot of $APD_{50}$, $APD_{75}$ and $APD_{90}$ with change in temperature (***P<0.001).**

A similar change was reflected in the QT interval, which was significantly prolonged from 178.7 ± 21.3 to 267.9 ± 32.6 to 591.7 ± 74.7 (in ms) (P<0.001), shown as a percentage change from baseline in Figure 4.5.

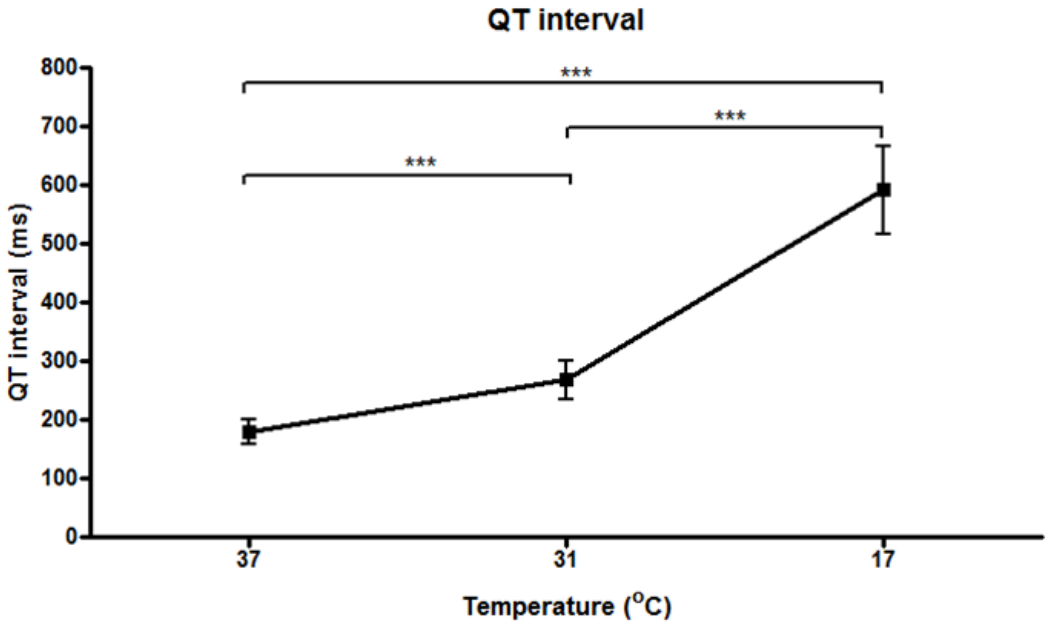


**Figure 4.5 QT interval**

**Change in QT interval from baseline with change in temperature (***P<0.001).**

## Dispersion of repolarisation

In addition to prolongation in repolarisation there was an increase in the degree of dispersion in repolarisation across the surface of the heart. Figure 4.6 shows typical contour maps of $APD_{90}$ during cooling. At 37°C, $APD_{90}$ ranged from 160-182ms, with longest $APD_{90}$ values located in the mid-myocardium and shortest $APD_{90}$ values at the base and apex of the heart. In general, the distribution of $APD_{90}$ stayed relatively homogeneous after cooling to 31°C, although, there were some pronounced changes on the LV by comparison to the RV, where $APD_{90}$ ranged from 218-253ms. However, once cooled to 17°C a more heterogeneous distribution of $APD_{90}$ values developed, with significant shortening of $APD_{90}$ values at the base and differences between the apex and mid-myocardium becoming diminished, where $APD_{90}$ ranged from 260-540ms. These findings are recapitulated in Figure 4.7 looking at mean values (3x3 pixel region) at the apex, mid and basal regions of the LV and RV.

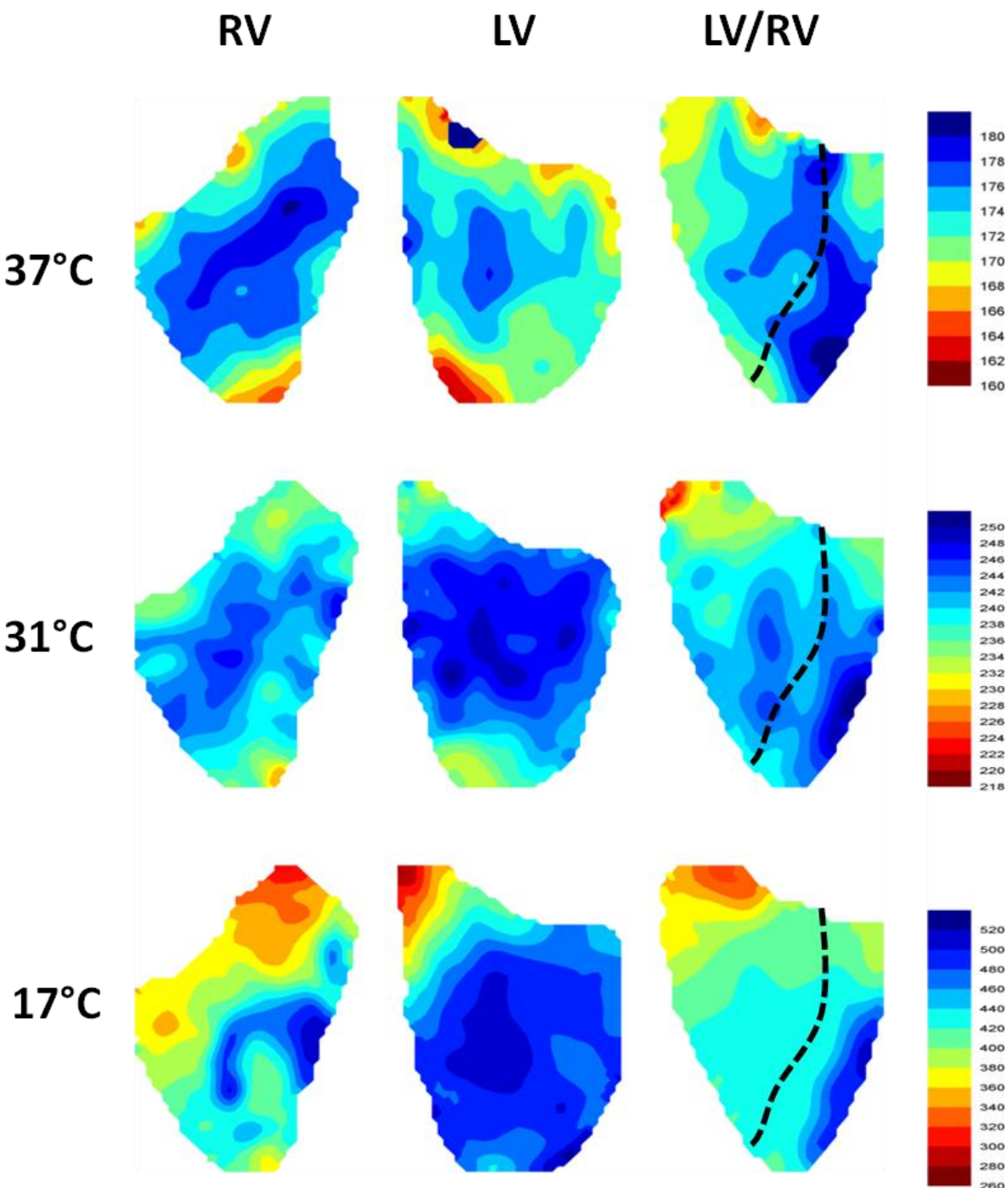


**Figure 4.6 Contour maps of action potential duration**

**Considering change in temperature from three views of the heart (RV, LV and LV/RV). The dashed line indicates the LV/RV border on the posterior surface of the heart.**

At 37°C, $APD_{90}$ at the mid-myocardium was significantly different from values at the apex and base of the heart, for both the LV and RV, with no significant differences in values between LV and RV, as depicted in Figure 4.7 and as illustrated in Figure 4.6. The mid-myocardial values for LV and RV compared against the apex and base of the heart were as follows: 182.2 ± 3.2 vs. 171.9 ±

4.8 ms (LV – mid vs. apex), 182.1 ± 2.4 vs. 169.5 ± 4.0 ms (RV – mid vs. apex), 182.2 ± 3.2 vs. 171.1 ± 3.9 ms (LV – mid vs. base) and 182.1 ± 2.4 vs. 174.3 ± 3.2 ms (RV – mid vs. base) ($P<0.05$). The relationship between apex, mid and base was unchanged during cooling to 31°C, though LV values were significantly prolonged compared to RV: 250.5 ± 3.2 vs. 240.9 ± 3.2 ms (LV – mid vs. apex), 242.1 ± 1.6 vs. 234.9 ± 3.2 ms (RV – mid vs. apex), 250.5 ± 3.2 vs. 243.3 ± 2.4 ms (LV – mid vs. base) and 242.1 ± 1.6 vs. 235.7 ± 3.2 ms (RV – mid vs. base) ($P<0.05$). At 17°C, the differences between LV and RV were accentuated. Differences between mid and apex were diminished: 491.2 ± 19.9 vs. 462.5 ± 19.2 ms (LV – mid vs. apex), 420.2 ± 24.0 vs. 421.8 ± 30.3 ms (RV – mid vs. apex), whilst the differences between mid and base were amplified: 491.2 ± 19.9 vs. 404.2 ± 25.5 ms (LV – mid vs. base) and 420.2 ± 24.0 vs. 334.7 ± 21.6 ms (RV – mid vs. base) ($P<0.05$). Furthermore, a significant difference between apex and base developed: 462.5 ± 19.2 vs. 404.2 ± 25.5 ms (LV – apex vs. base), 421.8 ± 30.3 vs. 334.7 ± 21.6 ms (RV – apex vs. base) ($P<0.05$).

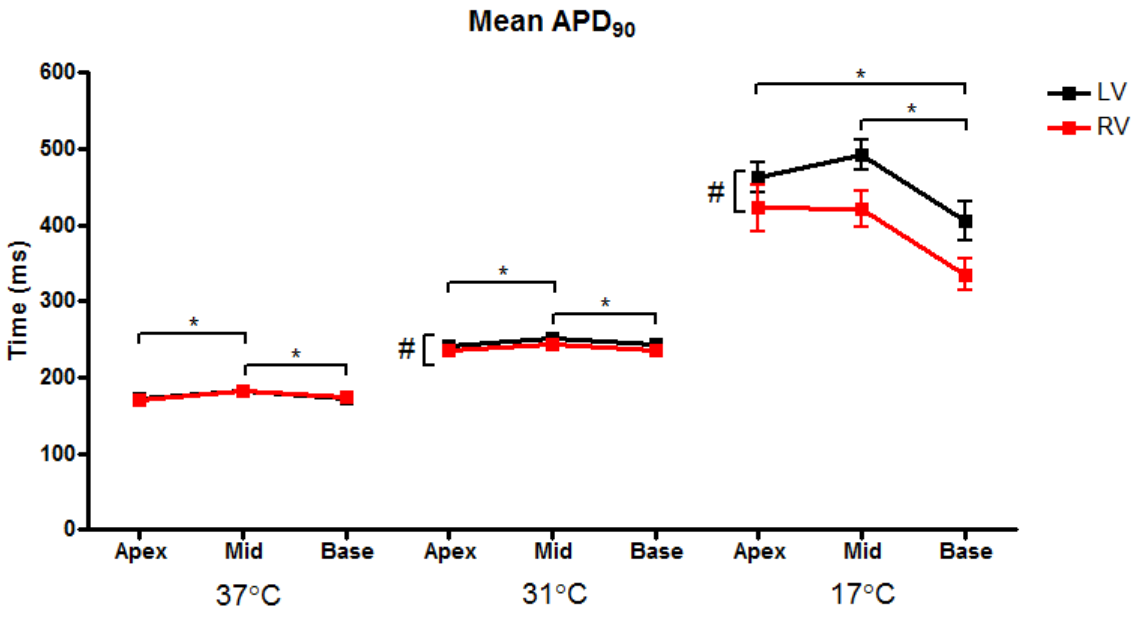


**Figure 4.7 Mean $APD_{90}$ across three regions of the heart**

**Considering changes in $APD_{90}$ across the apex, mid and base in the LV and RV with change in temperature. * The differences between apex, mid and base for LV and RV ($P<0.05$). # The differences between LV and RV ($P<0.05$).**

Dispersion of repolarisation can be more explicitly defined by the range of APD values ($APD_{50}$, $APD_{75}$ and $APD_{90}$) which existed over the surface of the heart, as

compared to baseline (Figure 4.8). Specifically, the range of $APD_{50}$ values during cooling were prolonged from 21.8 ± 2.9 to 36.2 ± 5.6 to 227.4 ± 25.8 (in ms), respectively. The range of $APD_{75}$ values during cooling was prolonged from 24.9 ± 3.3 to 30.3 ± 3.4 to 239.3 ± 30.3 (in ms) and $APD_{90}$ from 29.5 ± 3.8 to 36.1 ± 3.4 to 248.0 ± 34.5 (in ms). These changes in APD ranges were not significant between baseline and 31°C, but were significant when comparing differences between 37°C and 31°C against 17°C (P<0.001).

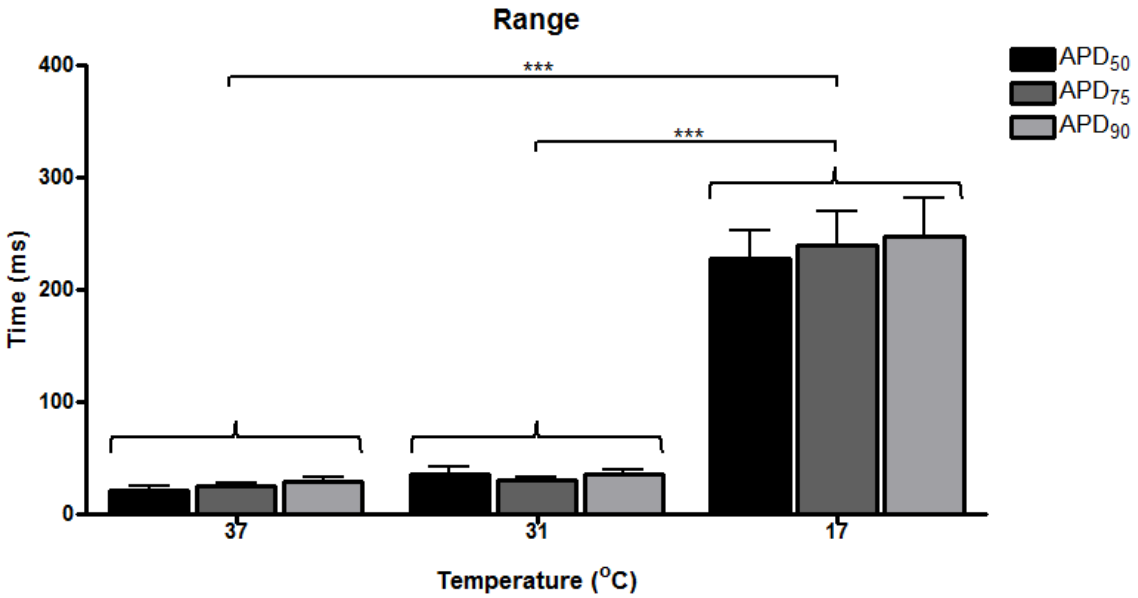


**Figure 4.8 Range of APD**

**Change in the range of $APD_{50}$, $APD_{75}$ and $APD_{90}$ values across the heart with change in temperature (***P<0.001).**

## Occurrence of arrhythmias

Some hearts developed VT/VF when cooled to 31°C and 17°C in contrast to 37°C where arrhythmias never occurred (Figure 4.9).

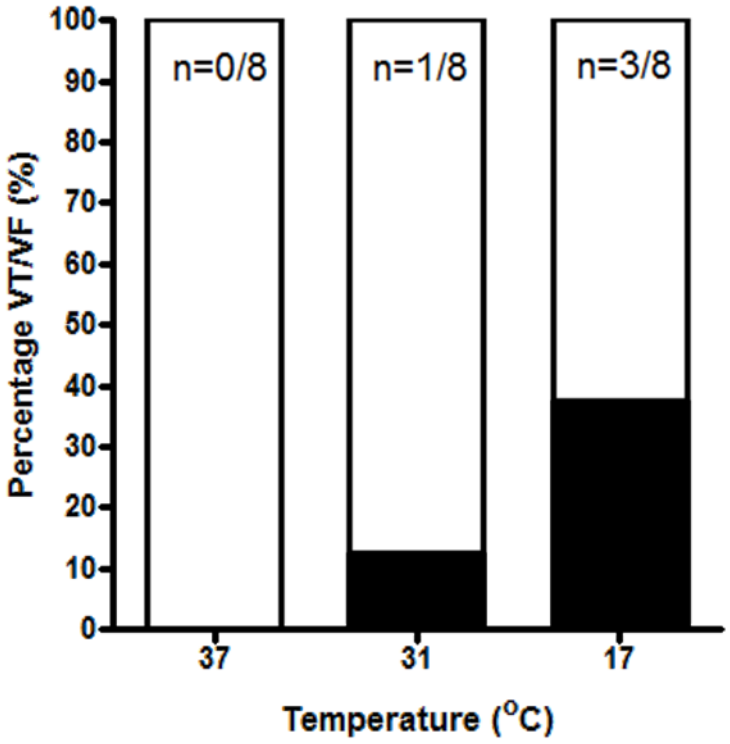


**Figure 4.9 Occurrence of VF/VT**

**Percentage occurrence of VF/VT as a proportion of total number of hearts (n=8), with change in temperature.**

## APD alternans

Significant APD alternans was defined as a mean beat-beat change ≥10ms (alternans threshold) (Figure 4.10). At 37°C and 31°C there was minimal beat-beat differences (1.2 ± 0.4ms and 1.9 ± 0.4ms, respectively). However, when cooled to 17°C there was a significant rise in the beat-beat difference (15.2 ± 5.4ms) ($P<0.05$). This was recapitulated when considering contour maps of beat-beat differences, as depicted in Figure 4.11. When comparing the beat-beat differences across the heart there was no clear pattern of alternans formation at any of the recorded temperatures. There was, however, the presence of spatially discordant alternans at 17°C.

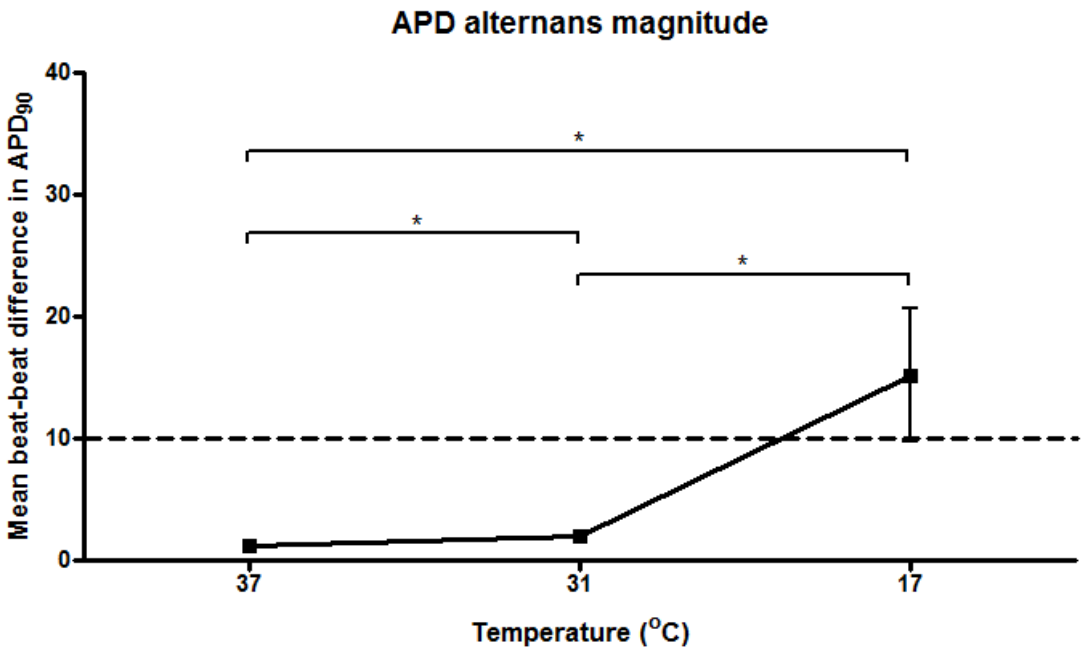


**Figure 4.10 APD alternans magnitude**

**Mean beat-beat difference in $APD_{90}$ (ms) with change in temperature. Dashed line indicates alternans threshold.**

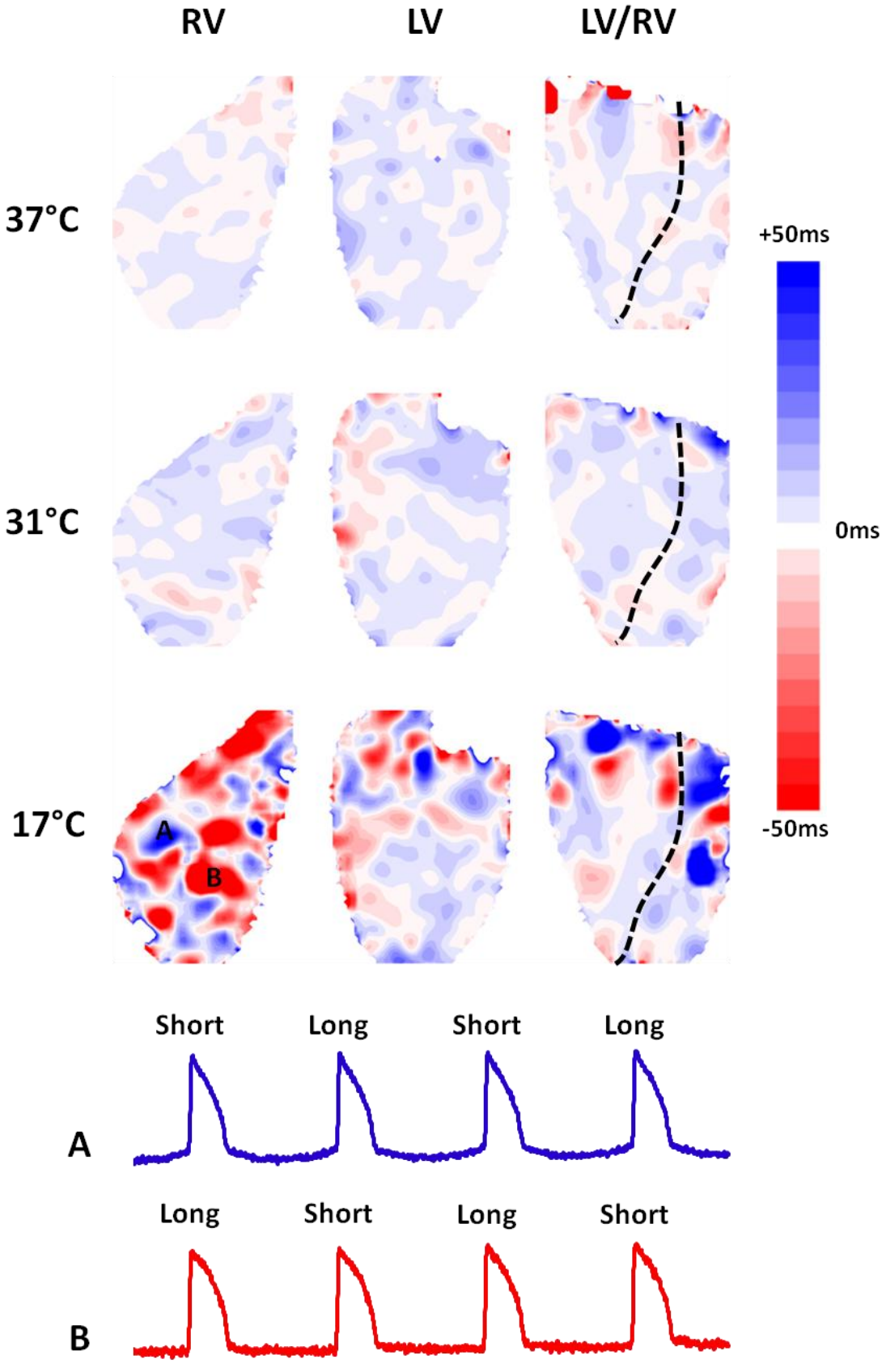


**Figure 4.11 Spatial pattern of alternans**

**A typical set of contour maps displaying the beat to beat difference at each imaged site from the three views (RV, LV and LV/RV) with change in temperature. The dashed line indicates the LV/RV border on the posterior surface of the heart. Optical AP traces recorded from marked regions on the RV at 17°C, with the duration of each individual AP indicated.**

## Delay in AV-node conduction

Compared to baseline, the minimum (earliest) $TAct_M$ occurred later during cooling of the heart, indicative of slowed AV-node conduction (122.2 ± 6.1 to 132.4 ± 7.5 to 295.9 ± 13.0ms) (Figure 4.12). These changes in minimum $TAct_M$ were not significant between baseline and 31°C, but were significant when comparing differences between both baseline and 31°C against 17°C ($P<0.001$). These changes were also reflected in the PR interval, which was prolonged from 73.3 ± 10.8 to 97.8 ± 13.7 to 224.1 ± 27.9 (in ms), shown as a percentage change from baseline in Figure 4.13. However, in this case the differences between baseline and 31°C were significant, in contrast to minimum $TAct_M$ and differences in PR interval between both baseline and 31°C against 17°C were significant ($P<0.001$).

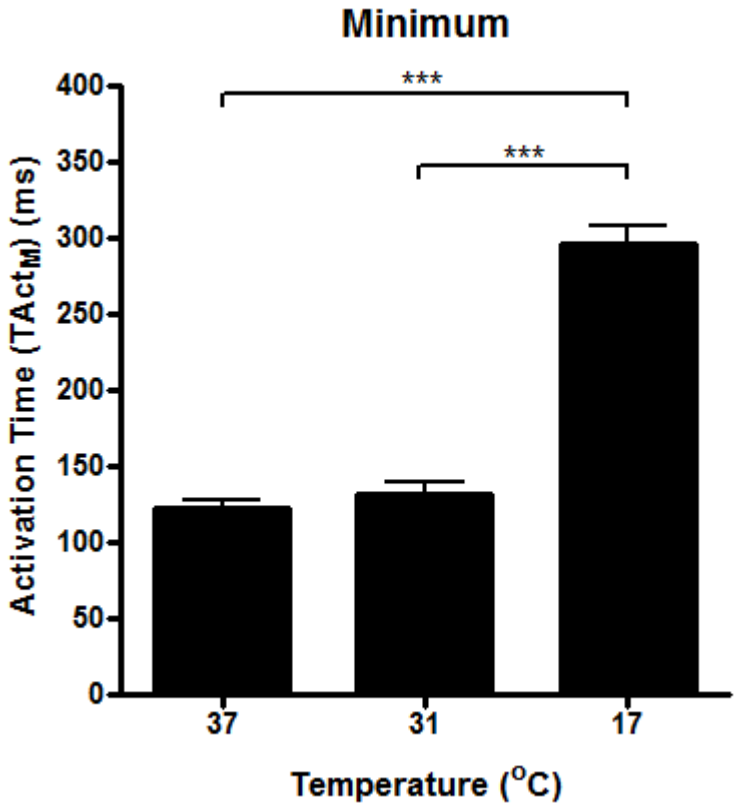


**Figure 4.12 Earliest activation time**

**Plot of change in the minimum (earliest) TActM with change in temperature (***P<0.001).**

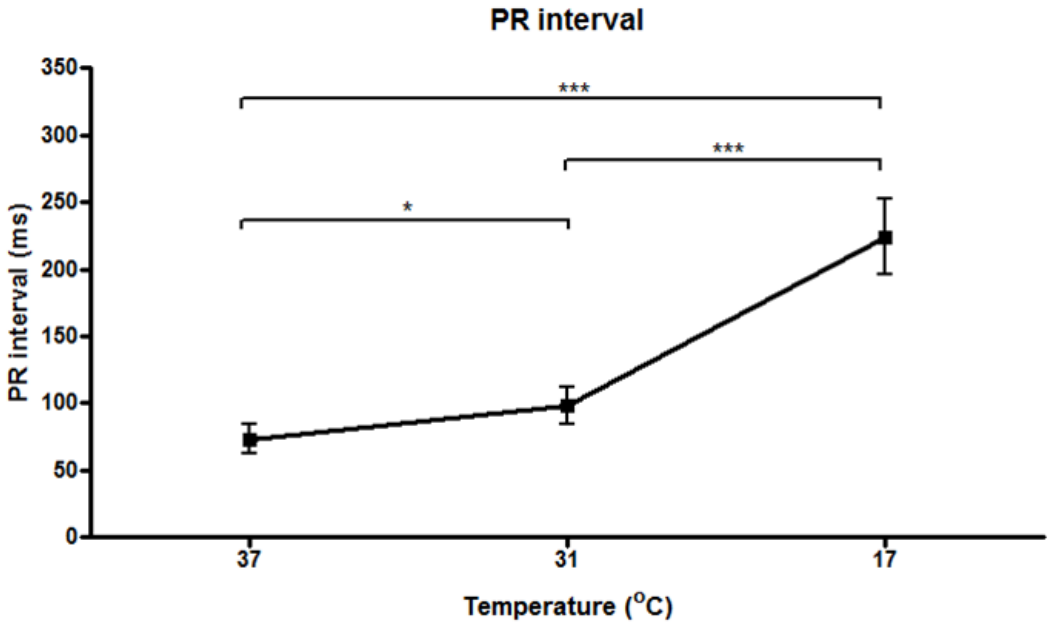


**Figure 4.13 PR interval**

**Change in PR interval from baseline with change in temperature (*P<0.05, ***P<0.001).**

## Slowed epicardial conduction

During cooling to 31°C, conduction velocity (CV) was significantly reduced by 33% from 52.8 ± 7.3 to 35.2 ± 5.2 cm/s (P<0.05). After further cooling to 17°C, a significant reduction of 63% in CV compared to baseline was present (52.8 ± 7.3 to 19.7 ± 3.7 cm/s, P<0.05).

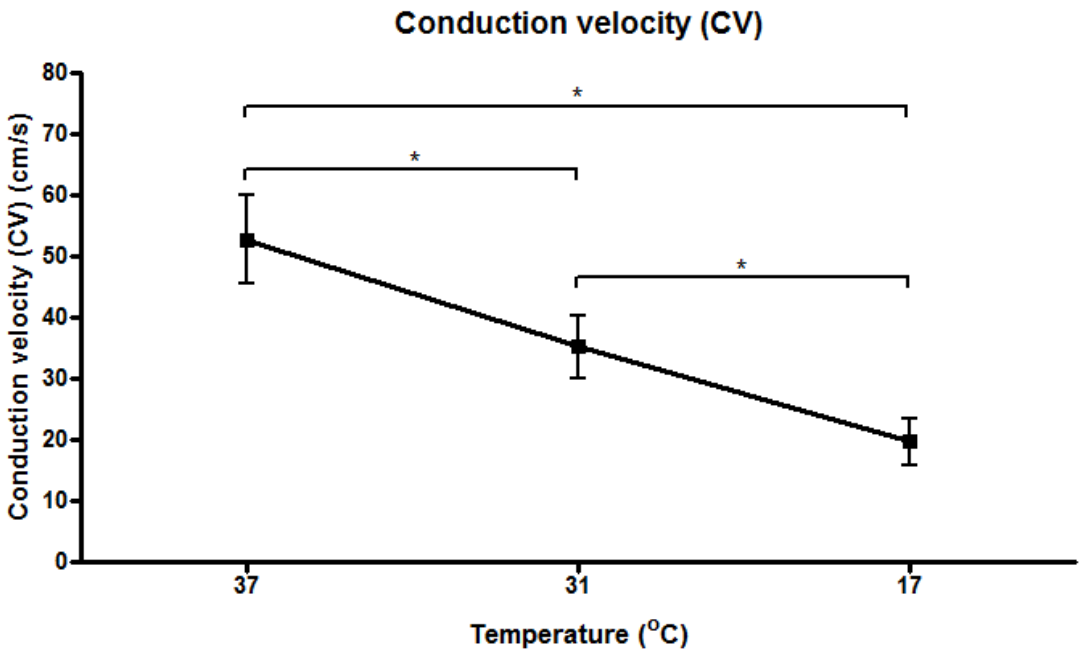


**Figure 4.14 Conduction velocity**

**Change in conduction velocity (CV) with change in temperature (*P<0.05).**

There was no significant change in the range of $TAct_M$ when cooling from 37°C to 31°C (14.6 ± 1.3 to 15.4 ± 1.3ms). However, when cooled to 17°C there was a significant increase in the range of $TAct_M$ (14.6 ± 1.3 to 15.4 ± 1.3ms to 60.5 ± 7.4ms, P<0.001) (Figure 4.15). The same outcome was reflected in the QRS interval, which was prolonged from 42.0 ± 7.2 to 48.6 ± 9.8 to 94.9 ± 16.6 (in ms) (P<0.001), shown as a percentage change from baseline in Figure 4.16.

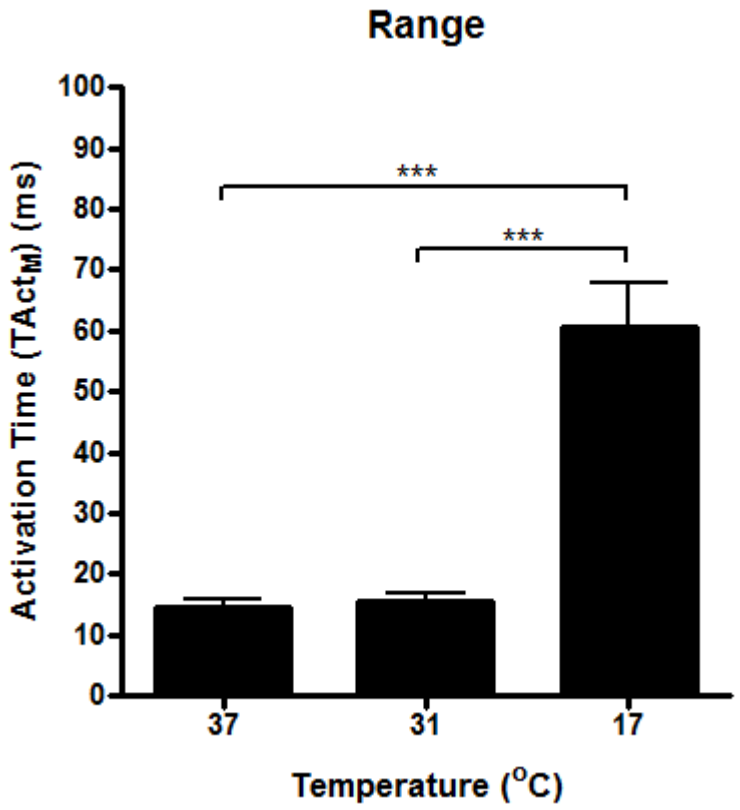


**Figure 4.15 Range of activation times**

**Change in the range of TAct$_M$ values across the heart with change in temperature (***P<0.001).**

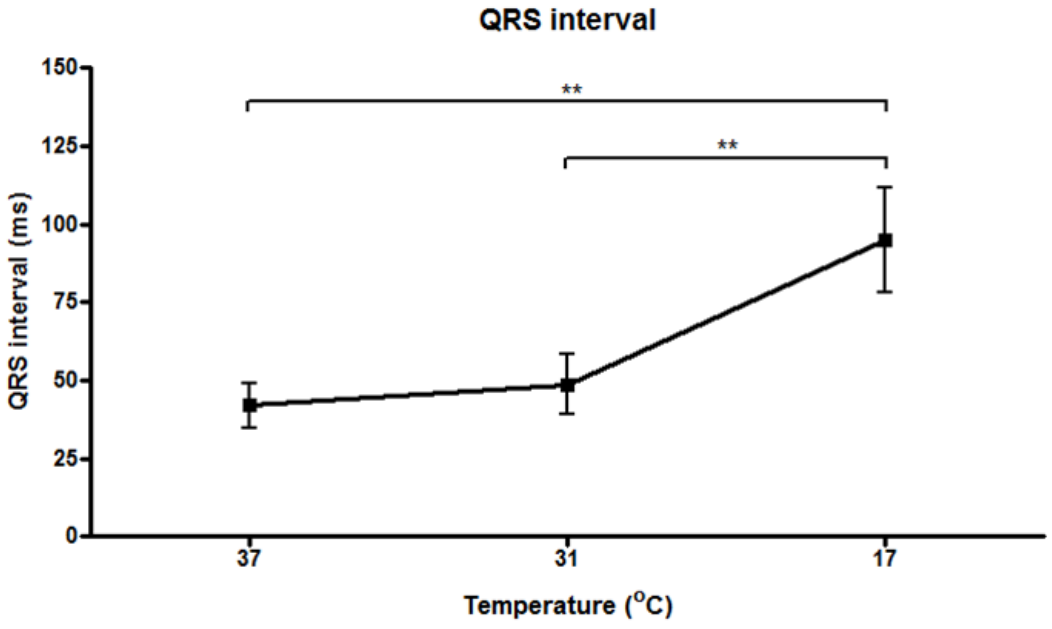


**Figure 4.16 QRS interval**

**Change in QRS interval from baseline with change in temperature (**P<0.01).**

## Pattern of activation

In Figure 4.17 is a set of representative contour maps of $TAct_M$ as the heart was cooled. Although there was a shift in both the minimum and range of $TAct_M$ as the heart was cooled the pattern of activation and direction of wavefront propagation remained relatively consistent and homogeneous at each temperature.

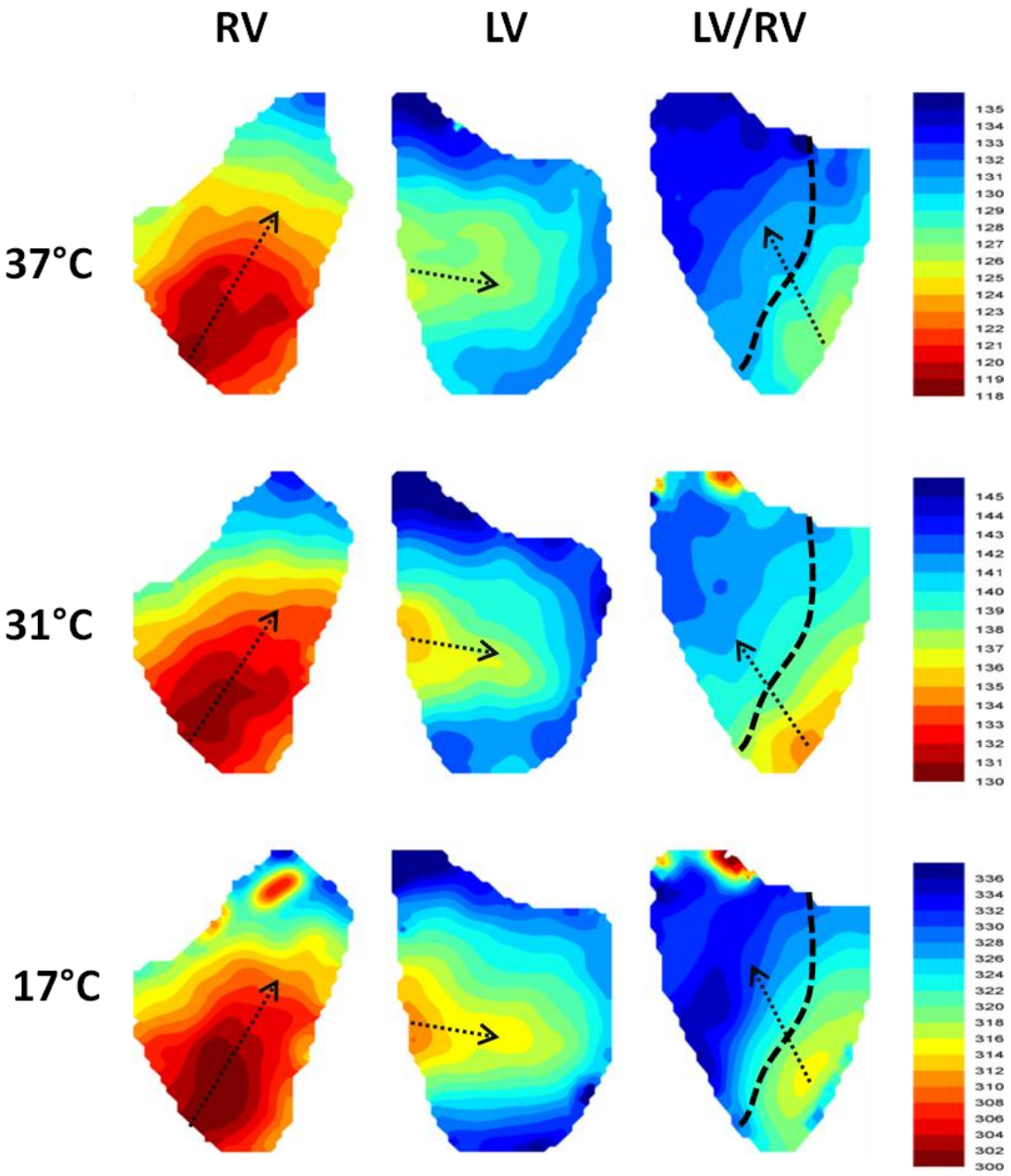


**Figure 4.17 Contour maps of activation time**

**Typical contour maps of $TAct_M$ with change in temperature from three views of the heart (RV, LV and LV/RV). The dashed line indicates the LV/RV border on the posterior surface of the heart.**

At 37°C and 31°C, $TAct_M$ was not significantly different across the apex, mid and base areas; nor were there significant differences between the LV and RV (Figure 4.18). Only at 17°C were there significant differences between the mid and base: 324.3 ± 5.4 vs. 350.1 ± 9.0 ms (P<0.05) (LV – mid vs. base), in addition to differences between the LV and RV (P<0.05).

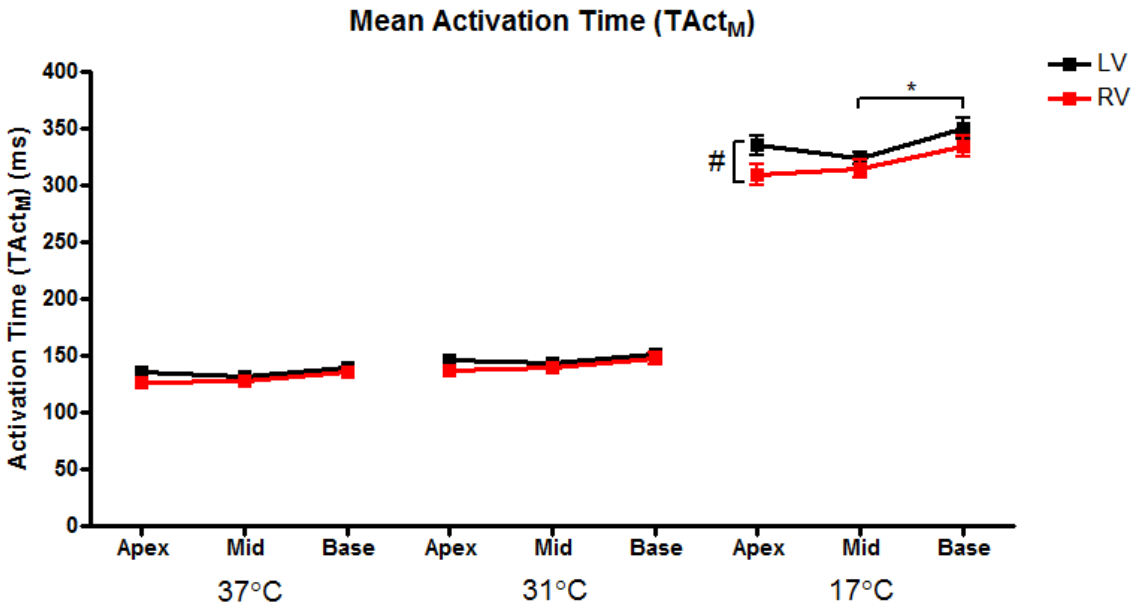


**Figure 4.18 Mean $TAct_M$ across the three regions of the heart**

**Considering changes in $TAct_M$ across the apex, mid and base in the LV and RV with change in temperature. * The differences between apex, mid and base for LV and RV (P<0.05). # The differences between LV and RV (P<0.05).**

# Discussion

Hypothermia is a well-known physiological paradigm, and its effects on the cardiovascular system have been well documented in several studies. Here the effects of hypothermia on the electrophysiology of the isolated rabbit heart were investigated using the panoramic optical mapping system, using temperatures that represent both therapeutic (31°C) and accidental (17°C) hypothermia in humans.

## Therapeutic hypothermia (31°C)

The major findings of the study based on both the optical and ECG measurements, when comparing baseline against therapeutic hypothermia (31°C) were as follows:

1) A significant prolongation in repolarisation, shown as an increase in APD (Figure 4.4) and QT interval (Figure 4.5), which can be attributed to the temperature dependant slowing of the kinetics of a number of ionic currents ($I_{to}$, $I_{Kr}$, $I_{Ca,L}$ and $I_{NCX}$) that govern repolarisation (Bjørnstad et al., 1995; Sprung et al., 1994, 1995; Bjørnstad et al., 1994; Marshall et al., 2002; Suleiman and Chapman, 1990; Liu et al., 1991; Gambassi et al., 1994; Mortensen et al., 1993).

2) There was no significant increase in the overall dispersion of APD times over the entire surface of the heart (Figure 4.6, Figure 4.7 and Figure 4.8), however, there was significant differences that developed when comparing times between LV and RV. CV is determined by multiple factors, including tissue excitability and intercellular resistance, the former linked to inward Na current amplitude, the latter determined by connexin mediated gap junctions. For equivalent distances, gap junction resistance has a greater contribution to transverse conduction velocity whilst Na channels/intracellular resistance has a greater involvement in longitudinal conduction. During hypothermia, it has been suggested that downregulation, lateralisation and de-phosphorylation of connexin 43 (Cx43) produces cellular uncoupling resulting in cells being able to express their intrinsic repolarisation characteristics, thus enhancing the dispersion of APD (Fedorov et al., 2008, 2005; Hsieh et al., 2009). However, this

effect is not sufficiently developed at 31°C to give rise to a significant difference in the dispersion of APD when compared to 37°C.

3) There was no significant presence of APD alternans and no clear pattern to the distribution of beat-beat differences on the surface of the heart, in correspondence with the similar occurrence of VT/VF arrhythmias at 31°C compared to 37°C (Figure 4.10, Figure 4.11).

4) Although there was no significant change in the earliest breakthrough time (minimum $TAct_M$) at 31°C, there was a significant increase in the PR interval (Figure 4.12, Figure 4.13). The conflicting finding over AV-node conduction may be as a result of low sample size and higher numbers may be required to ascertain whether this result is a true reflection of the underlying biology. This is under further investigation within current studies in the lab group.

5) A significant slowing in epicardial conduction velocity was observed during RV pacing, but slowed conduction was not present during RA pacing with respect to the QRS interval and the range of $TAct_M$, suggesting that this effect is reduced during RA pacing (Figure 4.15, Figure 4.16 and Figure 4.18). This finding is associated with the absence of any significant enhancement in APD dispersion at 31°C.

6) The changes to conduction were homogenous over the surface of the heart, resulting in a very similar pattern of activation across both ventricles at 31°C when compared to 37°C (Figure 4.17).

## Severe hypothermia (17°C)

Comparing baseline with severe hypothermia (17°C) there were a number of contrasting findings:

1) There was a significant increase in the dispersion of APD. The distribution of APD times over the surface of the heart became more heterogeneous, with pronounced differences between both the apex and base and mid and base of the heart, as well as marked differences between the LV and RV. Intrinsic differences in the repolarisation characteristics of isolated myocytes from the

apex to base and from the left to right ventricles are widely recognised. These characteristics are normally masked by the intercellular coupling of individual myocytes within the cardiac syncytium, which acts to attenuate voltage differences between cells. As discussed, a recent paper has shown that hypothermia causes an abrupt decrease in Cx43 expression potentially leading to reduced electrotonic coupling and conduction velocity (Hsieh et al., 2011). Therefore, during severe hypothermic conditions (17°C) increased intercellular resistance might lead to a significant increase in APD dispersion.

2) Spatially discordant APD alternans was present over the surface of the heart, which corresponded with the significant susceptibility and overall increase in the occurrence of VT/VF arrhythmias at 17°C (Figure 4.9).

3) There was a significant increase in the earliest breakthrough time (minimum $TAct_M$) matched with a significant increase in the PR interval, suggesting slowed AV-node conduction.

4) The significant slowing in epicardial conduction velocity observed during RV pacing was matched during RA pacing.

## General observations

At both hypothermic temperatures, there was an increase in APD and slowing in CV; only at 17°C, however, was there an observed significant increase in the dispersion of APD. This discrepancy may be attributed to the magnitude of the effect of intercellular uncoupling, potentially due to a hypothermic-induced Cx43 down regulation at 17°C compared to 31°C. These findings are consistent with the increased occurrence of VT/VF in these heart preparations at 17°C, where discordant alternans were observed. It is known that ventricular arrhythmias arise form disruptions in the normal sequence of activation and recovery of the heart. Enhanced dispersion in APD in conjunction with slowed conduction velocity is known to enhance the substrate for the development of re-entrant arrhythmias. This discrepancy in APD dispersion between 31°C and 17°C may also pose an explanation for the low incidence of arrhythmias in the clinical setting during therapeutic hypothermia.

This study indicates that cooling of the heart preparation results in a number of profound physiological changes in electrophysiology, where these changes are significantly more pronounced during severe hypothermia, leading to the likely increased susceptibility to arrhythmias at this temperature.

## Limitations

These experiments were carried out on isolated rabbit hearts which were therefore not under the normal autonomic modulation present *in vivo*. In addition, the time-dependent electrophysiological stability of the heart preparation limited recordings to only three temperatures at three discrete time points, such that the time course of changes between temperatures could not be mapped. *In vivo* cardiac output will typically decrease during cooling to severe hypothermia, in contrast to the constant retrograde perfusion used in this study. Recordings were made only from the epicardial surface, therefore electrophysiological events and gradients in the endocardial or transmural planes of the myocardium could not be assessed. Furthermore, APs from across the surface of the heart were not recorded simultaneously; instead, a series of three views of the heart were accumulated using a single camera, which required approximately 2 minutes to record.

## Conclusions

The panoramic optical mapping system was used to study the effects of hypothermia on cardiac electrophysiology. Distinct differences were observed between moderate and severe hypothermia, which suggests non-uniform effects of cooling on the electrophysiology of the heart.

# Chapter 5: Epicardial electrophysiology under different pacing conditions in normal hearts and hearts after chronic myocardial infarction

## Aims

The aim of these experiments was to investigate the effects of different modes of pacing on the activation and repolarisation sequence, and distribution of APD across the epicardial surface of the LV and RV. Specifically, single ventricular pacing and simultaneous and sequential bi-ventricular (BiV) pacing against RA pacing in both the normal (control) rabbit heart and a rabbit heart 8 weeks after permanent ligation of a coronary artery were compared.

## Introduction

This chapter develops further the work from Chapter 3 in an effort to understand the effects of alternative forms of pacing on the activation and repolarisation characteristics of the isolated rabbit heart. Initial studies in this thesis indicated an inverse relationship between APD and activation time suggesting a dominant role for electrotonic influences over cellular electrophysiology. This chapter investigates the activation and repolarisation patterns created during acute bi-ventricular pacing and the possible distinction between different interventricular offsets. Lastly, the effects of alternative forms of pacing in a rabbit model of chronic MI were also examined.

### Electrophysiological remodelling in heart failure

In the experimental setting, ventricular arrhythmias are more readily generated in hearts that have undergone remodelling following an MI. Re-entrant excitation has been demonstrated in Langendorff perfused human hearts explanted at the time of transplantation for end-stage heart failure. Within these studies, the structural arrangement of the scar, and particularly the surviving myocardial strands within the scar and in the border zone, appeared important for the initiation and maintenance of re-entry (de Baker et al., 1990).

The changes in electrophysiology which manifest in the remote, non-infarcted myocardium are also important (Misier et al., 1995). In heart failure, prolongation in APD is the most consistent change found in animals (Vermeulen et al., 1994) and humans (Vermeulen et al., 1994; Beuckelmann et al., 1993). The increased heterogeneity of APD in the remodelled hypertrophied LV can

result in dispersion of refractoriness, a critical substrate for the development of re-entrant tachyarrhythmias. In addition, hypertrophy-induced increase in interstitial tissue can impair cellular coupling further contributing to the occurrence of re-entry. The primary step in the development of early afterdepolarisations (EADs) is considered to be APD prolongation. In the hypertrophied rabbit wedge preparation EADs are more easily induced (Yan et al., 2001). Triggered activity from delayed afterdepolarisations (DADs) have been shown to be more easily induced in hypertrophied cardiomyocytes in the presence of B-adrenergic agonists (Barbieri et al., 1994) or under the influence of increased extracellular $Ca^{2+}$ (Aronson, 1981).

## Electrophysiological changes in rabbit chronic MI model

Our group has developed and extensively characterised a model of chronic MI produced by coronary arterial ligation in the rabbit (McIntosh et al., 2000; Pye et al., 1996; Ng et al., 1998; Pye and Cobbe, 1996). Following ligation, rabbits develop a chronic MI and have decreased survival compared to sham-operated controls. Ligated hearts have a lower VF threshold, suggesting that re-entry occurs more readily (Burton et al., 2000). Furthermore, this model readily displays to major areas of electrophysiological heterogeneity as a consequence of an MI. In the non-infarcted hypertrophied myocardium, APD is prolonged, as has been demonstrated in humans following an MI (Beuckelmann et al., 1993). In addition, prolongation in APD has been shown to be non-uniform across the transmural wall (McIntosh et al., 2000) and transmural dispersion of repolarisation is increased as measured in isolated cells. Secondly, there is a defined infarct border zone where surviving myocytes interdigitate with scar tissue at the epicardium and form a thin layer in the subendocardium. Local dispersion of refractoriness, estimated by the VF interval technique, is increased in this border zone (Burton et al., 2000).

## Cardiac resynchronisation therapy

Chronic heart failure is one of the most common causes of morbidity and mortality within Western society (Cowie et al., 1997). A significant proportion of patients suffering from chronic heart failure typically suffer from cardiac dyssynchrony, where delays in interventricular and intraventricular electrical

activation results in impaired mechanical performance. This is typically observed as a reduction in ejection fraction of ≤35% and conduction delays characterised by a QRS duration ≥120ms (Clark et al., 2008; Khan et al., 2007). Despite significant advances in pharmacological therapies: beta-blockers (Bristow, 2000), angiotensin-converting-enzyme (ACE) inhibitors or angiotensin II-receptor blockers (ARB) (Pitt et al., 2000; Flather et al., 2000; Swedberg and Kjekshus, 1988) and spironolactone (Pitt et al., 1999), there is still a poor prognosis for chronic heart failure patients.

Cardiac resynchronisation therapy (CRT) has emerged as an important therapeutic option for patients with heart failure due to systolic dysfunction and cardiac dyssynchrony. During a typical CRT procedure, both the right and left ventricle are paced simultaneously to synchronise ventricular contraction; this is commonly known as bi-ventricular pacing (BiV). However, CRT can be performed by pacing solely the left ventricle or pacing the right and left ventricle sequentially, with a predetermined offset.

Recent results of several observational and controlled multi-centre trials of bi-ventricular pacing show significant improvement in survival rates and the quality of life of patients, in addition to a marked increase in ventricular function, improvement in New York Heart Association (NYHA) functional class, reduced mitral regurgitation and increase in exercise duration (Young et al., 2003; Witte et al., 2008; Cleland et al., 2006; Linde et al., 2002, 2008; Abraham, 2002; Bristow et al., 2004; Cleland et al., 2005; Cazeau et al., 2001). More recently, CRT has been shown to have a reverse effect on LV remodelling and an overall reduction in ventricular size (Linde et al., 2010; Sutton et al., 2003; Rao et al., 2007). Despite a cut-off QRS duration of ≥120ms being adopted for characterising cardiac dyssynchrony, CRT has even been shown in some studies to be beneficial in patients with a normal QRS duration (<120ms) (Foley et al., 2011; Van Bommel et al., 2010). However, patients with normal QRS duration are currently not amongst the approved candidates for CRT.

To date, the optimal pacing regime and site of pacing have not been established, which may go some way to explaining some of the limitations of CRT, where certain groups of patients are non-responsive or where the beneficial effects of CRT diminish over time or in more rare cases patients

experience malignant arrhythmias (Cubbon and Witte, 2009; Abraham and Hayes, 2003; Min et al., 2014). With the growing use of CRT in the clinical setting, it is important to gain better understanding of how CRT works and how different pacing protocols affect the ventricular activation and repolarisation sequence.

# Methods

## Preparation of the rabbit hearts

In these experiments, a total of 8 New Zealand White rabbits (2.5kg-3.5kg) were used for optical mapping (n=4 control group and n=4 MI group). The rabbits were sacrificed and hearts Langendorff perfused as described in Chapter 2. To suppress motion artefacts the E-C uncoupler blebbistatin (10μM) was added to the perfusate and the preparation stained with voltage-sensitive dye, Di-4-ANEPPS (100μl of 1mg/ml).

## The rabbit chronic MI model

This study included the use of a well-established model of chronic MI produced by coronary arterial ligation in the rabbit (McIntosh et al., 2000; Pye et al., 1996; Ng et al., 1998; Pye and Cobbe, 1996). Following ligation, rabbits develop a chronic MI and have decreased survival compared to sham-operated controls.

The surgical procedures and *in vivo* echocardiography were all carried out by Mr Michael Dunne and Mrs Aileen Rankin in accordance with the UK Animals (Scientific Procedures) Act 1986 under Project License (PPL60/4206) and conform to the Guide for the Care and Use of Laboratory Animals published by the US National Institute of Health (NIH Publication No. 85-23, revised 1996).

Adult male New Zealand White rabbits were given premedication with 0.3 ml/kg intramuscular Hypnorm [fentanyl citrate (0.315mg/ml): fluanisone (10mg/ml), Janssen Pharmaceuticals]. Anaesthesia was induced with 0.25-0.5mg/kg midazolam (Hypnovel, Roche) given via a cannula in the marginal ear vein. The rabbit was intubated and ventilated using a Harvard small animal ventilator with a 1:1 mixture of nitrous oxide and oxygen with isoflurane at 2% and tidal volume of 50ml and frequency of 36 per minute. Rimadyl (long acting analgesia) was administered at 0.08mg/kg.

Local anaesthetic, Bupivacaine, was injected at the top of the 2nd, 3rd, 4th, 5th, 6th and 7th ribs. A left thoracotomy was performed through the 4th intercostal space. The left marginal artery (as defined in Fig. 1 of Lee et al.) was

ligated midway between the left AV groove and the cardiac apex, to produce an area of tissue blanching of 40-50% of the left ventricular surface, estimated upon ligation (Lee et al., 2004). In some hearts, in which this ligation produced a blanching area of <40-50%, an additional artery (or arteries) was ligated, e.g., posterior branch of the posterior division; circumflex branch of the posterolateral division; anterior interventricular branch of the anterior division. As there is relatively little collateral circulation in the rabbit, a homogenous apical infarct was produced occupying on average 14% of the total endocardial and epicardial surfaces towards the apex of the LV (Burton et al., 2000). Sham-operated animals underwent thoracotomy with the heart manipulated in a similar fashion to the MI group, but the artery was not tied.

If VF occurred during the procedure, defibrillation was undertaken with 5-10J epicardial DC shocks. Once the animal was stable, the thoracotomy was closed. The animal was then given 20ml of isotonic saline intravenously to replace perioperative fluid losses and allowed to recover in a warm clean environment with adequate monitoring for any early signs of distress. Analgesia was given with 0.04mg/kg intramuscular Vetergesic (buprenorphine hydrochloride 0.3 mg/ml, Reckitt & Colman Products Ltd) immediately after surgery and the next morning.

## Characterisation of the chronic MI model

The effects of the coronary artery ligation develop over a period of 8 weeks to allow for remodelling of the LV and for the heart to reach a chronic phase of MI. At which time, echocardiography was performed 1 week prior to sacrifice in order to assess *in vivo* cardiac function, using a 10MHz paediatric probe with a Siemans Acuson Ultrasound system.

For this procedure the rabbit was sedated with 0.3 mg/kg Hypnorm and a small region of anterior chest wall shaved to create a sufficient echo window. Echocardiographic examination reveals that the animal model has LV hypertrophy, decreased LV ejection fraction and significantly increased LA diameter and LV end diastolic diameter. Ejection fraction (EF) was measured from the short-axis view, taking the outline of the LV at end-diastole and end-systole to get the corresponding volumes, where EF was calculated as follows:

$$EF = \frac{end\ diastolic\ volume - end\ systolic\ volume}{end\ diastolic\ volume} \times 100$$

## Pacing protocol

Hearts were paced via the RA, RV apex and LV base at a cycle length of 300ms. In addition, hearts were paced in various modes of bi-ventricular pacing, with LV offsets at -5, 0, 5 and 10 ms with respect to the RV pacing stimulus, as illustrated in Figure 5.1 alongside a corresponding average AP.

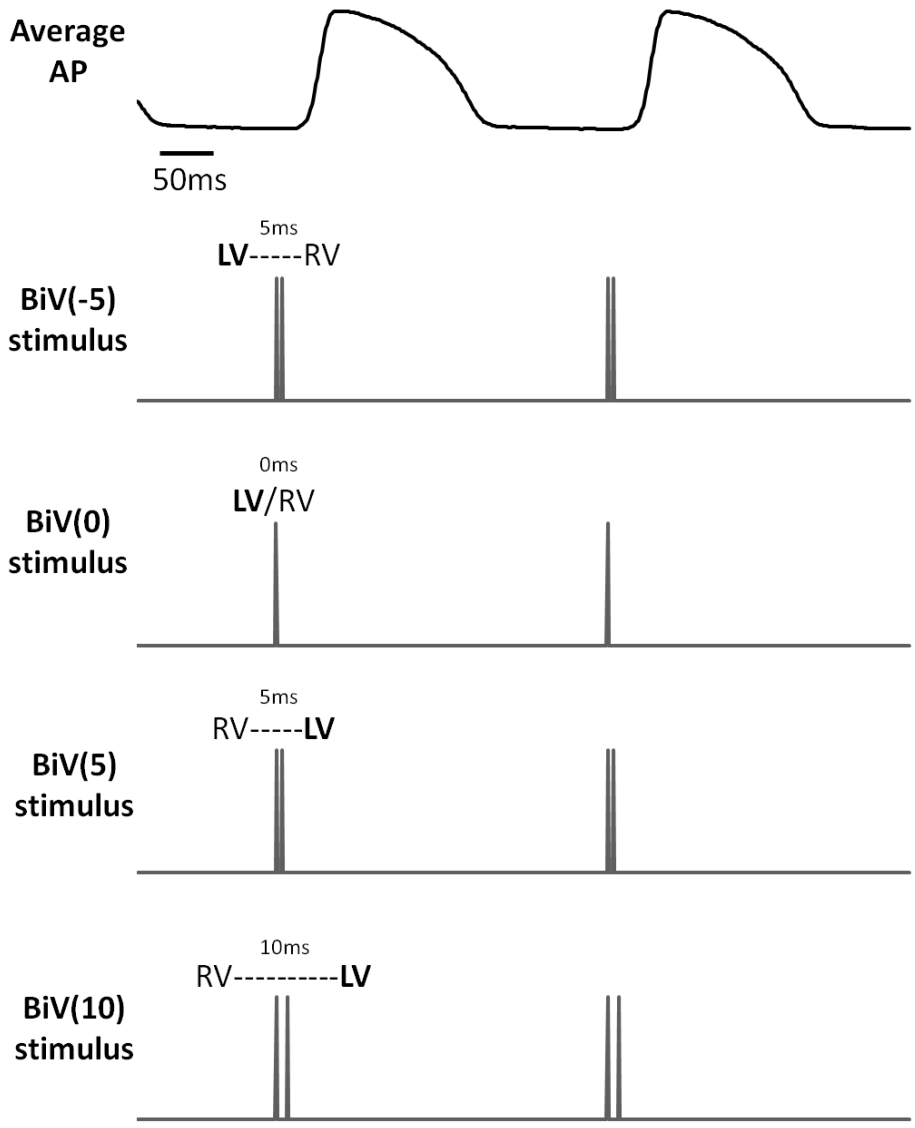


**Figure 5.1 BiV pacing**

**An average action potential signal shown alongside the different modes of BiV pacing, in reference to sequential BiV pacing with offsets (-5, 5 and 10, in ms) and the simultaneous BiV pacing with offset (0ms), where offsets are with respect to the RV stimulus.**

Figure 5.2 demonstrates the full pacing protocol used during experiments, with the sites of pacing depicted in Figure 5.3. As part of the pacing protocol, hearts were allowed to stabilise at each pacing regime for a minimum of 10s prior to recording. Simultaneous ECG recordings were made during experiments and viewed in real time during the course of the experiment, typical example of the ECG traces during the entire pacing protocol are shown in Figure 5.4.

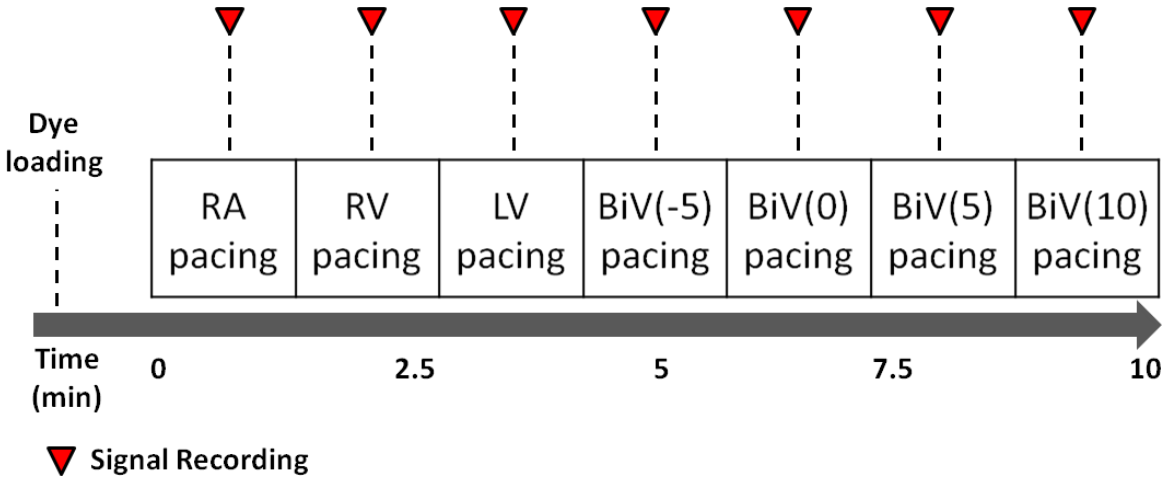


**Figure 5.2 Experimental pacing protocol**

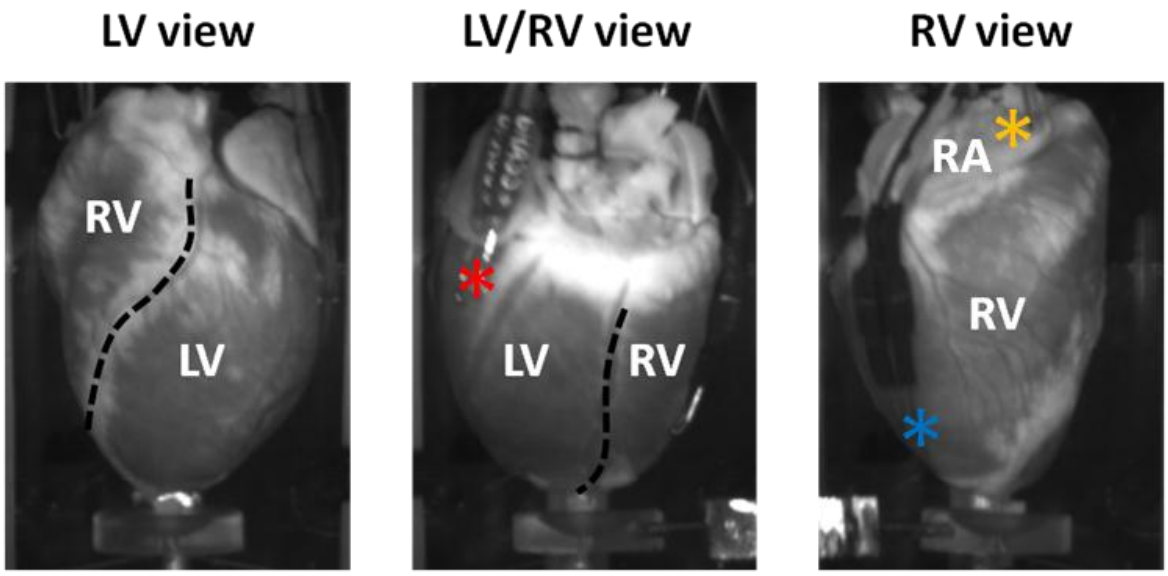


**Figure 5.3 Sites of pacing during experiments**
**(*-red LV base pacing, *-blue RV apex pacing and *-yellow RA pacing site)**

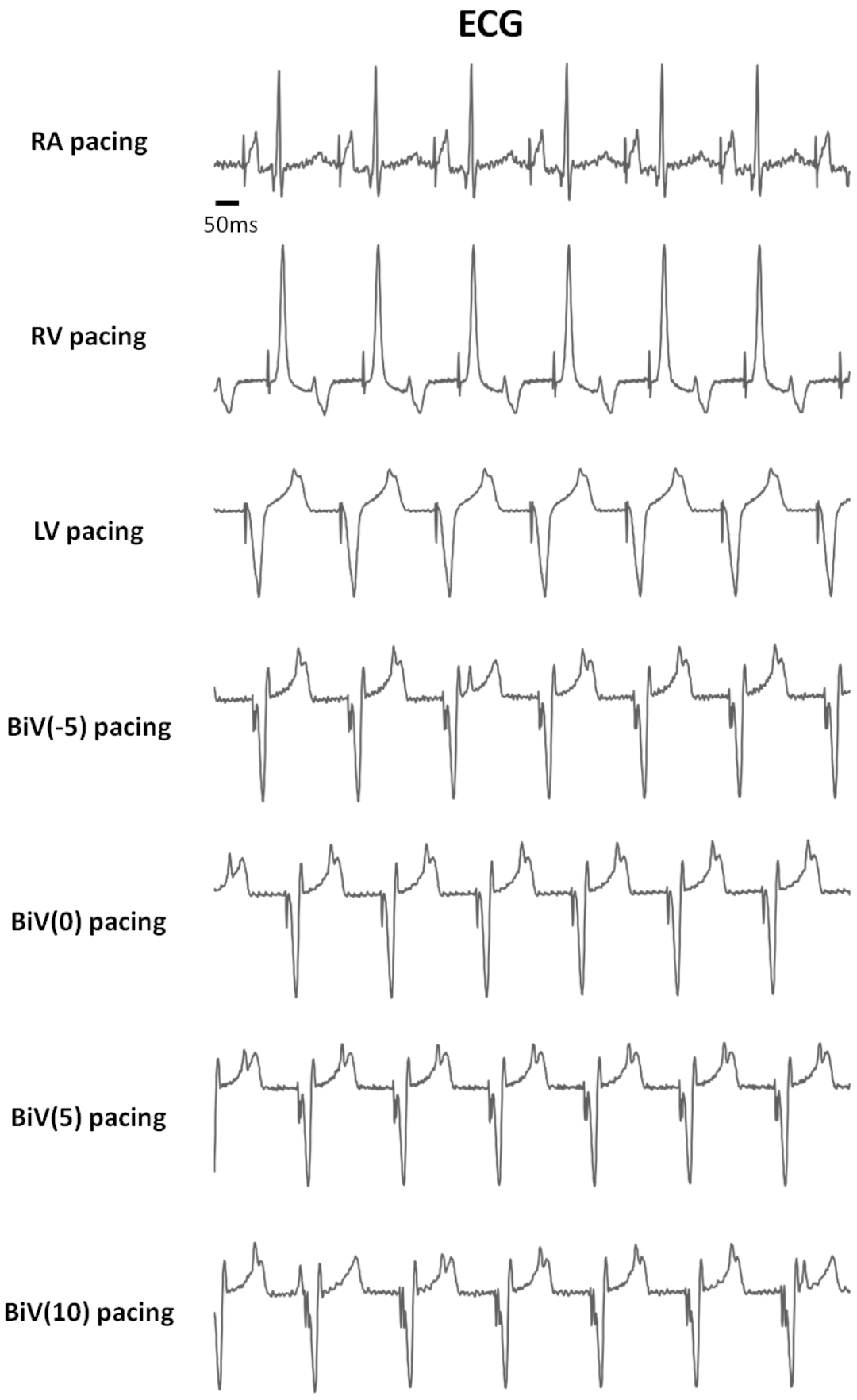


**Figure 5.4 Representative ECG traces**

**Example of ECG traces for each mode of pacing during the experiments**

## Data analysis

Analyses of optical data and ECGs were performed as described in Chapter 3. In this study, the electrophysiological parameters analysed were $TAct_M$ (activation time), $APD_{90}$ (action potential duration at 90% repolarisation), $TRepol_{90}$ (time at 90% repolarisation) and PR interval. During the selection of pixels from the MI optical data, it was necessary to exclude pixels that formed part of the infarct, due to the poor SNR in the infarct region. Therefore, the MI data shown is representative of the surviving myocardium.

# Results

## Part 1: Control group

### Atrio-ventricular conduction heterogeneity

During RA pacing there was a range of activation times across both the LV and RV that varied from heart to heart. The time of earliest activation varied significantly from heart to heart, ranging from 88 ms in LV of heart-1 to 103 ms in the LV of heart-4, analogous to the RV (Figure 5.5). This variation in epicardial breakthrough time could be due to differences in A-V nodal conduction, as discussed in depth in Chapter-3. These findings were corroborated by the corresponding heterogeneity present in the PR interval, as shown in Figure 5.6. The overall spread of activation times remained very similar from heart to heart with a coordinated activation present between LV and RV.

Despite the difference in time of earliest activation, in general, the range of activation times across the RV were greater than over the LV (Table 5.1), though this finding was not statistically significant.

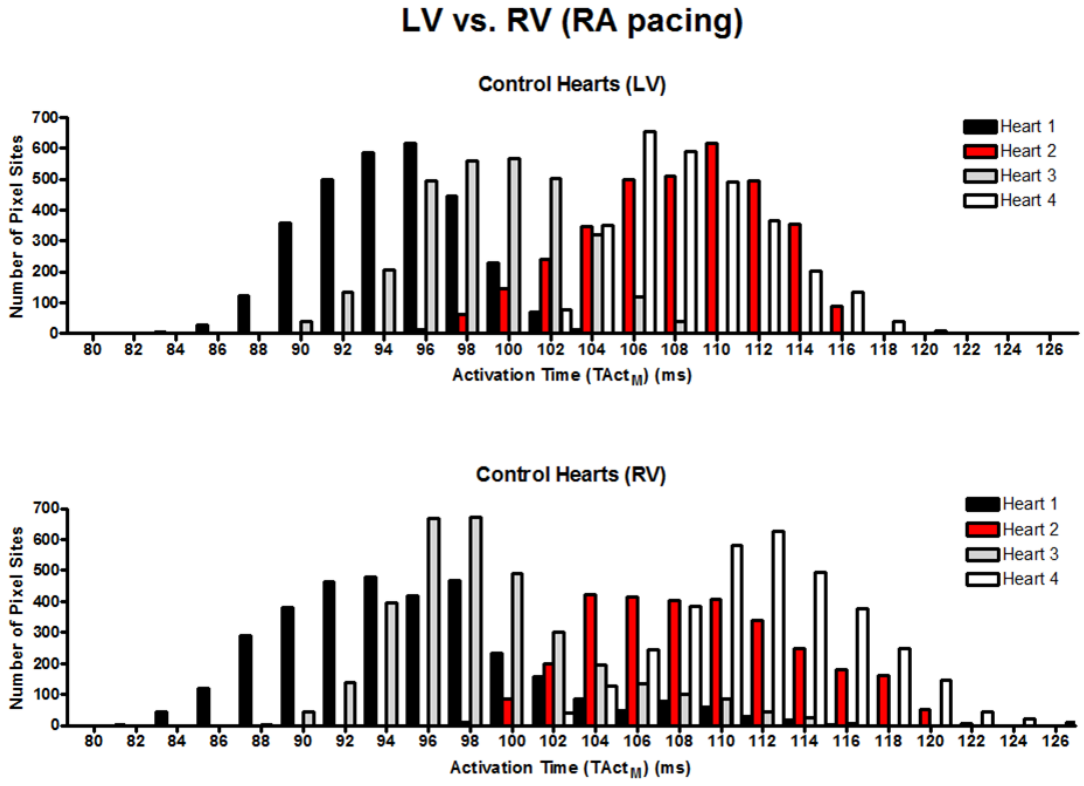


**Figure 5.5 Distribution of activation times (LV and RV) for each heart**

**Table 5.1 Statistics for the activation times of LV and RV of each heart during RA pacing**

| TActM | Heart 1 | Heart 2 | Heart 3 | Heart 4 |
|---|---|---|---|---|
| **LV** | | | | |
| Median | 94.0 | 108.0 | 99.0 | 108.0 |
| 5th Percentile | 88.0 | 100.0 | 92.0 | 103.0 |
| 95th Percentile | 100.0 | 114.0 | 105.0 | 115.0 |
| Range | 12.0 | 14.0 | 13.0 | 12.0 |
| **RV** | | | | |
| Median | 94.0 | 108.0 | 98.0 | 111.0 |
| 5th Percentile | 87.0 | 101.0 | 92.0 | 104.0 |
| 95th Percentile | 107.0 | 117.0 | 108.0 | 119.0 |
| Range | 20.0 | 16.0 | 16.0 | 15.0 |

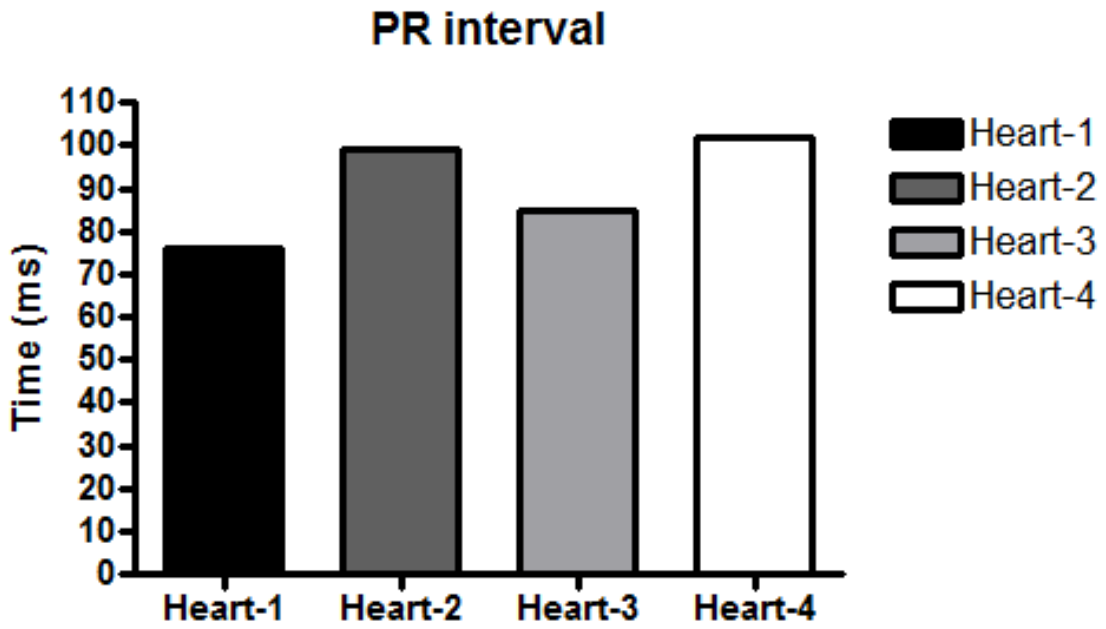


**Figure 5.6 PR interval for each heart**

RV and LV pacing show distributions of activation times that are overlapping but shifted relative to each other to give a larger overall range of activation times in comparison to RA pacing (Figure 5.7 & 5.9).In contrast, all forms of BiV pacing showed a coordinated interventricular activation distribution independent of offset, and which were more similar to those recorded during RA pacing. No significant differences were apparent in activation time distributions between different BiV pacing offsets. During both RV and LV pacing the overall spread of activation timings was greater in comparison to during RA pacing or any of the BiV pacing sequences. BiV pacing regimes showed a more similar range of activation times to during RA pacing.

During RA pacing, electrical activation propagated from the mid-ventricular and apex region and spread towards the base across the LV, whereas there was a clear apex to base spread of activation across the RV (Figure 5.8). Although both ventricles showed coordinated timing of activation, there was a larger proportion of earlier activation sites present on the RV. These findings were analogous to previous data presented in Chapter-3.

When pacing the heart via a single ventricle, a significant difference in earliest ($5^{th}$ percentile), median and latest ($95^{th}$ percentile) activation times was present in the un-paced ventricle, shown by the hash symbol (#) in Figure 5.9. This finding was in agreement with the split distributions and contours maps of activation times during LV and RV pacing. However, this difference did not manifest in the overall range of activation times, where there was no significant differences. On average, the range of activation times across the LV and RV were significantly increased when using any of the ventricular pacing regimes as compared to RA pacing (Figure 5.9), as summarised in Table 5.2. However, BiV pacing regimes showed a reduced range of activation times in comparison to single LV and RV pacing, though this result was not found to be statistically significant. In addition, the earliest and latest activation times were significantly reduced using any of the BiV pacing regimes in comparison to LV and RV pacing.

## Distribution and pattern of activation

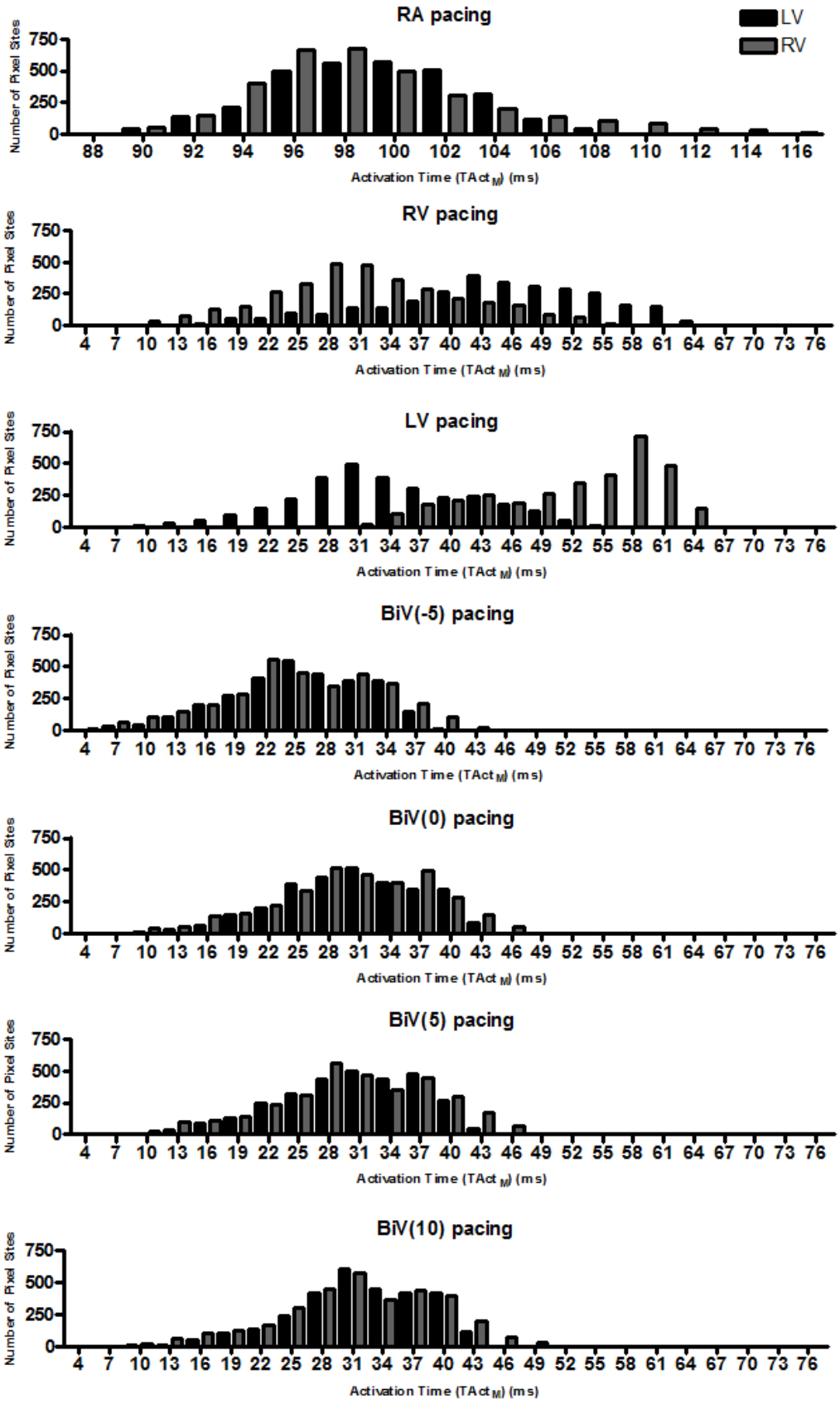


**Figure 5.7 Example of distribution of activation times for each pacing regime in one heart**

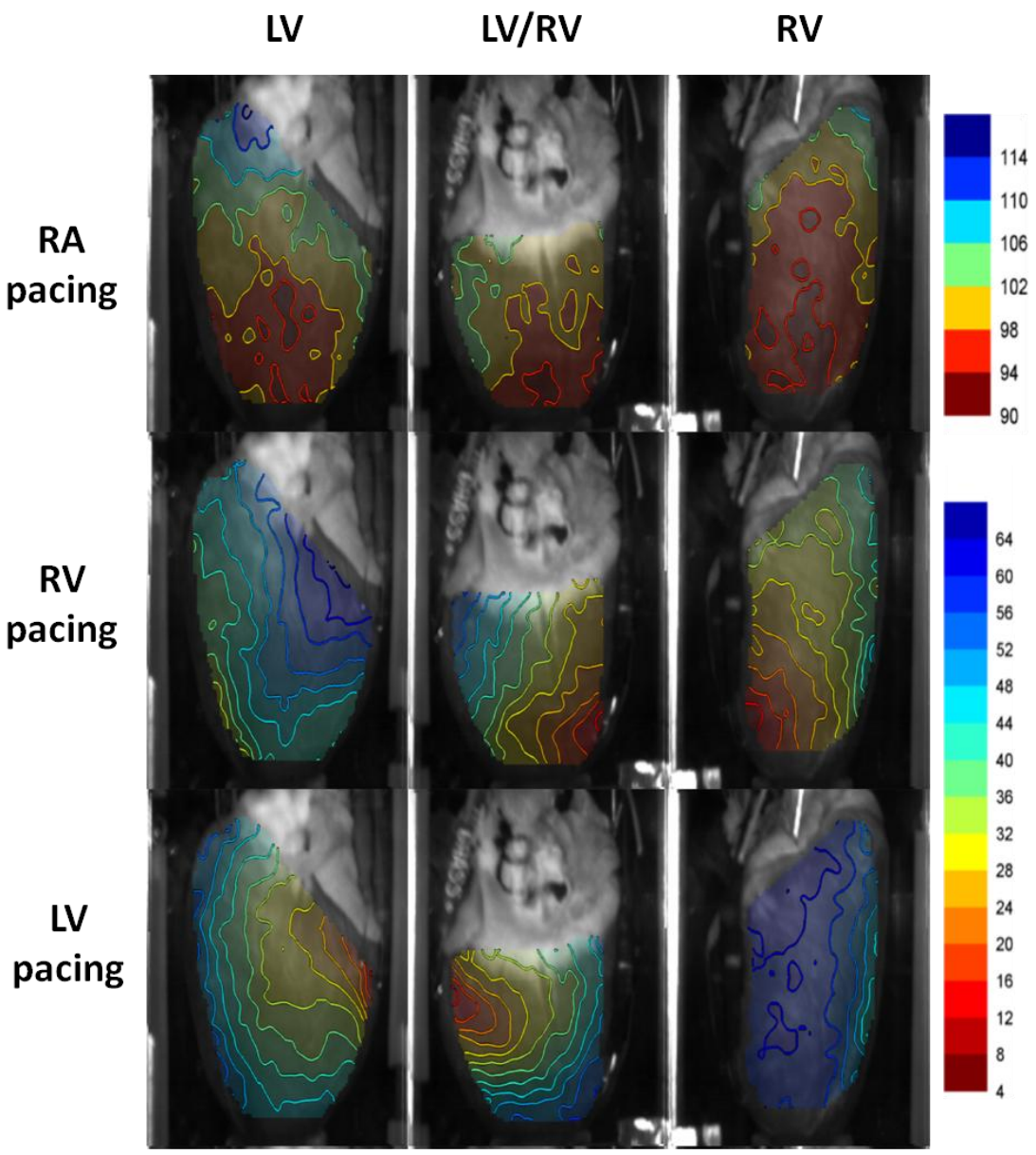
LV
LV/RV
RV
RA pacing
RV pacing
LV pacing
114
110
106
102
98
94
90
64
60
56
52
48
44
40
36
32
28
24
20
16
12
8
4

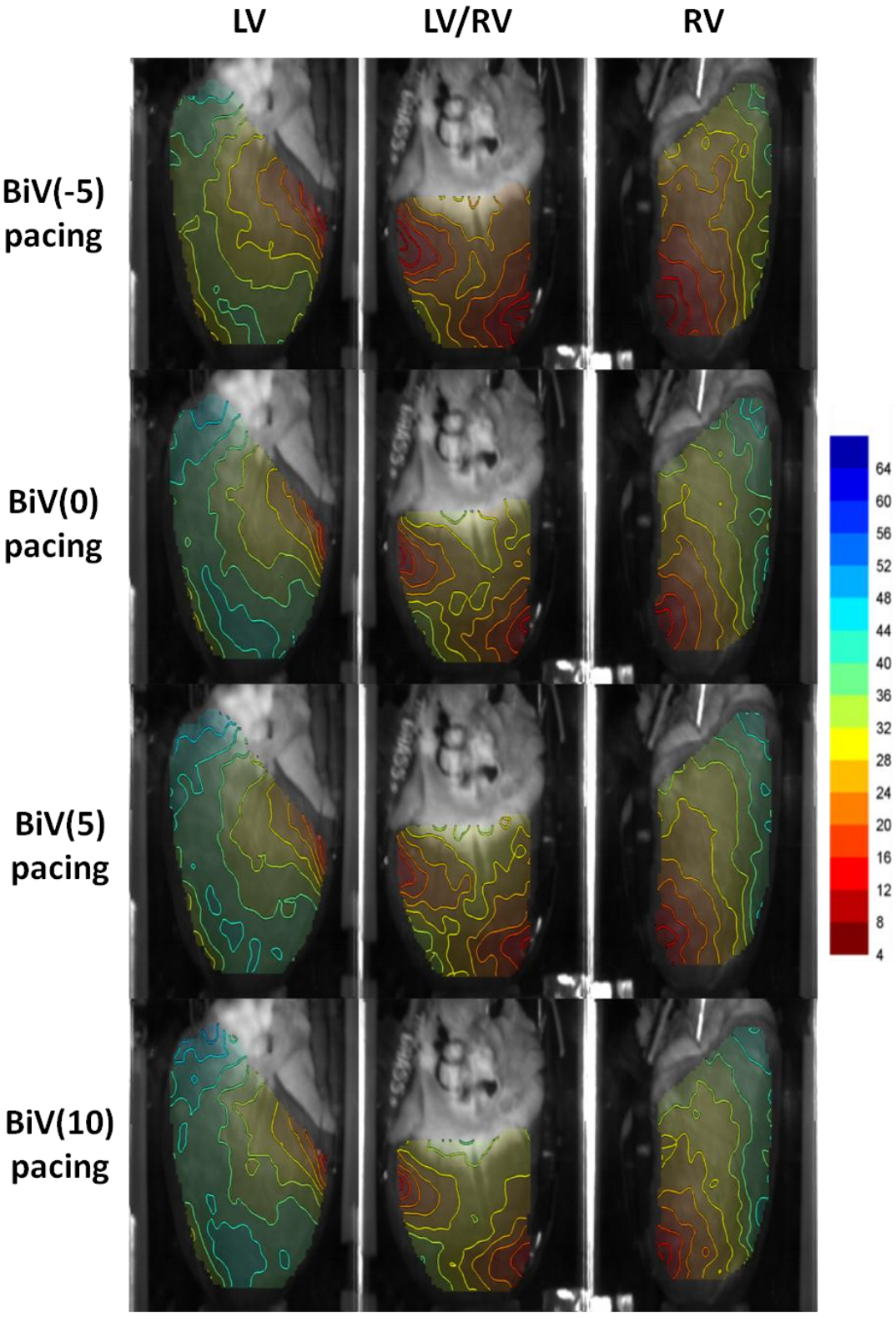


**Figure 5.8 Contour maps of activation time for each pacing regime**

**Typical isochronal contour maps of activation time for each pacing regime from the three views of the heart (LV, LV/RV and RV) [heart-3]. Times are in ms.**

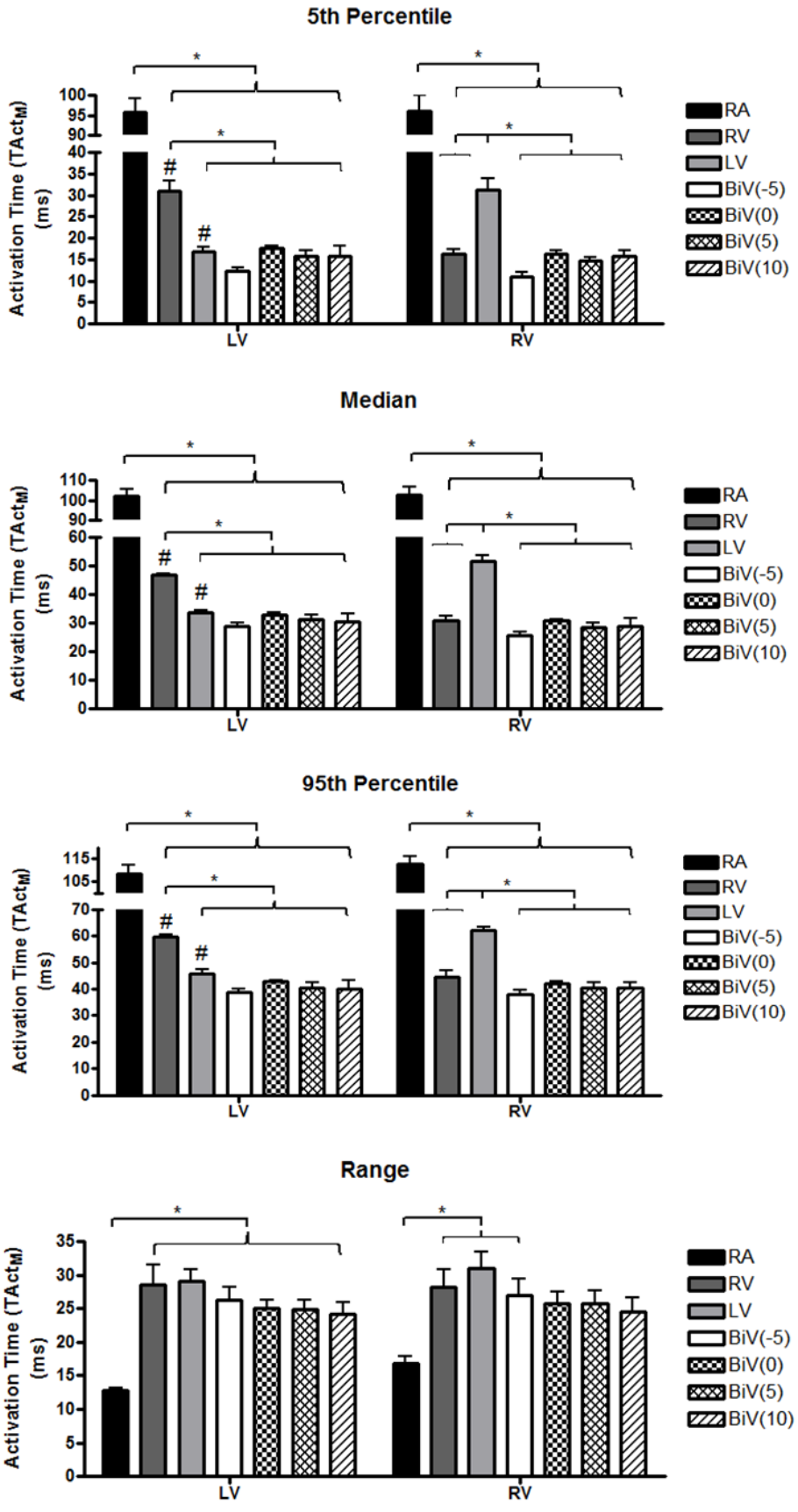


**Figure 5.9 Plots of activation time for each pacing regime**

**5$^{th}$ Percentile, Median, 95$^{th}$ Percentile and Range of values for activation time (where data is displayed as mean ± SE (n=4)). An * indicates a significant difference between pacing regimes. A # indicates significant difference between marked pacing on the LV and it's counterpart in the RV.**

**Table 5.2 Statistics for activation time for each pacing regime (where data is displayed in mean ± SE (n=4)).**

| | | RA | RV | LV | BiV(-5) | BiV(0) | BiV(5) | BiV(10) |
|---|---|---|---|---|---|---|---|---|
| Median | LV | 102.3±3.5 | 46.8±0.6 | 33.8±0.9 | 28.7±1.3 | 33±0.9 | 31.3±1.7 | 30.5±2.9 |
| | RV | 102.8±4 | 30.8±1.8 | 51.8±1.8 | 25.7±1 | 30.7±0.8 | 28.5±1.7 | 29.0±2.5 |
| 5th Percentile | LV | 95.8±3.5 | 31.0±2.5 | 16.8±1 | 12.3±0.8 | 17.7±0.6 | 15.7±1.4 | 15.8±2.4 |
| | RV | 96.0±3.9 | 16.3±1 | 31.3±2.6 | 11.0±1 | 16.3±0.8 | 14.8±0.7 | 15.8±1.4 |
| 95th Percentile | LV | 108.5±3.6 | 59.5±1 | 45.8±1.8 | 38.7±1.2 | 42.7±0.8 | 40.5±2.1 | 40.0±3.1 |
| | RV | 112.8±3.1 | 44.5±2.5 | 62.3±1.3 | 38.0±1.5 | 42.0±1 | 40.5±2.1 | 40.3±2.3 |
| Range | LV | 12.8±0.5 | 28.5±3.1 | 29.0±1.8 | 26.3±1.9 | 25.0±1.3 | 24.8±1.5 | 24.3±1.6 |
| | RV | 16.8±1.1 | 28.3±2.6 | 31.0±2.5 | 27.0±2.5 | 25.7±1.8 | 25.7±2 | 24.5±2.2 |

## Action potential duration

The range and distribution of APD times were very similar between LV and RV and in particular, only minor differences were apparent between individual hearts during RA pacing (Figure 5.10), as summarised in Table 5.3.

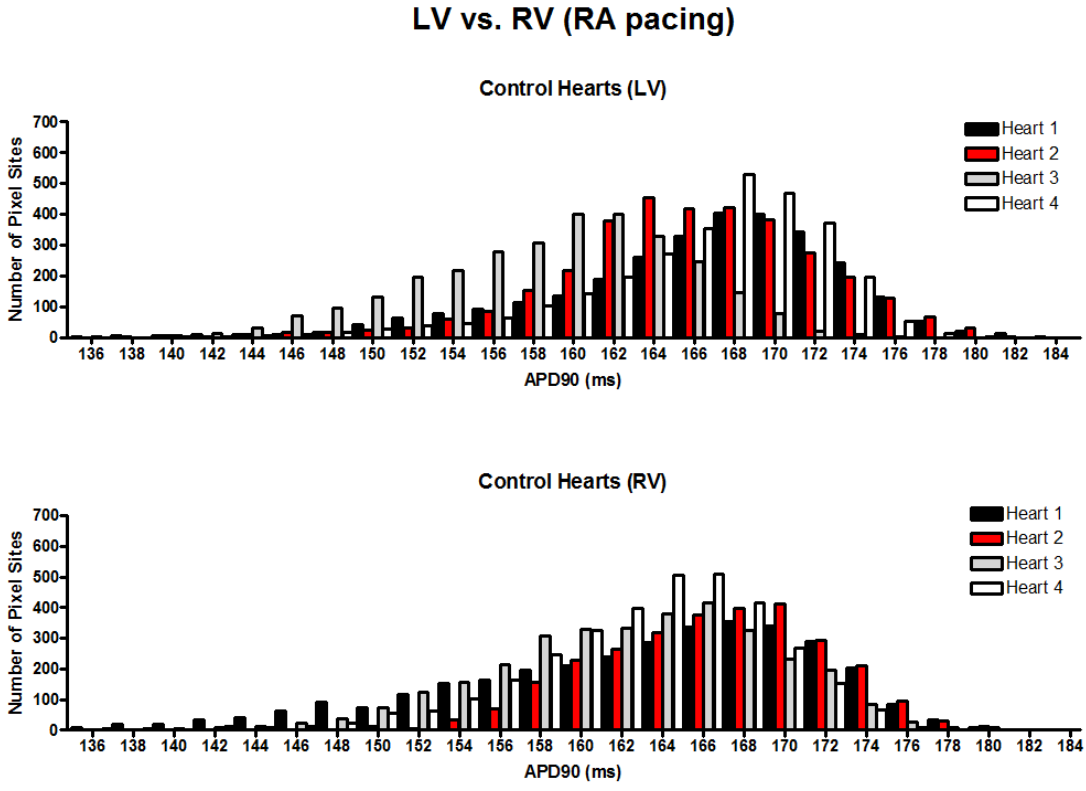


**Figure 5.10 Distribution of APD (LV and RV) for each heart**

**Table 5.3 Statistics for the APD of LV and RV of each heart during RA pacing**

| APD90 | Heart 1 | Heart 2 | Heart 3 | Heart 4 |
|---|---|---|---|---|
| **LV** | | | | |
| Median | 167.0 | 166.0 | 159.0 | 167.0 |
| 5th Percentile | 152.0 | 154.8 | 147.0 | 154.0 |
| 95th Percentile | 175.0 | 175.0 | 168.0 | 173.0 |
| Range | 23.0 | 20.2 | 21.0 | 19.0 |
| **RV** | | | | |
| Median | 164.0 | 166.0 | 163.0 | 164.0 |
| 5th Percentile | 146.0 | 157.0 | 150.0 | 152.0 |
| 95th Percentile | 174.0 | 174.0 | 172.0 | 171.0 |
| Range | 28.0 | 17.0 | 22.0 | 19.0 |

There was no significant change in the overall distribution of APD times (LV and RV) between any of the pacing regimes, with only subtle differences between LV and RV (Figure 5.11). This finding was in agreement with the corresponding contour maps of APD (Figure 5.12), which showed minimal changes in the pattern of APD across both the LV and RV, despite alterations in the range, pattern and distribution of activation times for different pacing sequences.

On average, there was no change in the range of APD times (LV and RV) for any of the pacing sequences (Figure 5.13), as summarised in Table 5.4.

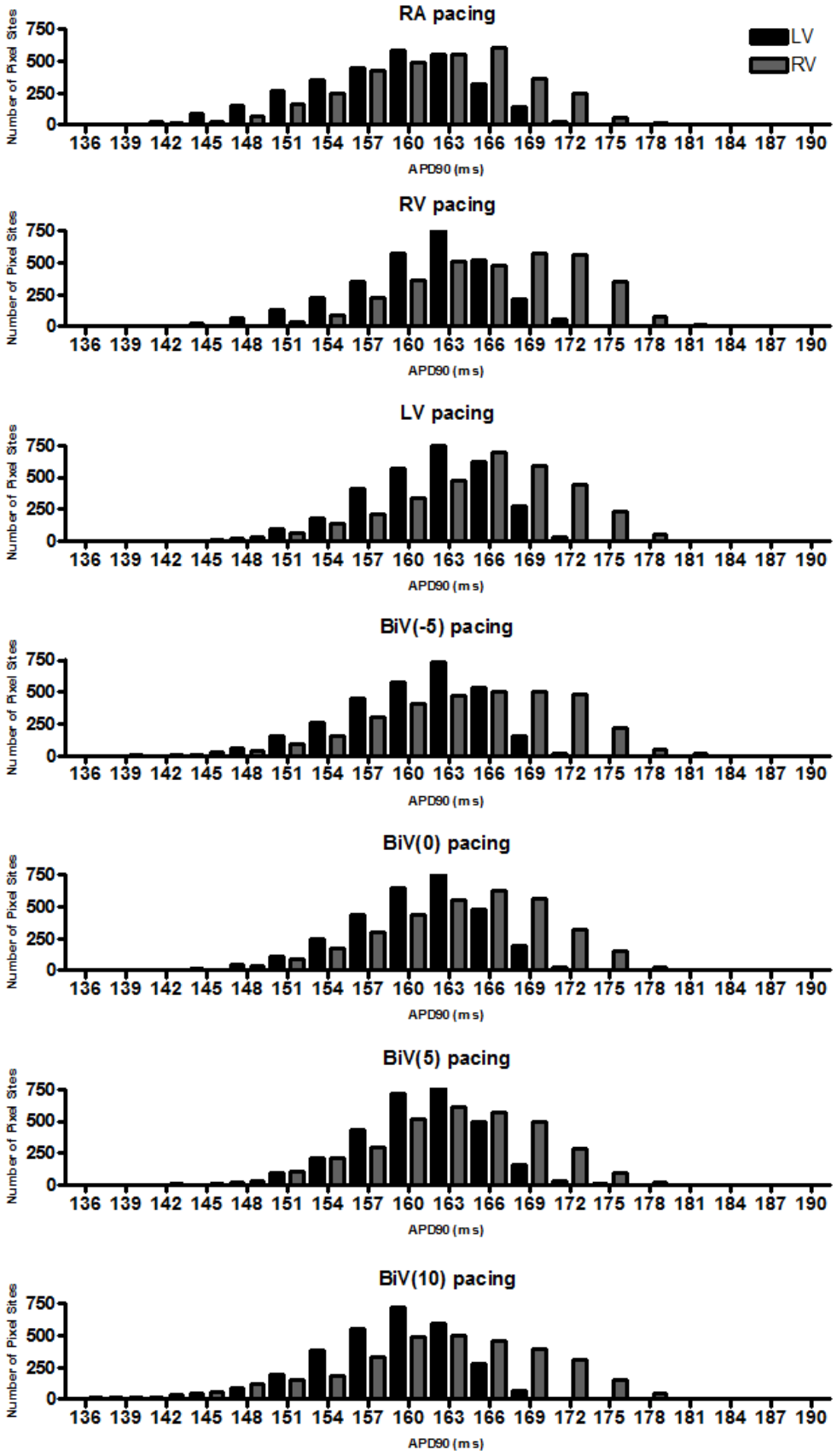


**Figure 5.11 Example of distribution of APD for each pacing regime**

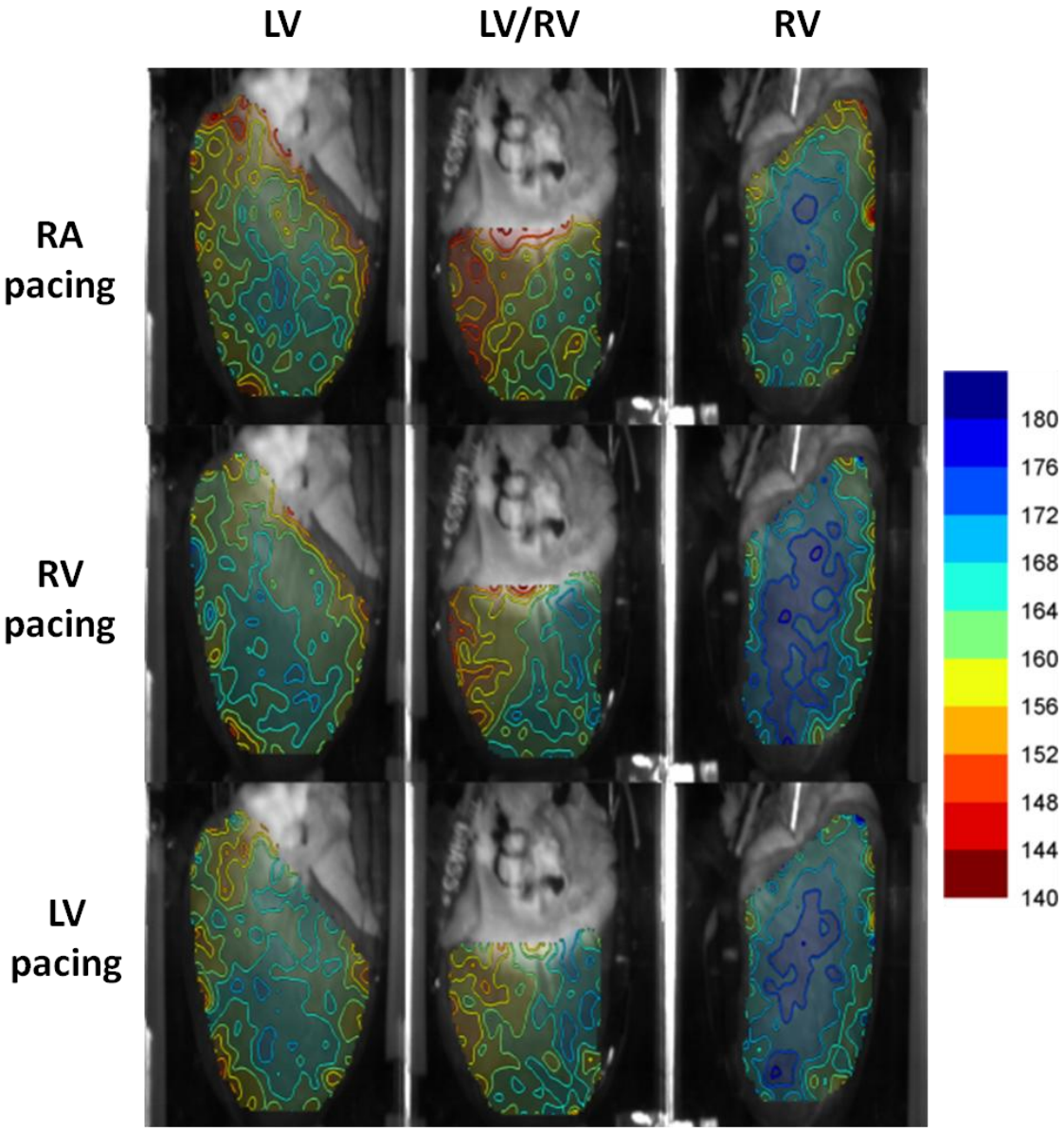
LV
LV/RV
RV
RA pacing
RV pacing
LV pacing
180
176
172
168
164
160
156
152
148
144
140

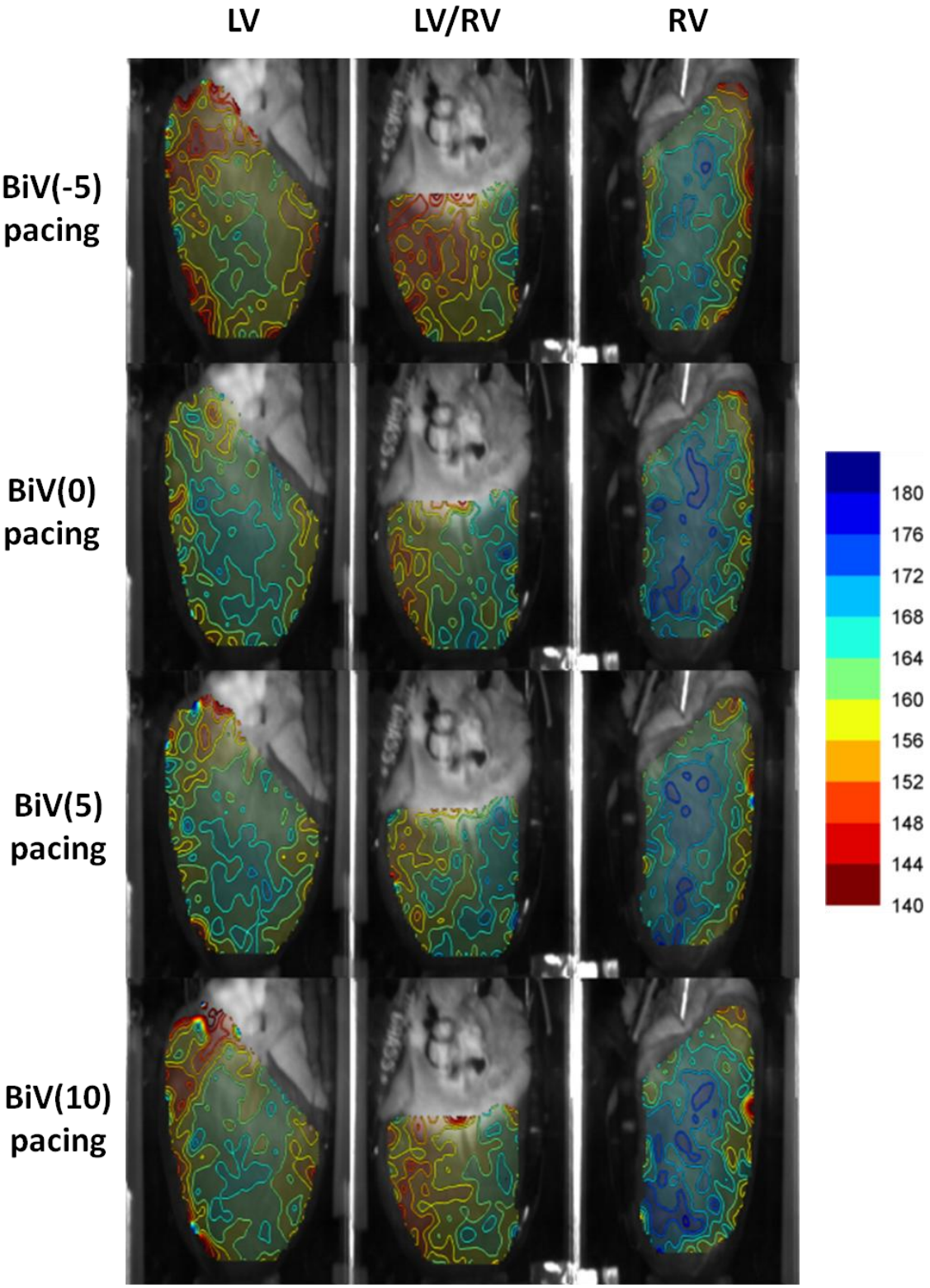


**Figure 5.12 Contour maps of APD for each pacing regime**

**Typical isochronal contour maps of action potential duration for each pacing regime from the three views of the heart (LV, LV/RV and RV) [heart-3]. Times are in ms.**

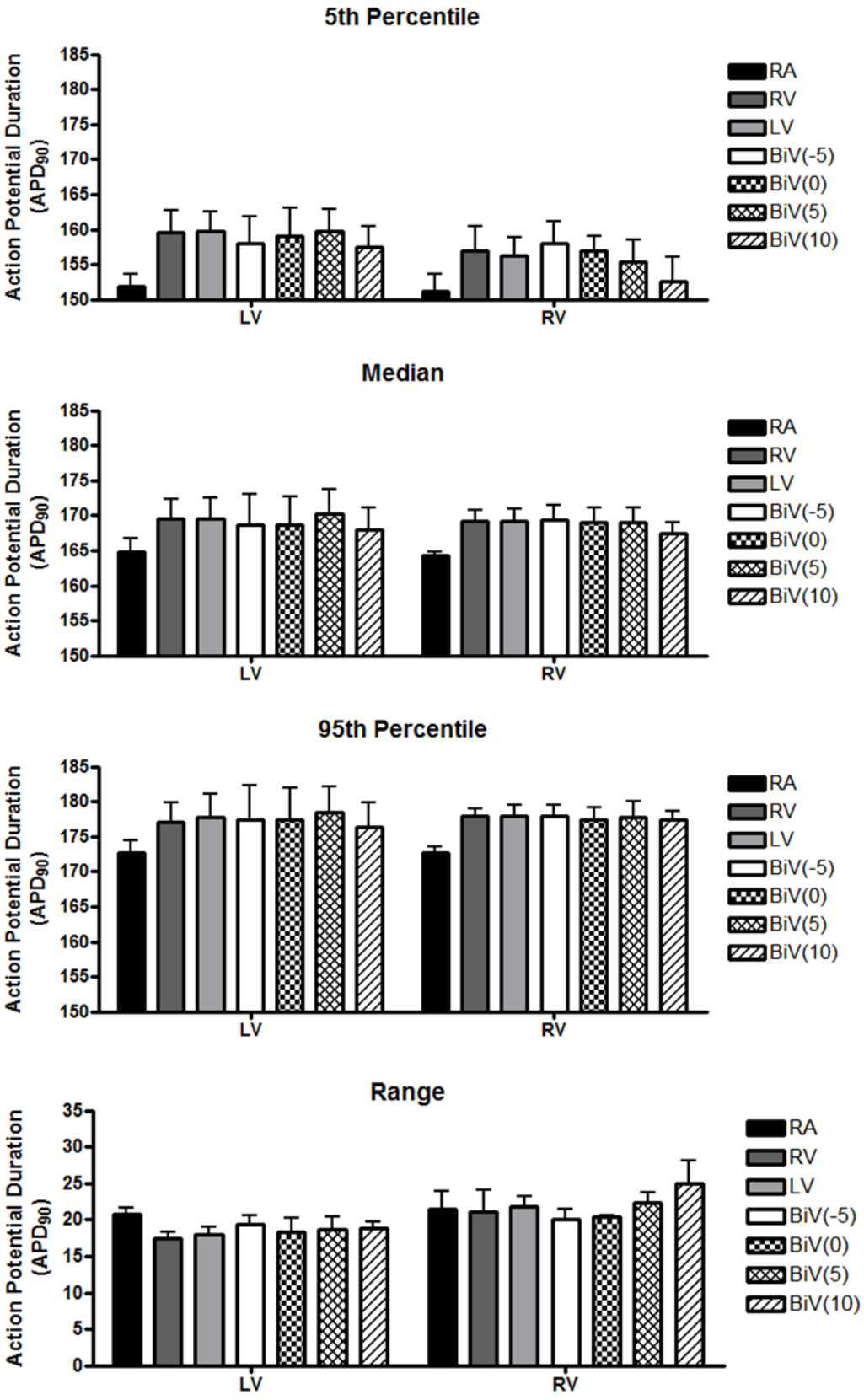


**Figure 5.13 Plots of APD for each pacing regime**

**5th Percentile, Median, 95th Percentile and Range of values for action potential duration (where data is displayed as mean ± SE (n=4)). An * indicates a significant difference between pacing regimes. A # indicates significant difference between marked pacing on the LV and it's counterpart in the RV.**

**Table 5.4 Statistics for APD for each pacing regime (where data is displayed in mean ± SE (n=4)).**

| | | RA | RV | LV | BiV(-5) | BiV(0) | BiV(5) | BiV(10) |
|---|---|---|---|---|---|---|---|---|
| Median | LV | 164.8±1.9 | 169.5±2.9 | 169.5±3.1 | 168.7±4.3 | 168.7±4.1 | 170.3±3.5 | 168.0±3.2 |
| | RV | 164.3±0.6 | 169.3±1.6 | 169.3±1.7 | 169.3±2.2 | 169.0±2.1 | 169.0±2.1 | 167.5±1.6 |
| 5th Percentile | LV | 152.0±1.8 | 159.5±3.3 | 159.8±2.9 | 158.0±3.8 | 159.0±4 | 159.8±3.1 | 157.5±3 |
| | RV | 151.3±2.3 | 156.9±3.6 | 156.3±2.7 | 158.0±3.1 | 157.0±2.1 | 155.4±3.1 | 152.5±3.5 |
| 95th Percentile | LV | 172.8±1.7 | 177.0±2.8 | 177.8±3.4 | 177.3±5 | 177.3±4.7 | 178.5±3.7 | 176.3±3.5 |
| | RV | 172.8±0.8 | 178.0±0.9 | 178.0±1.5 | 178.0±1.5 | 177.3±1.8 | 177.8±2.2 | 177.5±1.2 |
| Range | LV | 20.8±0.8 | 17.5±0.9 | 18.0±1.1 | 19.3±1.2 | 18.3±1.9 | 18.8±1.7 | 18.8±0.9 |
| | RV | 21.5±2.4 | 21.1±3 | 21.8±1.5 | 20.0±1.5 | 20.3±0.3 | 22.4±1.4 | 25.0±3.1 |

During RA pacing, an inverse relationship emerged between APD and activation times over both the LV and RV, where linear regression analysis showed a clear correlation between APD and activation time with a mean slope of -1.03 and -1.04 ($R^2$ = 0.57 and $R^2$ = 0.61) for the LV and RV, respectively (data summarised in Table 5.5).This relationship manifested as a transepicardial gradient in the apex-base axis, where longer APD times corresponded with earlier activation times at the mid-ventricular and apex regions and shorter APD times with later activation times at the base, as shown in Figure 5.14.

During any of the alternative forms of pacing, there was a very shallow relationship between APD and activation time with the absence of any significant trend, as shown for LV pacing in Figure 5.14. The mean slope of this relationship was -0.37 and -0.46 ($R^2$ = 0.26 and $R^2$ = 0.17) for the LV and RV, respectively, and the data are summarised in Table 5.5. There was a statistically significant decrease in the slope of the relationship when comparing RA to LV pacing in both the LV and RV. Multivariate statistical analysis revealed no affect of ventricle (LV or RV) on the variation in slope observed, with the majority of variation determined by the mode of pacing.

There was a common pattern of APD times in terms of epicardial position, which emerged as an APD gradient in the apex-base direction across the LV during all forms of pacing. The LV presented with longest APD times at the mid-ventricular and apex region and shorter APD times at the base, as shown in Figure 5.15, with no significant differences between the pacing regimes. The RV presented with purely longer APD times at the apex and shorter APD times at the base.

## Relationship between APD and activation time

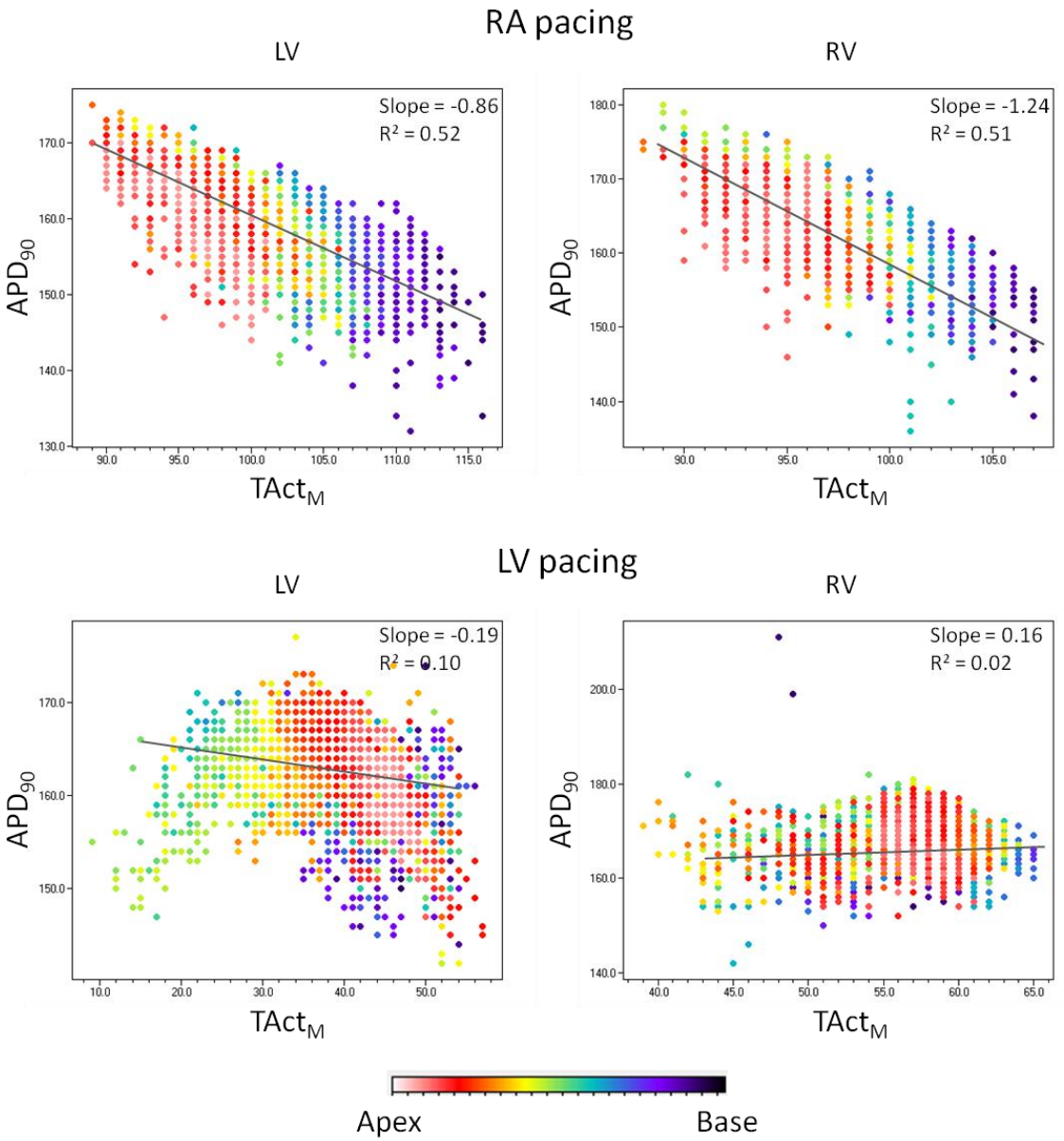


**Figure 5.14 Inverse relationship ($APD_{90}$ – $TAct_M$)**

**An example scatter plot showing the typical inverse relationship between action potential duration against activation time ($TAct_M$) for the LV and RV during RA pacing**

**Table 5.5 Mean relationship between APD and activation time**

| Control Group (n=4) | | RA pacing | LV pacing | P-value |
|---|---|---|---|---|
| LV | Slope | -1.03±0.1 | -0.37±0.07 | <0.01 |
| | $R^2$ | 0.57±0.08 | 0.26±0.07 | <0.05 |
| RV | Slope | -1.04±0.07 | -0.46±0.11 | <0.05 |
| | $R^2$ | 0.61±0.04 | 0.17±0.08 | <0.01 |

**Relationship between APD and epicardial position**

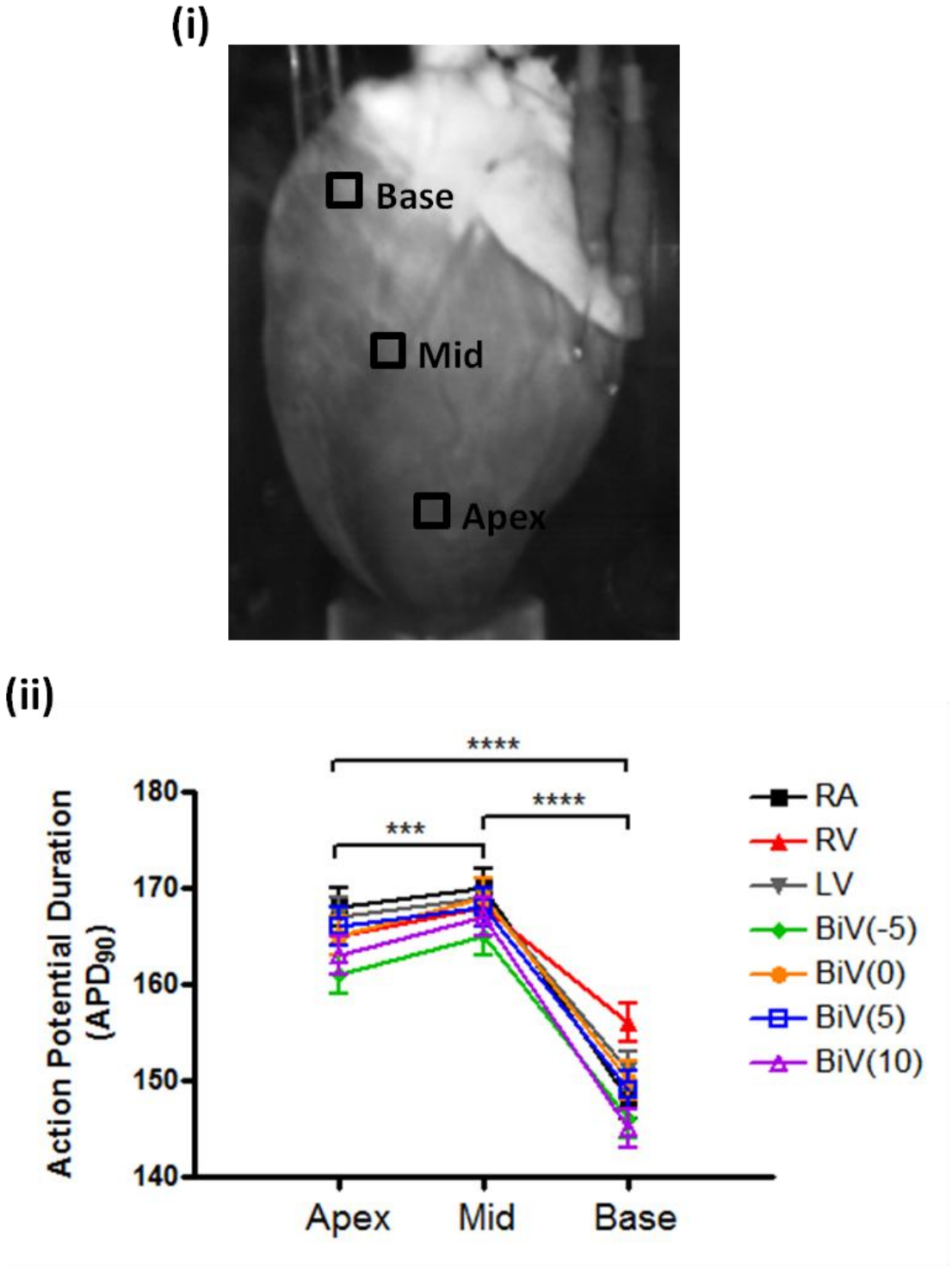


**Figure 5.15 Relationship between APD and epicardial position**

**(i) View of the LV epicardial surface with optical AP sampling regions for each epicardial position (apex, mid and base)**

**(ii) Plot of action potential duration against epicardial position for each form of pacing (***P<0.001 and ****P<0.0001).**

## Repolarisation

During RA pacing there was a range of repolarisation times across both the LV and RV that varied from heart to heart (Figure 5.16), and summarised in Table 5.6. Heart to heart variability may be attributed to the differences present in the individual activation sequences, illustrated previously in Figure 5.5.

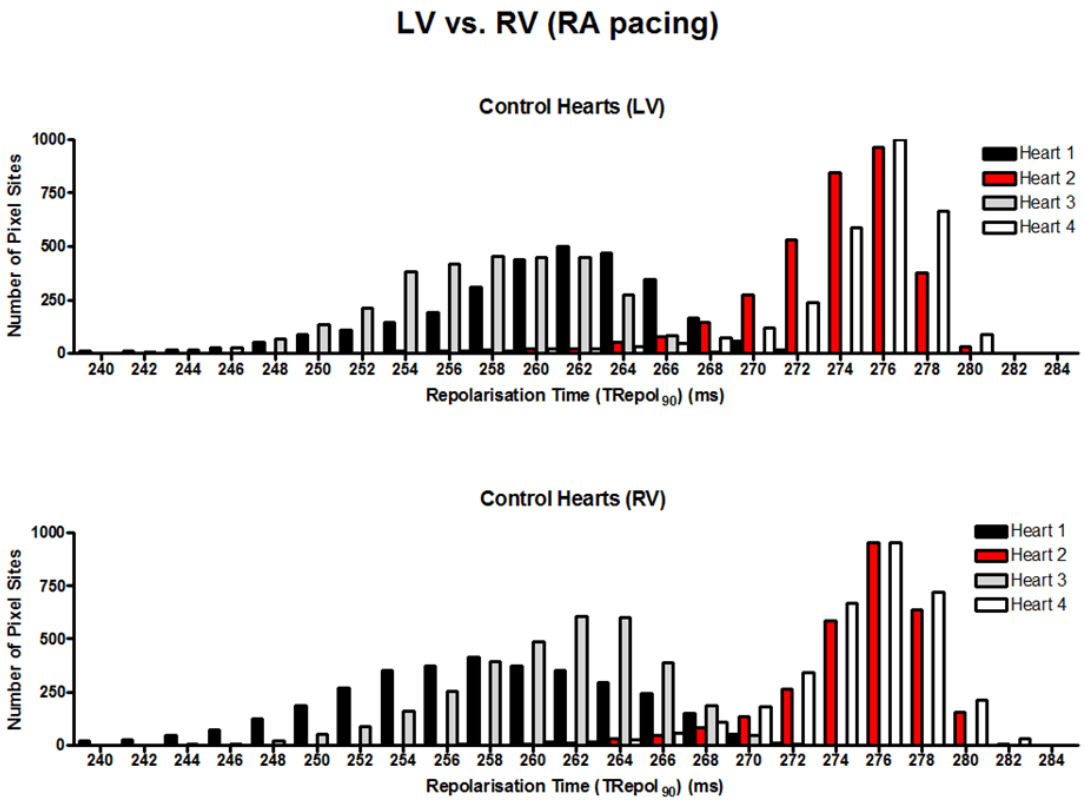


**Figure 5.16 Distribution of repolarisation times (LV and RV) for each heart**

**Table 5.6 Statistics for the repolarisation times of LV and RV of each heart during RA pacing**

| TRepol90 | Heart 1 | Heart 2 | Heart 3 | Heart 4 |
|---|---|---|---|---|
| **LV** | | | | |
| Median | 261.0 | 274.0 | 257.0 | 275.0 |
| 5th Percentile | 249.0 | 266.0 | 249.0 | 266.0 |
| 95th Percentile | 267.0 | 277.0 | 264.0 | 278.0 |
| Range | 18.0 | 11.0 | 15.0 | 12.0 |
| **RV** | | | | |
| Median | 257.0 | 275.0 | 261.0 | 275.0 |
| 5th Percentile | 246.0 | 268.0 | 252.0 | 267.0 |
| 95th Percentile | 267.0 | 279.0 | 267.0 | 279.0 |
| Range | 21.0 | 11.0 | 15.0 | 12.0 |

As was seen with the activation sequence, the repolarisation sequence showed significantly split distributions for LV and RV pacing in comparison to RA pacing (Figure 5.17).

Similar to the activation sequence, the distribution of repolarisation times were independent of pacing offset for all forms of BiV pacing. BiV pacing repolarisation distributions were comparable to RA pacing.

In general, the pattern of repolarisation followed the activation sequence with areas of earliest activation corresponding to areas of earliest repolarisation and vice versa (Figure 5.18). This phenomenon was present for all forms of pacing.

On average, the range of repolarisation times (LV and RV) were significantly increased when using any of the ventricular pacing regimes as compared to RA pacing (Figure 5.19 and Table 5.7). However, BiV pacing regimes showed a reduced range of repolarisation times in comparison to single LV and RV pacing.

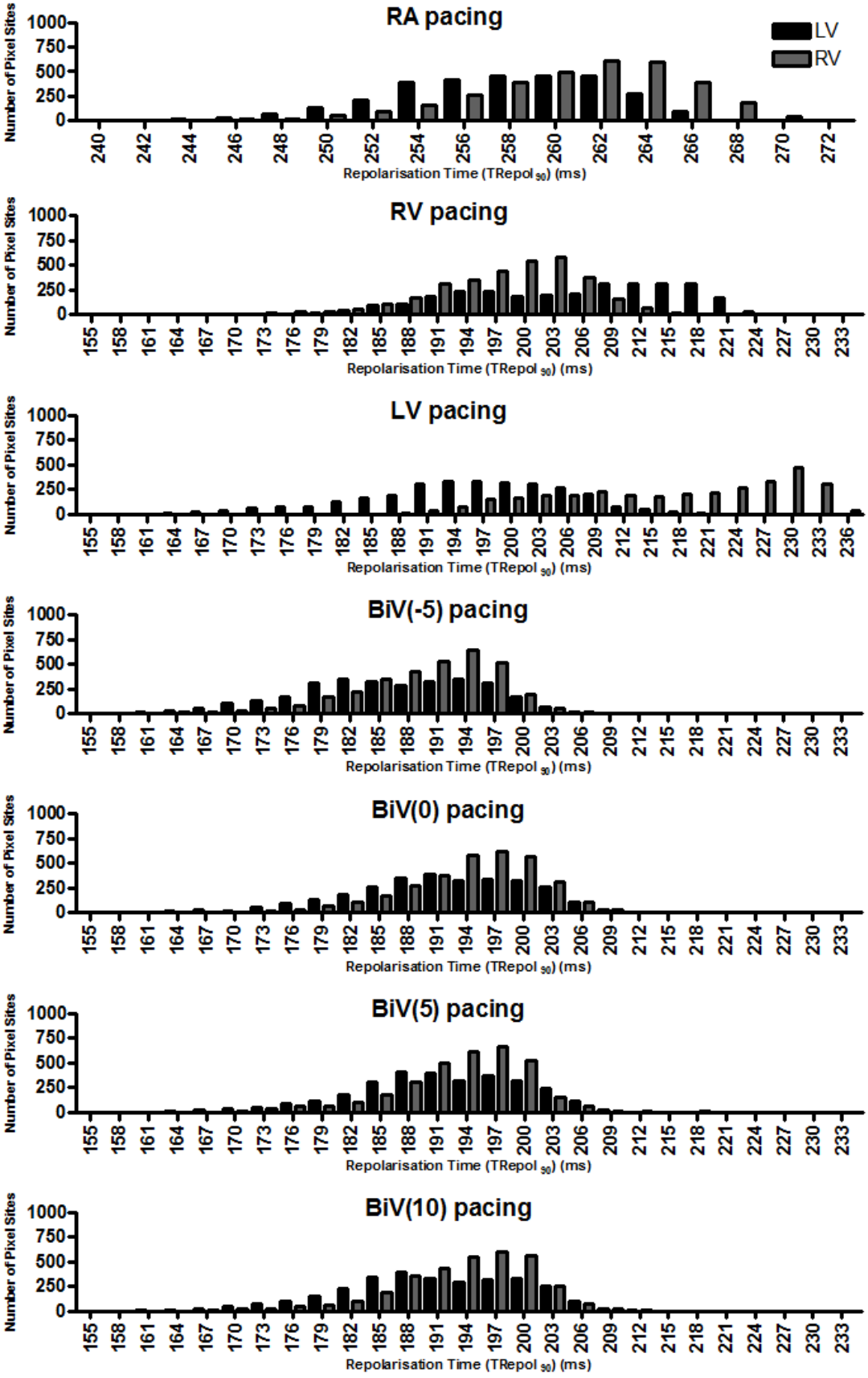


**Figure 5.17 Example of distribution of repolarisation times for each pacing regime**

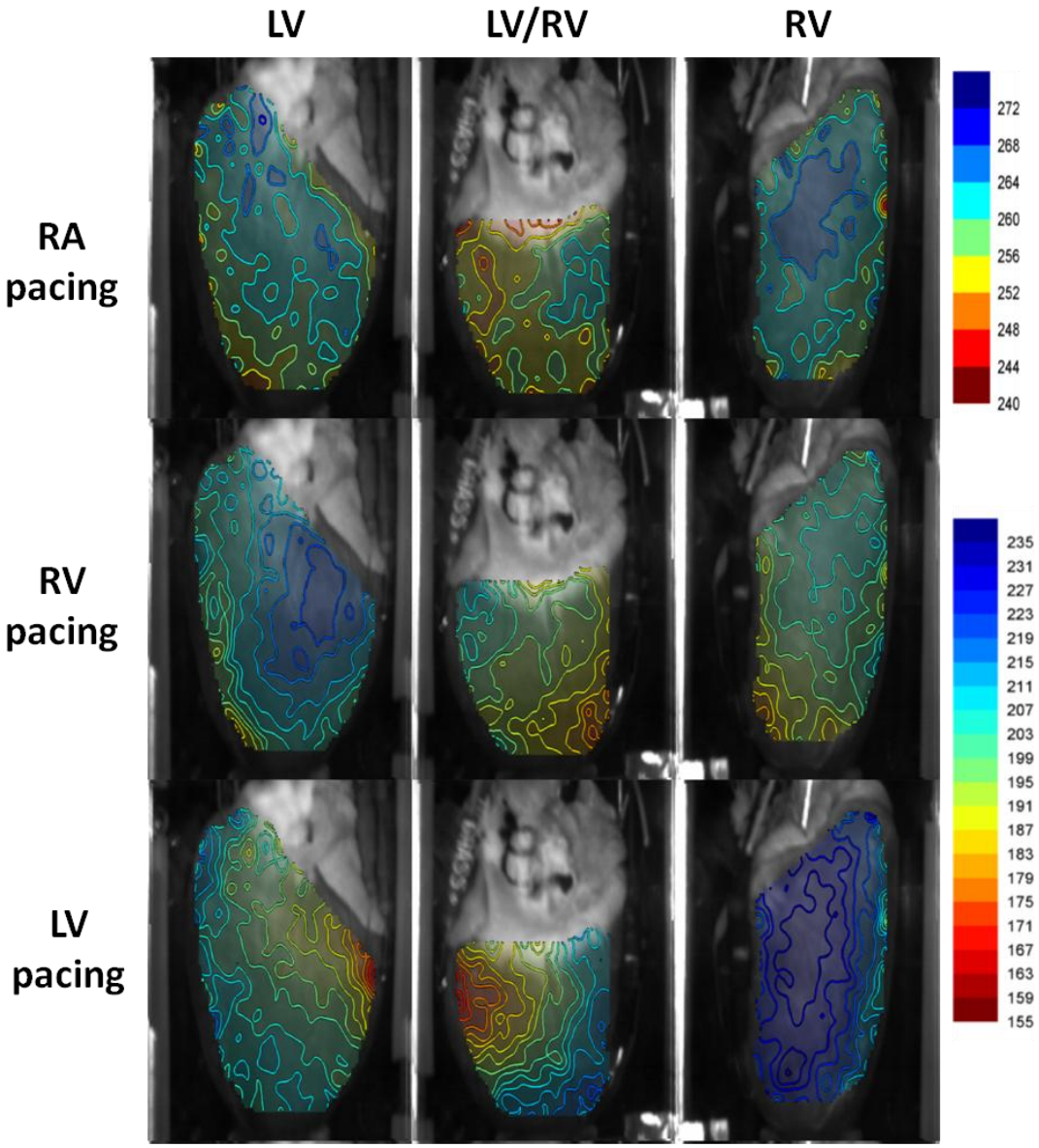
LV
LV/RV
RV
RA pacing
RV pacing
LV pacing
272
268
264
260
256
252
248
244
240
235
231
227
223
219
215
211
207
203
199
195
191
187
183
179
175
171
167
163
159
155

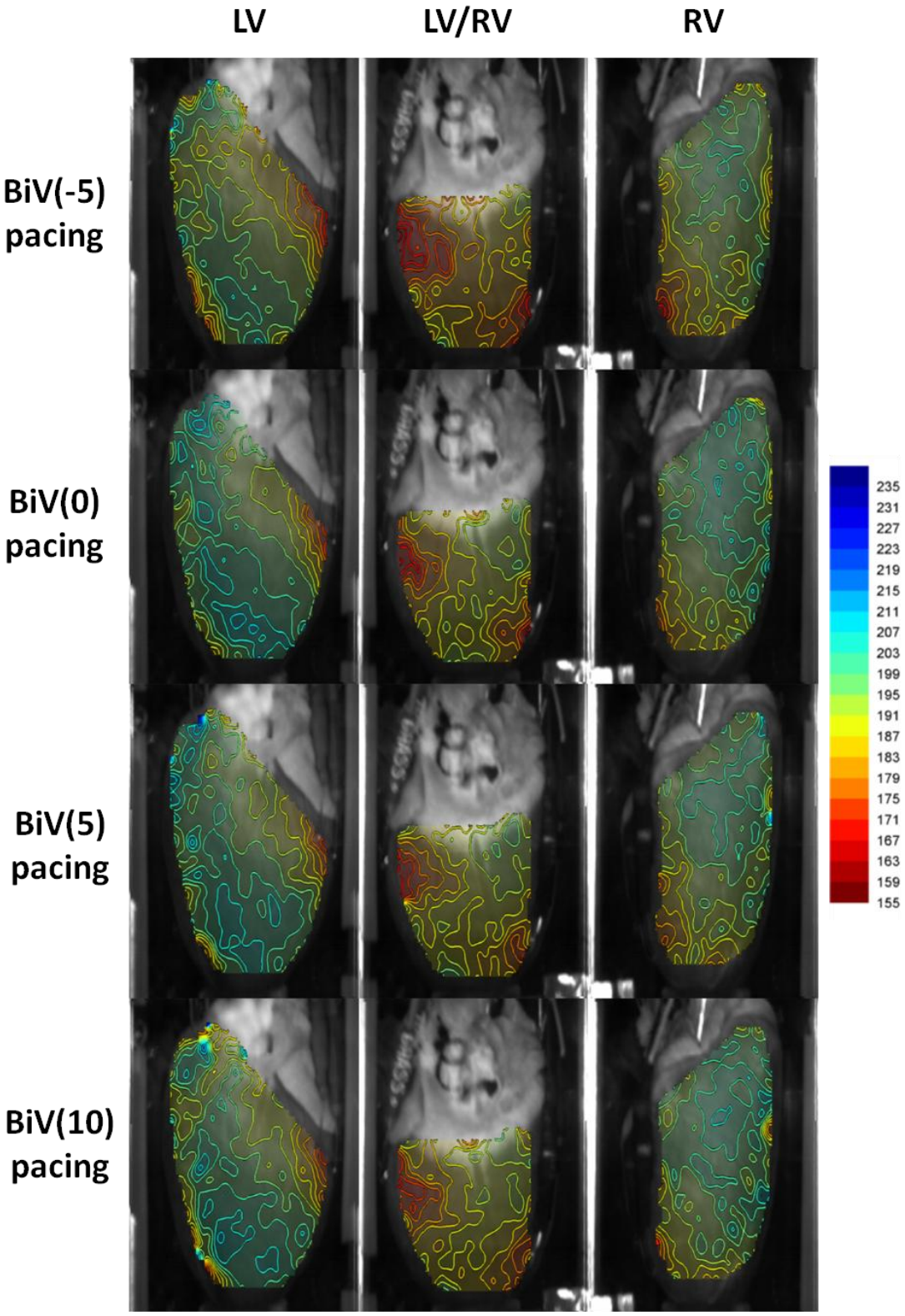


**Figure 5.18 Contour maps of repolarisation time for each pacing regime**

**Typical isochronal contour maps of repolarisation time for each pacing regime from the three views of the heart (LV, LV/RV and RV) [heart-3]. Times are in ms.**

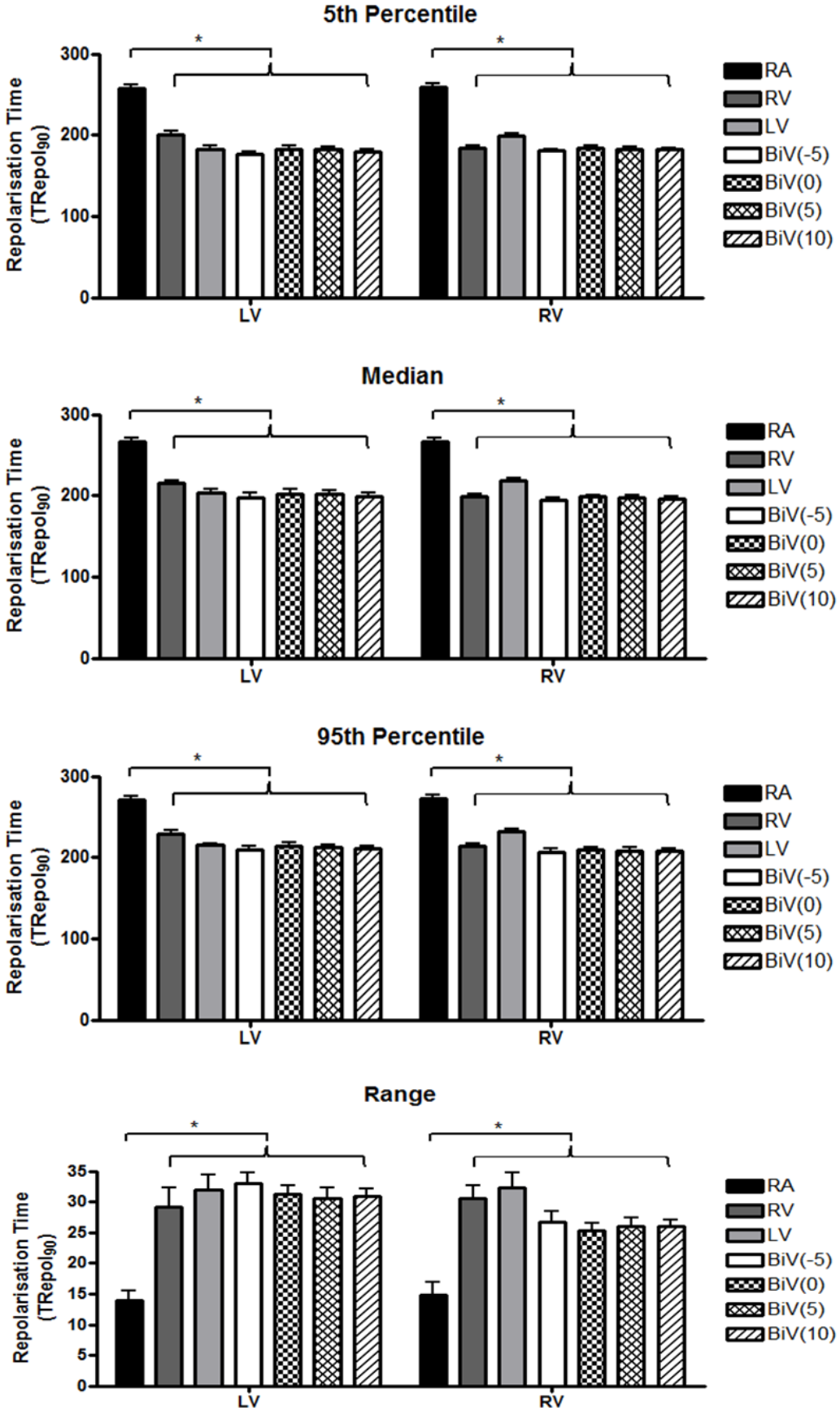


**Figure 5.19 Plots of repolarisation time for each pacing regime**

**5th Percentile, Median, 95th Percentile and Range of values for repolarisation time (where data is displayed as mean ± SE (n=4)). An * indicates a significant difference between pacing regimes. A # indicates significant difference between marked pacing on the LV and it's counterpart in the RV.**

**Table 5.7 Statistics for repolarisation time for each pacing regime (where data is displayed in mean ± SE (n=4)).**

| | | RA | RV | LV | BiV(-5) | BiV(0) | BiV(5) | BiV(10) |
|---|---|---|---|---|---|---|---|---|
| Median | LV | 266.8±4.6 | 215.5±3.3 | 204.0±3.7 | 198.0±5.7 | 202.3±5.4 | 201.8±4.2 | 198.8±4.3 |
| | RV | 267.0±4.7 | 199.0±3.2 | 218.5±2.7 | 195.0±2.3 | 198.7±2.3 | 197.0±3.2 | 196.3±2.5 |
| 5th Percentile | LV | 257.5±4.9 | 200.0±4.8 | 183.0±3.3 | 176.3±3.8 | 182.3±4.1 | 181.8±4 | 179.3±3.2 |
| | RV | 258.3±5.5 | 183.5±3 | 199.5±2.7 | 180.3±1.8 | 184.7±1.9 | 182.8±3.1 | 181.8±2.5 |
| 95th Percentile | LV | 271.5±3.5 | 229.3±3.8 | 215.0±2.6 | 209.3±4.8 | 213.7±4.4 | 212.3±3.9 | 210.3±3.9 |
| | RV | 273.0±3.5 | 214.0±3.1 | 231.8±3.7 | 207.0±3.6 | 210.0±3.1 | 208.7±3.8 | 207.8±2.8 |
| Range | LV | 14.0±1.6 | 29.3±3.1 | 32.0±2.3 | 33.0±1.7 | 31.3±1.3 | 30.5±1.8 | 31.0±1.1 |
| | RV | 14.8±2.3 | 30.5±2.2 | 32.3±2.5 | 26.7±1.9 | 25.3±1.2 | 26.0±1.5 | 26.0±1.1 |

## Part 2: MI group

### LV remodelling in MI group

Several parameters were used to characterise the degree of LV remodelling, as a result of the coronary artery ligation, in the model of chronic MI (MI group); they are summarised in Table 5.8. Although there were no significant differences in body weight between the control and MI group, coronary artery ligation led to a decrease in left ventricular ejection fraction (LVEF), an increase in left atrial diameter and an increase in left ventricular end-diastolic diameter (LVEDD) in the MI when compared to control group, changes that were all highly significant.

**Table 5.8 LV remodelling in MI hearts**

| Parameters (mean ± SE) | Control (n=4) | Chronic MI (n=4) | P-value |
|---|---|---|---|
| Body Weight (kg) | 3.0745 ± 0.14 | 3.194 ± 0.3 | 0.7305 |
| Lung Wet Weight (g) | 11.8 ± 0.3 | 13.5 ± 0.7 | <0.05 |
| LVEF (%) | 67.3 ± 0.4 | 35 ± 1.4 | <0.001 |
| LAD (mm) | 10.7 ± 0.1 | 12.6 ± 0.3 | <0.001 |
| LVEDD (mm) | 16.8 ± 0.4 | 21.9 ± 0.4 | <0.001 |

LAD = left atrial diameter, LVEDD = left ventricular end diastolic diameter, LVEF = left ventricular ejection fraction, mm = millimetres, SE = standard error. P values refer to an unpaired t-test.

### Atrio-ventricular conduction heterogeneity

As reported in the control group, there was a range of activation times across the LV and RV that varied from heart to heart during RA pacing (Figure 5.20 & Table 5.9).

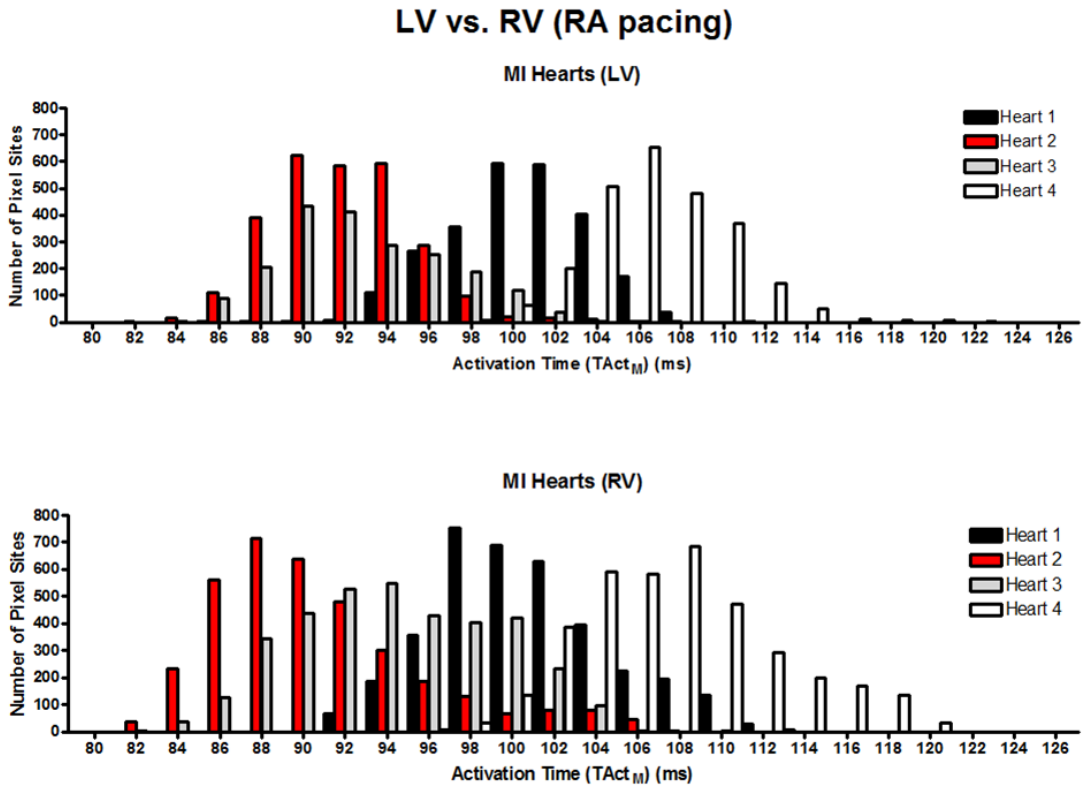


**Figure 5.20 Distribution of activation times (LV and RV) for each MI heart**

**Table 5.9 Statistics for the activation times of LV and RV of each MI heart during RA pacing**

| TActM | Heart 1 | Heart 2 | Heart 3 | Heart 4 |
|---|---|---|---|---|
| **LV** | | | | |
| Median | 100.0 | 91.0 | 92.0 | 106.0 |
| 5th Percentile | 95.0 | 87.0 | 87.0 | 101.0 |
| 95th Percentile | 105.0 | 97.0 | 99.0 | 111.0 |
| Range | 10.0 | 10.0 | 12.0 | 10.0 |
| **RV** | | | | |
| Median | 100.0 | 89.0 | 94.0 | 107.0 |
| 5th Percentile | 94.0 | 84.0 | 87.0 | 101.0 |
| 95th Percentile | 108.0 | 101.0 | 102.0 | 116.0 |
| Range | 14.0 | 17.0 | 15.0 | 15.0 |

Similar distributions of activation time were present in the MI group as compared with control group (Figure 5.21). These presented as a coordinated interventricular activation sequence during RA pacing. There were clearly split distributions of activation for both LV and RV pacing, and a return to a more coordinated interventricular activation sequence during any of the BiV pacing regimes regardless of offset. During both RV and LV pacing the overall spread of activation timings were greater in comparison to during RA pacing or any of the BiV pacing sequences. BiV pacing regimes showed a comparable range of activation times to during RA pacing.

In contrast to the control group, during RA pacing, activation wavefronts propagated purely from the mid-myocardium spreading outwards in the direction of the apex and base across the LV, as shown in Figure 5.22. However, the RV maintained its apex-base direction of activation sequence as in the control group.

On average, the range of activation times across the LV and RV were significantly increased when using any of the ventricular pacing regimes as compared to RA pacing (Figure 5.23), as summarised in Table 5.10. Across the LV and RV, there was a significant increase in the range of activation times during LV pacing in comparison to control group ($P<0.05$). In addition, the range of activation times during LV pacing in the MI group were significantly greater than any of the BiV pacing regimes across both the LV and RV ($P<0.05$).

## Distribution and pattern of activation

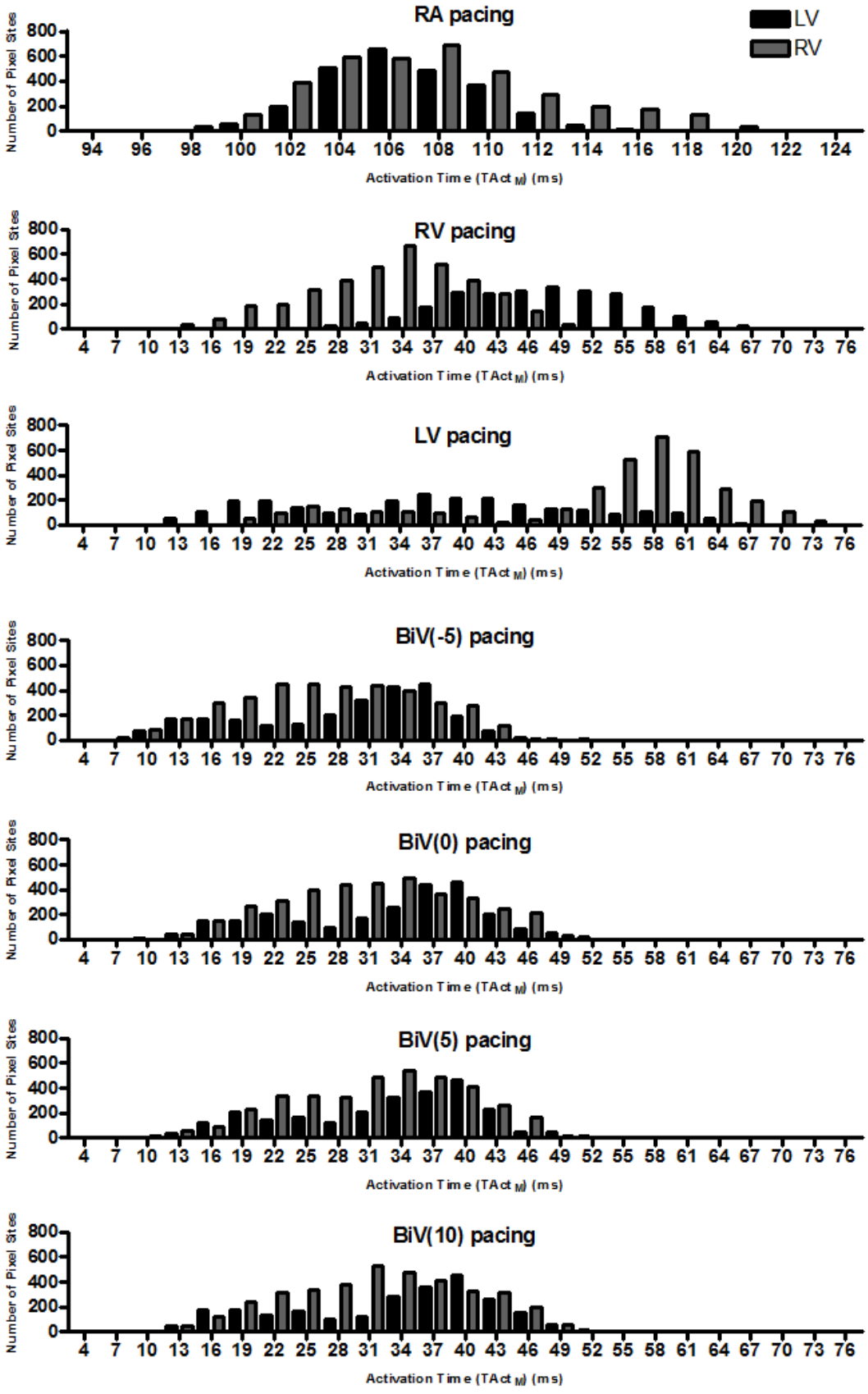


**Figure 5.21 Example of distribution of activation times for each pacing regime (MI heart)**

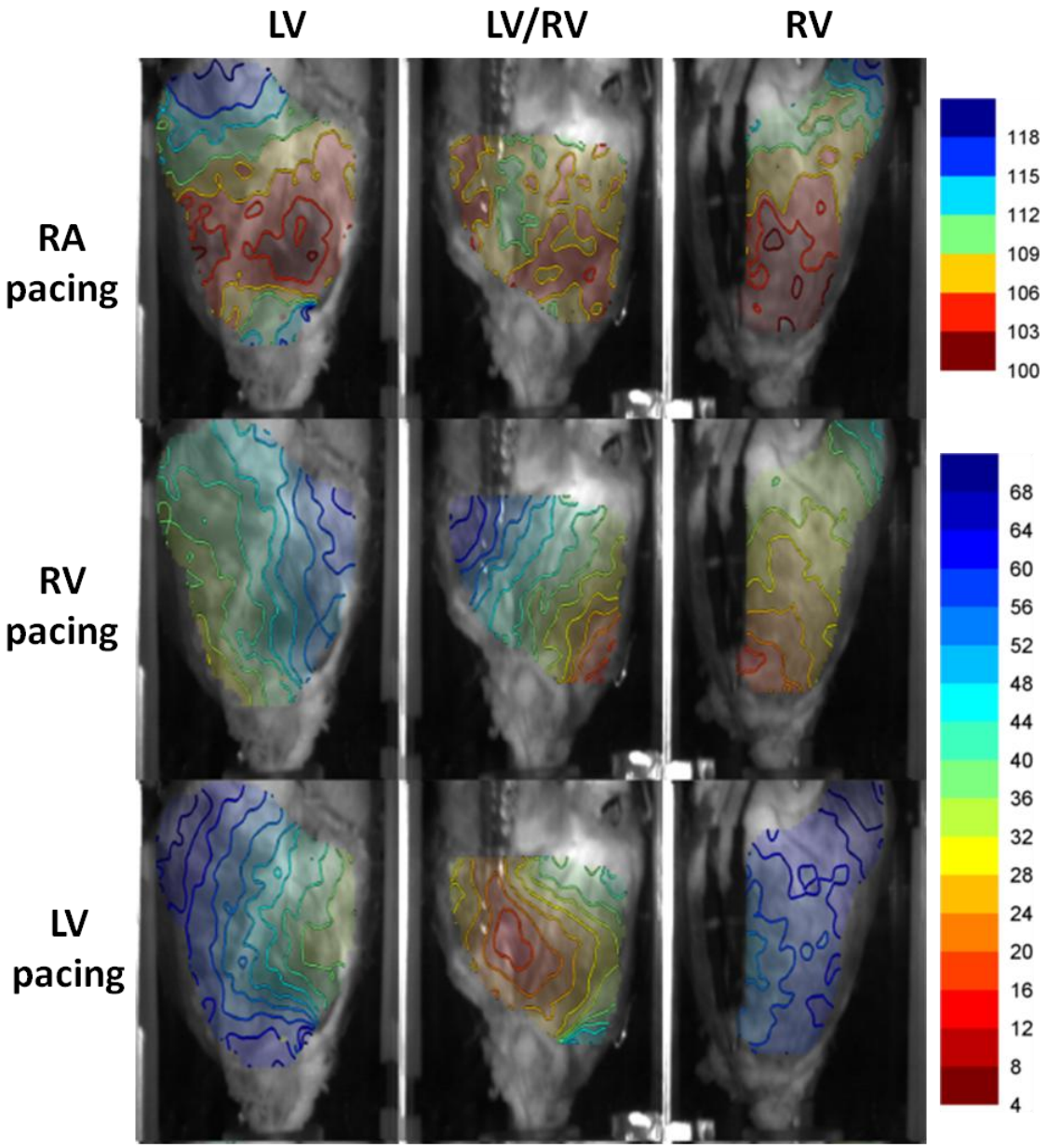
LV
LV/RV
RV
RA pacing
RV pacing
LV pacing
118
115
112
109
106
103
100
68
64
60
56
52
48
44
40
36
32
28
24
20
16
12
8
4

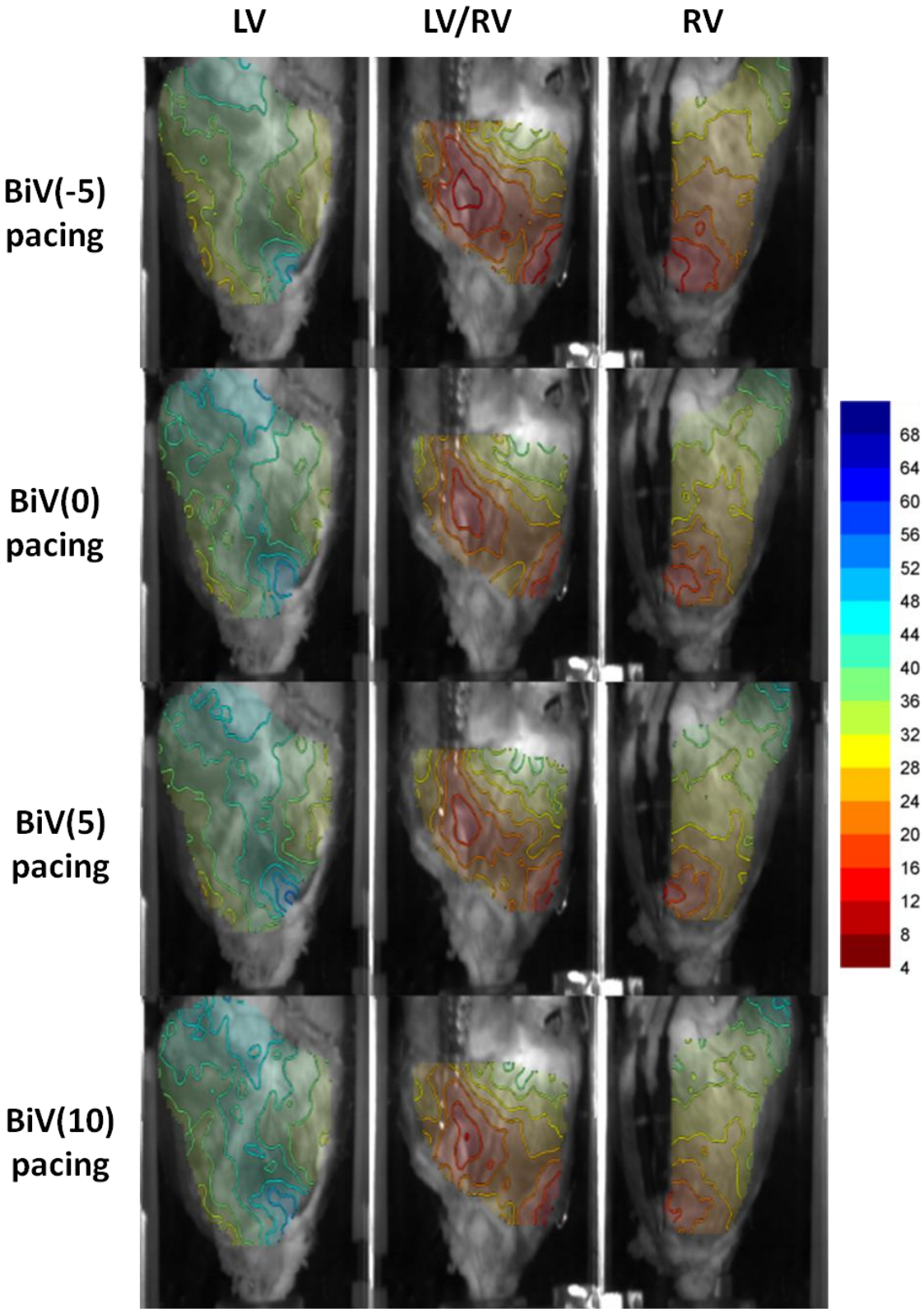


**Figure 5.22 Contour maps of activation time for each pacing regime (MI heart)**

**Typical isochronal contour maps of activation time for each pacing regime from the three views of the MI heart (LV, LV/RV and RV) [heart-4]. Times are in ms.**

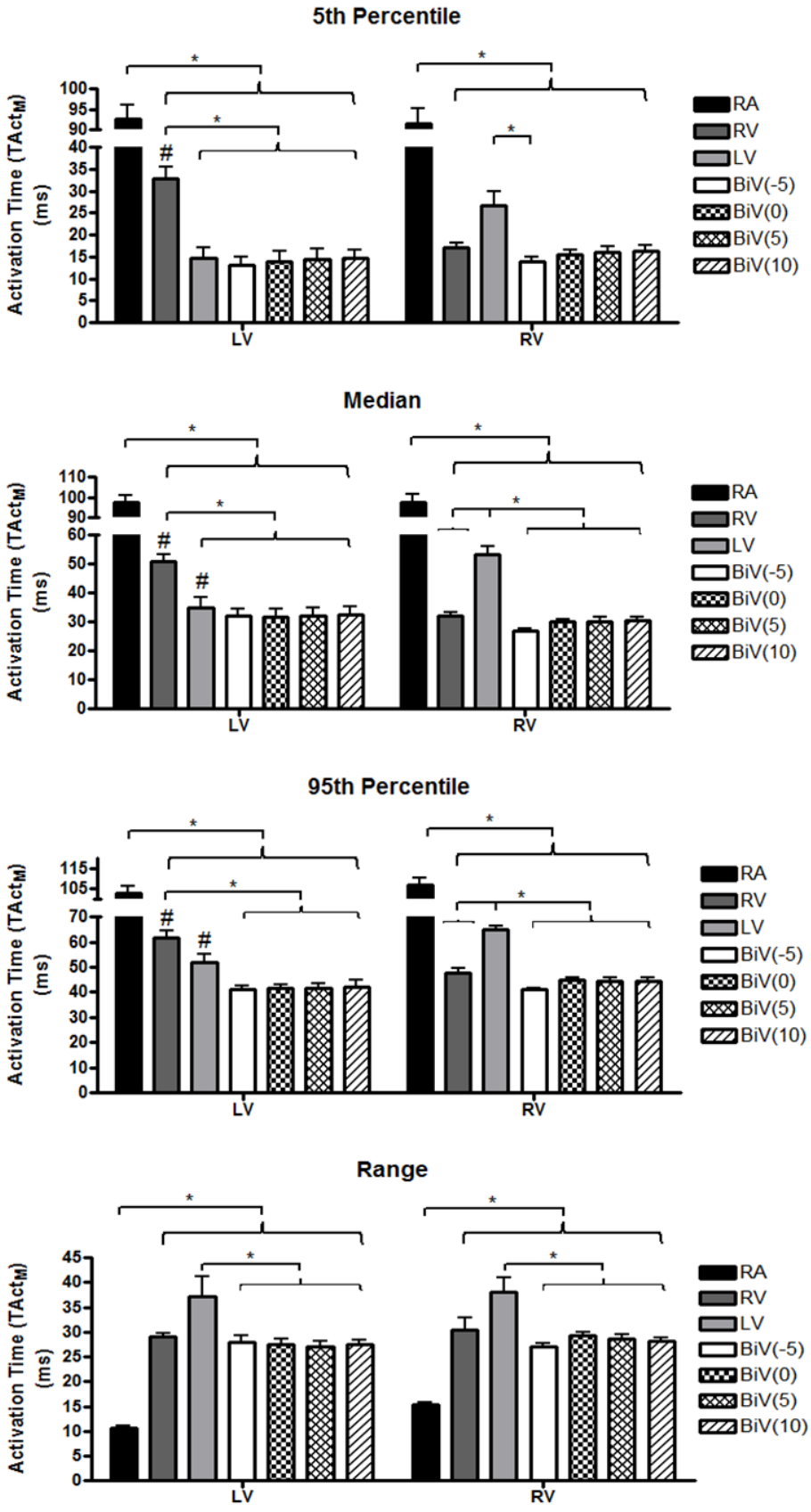


**Figure 5.23 Plots of activation time for each pacing regime (MI heart)**

**5$^{th}$ Percentile, Median, 95$^{th}$ Percentile and Range of values for activation time (where data is displayed as mean ± SE (n=4)). An * indicates a significant difference between pacing regimes. A # indicates significant difference between marked pacing on the LV and it's counterpart in the RV.**

**Table 5.10 Statistics for activation time for each pacing regime (MI heart) (where data is displayed in mean ± SE (n=4)).**

| | | RA | RV | LV | BiV(-5) | BiV(0) | BiV(5) | BiV(10) |
|---|---|---|---|---|---|---|---|---|
| Median | LV | 97.3±3.5 | 50.8±2.4 | 35.0±3.5 | 32.0±2.7 | 31.8±2.7 | 32.3±2.8 | 32.5±2.9 |
| | RV | 97.5±3.9 | 32.0±1.1 | 53.3±2.8 | 27.0±0.6 | 30.0±0.7 | 30.3±1.3 | 30.5±1.2 |
| Min | LV | 92.5±3.4 | 32.8±2.8 | 14.8±2.4 | 13.0±2.1 | 14.0±2.2 | 14.5±2.2 | 14.8±1.7 |
| | RV | 91.5±3.8 | 17.0±1.2 | 26.8±3.2 | 14.0±1.1 | 15.5±1.2 | 16.0±1.4 | 16.3±1.4 |
| Max | LV | 103.0±3.2 | 61.8±3.0 | 52.0±3.3 | 41.0±1.7 | 41.5±1.7 | 41.5±1.8 | 42.2±2.6 |
| | RV | 106.8±3.4 | 47.5±2.2 | 64.8±1.7 | 41.0±0.9 | 44.8±0.9 | 44.5±1.3 | 44.5±1.3 |
| Range | LV | 10.5±0.5 | 29.0±0.7 | 37.3±2.8 | 28.0±1.1 | 27.5±1.2 | 27.0±1.2 | 27.4±1.0 |
| | RV | 15.3±0.6 | 30.5±2.4 | 38.0±2.9 | 27.0±0.8 | 29.3±0.8 | 28.5±1.0 | 28.3±0.5 |

### Action potential duration

Similarly, to the control group, the range and distribution of APD times were comparable between LV and RV during RA pacing (Figure 5.24), as summarised in Table 5.11. However, there was increased heterogeneity in the overall range of APD times between hearts, evidenced by the increase in standard deviation (SD) (control group: 1.6 (LV) and 4.8 (RV), MI group: 6.6 (LV) and 7.8 (RV)). In addition, there was a significant increase in the range of APD times across the LV in the MI group (29.3 ± 3.3) in comparison to the control group (20.8 ± 0.8) ($P<0.05$), but not across the RV (where values are displayed as mean ± SE, in ms).

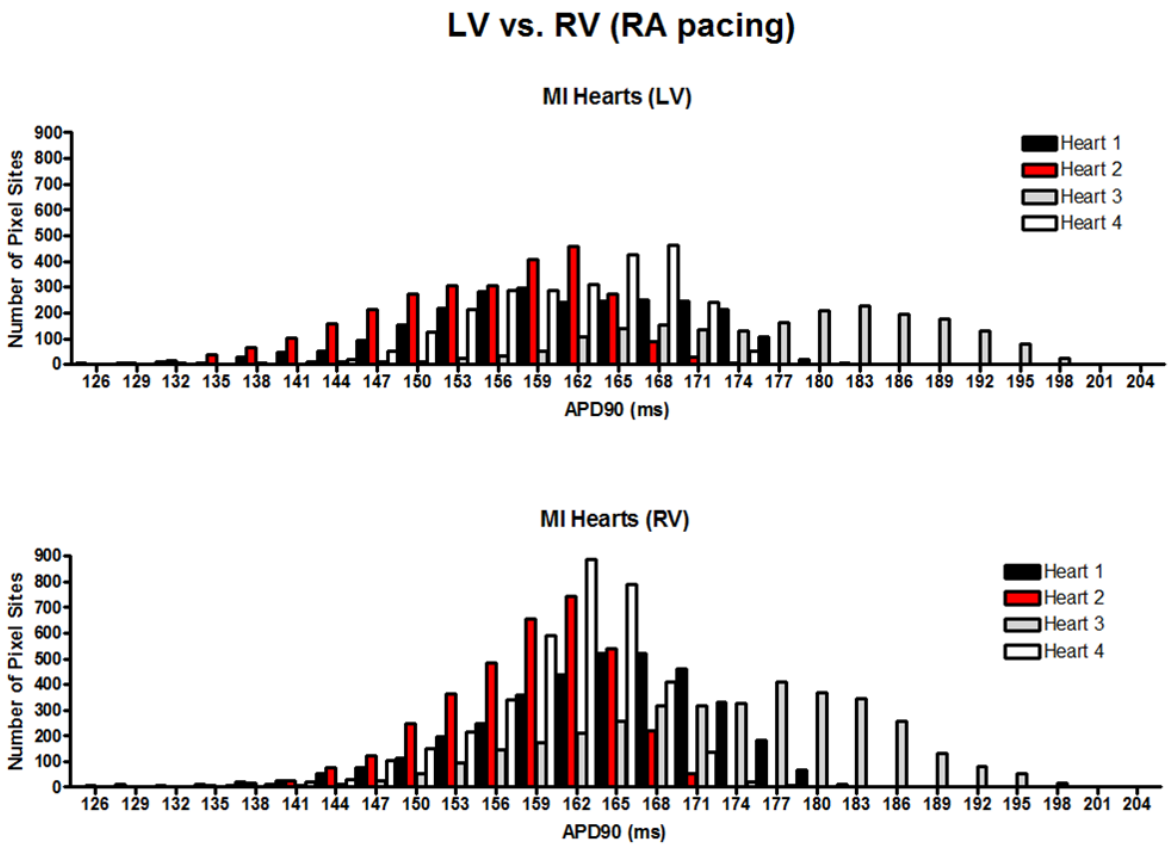


**Figure 5.24 Distribution of APD (LV and RV) for each MI heart**

**Table 5.11 Statistics for the APD of LV and RV of each MI heart during RA pacing**

| APD90 | Heart 1 | Heart 2 | Heart 3 | Heart 4 |
|---|---|---|---|---|
| **LV** | | | | |
| Median | 161.0 | 156.0 | 179.0 | 163.0 |
| 5th Percentile | 143.0 | 140.0 | 157.0 | 150.0 |
| 95th Percentile | 176.0 | 166.0 | 194.0 | 171.0 |
| Range | 33.0 | 26.0 | 37.0 | 21.0 |
| **RV** | | | | |
| Median | 165.0 | 160.0 | 174.0 | 162.0 |
| 5th Percentile | 147.0 | 147.0 | 154.0 | 149.0 |
| 95th Percentile | 177.0 | 167.0 | 190.0 | 169.0 |
| Range | 30.0 | 20.0 | 36.0 | 20.0 |

There was no significant change in the overall distribution of APD times (LV and RV) between any of the pacing regimes, the same as the control group (Figure 5.25). However, there was a very small shift in APD times when comparing RA pacing to all other forms of pacing, where this difference was not found to be significant ($P>0.05$, Kolmogorov-Smirnov test). This finding is reflected in the corresponding contour maps of APD (Figure 5.26), which showed minimal changes in the pattern of APD across both the LV and RV and the presence of a shift in APD.

On average, there was no change in the range of APD times (LV and RV) for any of the pacing sequences (Figure 5.27), as summarised in Table 5.12. MI group displayed a significant increase in the range of APD across the LV for all forms of pacing (RA: $P<0.05$; RV, LV, BiV(-5), BiV(0), BiV(5), BiV(10): $P<0.01$) when compared to control group. Though there was an increase in the range of APD across the RV when comparing the MI group to the control group, these findings were not statistically significant ($P>0.05$). Multiple comparisons were performed using a two-way ANOVA followed by a Tukey-Kramer post-test allowing for multiple comparisons where appropriate.

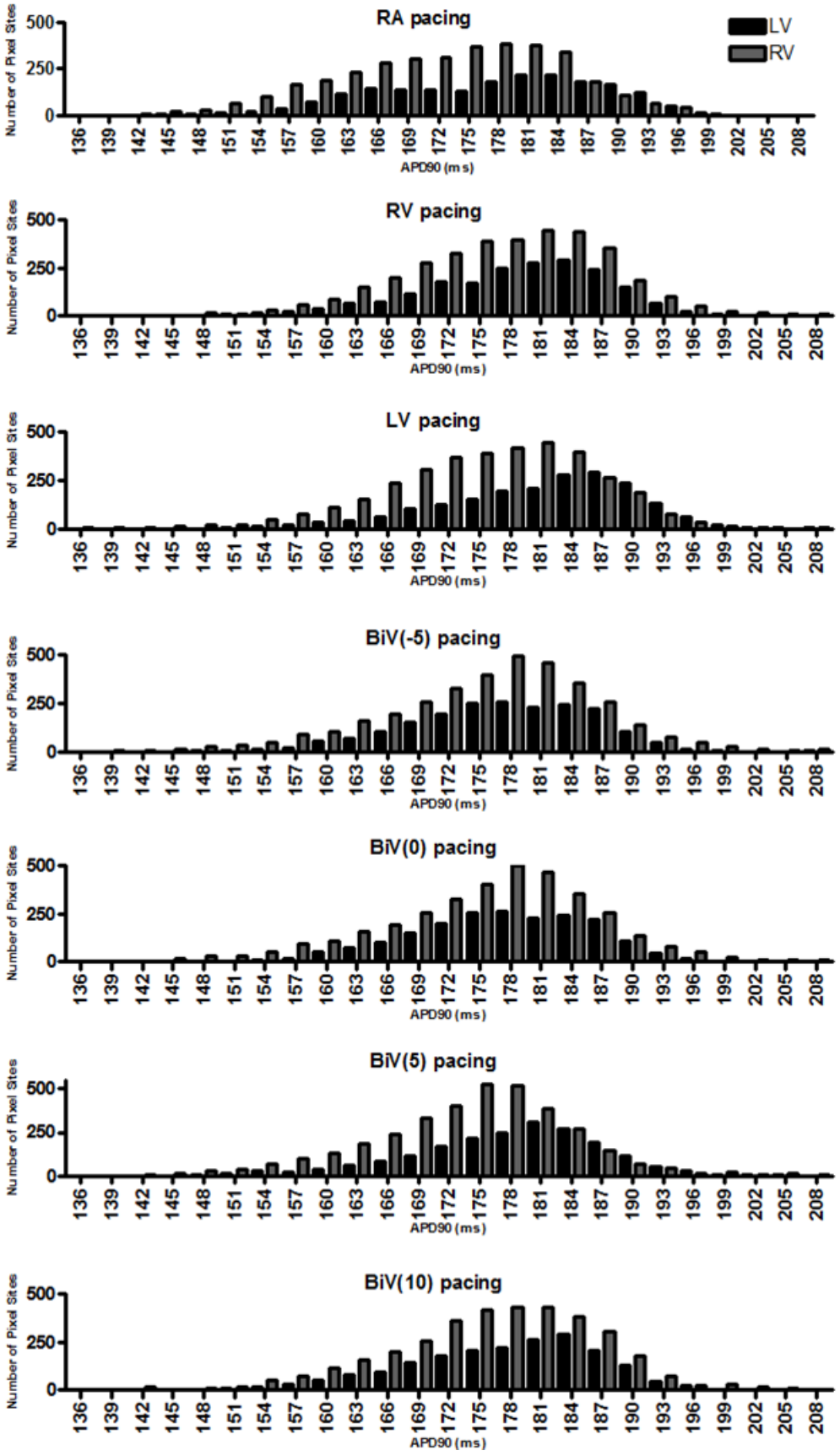


**Figure 5.25 Example of distribution of APD for each pacing regime (MI heart)**

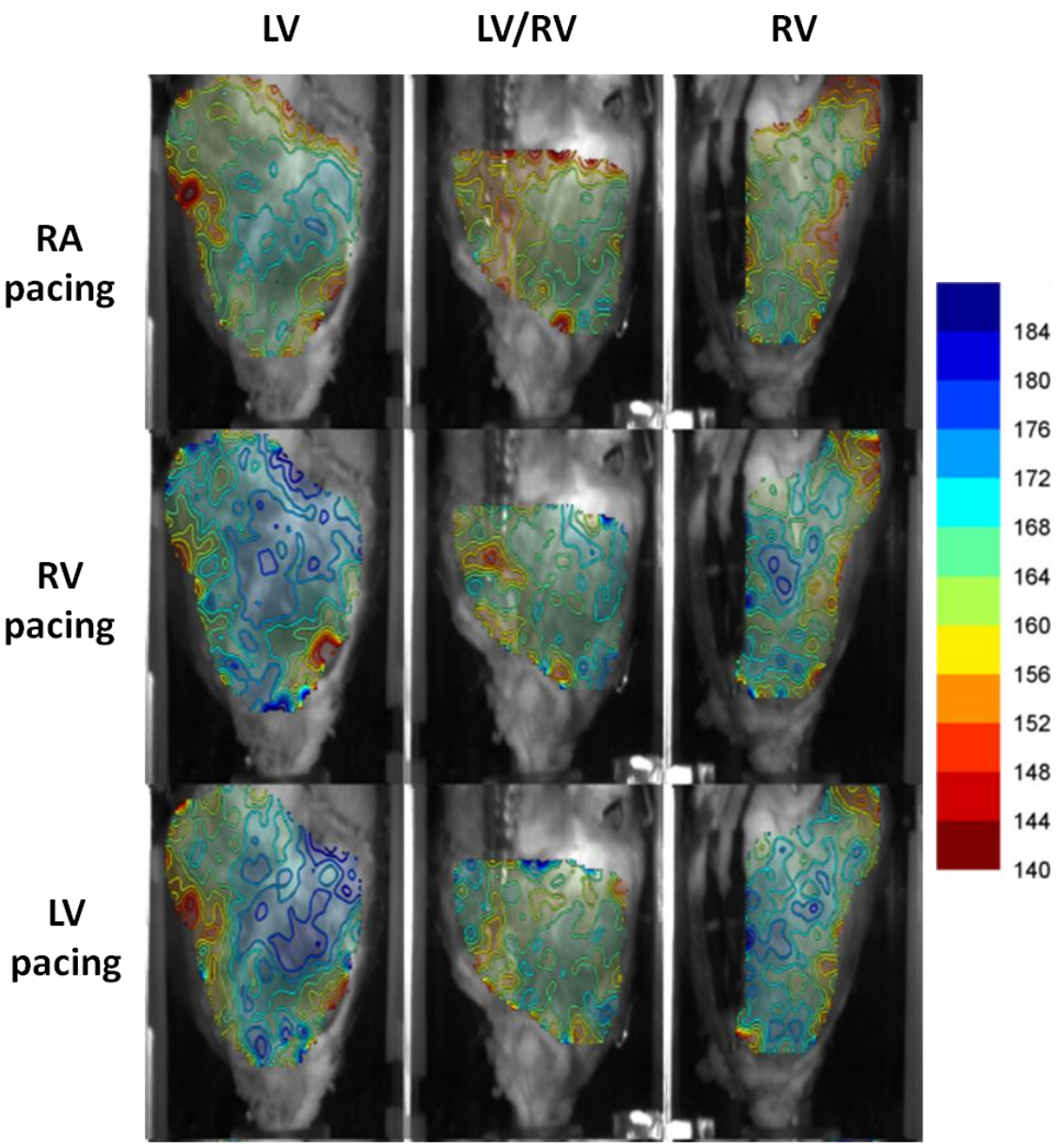
LV
LV/RV
RV
RA pacing
RV pacing
LV pacing
184
180
176
172
168
164
160
156
152
148
144
140

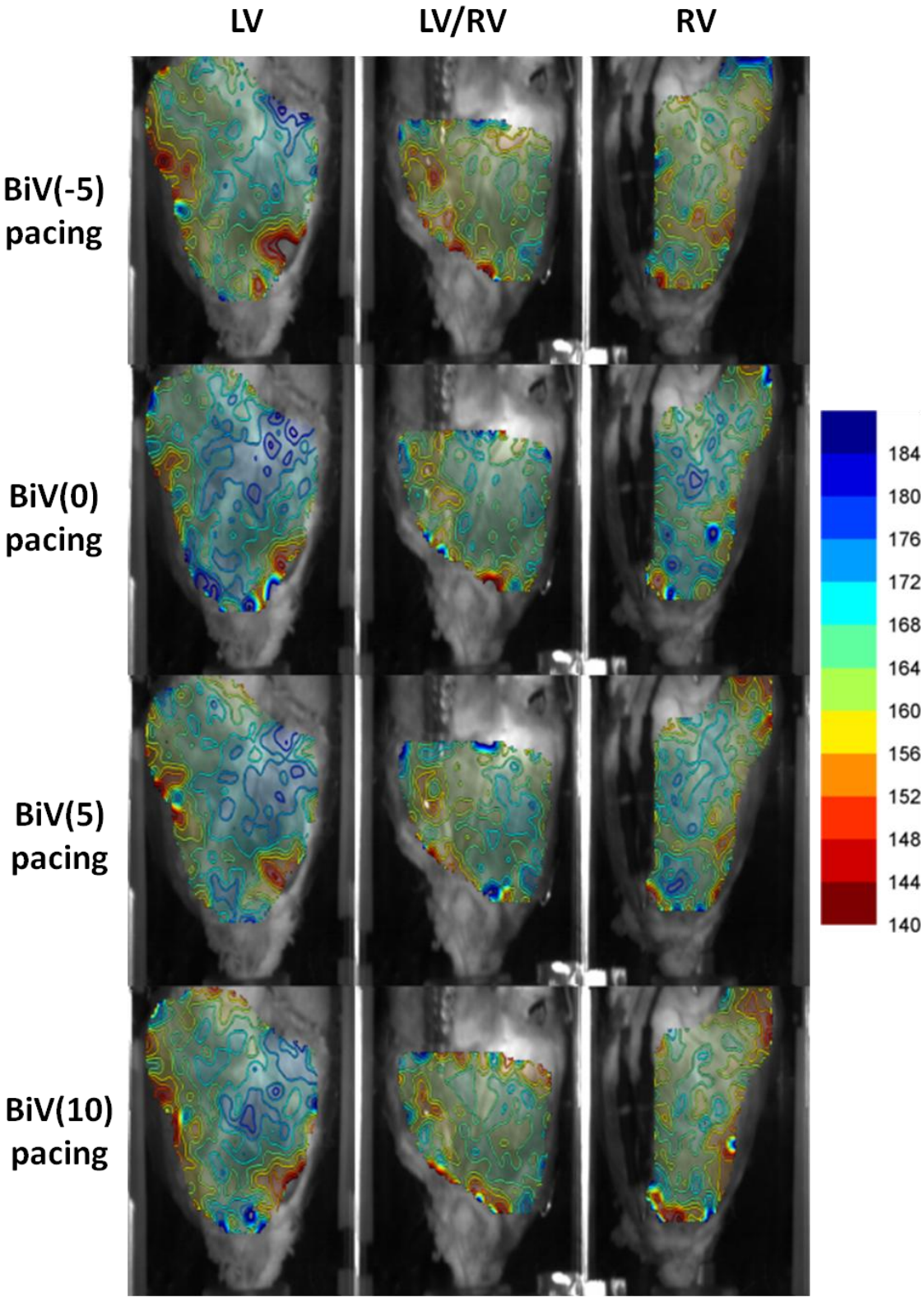


**Figure 5.26 Contour maps of APD for each pacing regime (MI heart)**

**Typical isochronal contour maps of action potential duration for each pacing regime from the three views of the MI heart (LV, LV/RV and RV) [heart-4]. Times are in ms.**

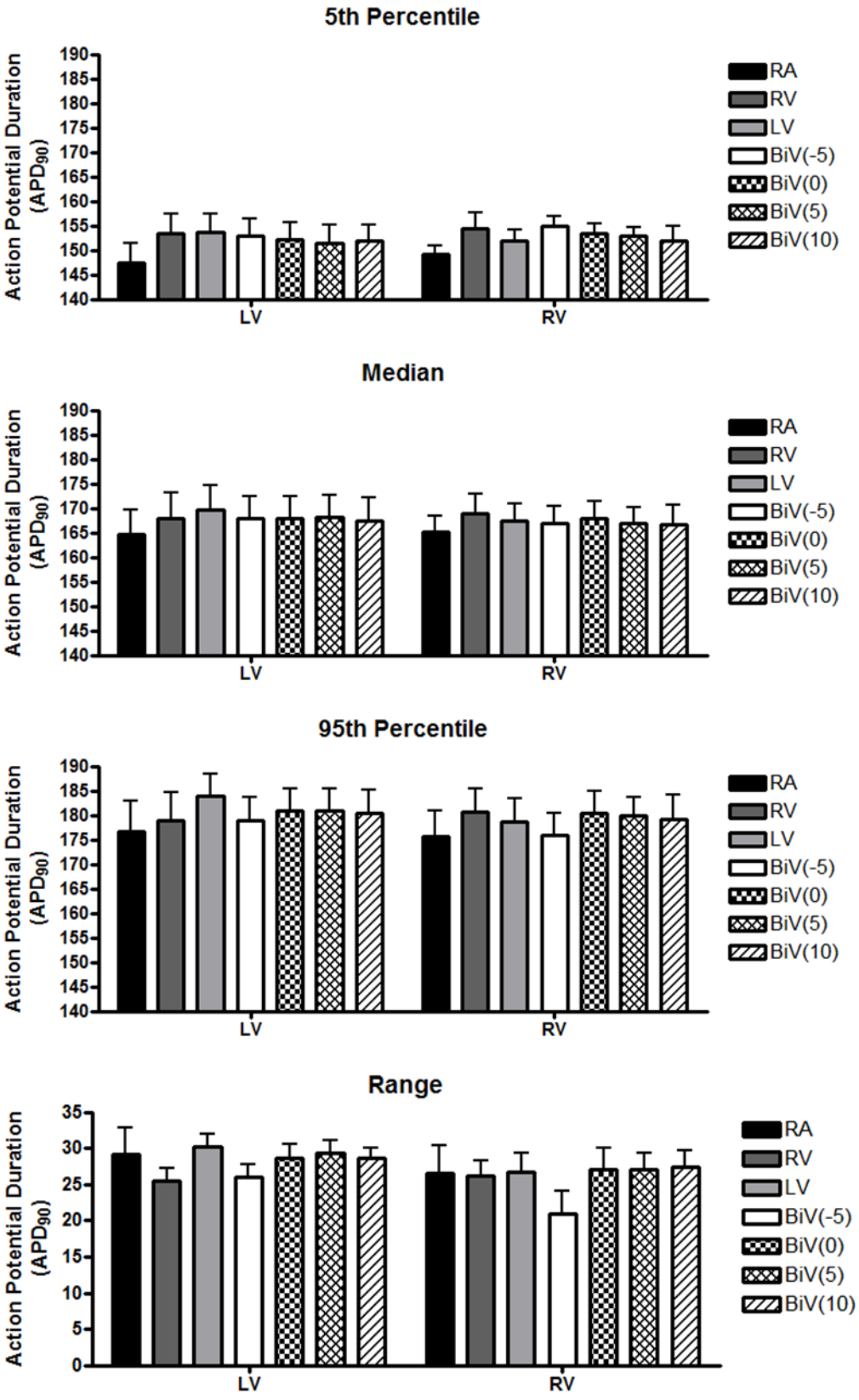


**Figure 5.27 Plots of APD for each pacing regime (MI heart)**

**5th Percentile, Median, 95th Percentile and Range of values for action potential (where data is displayed as mean ± SE (n=4)). An * indicates a significant difference between pacing regimes. A # indicates significant difference between marked pacing on the LV and it's counterpart in the RV.**

**Table 5.12 Statistics for APD for each pacing regime (MI heart) (where data is displayed in mean ± SE (n=4)).**

| | | RA | RV | LV | BiV(-5) | BiV(0) | BiV(5) | BiV(10) |
|---|---|---|---|---|---|---|---|---|
| Median | LV | 164.8±5 | 168.0±5.1 | 169.8±5.0 | 168.0±4.2 | 168.0±4.3 | 168.3±4.5 | 167.5±4.6 |
| | RV | 165.3±3.1 | 169.0±3.9 | 167.5±3.5 | 167.0±3.2 | 168.0±3.5 | 167.0±3.1 | 166.8±4.0 |
| Min | LV | 147.5±3.8 | 153.5±4.0 | 153.6±3.9 | 153.0±3.1 | 152.3±3.3 | 151.5±3.7 | 151.9±3.3 |
| | RV | 149.3±1.7 | 154.5±3.2 | 152.0±2.3 | 155.0±2.1 | 153.5±2.0 | 153.0±1.6 | 151.9±3.1 |
| Max | LV | 176.8±6.1 | 179.0±5.6 | 183.8±4.6 | 179.0±4.5 | 180.9±4.6 | 180.8±4.6 | 180.5±4.7 |
| | RV | 175.8±5.2 | 180.8±4.8 | 178.8±4.7 | 176.0±3.8 | 180.5±4.4 | 180.0±3.7 | 179.3±4.9 |
| Range | LV | 29.3±3.3 | 25.5±1.7 | 30.3±1.7 | 26.0±1.7 | 28.7±1.8 | 29.3±1.7 | 28.6±1.5 |
| | RV | 26.5±3.9 | 26.3±2.1 | 26.8±2.6 | 21.0±2.7 | 27.0±3.0 | 27.0±2.4 | 27.4±2.3 |

As was seen in the control group, an inverse relationship emerged between APD and activation time during RA pacing (Figure 5.28). Within the MI group, there was a mean slope of -0.95 and -1.52 ($R^2$ = 0.34 and $R^2$ = 0.47) for the LV and RV, respectively, where the data is summarised in Table 5.13. In contrast to the control group, this association manifested as longer APD times purely at mid-myocardium corresponding to earlier activation times, with shorter APD times at the apex and base of the LV corresponding generally with later activation times, as shown in Figure 5.28. However, the same apex-base relationship remained on the RV, as described previously for the control group.

During any of the alternative forms of pacing, there was a shallower relationship between APD and activation time with a poor correlation between the two parameters, as shown for LV pacing in Figure 5.28. The mean slope of this relationship was -0.35 and -0.5 ($R^2$ = 0.18 and $R^2$ = 0.15) for the LV and RV, respectively, where the data is summarised in Table 5.13. Similar to the control group, the MI group showed a comparable reduction in slope when alternative pacing's to RA pacing were employed. Again, there was no effect of ventricle (LV or RV) on the variation in slope observed, with the majority of variation determined by the mode of pacing.

A spatial gradient of APD formed between the mid-myocardium and the apex and base of the LV (Figure 5.29). The LV presented with longer APD times on the mid-myocardium, shorter APD times on the apex and even shorter APD times on the base. There were no significant differences between any of the pacing regimes, comparable with the control group.

## Relationship between APD and activation time

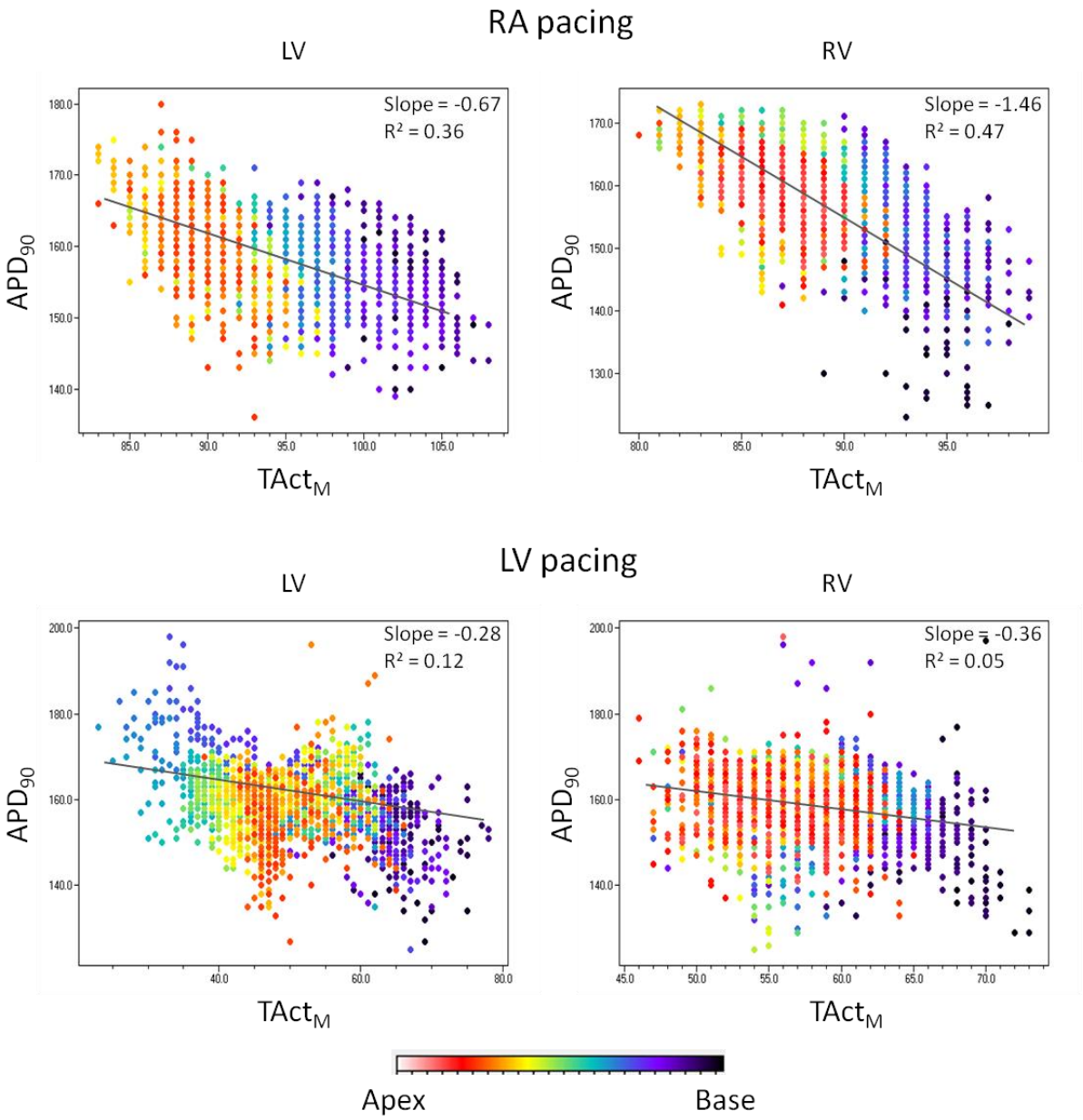


**Figure 5.28 Inverse relationship ($APD_{90}$ – $TAct_M$) (MI heart)**

**An example scatter plot showing the typical inverse relationship between action potential duration against activation time ($TAct_M$) for the LV and RV.**

**Table 5.13 Mean relationship between APD and activation time (MI heart)**

| MI Group (n=4) | | RA pacing | LV pacing | P-value |
|---|---|---|---|---|
| LV | Slope | -0.95±0.16 | -0.35±0.05 | <0.05 |
| | $R^2$ | 0.34±0.05 | 0.18±0.05 | 0.18 |
| RV | Slope | -1.52±0.21 | -0.5±0.22 | <0.05 |
| | $R^2$ | 0.47±0.1 | 0.15±0.07 | 0.07 |

**Relationship between APD and epicardial position**

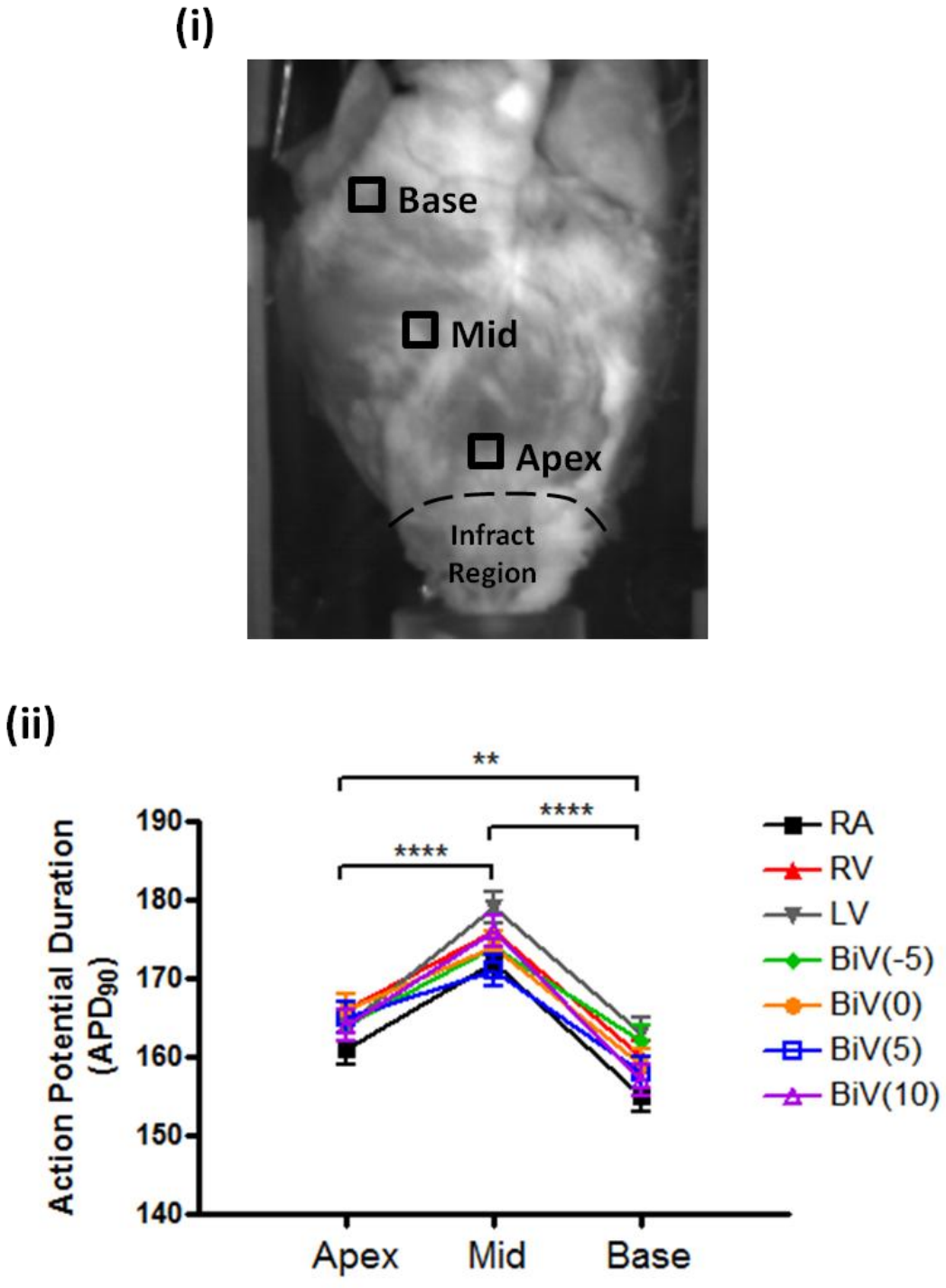


**Figure 5.29 Relationship between APD and epicardial position (MI heart)**

**(i) View of the LV epicardial surface with optical AP sampling regions for each epicardial position (apex, mid and base) and depiction of apical infarct region.**

**(ii) Plot of action potential duration against epicardial position for each form of pacing (**P<0.01 and ****P<0.0001).**

### Repolarisation

Similar to the control group, there was a range of repolarisation times across both the LV and RV for RA pacing that varied from heart to heart (Figure 5.30), as summarised in Table 5.14. Conversely, there was a significant increase in the range of repolarisation times across both the LV and RV in the MI group (23.0 ± 2.2 (LV), 24.0 ± 2.2 (RV)) in comparison to the control group (14.0 ± 1.6 (LV), 14.8 ± 2.3 (RV)) ($P<0.05$).

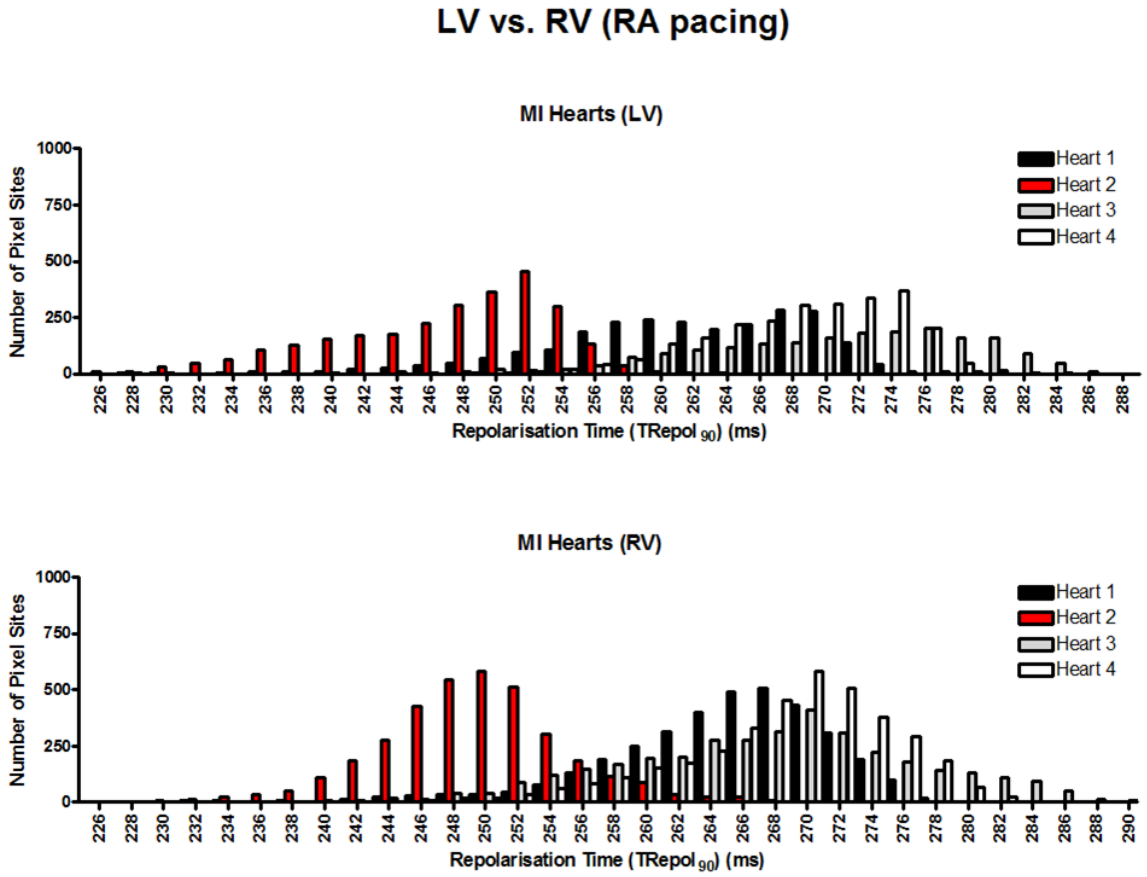


**Figure 5.30 Distribution of repolarisation times (LV and RV) for each MI heart**

**Table 5.14 Statistics for repolarisation times of LV and RV of each MI heart during RA pacing**

| TRepol90 | Heart 1 | Heart 2 | Heart 3 | Heart 4 |
|---|---|---|---|---|
| **LV** | | | | |
| Median | 262.0 | 248.0 | 271.0 | 269.0 |
| 5th Percentile | 246.0 | 234.0 | 254.0 | 258.0 |
| 95th Percentile | 271.0 | 255.0 | 282.0 | 276.0 |
| Range | 25.0 | 21.0 | 28.0 | 18.0 |
| **RV** | | | | |
| Median | 265.0 | 249.0 | 268.0 | 269.0 |
| 5th Percentile | 250.0 | 239.0 | 252.0 | 255.0 |
| 95th Percentile | 274.0 | 259.0 | 282.0 | 277.0 |
| Range | 24.0 | 20.0 | 30.0 | 22.0 |

A concordance between the activation and repolarisation sequence existed in the MI group, similar to that seen in the control group. When considering the distributions of repolarisation times, a marked division in distributions for LV and RV pacing was present, in comparison to RA pacing, where this division was heightened during LV pacing (Figure 5.31).

Similar to the activation sequence, the distribution of repolarisation times were independent of pacing offset for all forms of BiV pacing, where BiV pacing repolarisation distributions were comparable to RA pacing.

In general, the spatial pattern of repolarisation followed the activation sequence with areas of earliest activation corresponding to areas of earliest repolarisation and vice versa (Figure 5.32). This phenomenon was present for all forms of pacing.

On average, the range of repolarisation times (LV and RV) were significantly increased when using any of the ventricular pacing regimes as compared to RA pacing (Figure 5.33), as summarised in Table 5.15. However, BiV pacing regimes showed a reduced range of repolarisation times in comparison to single LV and

RV pacing, though this difference was not statistically significant. These findings were all in concordance with activation time.

MI group displayed a significant increase in the range of repolarisation times across the LV and RV for all forms of pacing, except RV pacing (RA, LV, BiV (-5), BiV (0), BiV (5) and BiV (10) pacing: $P<0.05$) when compared to control group. Although there was an increase in the range of repolarisation times across the LV and RV during RV pacing, this difference was not found to be statistically significant.

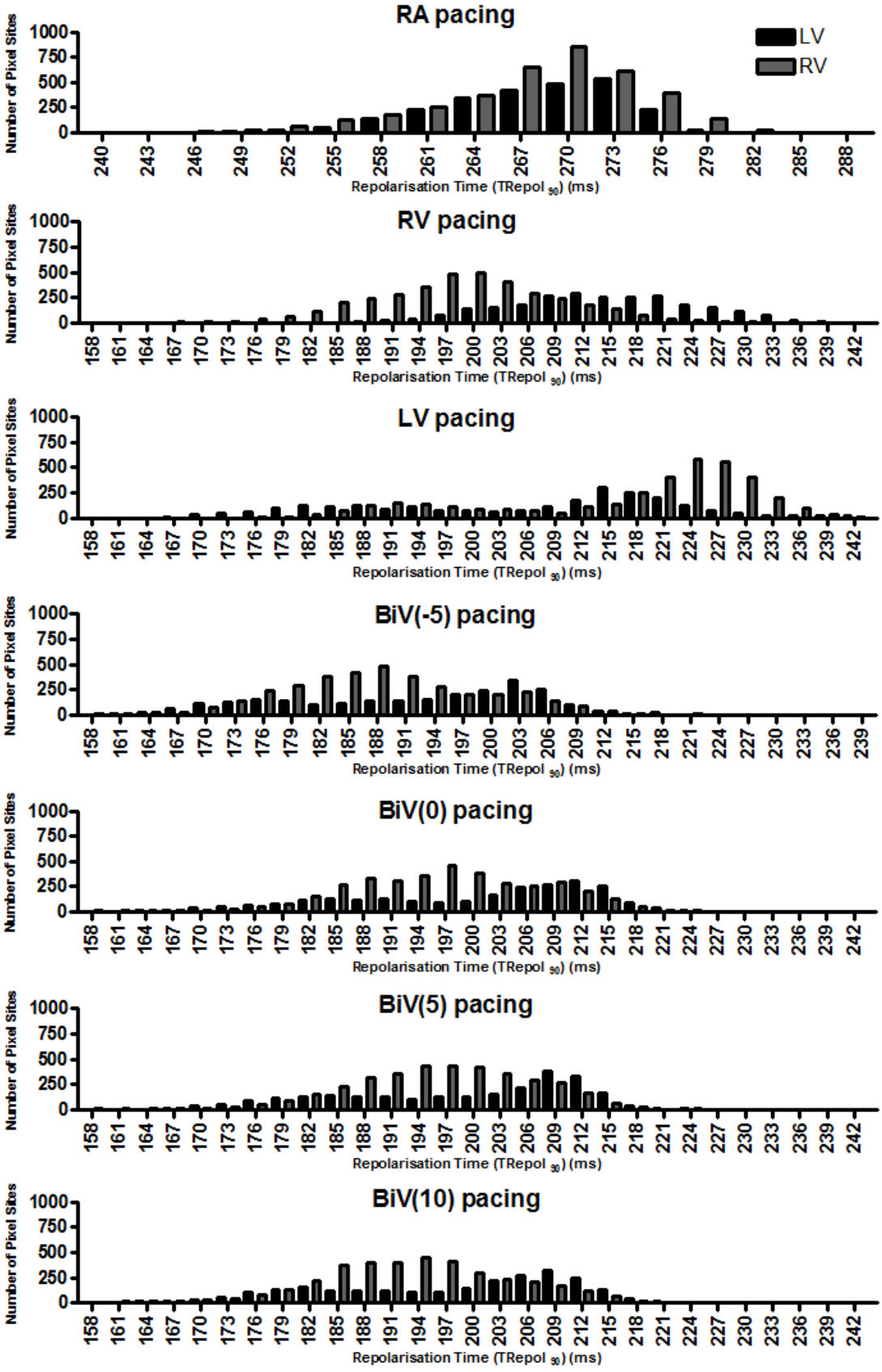


**Figure 5.31 Example of distribution of repolarisation times for each pacing regime (MI heart)**

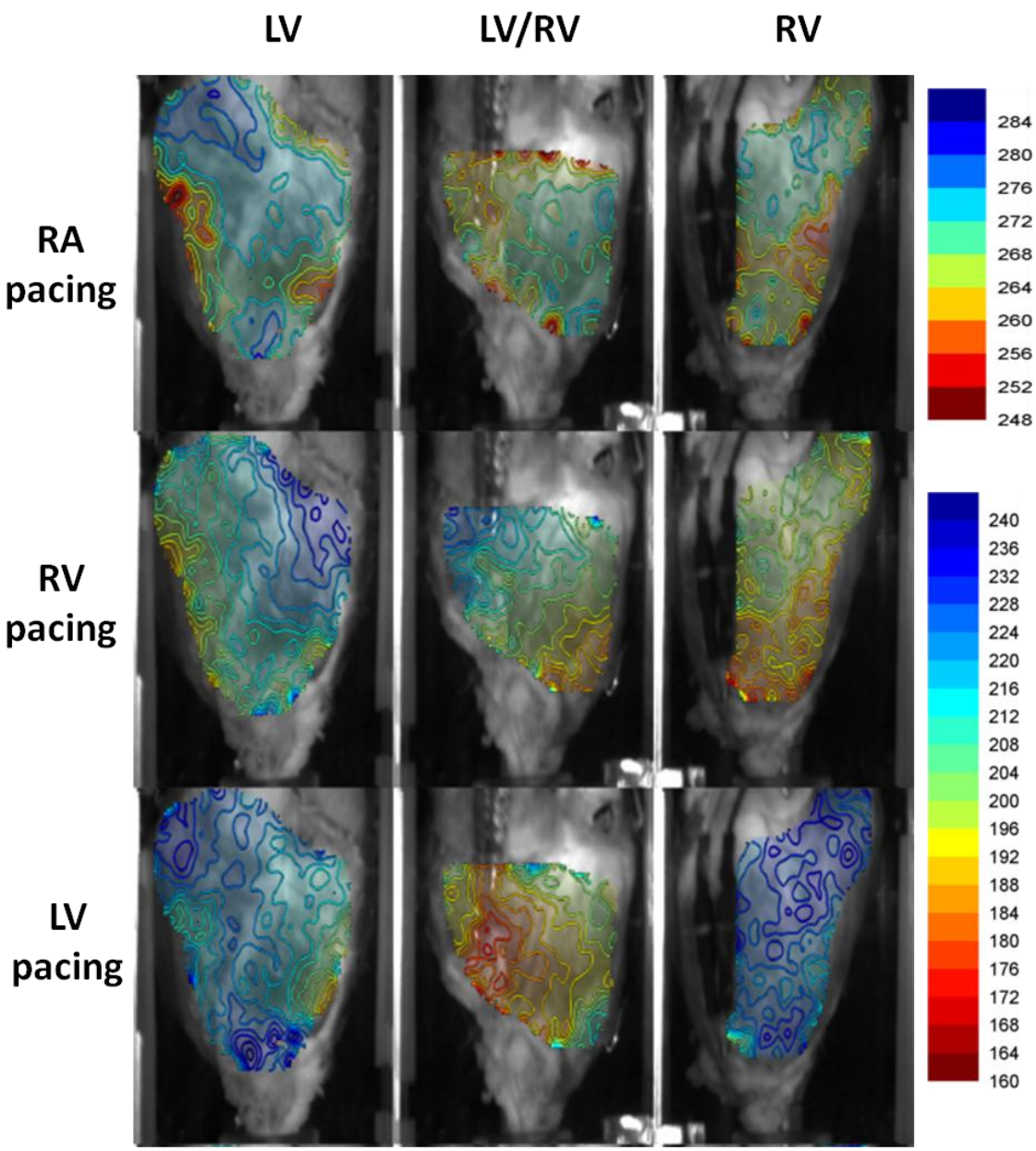
LV
LV/RV
RV
RA pacing
RV pacing
LV pacing
284
280
276
272
268
264
260
256
252
248
240
236
232
228
224
220
216
212
208
204
200
196
192
188
184
180
176
172
168
164
160

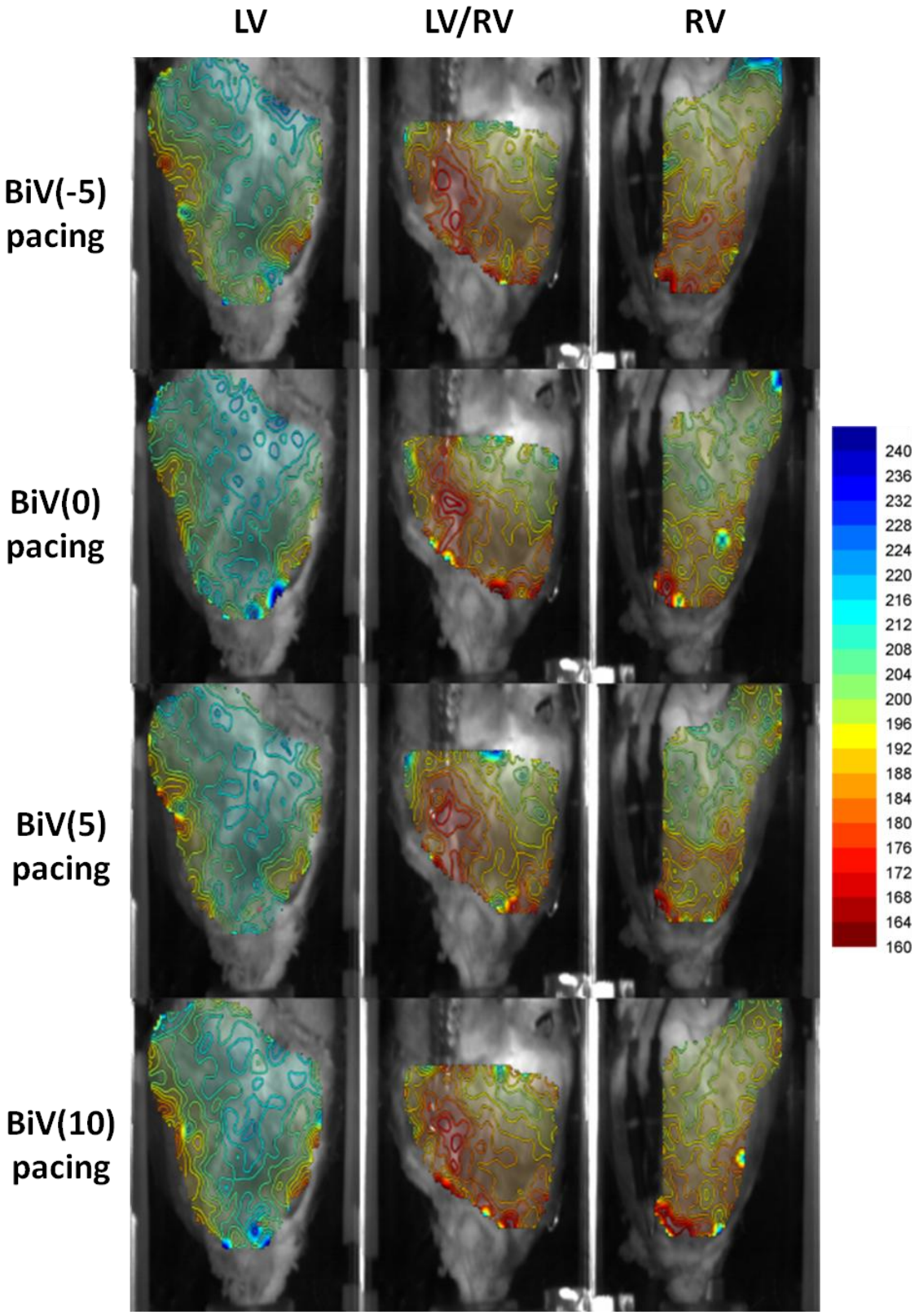


**Figure 5.32 Contour maps of repolarisation time for each pacing regime (MI heart)**

**Typical isochronal contour maps of repolarisation time for each pacing regime from the three views of the MI heart (LV, LV/RV and RV) [heart-4]. Times are in ms.**

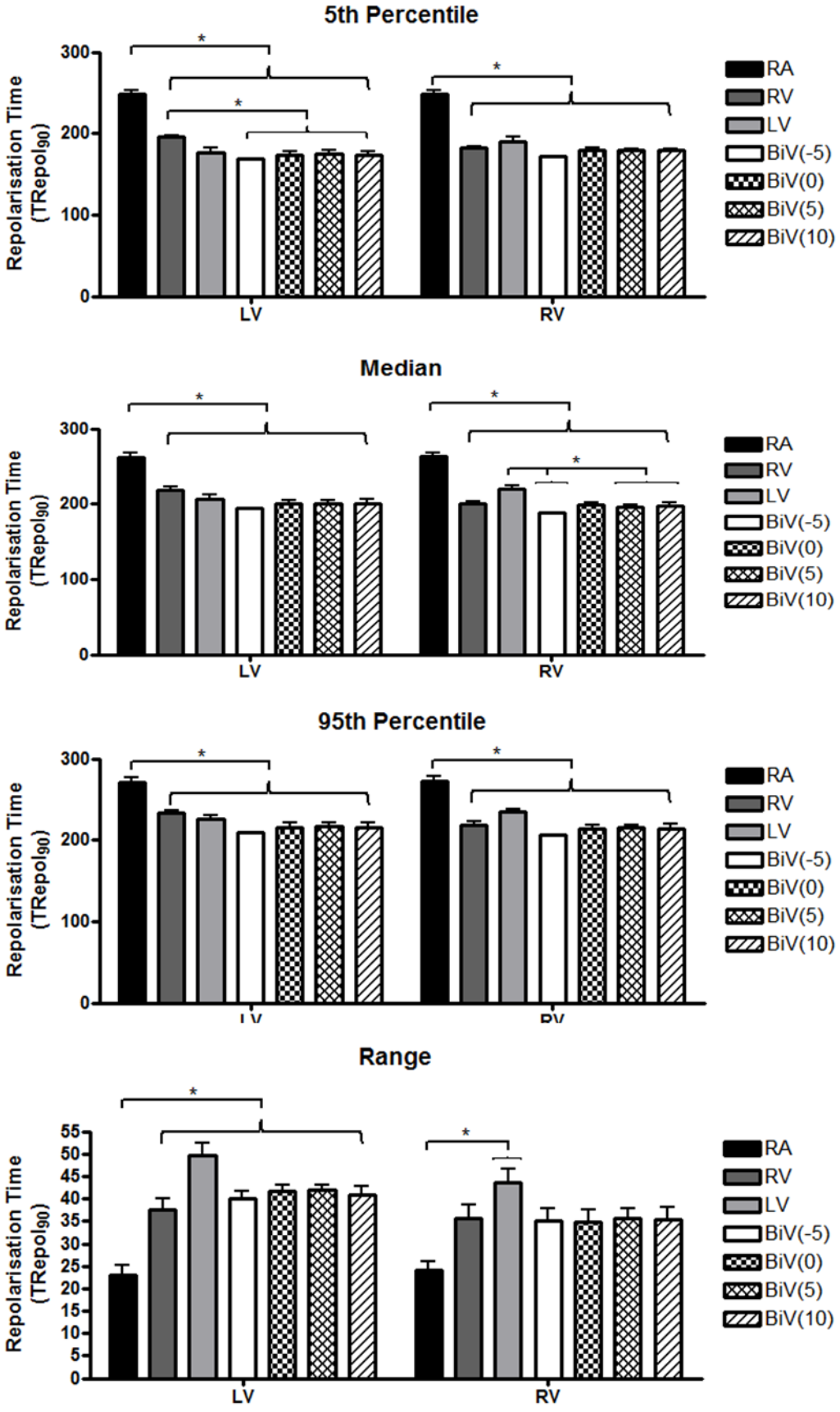


**Figure 5.33 Plots of repolarisation time for each pacing regime (MI heart)**

**5th Percentile, Median, 95th Percentile and Range of values for repolarisation time (where data is displayed as mean ± SE (n=4)). An * indicates a significant difference between pacing regimes. A # indicates significant difference between marked pacing on the LV and it's counterpart in the RV.**

**Table 5.15 Statistics for repolarisation time for each pacing regime (MI heart) (where data is displayed in mean ± SE (n=4)).**

| | | RA | RV | LV | BiV(-5) | BiV(0) | BiV(5) | BiV(10) |
|---|---|---|---|---|---|---|---|---|
| Median | LV | 262.5±5.2 | 218.8±3.8 | 207±5 | 195±5.1 | 200±5.1 | 200.4±5.2 | 201±5.4 |
| | RV | 262.8±4.7 | 200.5±3.1 | 220.5±4.6 | 188±3.1 | 198.5±3.1 | 196.5±2.7 | 197.5±4 |
| Min | LV | 248±5.3 | 195.6±1.3 | 176.3±5.9 | 169±4.3 | 174.2±4.3 | 174.3±5 | 174±4.1 |
| | RV | 249±3.5 | 182.5±1.7 | 190.7±4.9 | 172±1.8 | 180±1.8 | 179.5±1.7 | 178.8±2.5 |
| Max | LV | 271±5.8 | 233.3±2.8 | 226±4.3 | 209±5.5 | 215.8±5.5 | 216.3±5.1 | 214.9±5.9 |
| | RV | 273±4.9 | 218.3±4.4 | 234.3±3.3 | 207±4.4 | 214.7±4.4 | 215.3±3.4 | 214.3±5.2 |
| Range | LV | 23±2.2 | 37.7±2.4 | 49.8±2.7 | 40±1.6 | 41.6±1.6 | 42±1.2 | 40.9±1.9 |
| | RV | 24±2.2 | 35.8±2.8 | 43.5±3.2 | 35±2.9 | 34.7±2.9 | 35.8±2.1 | 35.5±2.7 |

# Discussion

Following the results of Chapter 3, the study described in this chapter investigates the relationship between activation time and APD further using several pacing regimens applied to normal hearts and hearts with an apical infarct. The effects of various forms of ventricular pacing procedures (RV, LV, BiV(-5), BiV(0), BiV(5), BiV(10)) were studied in both the normal rabbit heart (control group) and a rabbit model of chronic MI (MI group).

## A-V nodal conduction

In agreement with Chapter 3, there were significant differences in the time at which electrical epicardial breakthrough occurred (earliest activation time) across both the LV and RV when comparing individual hearts. This phenomenon was present across both the control and the MI group. For further details see Chapter 3.

## Effects of activation sequence on APD and repolarisation in the control group

An inverse relationship emerged between APD and activation time, which occurred only during RA pacing, as observed previously in Chapter 3. This relationship has been attributed to electrotonic interactions between neighbouring cells where it has been previously observed during physiological activation sequences. Electrotonic effects will tend to make repolarisation times more uniform across the heart. In both humans and canines, APD and activation times have been measured via unipolar and bipolar electrograms and shown a strong inverse linear relationship across both the epicardial and endocardial surfaces during sinus rhythm (Yuan et al., 2001; Franz et al., 1987; Chauhan et al., 2006; Hanson et al., 2009; Yue et al., 2005; Toyoshima and Burgess, 1978; Furukawa et al., 2000; Laurita et al., 1996). However, few studies have quantified the effects of alternative forms of pacing on this relationship and the overall dispersion of repolarisation. Therefore, this study investigates the effect of different activation sequences on this relationship and the outcome on the dispersion of repolarisation.

In this study, the strong inverse relationship between APD and activation time during RA pacing diminishes during any form of ventricular pacing (Figure 5.14). When comparing spatial differences in APD times across pacing regimes, there was a clear gradient from the longest APD times at the mid-ventricular and apex regions to the shortest APD times at the base (Figure 5.15). This APD gradient was maintained across all forms of pacing. This suggests that, regardless of the acute activation wavefront the intrinsic repolarisation characteristics of the cells is the dominant feature in the distribution of APD times across the epicardial surface, with electrotonic interactions having reduced influence on the overall dispersion of APD times over a short time scale. The apparent correlation between activation time and APD seen during RA pacing therefore is not a consequence of instantaneous electrotonic influences on myocyte electrophysiology as seen in previous studies on rabbit transmural electrophysiology (Myles et al., 2010). One possibility is that the relation seen during RA pacing shows a correlation due to longer-term influences of activation pattern on myocyte electrophysiology as suggested by the studies of (Costard-Jäckle et al., 1989).

This finding is supported by a computational study of the rabbit heart where they tested various pacing sites across the epicardial surface and found that intrinsic cellular heterogeneity had a greater impact on the dispersion of APD, regardless of the activation sequence (Sampson and Henriquez, 2005). Similar findings have been observed in both experimental and computational studies of swine hearts, where spatial distributions of APD were poorly associated with activation sequence for different pacing locations (Liang et al., 2005; Kongstad et al., 2002; Lacroix et al., 1999; Walton et al., 2013). Sampson's computational study predicted that the shape of the cardiac AP would play an important role in the influence of electrotonic interactions (Sampson and Henriquez, 2005). In rabbit, the cardiac AP has a dominant plateau phase morphology, similar to swine, such that sites that are activated early in the sequence will remain in a relatively depolarised state long after activation. Consequently, this suggests that electrotonic modulation of APD would be mitigated in rabbit hearts due to the reduction in the spatial gradient of transmembrane potential during the repolarisation phase.

In contrast, in an experimental study of rat heart a strong correlation between activation sequence and APD for different pacing sites was shown (Walton and Bernus, 2009). Similarly, in a computational study of murine hearts, the influence of electrotonic currents was a dominant feature in the modulation of APD (Sampson and Henriquez, 2005). Murine and rat hearts have a reduced overall tissue geometry compared with larger mammals and more importantly, they lack an AP with a plateau phase, exhibiting a triangular AP morphology. Both these factors could give rise to greater transmembrane potential gradients for the whole repolarisation phase and generate stronger correlations between APD and activation time mediated by electrotonic modulation.

In rabbit wedge preparations in the transmural plane, a shortening of APD was observed as the distance from the site of activation increased during both endocardial and epicardial stimulation protocols (Myles et al., 2010). In this study, electrotonic modulation of APD dominated over intrinsic cellular differences in the transmural plane. This may be because of the short conduction pathway and reduced coupling resistance in the transmural plane, as well as the proximity to the pacing site, consistent with a previous study showing that electrotonic modulation effects were greatest nearest the site of stimulation (Zubair et al., 1994).

## Comparison of short to long term effects of activation sequence on APD

An important consideration from these findings is the time period of stimulation. In a previous study within rabbit hearts, the same loss of inverse relationship between APD and activation time occurred when reverting from RA pacing to ventricular pacing for a short period (~5 minutes) (Costard-Jäckle et al., 1989). However, the same study shows that after an extended period of the same pacing (~120 minutes) there is a return of a strong inverse relationship, seen as a slow adaptation in APD to the change in activation sequence. Considering the observations of both the current study and those of Costard-Jackle et al. would suggest that the myocardium undergoes a form of electrical remodelling through electrical stimulation whereby there is a slow response and adaptation of APD over ~120mins. The observations of the current study are at variance with the existing literature, which suggests that the spatial and temporal distribution of

APD within the myocardium is the result of interplay between intrinsic cellular properties and electrotonic interactions, which can occur instantaneously. Furthermore, electrotonic interactions are a passive electrical phenomenon, which occurs over a short time course (<1s) in comparison to the long time course (over hours) of the changes seen in APD by Costard-Jäckle et al. This suggests that there is an alternative intracellular mechanism that is modulating APD via the activation sequence over an extended time interval, such that the cells are able to sense the change in activation sequence. This has been alluded to in previous literature, in terms of a form of rudimentary cardiac memory, whereby the current behaviour of the heart depends on previous episodes of pacing (Yu et al., 1999; Shvilkin et al., 1998; Krebs et al., 1998; Rosenbaum et al., 1982; Rozanski et al., 1997; Costard-Jäckle et al., 1989). However, the underlying molecular and cellular mechanisms involved in this electrical remodelling are still unknown.

The influence of electrotonic coupling between cells is determined by the density and distribution of gap junctions, where the assembly and degradation of gap junction proteins may play an important role in the electrical remodelling of the myocardium. In other work that examined the ion channel expression during chronic pacing conditions, an increase in the expression and activity of $I_{to}$ resulting in a prolongation in APD in isolated rabbit ventricular myocytes was observed (Rozanski et al., 1997). The key question is how the direction of the activation sequence triggers these possible changes in ion channel expression and activity of gap junctional proteins, thereby modulating APD. Though only speculation, one possible mechanism may be through mechano-electrical feedback effects. Mechano-electrical feedback is a phenomenon in which changes in myocardial stretch or loading conditions results in the modulation of cardiac electrophysiological properties (Kohl and Sachs, 2001). The underlying mechanisms are associated with the effects of cardiac stretch on mechano-sensitive and stretch-activated channels. Specifically, the stretch-induced changes in $Ca^{2+}$ flux (Allen and Kentish, 1985; Kentish and Wrzosek, 1998), $Ca^{2+}$ handling (Gamble et al., 1992; White et al., 1993) and sensitivity to $Ca^{2+}$ (Allen and Kurihara, 1982), which would be altered in relation to a change in activation sequence. Therefore, the changes observed in APD are likely a result of the complex interaction of a number of signalling pathways, due to the triggering of

mechano-electrical feedback effects in response to changes in activation sequence.

## Effects on the dispersion of repolarisation

Alongside activation time, the distribution and pattern of repolarisation was altered to a similar degree (Figure 5.17 and Figure 5.18), in correspondence with the change in activation sequence for each form of pacing. In general, both the activation and repolarisation sequences were in concordance with each other, meaning that sites of earliest activation corresponded with sites of earliest repolarisation and vice versa. Considering the previous observations comparing short to long term effects of activation sequence, it can assumed that the dispersion of repolarisation is a dynamic property which is dependent on both the current activation sequence, the previous activation sequence and the time course of stimulation. In acute pacing conditions, the main determinant of the dispersion of repolarisation would be the combined current activation sequence and current distribution of APD as a result of the previous activation sequence. However, in the chronic pacing condition, one would expect the dispersion of repolarisation to be primarily due to the current activation sequence, based on the study by Costard-Jäckle et al. (1989).

In this study, a dissociation of the relationship of APD vs. activation time was seen resulting in a diminished inverse relationship when alternative forms of pacing were used, and an increase in the heterogeneity of repolarisation. Increased heterogeneity of repolarisation is known to increase the propensity for the initiation of re-entrant ventricular arrhythmias due to conduction block, when conduction velocity is slowed.

If the slow adaptation in the spatial and temporal distribution of APD seen by Costard-Jäckle et al. were to occur, this would act to restore the relationship between APD and activation time, resulting in repolarisation being more homogenously distributed across the myocardium.

## Characterisation of the model of chronic MI

Heart failure is a multifaceted clinical syndrome, which is difficult to recapitulate in experimental models. In the current study, a rabbit model of chronic MI following coronary artery ligation was used, where the current model has been extensively characterised previously (Pye and Cobbe, 1992; Pye et al., 1996; Ng et al., 1998; Burton et al., 2000).

The most common experimental models of heart failure typically employ either combinations of pressure/volume overload or rapid pacing in order to induce heart failure (Wiegerinck et al., 2008; Akar and Rosenbaum, 2003). A negative consequence of pacing-induced heart failure is thinning of the LV wall, instead of inducing LV hypertrophy, a common marker of heart failure (Akar and Rosenbaum, 2003). In addition, the LV remodelling and hemodynamic abnormalities of pacing-induced heart failure are reversible on termination of pacing (Moe and Armstrong, 1999).

In the current study, comparable changes in standard parameters describing the degree of LV remodelling were observed, in line with the previously published data. Principally, there was a 32% decrease in LVEF, an 18% increase in LAD and a 30% increase in LVEDD.

## Effects of chronic MI on electrophysiological parameters

### Right atrial pacing

During RA pacing, activation wavefronts in the MI group propagated from the mid-myocardium towards the apex and base across the LV, while the RV maintained its apex-base direction of activation sequence (Figure 5.22). This pattern of activation sequence was the same as the control group. A similar pattern of electrical activation was observed in the same rabbit model of chronic MI with earliest activation occurring in the mid-myocardial region (Walker et al., 2007). In contrast to this study where no significant differences in the time to earliest activation on the epicardial surface were seen, they reported a ~20ms delay in their MI group in comparison to their control group. This extra delay was attributed to an increased AV-nodal delay (Walker et al., 2004).

The current experiments appeared to show an increase in heart-heart variability in the range of APD times within the MI group in comparison to the control group, but there was insufficient numbers to establish statistical significance.

The MI group displayed a significant increase in the range of APD across the LV during RA pacing when compared to the control group (Figure 5.13 and Figure 5.27). However, no significant differences were found when comparing the range of APD times across the RV. This elevation in the range of APD emerged from heterogeneous changes in APD across different regions of the epicardial surface. A number of studies have identified prolongation of APD in following an MI, in either isolated myocytes (McIntosh et al., 2000; Beuckelmann et al., 1993) or intact myocardium (Yan et al., 2001; Akar and Rosenbaum, 2003; Poelzing et al., 2005). Conversely, the data presented shows both shortening and prolongation in APD in a non-uniform distribution across the epicardium. There was a significant increase in the dispersion of repolarisation across the LV during RA pacing . Therefore, with the absence of any significant changes in the activation sequence due to remodelling within the non-infarcted myocardium, the increase in dispersion of repolarisation was directly linked to the elevated range of APD.

An inverse relationship emerged between APD and activation time during RA pacing. The slope of this relationship in the LV was comparable to the control group, with only minor differences. There was a marked change in the slope of the relationship across the RV when comparing the MI group to the control group, but this difference was not found to be statistically significant, due to the insufficient numbers and increased variation between MI hearts. Not dissimilar from the control group, the association between APD and activation manifested as longer APD times at mid-myocardium corresponding to earlier activation times and significantly shorter APD times at the apex and base of the LV corresponding with later activation times, respectively. In the RV the same apex-base distribution between APD and activation time as the control group was observed.

### Ventricular pacing

Similar to during RA pacing, there were no significant differences in the distribution and range of activation times across the epicardial surface when

comparing the MI group to the control group for ventricular pacing regimes (Figure 5.9 and Figure 5.23). Moreover, there were no significant alterations in activation times when comparing bi-ventricular offsets.

The MI group exhibited a significant increase in the range of APD across the LV for all forms of ventricular pacing when compared to the control group (Figure 5.13 and Figure 5.27). However, no significant differences were found when comparing the range of APD across the RV.

During all of the ventricular forms of pacing, there was a diminished relationship between APD and activation time with a poor correlation between the two parameters (Figure 5.28), equivalent to the control group.

When assessing the spatial pattern of APD times across the epicardial surface, a gradient formed between the mid-myocardium and the apex and base of the LV. The LV presented with longer APD times on the mid-myocardium, shorter APD times on the apex and even shorter APD times on the base (Figure 5.29). There were no significant differences between any of the pacing regimes, comparable with the control group.

In agreement with the control group, a concordance between the activation and repolarisation sequence existed in the MI group. The MI group displayed a significant increase in the range of repolarisation times across the LV and RV for all forms of pacing, except RV pacing when compared to control group (Figure 5.33). Although there was an increase in the range of repolarisation times across the LV and RV during RV pacing, this difference was not found to be statistically significant.

Despite significant remodelling within the non-infarcted myocardium, there were no significant effects on conduction based on the observed activation times. However, heterogeneous changes in APD across the epicardium were observed with greater site-to-site variation between neighbouring sites, consistent with previous reports of MI-induced effects on APD. The reason for the non-uniform changes in APD is likely a combination of the degree of remodelling in different regions of the myocardium and the regional differences in intrinsic ionic current densities.

## Future Directions

Future studies will be aimed at investigating the effects of chronic pacing using the panoramic optical mapping system and determine whether the heart undergoes the same slow modulation of APD after an MI. In addition, the investigation of species-dependency and the effects of membrane resistance, intercellular coupling and rate dependency of the relationship between APD and activation time would be of interest.

## Limitations

In this study, all optical mapping recordings were done in the presence of blebbistatin (E-C uncoupler) in order to negate the effects of motion artefacts on the optical recordings. Recordings were made only from the epicardial surface, so no electrophysiological information with regards to the endocardial or transmural plane of the myocardium could be assessed.

## Conclusions

This study investigated the changes in epicardial electrical activity under various pacing conditions in both normal hearts and in a rabbit model of chronic MI. In these experiments, there were significant changes in the pattern of electrical activation corresponding with the changes in pacing regime. However, there were no significant alterations in the pattern and range of APD across the epicardial surface. This suggests that the activation sequence is the main determinant of the dispersion of repolarisation.

The overall observations in this study are in contradiction with the current literature, which suggests that the spatial and temporal distribution of APD within the myocardium is the result of interplay between intrinsic cellular properties and electrotonic interactions. A key finding of this study was that there exists an apparent correlation between activation time and APD, which is a consequence of a physiological epicardial activation pattern that activates mid and apical regions early and basal regions late in the sequence. This coincides with the spatial distribution of APD and this generates an apparent correlation. During acute ventricular pacing regimens, the activation sequence is disrupted but the apex-mid-base distribution of APD values remain. Further work is required to determine whether prolonged periods of ventricular stimulation will cause electrical remodelling and restore the inverse relationship between activation time and APD.

Despite significant remodelling within the non-infarcted myocardium of the chronic MI hearts, there were no significant effects on conduction based on the observed activation times. However, heterogeneous changes in APD across the epicardium were observed, consistent with previous reports of MI-induced effects on the distribution of APD.

# Chapter 6: Development of a 3D model of active and passive properties of rabbit left ventricle

## Aims

The aim of this study was to develop a 3D computational model of the rabbit left ventricle that simulates the passive and active mechanical properties of the ventricle. The initial plan was to use the information on the activation sequence of the LV gained from optical mapping studies to help predict the mechanical consequences of physiological and non-physiological activation patterns on the mechanical performance of the ventricle.

## Introduction

Computational models play an essential role in our understanding of the complex electrical and mechanical behaviour of the heart. Increasingly computational simulations incorporate experimental measurements and provide important insights into the physiology and pathophysiology of the heart (Bishop et al., 2007; Trayanova et al., 2006; Hunter et al., 2003, 2001).

An advantage of computational models is the capability to acquire functional information from the entire three-dimensional volume at a high spatial and temporal resolution, limited only by the computational resources available. A number of realistic ventricular models have been developed for human (Potse et al., 2006), pig (Stevens et al., 2003), canine (Nielsen et al., 1991), rabbit (Vetter and McCulloch, 1998; Bishop et al., 2010; Trayanova et al., 2002) and mouse (Henriquez et al., 2004). In contrast, measurements from experimental preparations are limited by the range of parameters than can be recorded and from inherent experimental and biological variability. All models involve assumptions and simplifications of real cardiac tissue, its microstructure and electrophysiological and mechanical properties. This is a limitation of models in general, which is why an important consideration in designing any model is to capture enough detail at a particular level of complexity to offer mechanistic insight that compliments the experimental work.

For the purposes of creating a computational model, the heart wall is assumed to be composed of cardiomyocytes arranged in bundles of muscle fibres across three distinct layers: thin inner layer (endocardium), thick middle layer (mid-myocardium) and the outer layer (epicardium). The muscle fibre orientation

varies with position across the ventricular wall, where the predominant fibre direction (the fibre vector in the plane spanned by the circumferential direction and the local longitudinal direction) rotates from approximately -50° to -70° at the sub-epicardium, to about 0° at the mid-myocardium and to approximately +50 to+70 at the sub-endocardium (Holzapfel and Ogden, 2009). These fibre orientations are primarily based on histological measurements from sections of the LV wall, where the fibres are organised as laminar sheets tightly bound by endomysial collagen and loosely bound by perimysial collagen (Streeter Jr et al., 1969; LeGrice et al., 1995; Sands et al., 2005). Consequently, rule-based methods have been developed to parameterise the fibre orientation in models based on these measurements (Potse et al., 2006; Bishop et al., 2009; Wang et al., 2013). Rule-based reconstructions yield muscle fibre arrangements that are reasonably close to those derived from diffusion tensor magnetic resonance imaging (DT-MRI) datasets. However, because rule-based methods are based on histological measurements that are derived from isolated sections of the LV wall discrepancies still exist between these two approaches.

The material properties of the myocardium are based on experimental data available from animal models. Measurements from biaxial tests on the passive elasticity of canine and swine myocardium have been performed (Dokos et al., 2002; Demer and Yin, 1983; Novak et al., 1994; Smaill and Hunter, 1991; Yin et al., 1987). These experiments demonstrate a strong anisotropic behaviour of the myocardium, based on a complete set of simple shear tests. Although the passive mechanical response of the myocardium has been well characterized in swine and canine, there is a lack of experimental data available for other species.

In an experimental study by Vossoughi et al., myocardial tissues were established as behaving as an incompressible hyperelastic material (Vossoughi et al., 1980). Hyperelasticity is a type of constitutive model to describe non-linear elastic behaviour of materials and their response to large deformations. In general, constitutive laws and models incorporate a specific set of equations, which describe the responses of a material or substance to an external field or force. In initial models of ventricular myocardium, constitutive laws were based on isotropic material descriptions (Demiray, 1976). Subsequent studies

developed transversely isotropic models to account for the anisotropy of the myocardium (Costa et al., 1996; Guccione et al., 1991; Humphrey et al., 1990, 1990). In these constitutive models, some of the key mechanical properties of myocardial tissue were described. However, these constitutive models lack a proper description of the orthotropic nature of soft tissue. A material that is orthotropic can be defined as having material properties which differ in three perpendicular directions (e.g. axial, radial and circumferential). Hunter et al. generated a constitutive model called the pole zero model as one of the first orthotropic constitutive models of ventricular myocardium, by using a separate pole for each defined axis (axial, radial and circumferential) (Hunter et al., 1997). Costa et al. and Schmid et al. followed this by developing other orthotropic models based on Fung-type (exponential) strain-energy functionals (Schmid et al., 2006; Costa et al., 2001). Based on earlier transversely isotropic models, these models are partially structure-based and partly phenomenological. For a detailed account of constitutive models of passive elasticity of myocardial tissues, see (Schmid et al., 2008, 2006; Holzapfel and Ogden, 2009).

In general, the current constitutive laws for modelling cardiac muscle rely on phenomenological representations of the complex fibre structure of the myocardium, where the material parameters in many of these models do not have clear physical meaning. Subsequently, entirely structure-based constitutive models have also been developed, based on changes in the waviness of the fibres generated by the tissue strain (Horowitz et al., 1988). A limitation of this model is the complications in implementing it numerically, in addition to its transversely isotropic behaviour. In a study by Holzapfel et al., they propose a novel structure-based constitutive model of the ventricular myocardium that describes the locally orthotropic tissue microstructure by expressing the strain energy functional using fibre-based material invariants (Holzapfel and Ogden, 2009). The strain-energy functional has eight material parameters with relatively clear physical meanings in the incompressible case. Furthermore, their model is able to assure strong ellipticity and convexity properties that form a vital part of the model both mathematically and physically.

After specifying the constitutive model, the equilibrium equations are closed by choosing suitable boundary conditions, and these equations are solved numerically. Various numerical methods currently exist to solve such problems; the finite element (FE) method is arguably the most appropriate. Over the years, numerous earlier FE-based simulation studies of cardiac mechanics have been generated. Costa et al. using prolate spheroidal coordinates and cubic Hermite elements built a thick-walled ellipsoidal model of the passive mechanics of the LV (Costa et al., 1996). Vetter and McCulloch studied the rabbit LV in diastole using a three-dimensional FE method (Vetter and McCulloch, 2000). Nash and Hunter developed an FE framework for large-deformation heart simulation using the pole-zero constitutive law (Nash and Hunter, 2000). Stevens et al. developed a three-dimensional heart model based on anatomic data from the swine heart and performed numerical simulations using that model (Stevens et al., 2003). They also evaluated the sensitivity of material parameters of the pole-zero constitutive law and found that the parameters of this model are coupled, primarily through the incompressibility constraint. These observations suggested that the pole-zero law might need to be reformulated to achieve a better separation of material parameters associated with deviatoric stresses. Deviatoric stresses are related to changes in shape, whilst hydrostatic stresses are related to volume changes.

To simulate the heart during both diastole and systole, it is necessary to model active tension generation. Active models of the heart that incorporate transmural variations in fibre orientation and non-linear hyperelastic passive responses have been developed by various groups (Huyghe et al., 1992; Bovendeerd et al., 1992; Guccione et al., 1995). Nash et al. developed a FE framework for large-deformation heart simulation using the ‘pole-zero’ constitutive law and a simplified model for active contraction to predict myocardial strain at end-systole (Nash and Hunter, 2000). Usyk et al. considered the effects of active stress with and without active transverse components, and they found that systolic shear strains are more accurately predicted when transverse components are included in the description of active stress (Usyk et al., 2000). Kerckhoffs et al. developed a multi-scale model of the canine ventricles that was coupled to lumped systemic and pulmonary circulation models, thereby enabling realistic multi-beat simulations (Kerckhoffs et al.,

2007). More advanced models that include descriptions of electrical activation that are based on the monodomain or bidomain models of electrical excitation propagation have also been developed (Eriksson et al., 2013; Aguado-Sierra et al., 2011). Such models may be used to investigate the effects of ventricular pacing on cardiac function (Kuijpers et al., 2012; Niederer et al., 2011; Kerckhoffs et al., 2009).

Currently very few studies that model the structural mechanics of the heart account for intracardiac fluid dynamics and fluid–structure interactions (FSI). Fluid structure interactions account for the interaction between a deformable structure (e.g. heart) and an internal fluid (e.g. blood). A possible reason for this gap in current models is the subsequent additional computational cost and challenges posed in solving the Navier–Stokes equations. Several groups have developed FSI models of the LV using the arbitrary Lagrangian–Eulerian (ALE) approach. For example, one group has coupled FSI and electrophysiological dynamics in a LV model (Watanabe et al., 2004). Nordsletten et al. developed a non-conforming ALE framework for simulating blood flow and myocardial dynamics in both the diastolic and systolic phases of the cardiac cycle that coupled the fluid and solid via a Lagrange multiplier field defined on the fluid–solid interface (Nordsletten et al., 2011). In addition, McCormick et al. used this model to investigate the impact of a left-ventricular assist device on overall LV pump function (McCormick et al., 2011). The ALE approach is a natural extension of the FE method to FSI problems, but such schemes may yield significant computational difficulties due to dynamic mesh generation caused by large structural deformations. The immersed boundary (IB) method (Peskin, 2002) is an alternative approach to FSI that was introduced by Peskin to simulate the fluid dynamics of heart valves (Peskin, 1972). Subsequently, it was extended by Peskin and McQueen to simulate the dynamics of the heart, its valves and the nearby great vessels (Peskin, 1997; McQueen and Peskin, 1997; Kovacs et al., 2001; McQueen and Peskin, 2002; Griffith et al., 2007, 2010).

The IB approach to FSI treats the particular case in which an incompressible structure (heart) is immersed in a viscous incompressible fluid (blood), using a Lagrangian description of the deformations and stresses of the immersed structure and an Eulerian description of the momentum, viscosity and

incompressibility of the coupled fluid–structure system. Interaction between Lagrangian and Eulerian variables is mediated by integral transforms with Dirac delta function kernels. When the continuous equations are discretised, the Eulerian equations are approximated on a Cartesian grid and the Lagrangian equations are approximated on a curvilinear mesh. A key feature of the IB method is that it does not require dynamically generated body-conforming discretisations of the fluid and solid. Instead, the Lagrangian mesh overlays the Eulerian grid, and interplay between Lagrangian and Eulerian quantities occurs via discretisations of the integral transforms involving regularized delta function kernels. The IB method thereby effectively circumvents the mesh distortion problems of ALE methods for systems involving large structural deformations.

In this study, a computational model was created to describe the passive and active mechanical properties of the rabbit left ventricle. The model was able to incorporate an invariant-based orthotropic constitutive model (Holzapfel and Ogden, 2009) of the passive elastic response of the LV and a detailed description of excitation-contraction coupling and active force generation (Niederer et al., 2006), in addition to incorporating fluid-structure interactions using a version of the finite-element immersed boundary framework (Griffith and Luo, 2012). Cardiac anatomy was derived from DT-MRI scans of rabbit hearts, using a rule-based approach to reconstruct fibre and sheet orientation.

## Methods

The model incorporates a realistic 3D anatomical model representing the rabbit LV geometry, muscle fibre orientation and laminar sheet orientation. Coupled with the anatomical model is a passive model of the ventricular myocardium based on a structure-based constitutive model, following Holzapfel and Ogden (2009), and a model of excitation-contraction based on the original model by Niederer and Hunter (Holzapfel and Ogden, 2009; Niederer et al., 2006). The framework used for solving the model, where an elastic structure is assumed to be immersed in a viscous incompressible fluid, is the immersed boundary (IB) method (Peskin, 2002). The current version of the IB method is being implemented through the open-source immersed boundary adaptive mesh refinement (IBAMR) software, developed by Boyce Griffith (Griffith, 2015). The IBAMR software provides support for distributed-memory parallelism and adaptive mesh refinement, where the implementation and function of the IB method relies upon a number of high-quality third party software libraries: SAMRAI (Hornung and Kohn, 2002; Hornung et al., 2006), PETSc (Arge and Langtangen, 1997; Balay et al., 2011), hypre (Falgout and Yang, 2002) and libMesh (Kirk et al., 2006).

One of the key packages which supports spatial adaptive discretisation within the model is SAMRAI. SAMRRAI is an object orientated C++ software library which enable numerical, algorithmic, parallel computing with its main focus on applying structured adaptive mesh refinement tools. In the context of the current modelling approach, spatial adaptivity of the mesh is of vital importance to sustain computational efficiency. The LV is modelled by a number of partial differential equations, where the numerical solution to these set of governing equations are approximated across a discrete domain (mesh). Naturally, the spatial discretisation used (mesh spacing), is the main determinant of numerical accuracy and computational cost of the model. The adaptive mesh refinement (AMR) method used as part of the SAMRAI software library provides an important framework for applying different mesh spacing within different regions of the global mesh allowing fine spatial and temporal resolution at vital features, as illustrated in the example in Figure 6.1. All simulations were performed at the School of Mathematics and Statistics at University of Glasgow using Linux servers with dual six-core Intel Xeon X5650 2.67GHz CPUs and 32GB RAM.

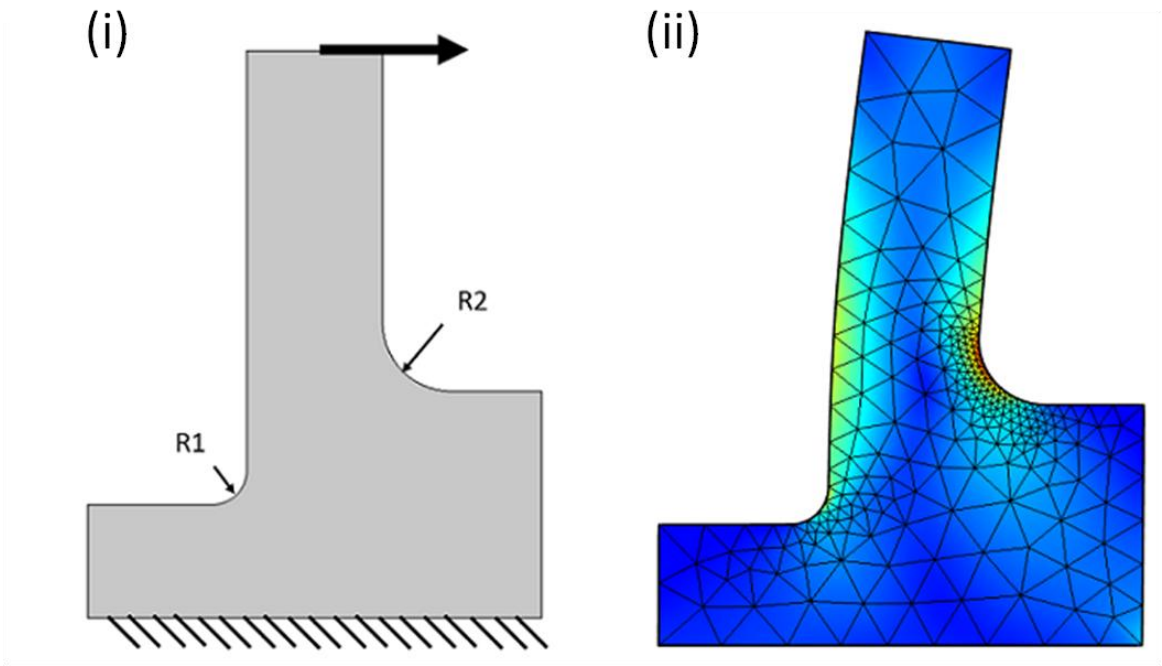


**Figure 6.1 Example of SAMRAI**

**Simple mechanical problem where a bracket is fixed at the bottom and a load is applied at the top as indicated by the arrow with two different fillet radii (R1 and R2). The model predicts where the peak stresses will occur within the structure (red=high stress and blue =low stress). The decision of element size is based on the balance of accuracy and practicality, where fine mesh elements will give very accurate results but impractical computational times, whereas coarse mesh element introduce more error into the model but can be computed very quickly. Through adaptive mesh refinement elements are adjusted to resolve local peak stress by reducing element size in areas with large degrees of stress, whilst retaining large element size in areas devoid of stress to avoid unnecessary additional computational load (courtesy of Comsol).**

## Left ventricular anatomical model

Using diffusion tensor imaging (DTI) is it possible to acquire diffusion-weighted images of the entire heart to map out its 3D geometry (Figure 6.2). Image datasets were obtained from healthy New Zealand White rabbits to develop an anatomically detailed computational cardiac model that would closely mimic the hearts that were used during the optical mapping experiments. The datasets were made available through collaboration with Dr Stephen Gilbert, where the tissue preparation and DTI imaging is described in detail in the following study (Gilbert et al., 2009).

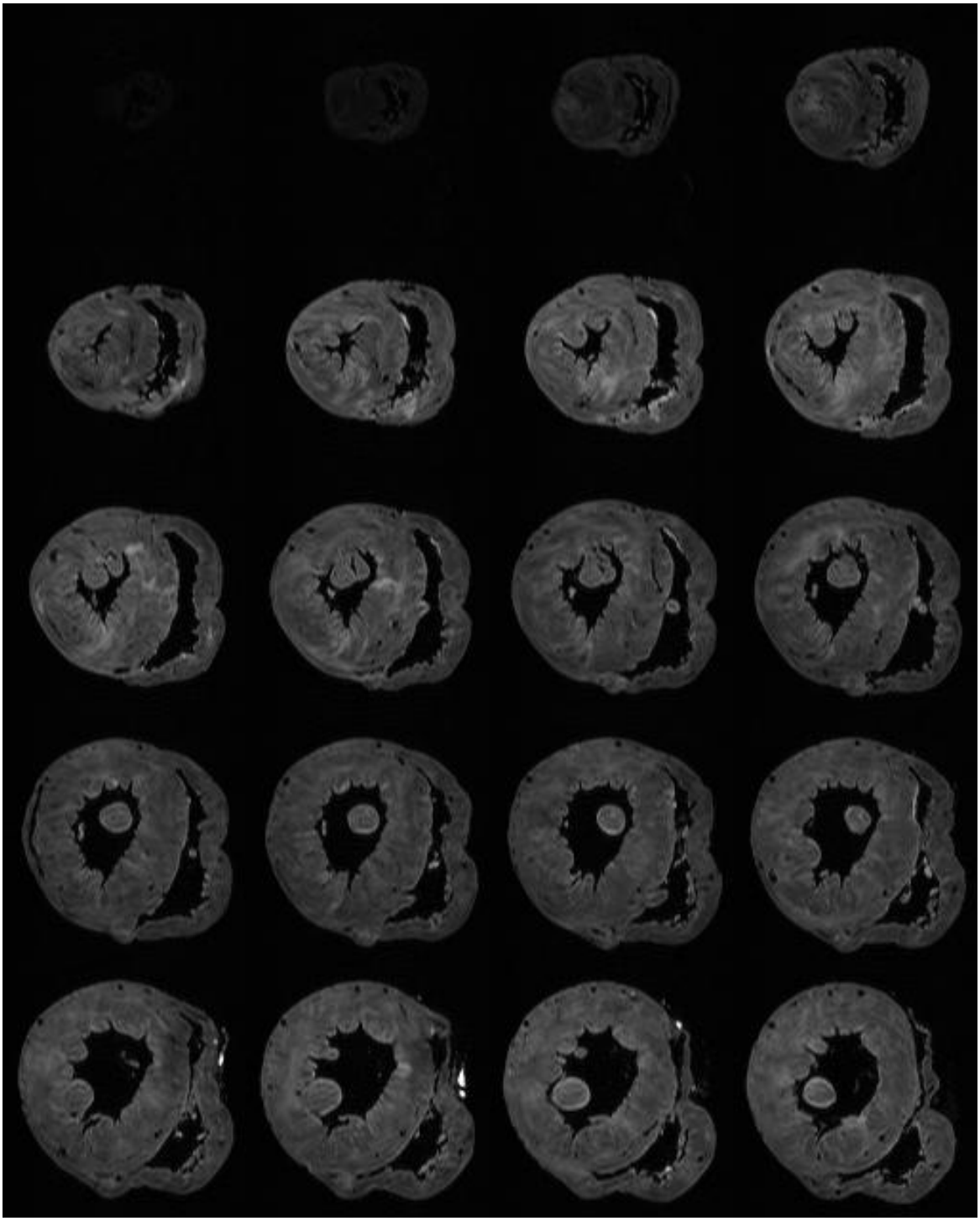

**Figure 6.2 DTI axial slices**
**Subsample of axial DTI slices from diffusion tensor imaging of healthy rabbit heart.**

## Image processing

In order to construct a detailed anatomical computational cardiac model, geometrical information was extracted from the DTI data. Seg3D (Scientific Computing and Imaging Institute, University of Utah, USA), an open-source

software package was used to process the image data (CIBC, 2015). The diffusion-weighted images had a resolution of 128 x 128 x 165 voxels, which included the entire heart volume (left and right ventricle); with a voxel size of 200 μm. Datasets were initially cropped to exclude any voxels which did not form part of the heart volume. The voxel image stacks were then spatially filtered using a Gaussian filter with uniform window size of 3 x 3. Using a conservatively set threshold criterion, based on a low intensity value, an initial image mask selection of the myocardium within the image volume could be made (Figure 6.3). Manual morphological operations were applied in order to remove any isolated voxels and to fill any holes. To delineate the RV from the LV a polyline selection was drawn (Figure 6.4). Using the polyline tool voxels that formed part of the RV could be completely removed from the final voxel image stack (Figure 6.5). Finally, to create a hollow LV chamber for development of the final volume mesh the valve leaflets and papillary muscles were manually removed from the final voxel image stacks (Figure 6.6).

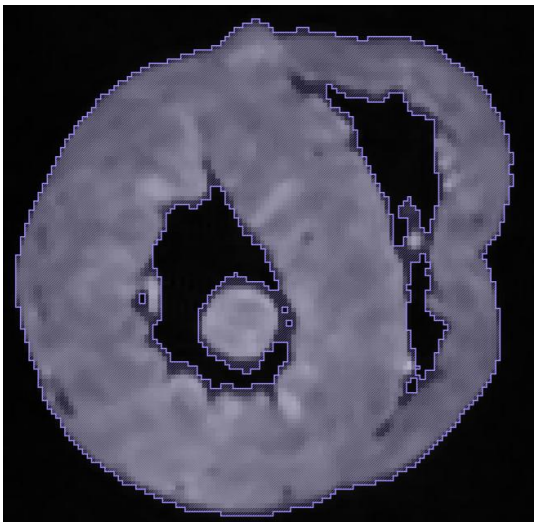

**Figure 6.3 Initial threshold mask selection overlaid over axial DTI slice.**

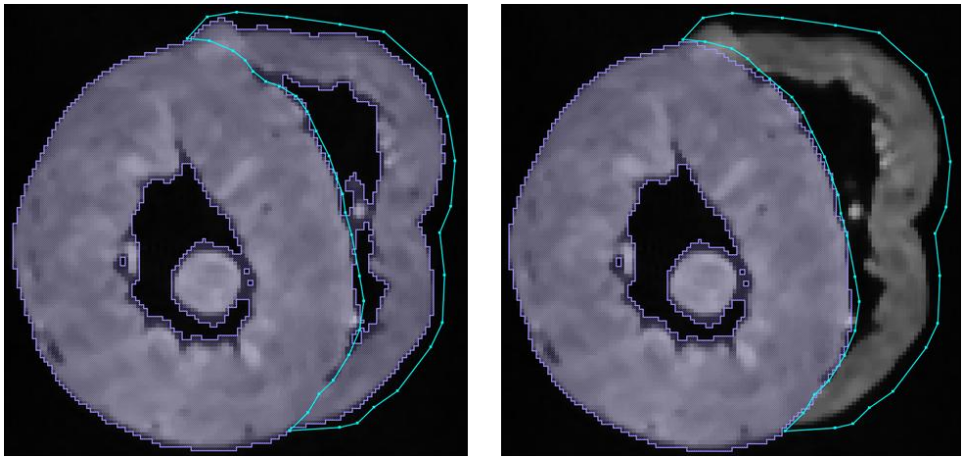

**Figure 6.4 Polyline drawn around RV and mask selection excluded.**

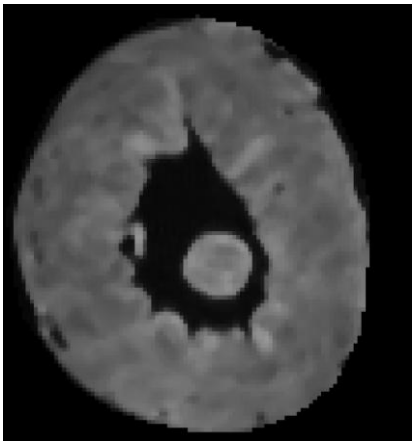

**Figure 6.5 Image volume created excluding voxels deemed part of the RV.**

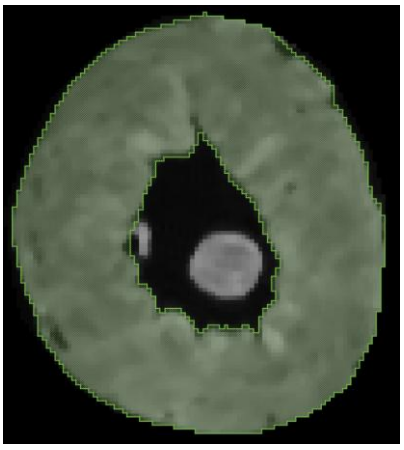

**Figure 6.6 Final mask selection**

**Mask selection of LV with papillary muscles and valve leaflets manually removed from the final selection.**

### Volume meshing

The final segmented voxel image stack was then exported as a binary file (made up of zeros and ones) into Simpleware. Using the Simpleware ScanIP software environment (Simpleware Ltd Exeter, UK) the volume masks from Seg3D were smoothed to remove any unwanted rough edges and finally used to build a surface mesh that could be read into Sandia National Laboratory's, CUBIT mesh generation toolkit. Using CUBIT a tetrahedral finite element mesh (~20000 node points, making up ~100000 tetrahedral elements) was created and three surfaces (endocardium, epicardium and base) defined for the purpose of setting boundary conditions in the final model (Figure 6.7).

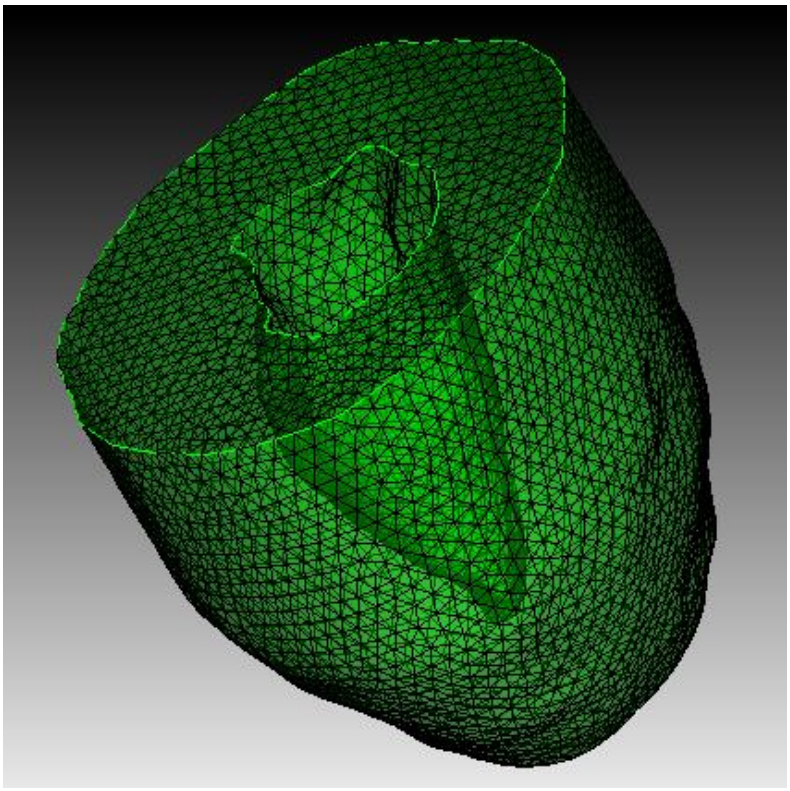

**Figure 6.7 Volume mesh**
**Tetrahedral volume mesh of the rabbit LV generated from Cubit.**

**Myocardial fibre-sheet orientation**

Accurate physiological representation of the myocardial fibre and sheet structure form essential components of a realistic model of the heart, playing an important role in both the mechanics and the electrical activity of the heart. In this study, a rule-based approach was implemented to generate the fibre and sheet orientation.

Rule-based fibre-sheet orientation is an idealised approach, which assumes a spatially varying helix angle at each node within the mesh. Based on the work by Potse et al., two intramural distances were calculated: $d_{endo}$ and $d_{epi}$ (Potse et al., 2006). These two distance parameters are a measure of the distance from each node of the mesh to the endocardial and epicardial surface, respectively. A normalised thickness parameter *e* is then defined for each node of the mesh by:

$$e = \frac{d_{endo}}{d_{endo} + d_{epi}} \quad \textbf{(6.1)}$$

where $e = 0$ along the endocardial surface and $e = 1$ along the epicardial surface.

The local coordinate system ($\mathbf{w_c}$, $\mathbf{w_l}$, $\mathbf{w_r}$) is defined so that $\mathbf{w_c}$ is the circumferential direction (with respect to the apex-base axis of the LV); $\mathbf{w_r}$ is the radial direction, oriented to point transmurally from the endocardial surface towards the epicardial surface; and $\mathbf{w_l} = \mathbf{w_r} \times \mathbf{w_c}$, as illustrated in Figure 6.8 (Wang et al., 2013).

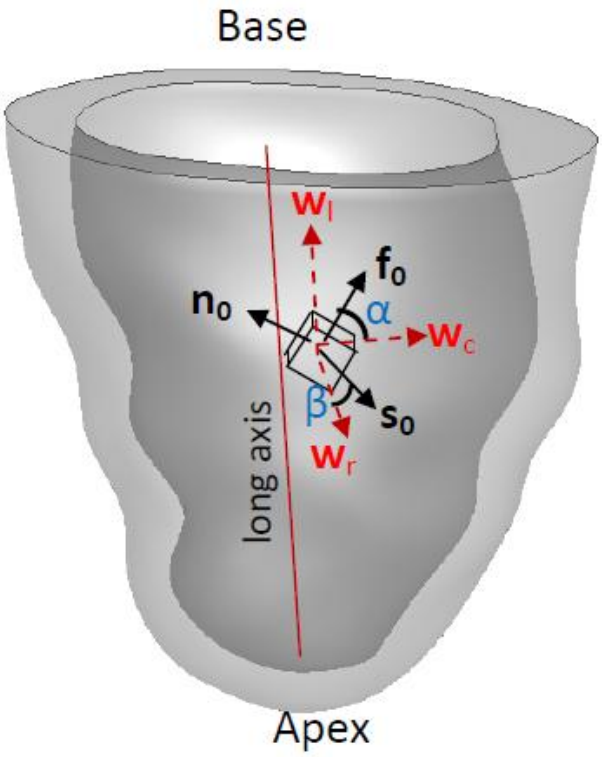


**Figure 6.8 Coordinate system**

**The local coordinates and fibre structure of the left ventricle in which ($f_0$, $s_0$, $n_0$) are the fibre, sheet and sheet normal axes, respectively. Local circumferential, longitudinal and radial axes are defined as ($w_c$, $w_l$, $w_r$), respectively. The helix angle α is defined by the angle between $f_0$ and $w_c$ in the plane spanned by $w_c$ and $w_l$, and the sheet angle β is defined to be the angle between $s_0$ and $w_r$ in the plane spanned by $w_l$ and $w_r$.**

To account for transmural rotation in the fibre, a spatially varying helix angle α, which is the angle between the fibre axis $\boldsymbol{f_0}$ and the circumferential axis $\mathbf{w_c}$ in the plane spanned by $\mathbf{w_c}$ and $\mathbf{w_l}$, is defined for each element in the mesh via:

$$\propto = R(1 - 2\bar{e}_{av})^n \qquad \textbf{(6.2)}$$

where R is the maximum fibre angle on the endocardial surface, $\bar{e}_{av}$ is the average value of $e$ at the nodes of the element in question, and n is an empirically determined constant.

R is set to 60 to give a fibre direction that varies linearly from -60° at the epicardial surface to +60° at the endocardial surface, where n is an odd integer. In the recent study of Bishop et al., a value of n = 1 was shown to provide a better match to measured DT-MRI data, in contrast to the value used in the

study of Potse et al. (n = 3) (Bishop et al., 2009; Potse et al., 2006). Hence, n was set to equal 1.

The sheet angle β, which is the angle between the sheet axis $\mathbf{s_0}$ and the radial axis $\mathbf{w_r}$ in the plane spanned by $\mathbf{w_r}$ and $\mathbf{w_l}$, was calculated via:

$$\beta = T(1 - 2\bar{e}_{av}) \quad \textbf{(6.3)}$$

where T is the maximum sheet angle on the endocardial surface. Based on LeGrice et al., T was set to 45 to give a sheet direction that varies linearly from -45° at the epicardial surface to +45° at the endocardial surface (LeGrice et al., 1995).

Using this form of fibre-sheet orientation assumes a spatially homogenous distribution throughout the myocardium with variation only in the transmural direction, as shown in Figure 6.9 for fibre and sheet orientation.

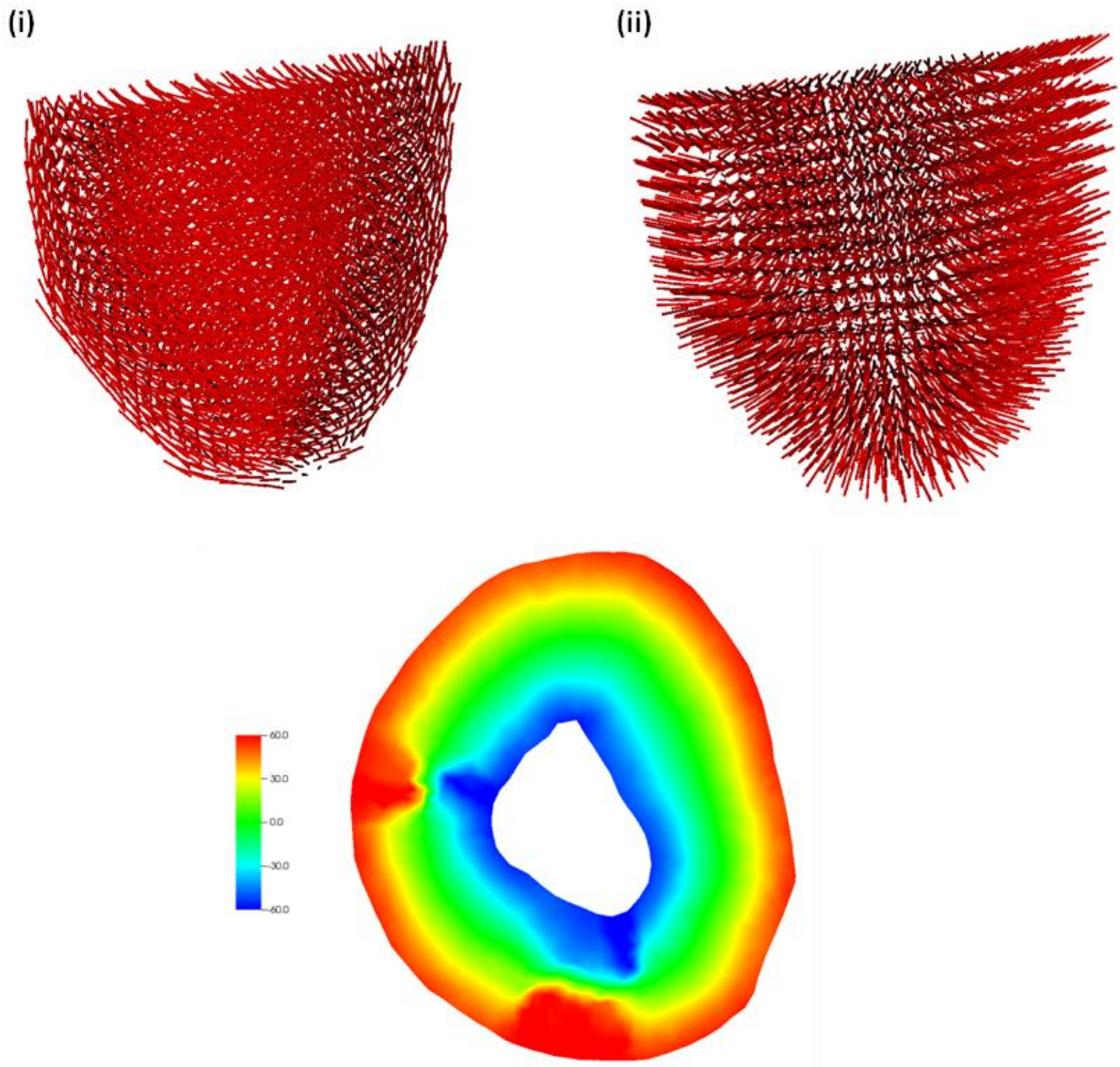


**Figure 6.9 Rule based fibre-sheet orientation**

**(i) Fibre orientation**

**(ii) Sheet orientation**

**(iii) Helix angle distribution**

## Immersed boundary method

The immersed boundary (IB) formulation is based on a Lagrangian description of the immersed elastic structure, in this case the LV, and a Eulerian description of the momentum, viscosity and incompressibility of the fluid system, where the two sets of variables are coupled via integral transforms with delta function kernels.

This means the fluid is within the Eulerian frame of reference, where properties of the fluid are described at the coordinates of the point of observation. Therefore, properties such as the velocity components (u, v and w) and pressure (p) of the fluid as functions of their spatial position (x, y and z) and time (t) were considered. These fluid properties can then be expressed in the form:

$$u = u(x, y, z, t) \quad \textbf{(6.4)}$$

$$v = v(x, y, z, t) \quad \textbf{(6.5)}$$

$$w = w(x, y, z, t) \quad \textbf{(6.6)}$$

$$p = p(x, y, z, t) \quad \textbf{(6.7)}$$

The elastic structure was considered within the Lagrangian frame of reference, where the trajectories of the particles that make up the elastic structure are followed, expressing their location in terms of time only. The velocity components of the structure can then be expressed in the form:

$$x = x(t) \quad \textbf{(6.8)}$$

$$y = y(t) \quad \textbf{(6.9)}$$

$$z = z(t) \quad \textbf{(6.10)}$$

$$u = \frac{dx}{dt} = u(t) \tag{6.11}$$

$$v = \frac{dy}{dt} = v(t) \tag{6.12}$$

$$w = \frac{dz}{dt} = w(t) \tag{6.13}$$

This convention of defining fluids as Eulerian and structures as Lagrangian is used mainly due to the fact that it is easier to represent and treat these separate entities mathematically in these forms. The Eulerian variables are defined on a fixed Cartesian mesh, while the Lagrangian variables are defined on a curvilinear mesh. The Lagrangian and Eulerian coordinate systems can be visualised as in Figure 6.10 (Griffith and Luo, 2012).

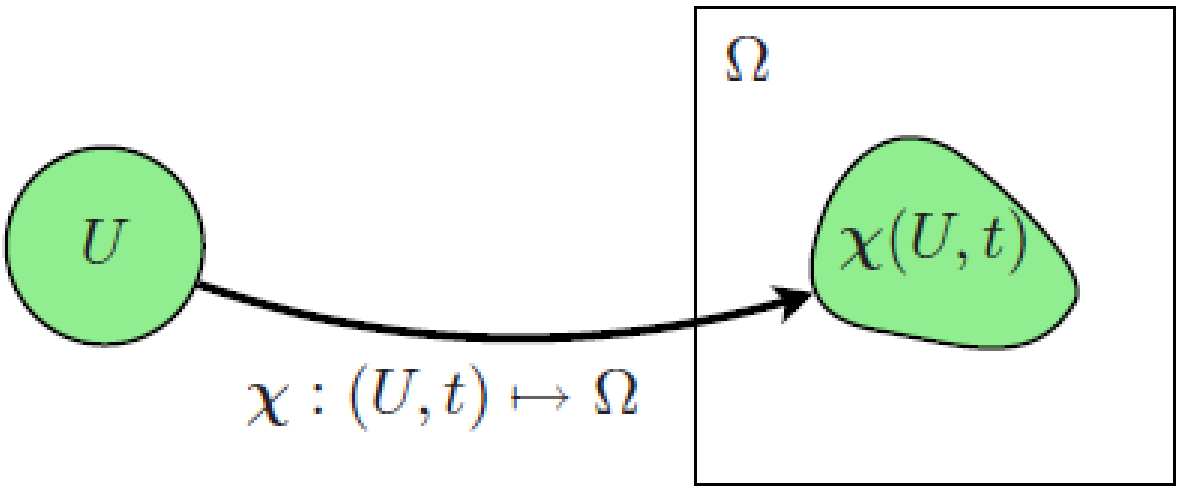


**Figure 6.10 Lagrangian and Eulerian coordinate systems**

**U is the Lagrangian coordinate domain within the reference configuration showing the mapping (χ) to the current configuration χ (U, t) where it is immersed in fluid defined within the Eulerian coordinate domain.**

## Passive model of the myocardium

### Framework and background

The framework used for passive modelling of the myocardium is based on work by Holzapfel and Ogden (2009) which employs a structure-based constitutive model, where the LV myocardium is treated as an inhomogeneous, thick-walled, non-linearly elastic and incompressible material.

Before discussing the specifics of the constitutive model, it is first worth briefly summarising the basis on which the assumptions of modelling the mechanical behaviour of the passive ventricular myocardium are made. The passive myocardial tissue can be treated as an orthotropic material, which has three mutually orthogonal planes, each with its own distinct material responses. This can be clearly seen from work by Dokos et al., where they carried out simple shear tests on passive ventricular myocardium from pig, illustrated in sequence showing the cut-out section of myocardium from the equator of the heart (Figure 6.11), the separate modes of shear tests (Figure 6.12) and finally the experimental results (Figure 6.13) (Dokos et al., 2002). The myocardium exhibits spatial and time dependence changes based on the amount of shear. In addition, the tissue shows highly non-linear behaviour, exhibiting the viscoelastic effect, illustrated by the relatively low hysteresis between loading and unloading (Figure 6.13). However, due to time scale of the cardiac cycle which is fast in comparison to the slow relaxation response of the viscoelastic effect, the myocardium is treated as elastic, as mentioned previously.

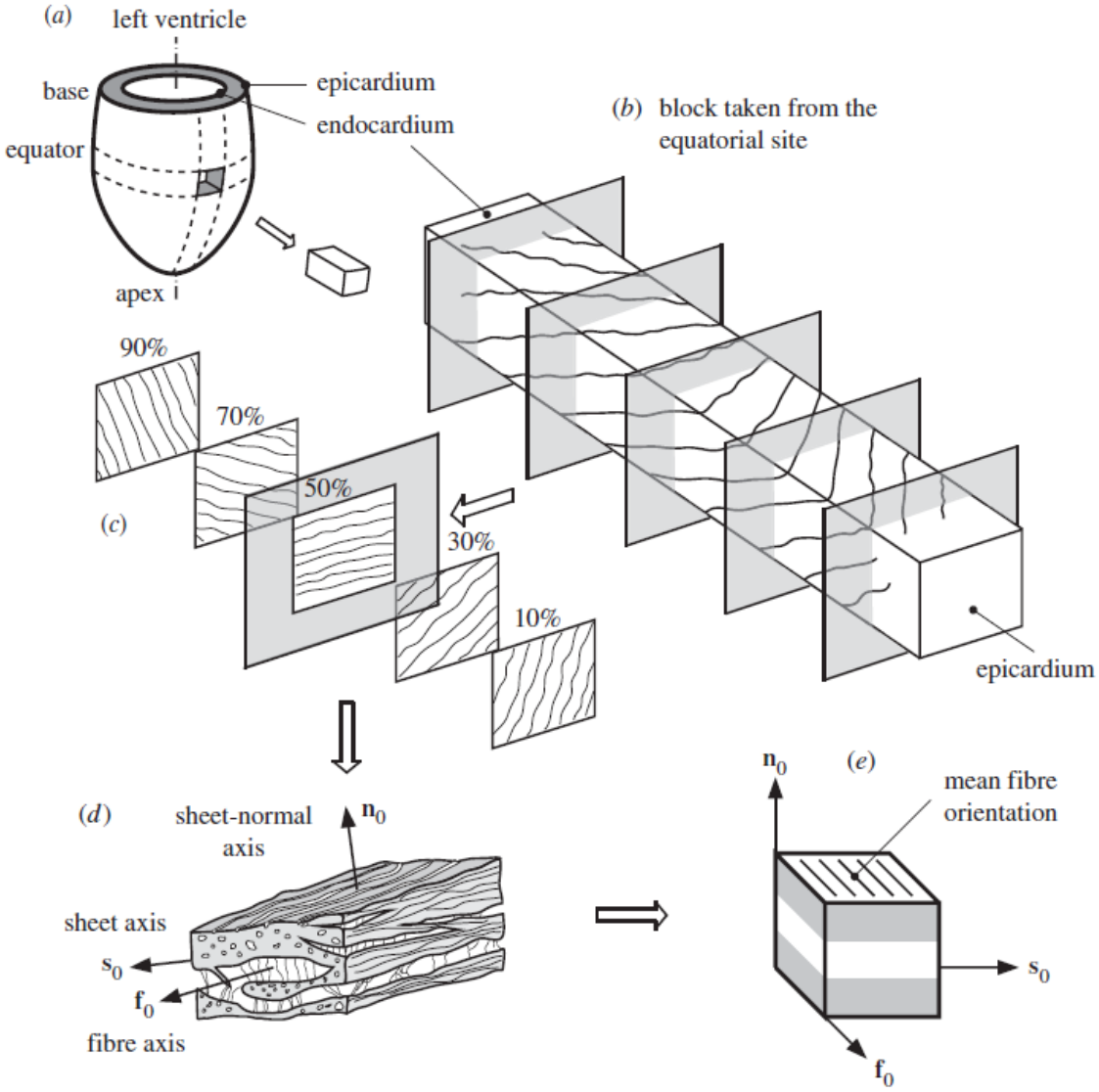


**Figure 6.11 Schematic diagram of myocardial shear tests**

**(a) the cube section of ventricular myocardium cut out from the equator, (b)(c) the fibre direction and structure taking slices in the transmural direction, (d) the layers of myocytes and collagen fibres between laminar sheets with corresponding material axis shown as the fibre axis ($f_0$), laminar sheet axis ($s_0$) and the sheet normal axis ($n_0$) and (e) the layered cube of ventricular myocardium (Holzapfel and Ogden, 2009).**

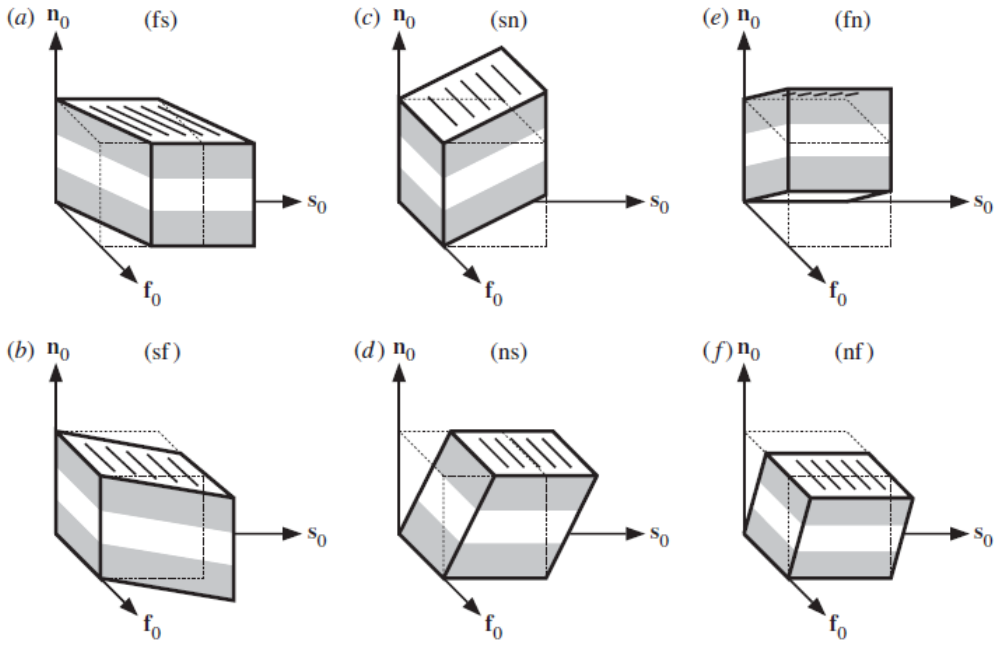


**Figure 6.12 Modes of shear tests**

**Illustrations of six modes of simple shear tests for cubes of myocardium where each mode is a strain deformation in the (ij) plane. The first letter for each mode represents the normal vector of the face that is sheared, with the second letter denoting the direction that the face is shifted (Holzapfel and Ogden, 2009).**

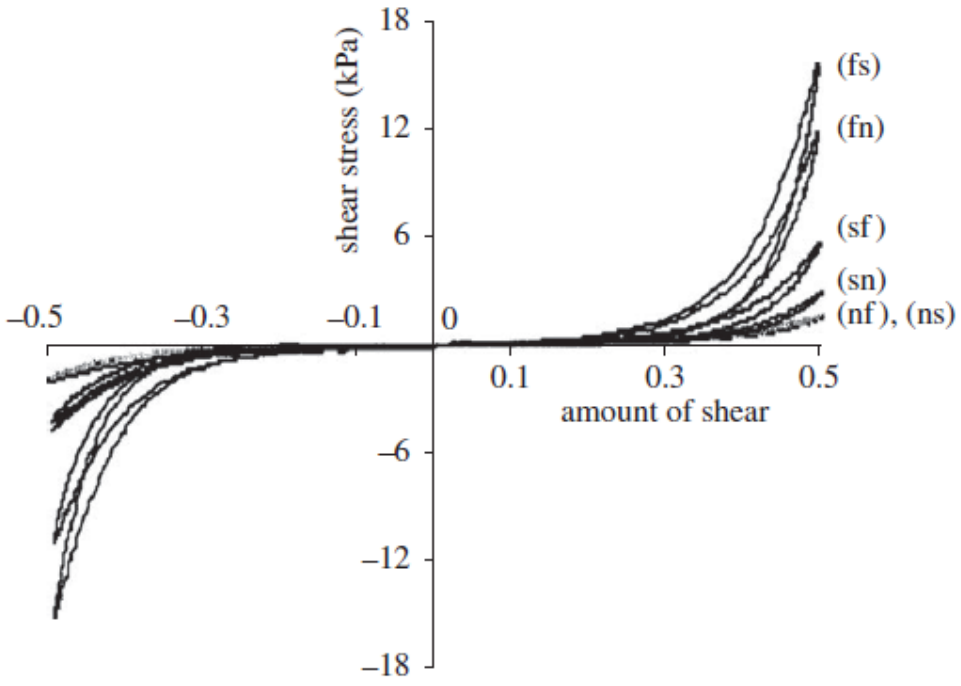


**Figure 6.13 Material responses**

**Considering different modes (ij) of simple shear test on cubes of myocardium, as shown in Figure 6.12, with shear stress against the amount of shear (Dokos et al., 2002). The first letter for each mode represents the normal vector of the face that is sheared, with the second letter denoting the direction that the face is shifted.**

The myocardium was assumed to be incompressible, as with other soft biological tissues, where experiments by Vossoughi et al. showed that myocardial tissue specimens subjected to various degrees of hydrostatic stress are essentially incompressible (Vossoughi et al., 1980).

A number of studies have looked at measuring residual stresses; Omens et al. in rat hearts and Costa et al. in dog hearts (Costa et al., 1997; Omens and Fung, 1990). In addition, there have been a number of theoretical computational models that have simulated residual stresses (Rachev, 1997; Rodriguez et al., 1994). Each set of studies suggested that the unloaded myocardium is residually stressed. In particular, experimental studies show that the residual stress is compressive circumferential in the endocardium and tensile circumferential in the epicardium (Costa et al., 1997; Omens and Fung, 1990). Changes in residual stress are also suggested to be influenced by myocardial growth (i.e. cardiac hypertrophy) and remodelling (Rachev, 1997; Rodriguez et al., 1994). In addition, residual stresses have been recognised as being important within arterial wall mechanics (Holzapfel and Ogden, 2003; Holzapfel et al., 2000). However, accurately quantifying three-dimensional stresses experimentally can be very difficult; furthermore, how these measurements translate to the real heart is still under debate and as such very few modelling groups have pursued its application. Therefore, within this model of passive myocardium residual stresses have been omitted, considering the structure of the myocardium with respect to a stress-free reference configuration.

### Constitutive model

Considering the myocardium as a continuum body, where the distribution of stress is expressed as a piecewise continuous function of space and time, there exists both a reference configuration ($B_0 \subset \mathbb{R}^3$) and a current configuration ($B_t \subset \mathbb{R}^3$). These configurations are related by a time-dependent mapping $\boldsymbol{\chi} : B_0 \times [0, T] \rightarrow B_t$. Therefore, letting $\boldsymbol{X} \in B_0$ denote coordinates in the reference configuration and $\boldsymbol{x} \in B_t$ denote coordinates in the current configuration, the deformation gradient tensor associated with the motion ($\boldsymbol{x} = \boldsymbol{\chi}(\boldsymbol{X}, t)$) can be defined as $\boldsymbol{F} = \partial\boldsymbol{\chi}/\partial\boldsymbol{X}$.

Constitutive models are described in terms of the principal stresses. Principal stresses, commonly known as the principal invariants, define the stress state of the material (LV) at any given point, where they are invariant to changes in orientation. In this case the constitutive model is described in terms of the invariants of the right Cauchy-Green deformation tensor ($\boldsymbol{C} = \boldsymbol{F^T F}$), where the principal invariants of $\boldsymbol{C}$ are:

$$I_1 = tr(\boldsymbol{C}), \quad I_2 = \frac{1}{2}\,[I_1^2 - tr(\boldsymbol{C^2})], \quad I_3 = \det(\boldsymbol{C}). \tag{6.14}$$

Using the material axis (fibre axis ($\boldsymbol{f_0}$) and laminar sheet axis ($\boldsymbol{s_0}$)), as described and illustrated previously, the quasi-invariants can be defined to allow the model to characterise the material responses in these preferred directions within the reference configuration. The fibre and sheet quasi-invariants, with the addition of the fibre-sheet quasi-invariant can be defined as:

$$I_{4f} = \boldsymbol{f}_0.(\boldsymbol{C f_0}), \quad I_{4s} = \boldsymbol{s}_0.(\boldsymbol{C s_0}), \quad I_{8fs} = \boldsymbol{f}_0.(\boldsymbol{C s_0}). \tag{6.15}$$

When considering the principal invariants, also known as the isotropic invariants, $I_1$ can be interpreted as describing the underlying non-collagenous, non-muscular matrix, where these characteristics are modelled as an exponential function of $I_1$, commonly known as a Fung-type expression, within the strain energy function (Demiray, 1976). To satisfy the incompressibility condition, it is necessary that $J = \det(\boldsymbol{F}) = 1$, therefore, $I_3 = 1$. In order to reproduce the stiffening behaviour in the fibre direction, as seen in the experimental results by Dokos et al. (Figure 6.13), it is suitable to use an exponential function of $I_{4f}$. Similarly for the sheet direction, an exponential function of $I_{4s}$ is used. When these directions are under tension these terms will give a pronounced contribution to the strain energy and a minimal contribution under compression. As the fibres do not support compression these terms are only included within the strain energy function when $I_{4f}$ and $I_{4s}$ are greater than 1. The characteristics of the two invariants ($I_{4n}$ and $I_2$) are already supplied by the other invariants, which are adequate to model the features of the simple shear tests.

However, in order to incorporate the two curves (fs and fn) from Figure 6.13, it is necessary to include an additional exponential term using the invariant $I_{8fs}$, which defines the fibre-sheet interaction. It is not necessary, however, to incorporate $I_{8fn}$ and $I_{8sn}$ where the two curves (nf and ns) are not pronounced within Figure 6.13. Typically, an additional term would be necessary to enforce incompressibility, but this is already defined by the fluid-structure interaction through the IB method, therefore it can be omitted from the strain-energy function here.

The structure-based strain energy function, following Holzapfel and Ogden (2009), is:

$$\begin{aligned} W\left(I_1, I_{4f}, I_{4s}, I_{8fs}\right) = {} & \frac{a}{2b}\exp[b(I_1-3)] \\ & + \frac{a_f}{2b_f}\left\{\exp\left[b_f\left(I_{4f}-1\right)^2\right]-1\right\} \\ & + \frac{a_s}{2b_s}\left\{\exp[b_s(I_{4s}-1)^2]-1\right\} \\ & + \frac{a_{fs}}{2b_{fs}}\left\{\exp\left[b_{fs}\left(I_{8fs}\right)^2\right]-1\right\} \end{aligned} \tag{6.16}$$

where $a$, $b$, $a_f$, $b_f$, $a_s$, $b_s$, $a_{fs}$ and $b_{fs}$ are non-negative material parameters. The $a$ material parameters are defined in terms of units of dyne/cm$^2$ and $b$ material parameters are dimensionless.

From the strain-energy function defined above, the first Piola-Kirchkoff stress tensor can be defined as:

$$\begin{aligned} \boldsymbol{\sigma}_p = {} & a\exp[b(I_1-3)]\,\boldsymbol{F} \\ & + 2a_f\left(I_{4f}-1\right)\exp\left[b_f\left(I_{4f}-1\right)^2\right]\boldsymbol{f}\otimes\boldsymbol{f} \\ & + 2a_s\left(I_{4s}-1\right)\exp[b_s(I_{4s}-1)^2]\;\boldsymbol{s}\otimes\boldsymbol{s} \\ & + a_{fs}I_{8fs}\exp\left[b_{fs}\left(I_{8fs}\right)^2\right](\boldsymbol{f}\otimes\boldsymbol{s}+\boldsymbol{s}\otimes\boldsymbol{f}) \end{aligned} \tag{6.17}$$

where $\boldsymbol{f} = \boldsymbol{F}\boldsymbol{f_0}$and $\boldsymbol{s} = \boldsymbol{F}\boldsymbol{s_0}$ define the fibre and sheet axis in the deformed (current) configuration, respectively.

## Active modelling

In this study, active tension (*T*) is determined by the active contraction model of Niederer et al. (Niederer et al., 2006). The framework used for modelling active contraction can be summarised by the following flow diagram (Figure 6.14):

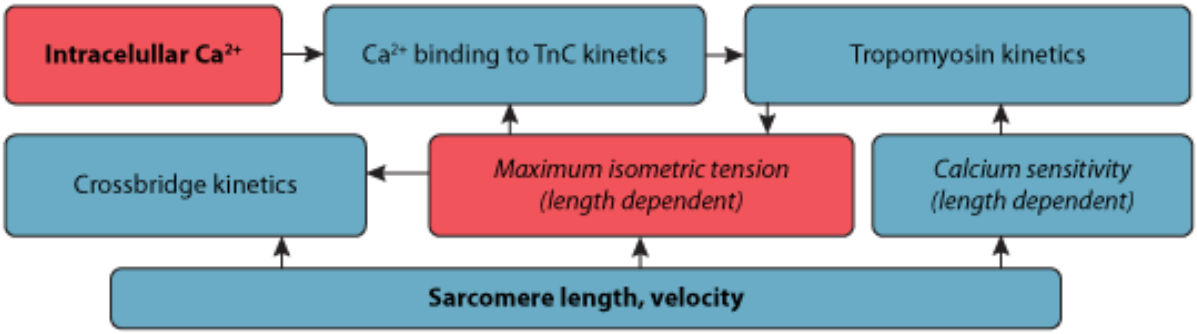


**Figure 6.14 Framework of excitation-contraction model (Niederer et al., 2006).**

The Niederer et al. model consists of six dynamic variables, defined as a set of ODE equations, where the iterative scheme used for solving the system of ODEs is by the second order Runge-Kutta method. The first ODE to consider is of the steady-state binding of $Ca^{2+}$ to Troponin C (TnC), described by the Hill equation (with a Hill coefficient of 1):

$$\frac{d[Ca^{2+}]_{Trpn}}{dt} = k_{on}[Ca^{2+}]_i\left([Ca^{2+}]_{TrpnMax} - [Ca^{2+}]_{Trpn}\right) - k_{off}(T)[Ca^{2+}]_{Trpn} \quad (6.18)$$

where $[Ca^{2+}]_{Trpn}$ defines the concentration of $Ca^{2+}$ to bind to TnC site II, $[Ca^{2+}]_{TrpnMax}$ defines the maximum concentration of calcium ions that bind to TnC site II, $[Ca^{2+}]_i$ is the intracellular calcium concentration, $k_{on}$ is the rate of binding and $k_{off}$ is the tension-dependent (T) rate of unbinding.

The remaining ODEs require a more detailed explanation to explain their importance within the model. Based on an initial approximation intracellular calcium concentration $[Ca^{2+}]_i$ it is assumed to be homogeneous across the whole

heart and purely time dependent, where it is defined at each node by (Niederer et al., 2009):

$$\frac{d[Ca_{2+}]_i}{dt} = \left(\frac{Ca_{Max} - Ca_d}{\tau Ca_a}\right) exp\left(1 - \frac{t}{\tau Ca_a}\right) \quad \textbf{(6.19)}$$

where t is the time and the remaining parameters ($Ca_{Max}$, $Ca_d$ and $\tau Ca_a$) are constants fitted to experimental measurements by Beuckelmann et al. on isolated ventricular myocytes (Beuckelmann and Erdmann, 1992).

This model assumes that $Ca^{2+}$ rapidly binds to troponin and ignores tension-dependent binding of $Ca^{2+}$ to troponin. One of important features of the model is in incorporating the length-dependent $Ca^{2+}$ sensitivity component of the Frank Starling Law by:

$$\gamma = \left(\frac{[Ca^{2+}]_{Trpn}}{Ca_{Trpn50}}\right)^n \quad \textbf{(6.20)}$$

where $\gamma$ acts as a non-linear length-dependent scalar, with $[Ca^{2+}]_{Trpn}$ defining the concentration of $Ca^{2+}$ to bind to Troponin C (TnC) site II, $Ca_{Trpn50}$ defining the concentration of $Ca^{2+}$ to bind to TnC at half-activation and $n$ which gives a phenomenological representation of nearest neighbour interactions between tropomyosin and/or crossbridges.

This leads nicely onto the definition of the fraction of activation sites defined by the following ODE:

$$\frac{dz}{dt} = \propto_0 \gamma(1 - z) - \propto_{r1} z - \propto_{r2} \frac{z^{n_r}}{z^{n_r} + K_z^{n_r}} \quad \textbf{(6.21)}$$

where $z$ defines the fraction of actin sites available for crossbridge binding, $\propto_0$ denotes the activation rate and $\propto_{r1}$, $\propto_{r2}$, $n_r$ and $K_z$ correspond to slow and fast relaxation parameters.

The level of isometric tension generated is assumed to be proportional to the fraction of crossbridges bound to actin, defined as:

$$T_0 = T_{0Max} \frac{Z}{Z_{Max}} \quad (6.22)$$

where $T_0$ is the isometric tension, $T_{0Max}$ is the maximum tension at full activation for a given sarcomere length and $z_{Max}$ is the maximum fraction of available actin sites.

In addition, this model incorporates cross-bridge kinetics in the form of the fading memory model (Hunter et al., 1998). Various experiments on cardiac muscle showed a number of distinct observations, following a rapid reduction in sarcomere length ($\lambda$), as shown in Figure 6.15 (Nickerson et al., 2001):

(i) the sudden drop in tension following the change in sarcomere length ($T_0 \rightarrow T_1$)

(ii) the slow recovery to equilibrium

(iii) the rapid recovery of tension with a small oscillation

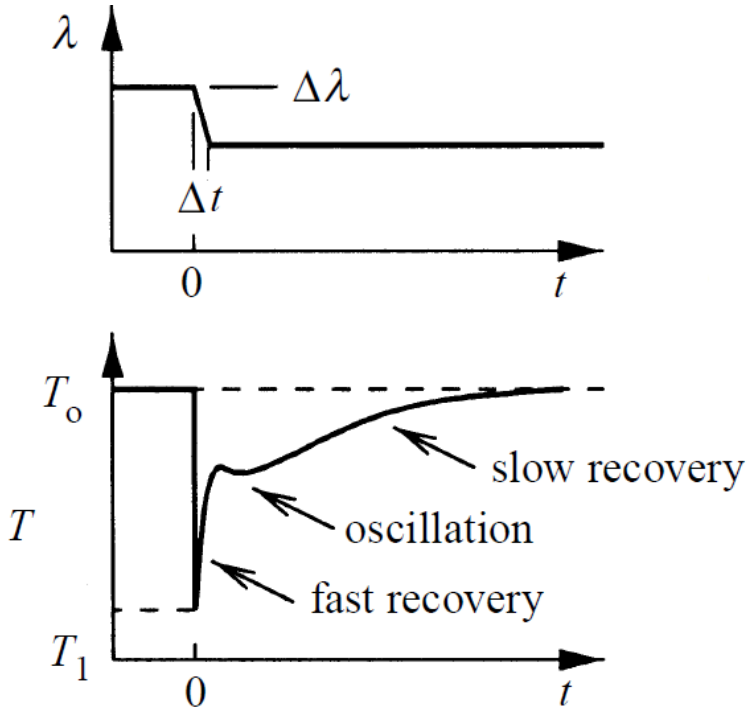


**Figure 6.15 Tension recovery**

**The recovery of tension (T) (lower figure), following the reduction in sarcomere length (λ) (top figure), where different phases of tension recovery are indicated (Nickerson et al., 2001).**

The aim of the fading memory model is to provide a method to represent the development of tension associated with crossbridge kinetics phenomenologically, including the observations discussed above. The fading memory model consists of a non-linear static and linear time-dependent component which describes the relationship between tension and sarcomere sliding velocity. The linear time-dependent component is described by the sum of three exponential processes:

$$Q_i = A_i \int_{-\infty}^{t} exp^{-\propto_i (t-\tau)} \frac{d\lambda_e}{dt} d\tau \qquad (i = 1, \dots, 3) \tag{6.23}$$

where $Q_i$ represents the value of the integral associated with the development of tension in crossbridge kinetics and $\lambda_e$ is the extension ratio for sarcomere length, defined as the sarcomere length $\lambda$ divided by the resting sarcomere length of 2μm. The remaining parameters $\propto_i$ and $A_i$ denote rate constants.

The remaining three ODE's are the time derivatives of $Q_i$, written as:

$$\frac{dQ_i}{dt} = A_i \frac{d\lambda_e}{dt} - \propto_i Q_i \qquad (i = 1, \dots, 3) \tag{6.24}$$

It can be assumed that during constant velocity experiments $\left(\frac{d\lambda_e}{dt} = -V\right)$, where $\lambda_e$ is the extension ratio for sarcomere length and V is sarcomere velocity. The linear component of the model will then be equal to:

$$\sum_{i=1}^{n} Q_i = -V \sum_{i=1}^{n} \frac{A_i}{\propto_i} \tag{6.25}$$

The extended form of the original Hill equation, incorporating both positive and negative velocities, can be defined as:

$$-V\frac{1}{aV_0} = \begin{cases} \dfrac{T/T_0 - 1}{T/T_0 + a} & V > 0 \\ \dfrac{T/T_0 - 1}{2 + a - T/T_0} & V < 0 \end{cases} \tag{6.26}$$

Using the relationship in equation-(6.25), setting the sum of $\frac{A_i}{\propto_i} = \frac{1}{aV_0}$, the extended Hill equation can be coupled with the linear-dependent component, thus giving the full form for active tension within the Niederer et al. model:

$$T = \begin{cases} T_0 \dfrac{\sum_{i=1}^{n} Q_i + 1}{1 - \sum_{i=1}^{n} Q_i} & \sum_{i=1}^{n} Q_i < 0 \\ T_0 \dfrac{1 + (2 + a)\sum_{i=1}^{n} Q_i}{1 + \sum_{i=1}^{n} Q_i} & \sum_{i=1}^{n} Q_i > 0 \end{cases} \tag{6.27}$$

where $T$ is the level of active tension.

Hence the active stress tensor, applying the active tension along the fibre direction is:

$$\boldsymbol{\sigma_a} = JT\boldsymbol{f} \tag{6.28}$$

where $J = \det \boldsymbol{F}$ denotes the Jacobian determinant and $\boldsymbol{f} = \boldsymbol{F}\boldsymbol{f_0}$ denotes the fibre direction in the deformed (current) configuration, noting that $\boldsymbol{F}$ is the deformation gradient and $\boldsymbol{f_0}$ is the fibre axis as seen earlier in Figure 6.8.

Adding the passive and active part of the model together gives the overall stress tensor incorporating both the passive and active characteristics of the myocardium:

$$\begin{aligned}\boldsymbol{\sigma} = {} & a exp[b(I_1 - 3)]\boldsymbol{F} \\ & + 2a_f(I_{4f} - 1)exp\left[b_f(I_{4f} - 1)^2\right]\boldsymbol{f} \otimes \boldsymbol{f} \\ & + 2a_s(I_{4s} - 1)exp[b_s(I_{4s} - 1)^2]\,\boldsymbol{s} \otimes \boldsymbol{s} \\ & + a_f I_{8fs} exp\left[b_{fs}(I_{8fs})^2\right](\boldsymbol{f} \otimes \boldsymbol{s} + \boldsymbol{s} \otimes \boldsymbol{f}) \\ & + JT\,\boldsymbol{f}\end{aligned} \tag{6.29}$$

## Boundary, loading and driving conditions

To constrain the motion of the LV, a penalty term is applied which effectively imposes zero axial and circumferential displacements along the basal plane. Radial displacements are not penalised, and the remainder of the LV is left unconstrained. A combination of zero normal traction and zero tangential velocity boundary conditions along $\partial\Omega$ are imposed, as shown in the schematic in Figure 6.16, courtesy of (Gao et al., 2014). In addition, for an incompressible fluid these boundary conditions imply that the pressure is zero along $\partial\Omega$. The boundary conditions are imposed using an efficient multigrid-pre-conditioned Krylov method in the simulations, as implemented in previous models (Griffith, 2009, 2012).

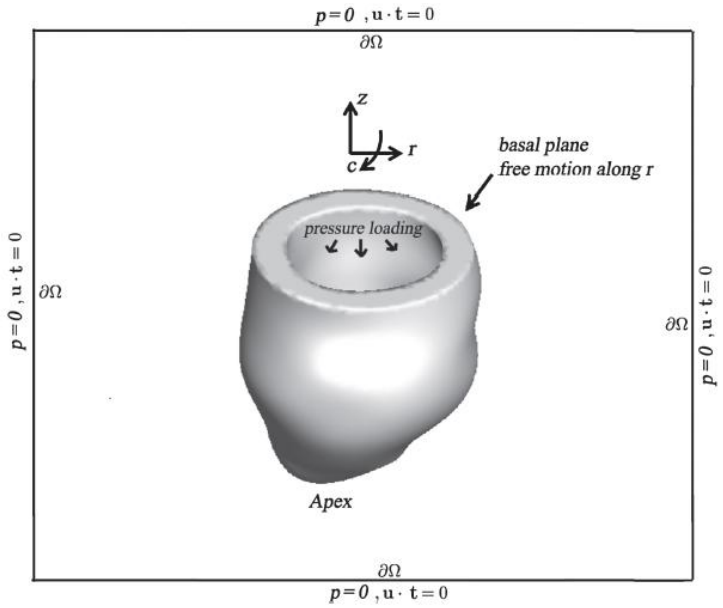


**Figure 6.16 Boundary and loading conditions in simulation domain**

**LV cavity pressure loading is applied to the endocardial surface. Motion in the basal plane are fixed in the circumferential (*c)* and axial (*z)* directions, where motion is only permitted in the radial (*r)* direction. The entire computational domain is defined by the black box, where zero pressure and tangential slip is applied along ∂Ω, where u is the Eulerian velocity and t is the unit tangential vector.**

During the simulations, a time-dependent but spatially uniform pressure load is applied to the endocardial surface of $\partial\Omega^s(t)$ (Wenk et al., 2011; Wang et al., 2013). Pressure is initially increased to an end-diastolic value (8mmHg) to allow the LV cavity to reach its end-diastolic volume. The chosen end-diastolic pressure was based on the previous study by Ng et al. in the same rabbit model

(Ng et al., 2002). Once end-diastolic pressure is reached, the imposed function of intracellular calcium concentration simultaneously increases to its peak value generating contraction of the LV.

## Discretisation and implementation

In the simulations, the domain Ω was defined as a 15cm x 15cm x 15cm box that was discretised with grid spacings $\Delta x = \Delta x_1 = \Delta x_2 = \Delta x_3 = 0.238$cm, corresponding to a regular 63 x 63 x 63 Cartesian grid. A time step size of 6.10e-5s was used throughout the simulations. A detailed account of the numerical time stepping and spatial discretisation schemes employed are provided by (Griffith and Luo, 2012).

# Results

The aim of this study was to develop a 3D computational model of the rabbit left ventricle that simulates the passive and active mechanical properties of the ventricle. This results section will discuss the resulting output of the model with respect to the mechanical output and overall performance and stability of the model during simulation.

Prior to activation, the heart was uniformly loaded over the endocardial surface by a pressure applied over a 60ms time interval, giving a final pressure of 8mmHg. This was imposed via a linear ramp function, as seen in Figure 6.17; where this depicts the pressure loading function applied not the actual pressure in the LV cavity.

## Pressure loading

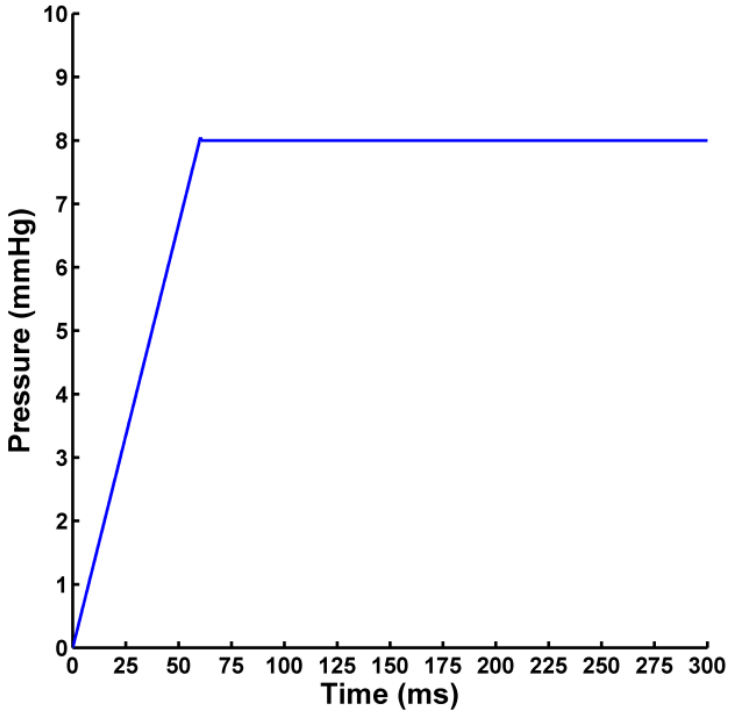


**Figure 6.17 Pressure loading over the endocardial surface**

**Linear pressure ramp function to apply pressure loading over 60ms with a final constant pressure of 8mmHg applied on the endocardial surface.**

Activation was uniform throughout the LV by imposing a prescribed intracellular calcium transient homogenously across the mesh, generated by the Niederer et al. active contraction model (Figure 6.18).

## Homogeneous intracellular calcium

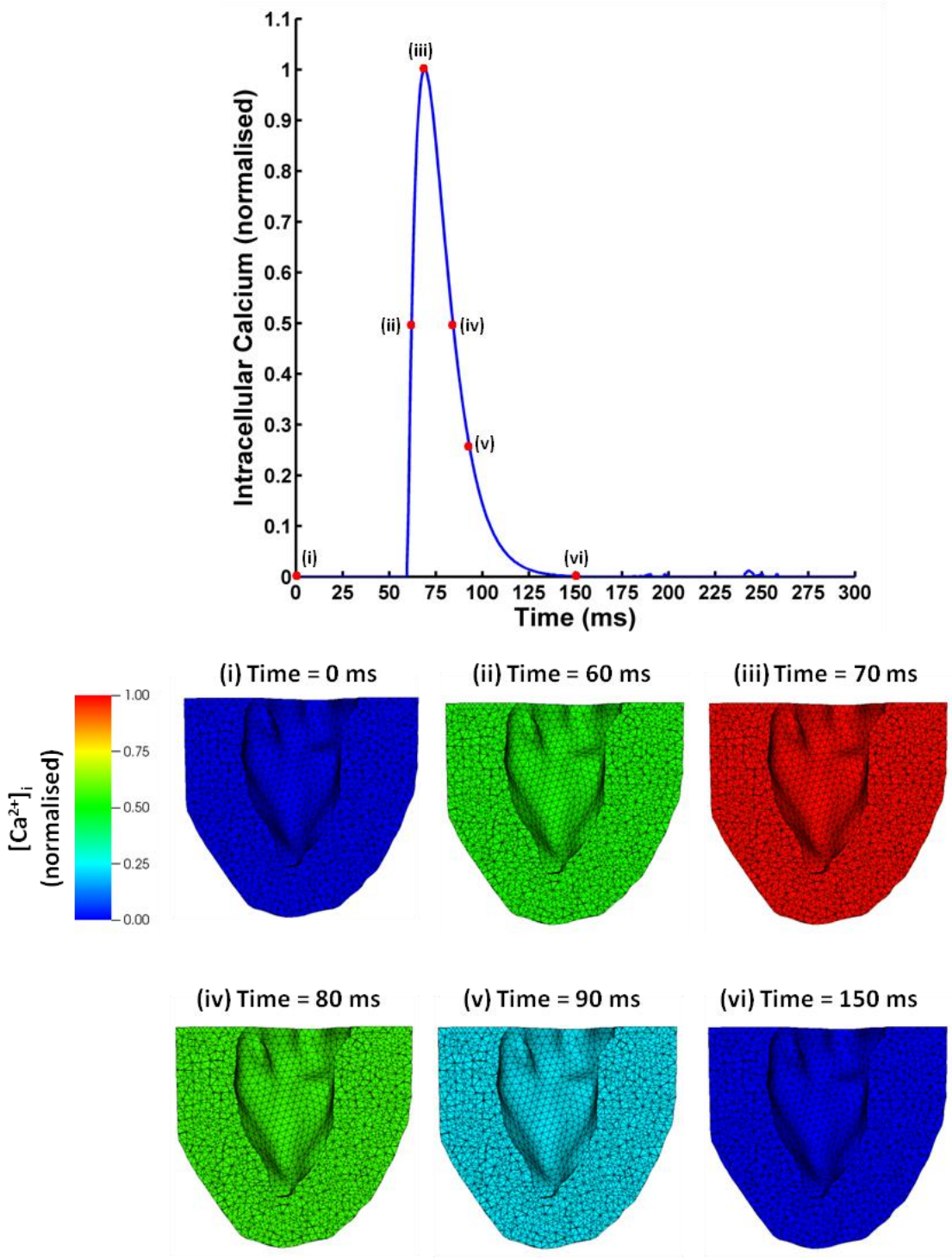


**Figure 6.18 Homogenous intracellular calcium loading across the LV**

**Intracellular calcium time course profile applied to each node of the mesh where the change in intracellular calcium concentration (normalised) is shown across a mid slice of the mesh.**

The generated fluid flow patterns show the initial pressure loading of the LV cavity and resulting displacement of the LV during filling, where the distribution of displacement was relatively uniform across the LV wall (Figure 6.19). During contraction, there is a clear strong fluid ejection and closing of the LV cavity.

During pressure loading, there was an initial inflection in displacement due to filling of the LV cavity, as shown in the time profile of max displacement in Figure 6.20. However, there was the presence of a notch in the displacement profile. This could be explained by oscillations caused by residual displacement after pressure loading. At initiation of contraction caused by a rise in intracellular calcium, the LV cavity contracted rapidly, reaching peak contraction at 80ms, until finally proceeding along its relaxation phase. When considering the three-dimensional distributions of displacement, there were large displacements present in the apex of the LV in comparison to the basal regions, with an average displacement at peak contraction of 4.44 ± 2.27 mm (mean ± SD). There was a reasonably uniform displacement across the LV wall in the transmural axis when considering the mid slice. However, there were discrepancies and heterogeneity between certain regions around the apex of the LV, shown as high levels of displacement in red and low levels of displacement in blue, as shown in Figure 6.20. In addition, there was a significant rotation in the LV during contraction, which was most pronounced at the apex.

Three-dimensional distributions of active tension were computed across the mid-slice, base and apex of the LV (Figure 6.21). In general, the distributions of active tension were relatively homogenous throughout the LV, with a peak tension of 22mN/mm$^2$ and average tension of 4.67 ± 2.03 mN/mm$^2$ (mean ± SD). Transmural distributions in active tension across various paths from the base to the apex of the LV were computed, as shown in Figure 6.22. In general, the change in tension from endocardium to epicardium was similar across all paths. However, path 1 and path 6 at the apex and base, respectively, displayed contrasting relationships between tension and transmural position. A typical pattern of tension emerged, where the highest values of tension resided on the endocardial surface (6.26 ± 1.72), and tension decreased in the direction of the mid-myocardium (3.96 ± 1.15), until increasing towards the epicardial surface

(4.98 ± 1.01), where values are displayed as mean ± SD and units are in $mN/mm^2$.

## Pattern of fluid flow

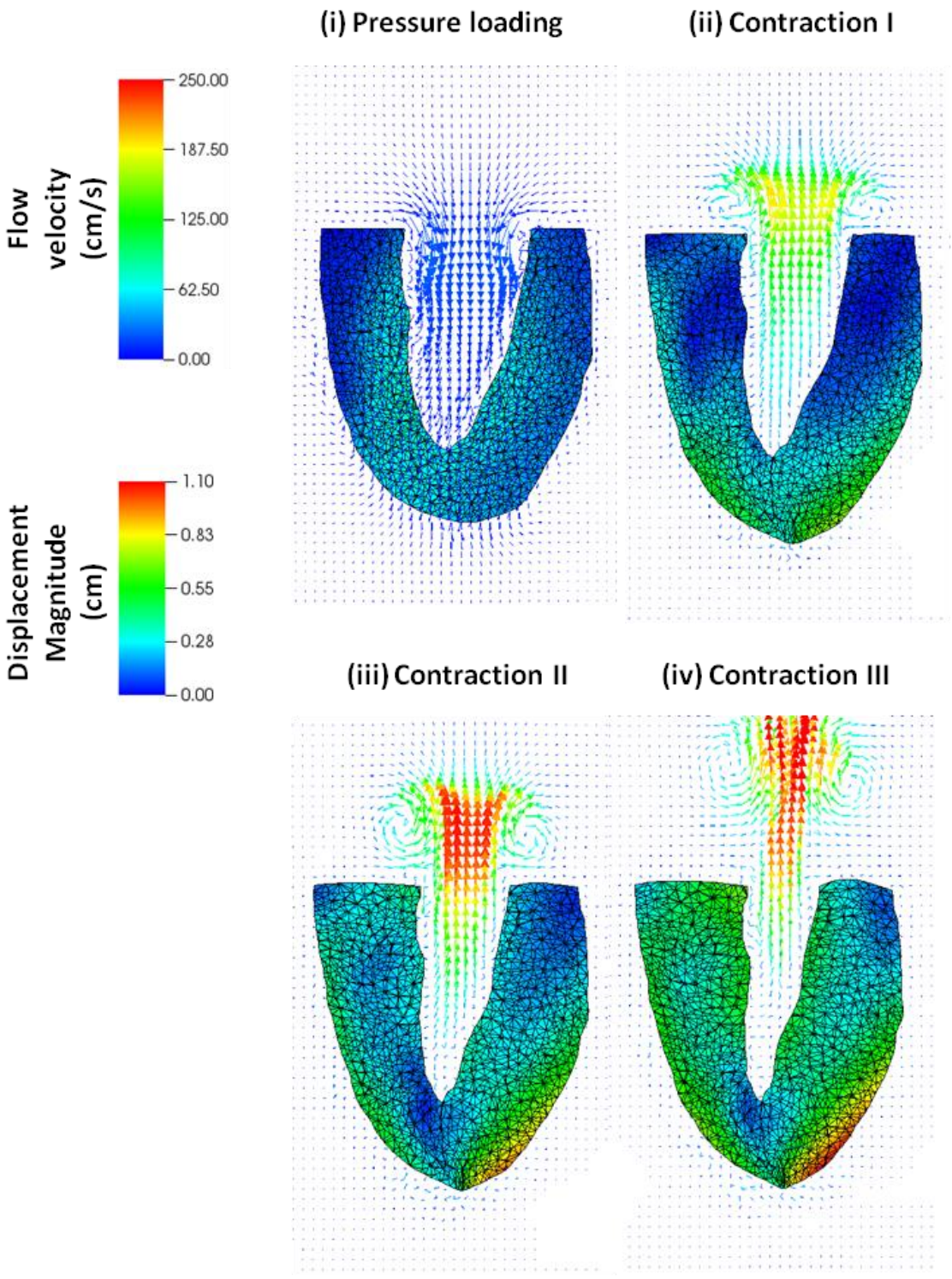


**Figure 6.19 LV fluid flow patterns**

**Pressure loading (i) and three phases during contraction ((ii),(iii) and (iv)), with fluid velocity shown in cm/s alongside displacement magnitude for each element within the mesh (in cm).**

## Distribution of displacement

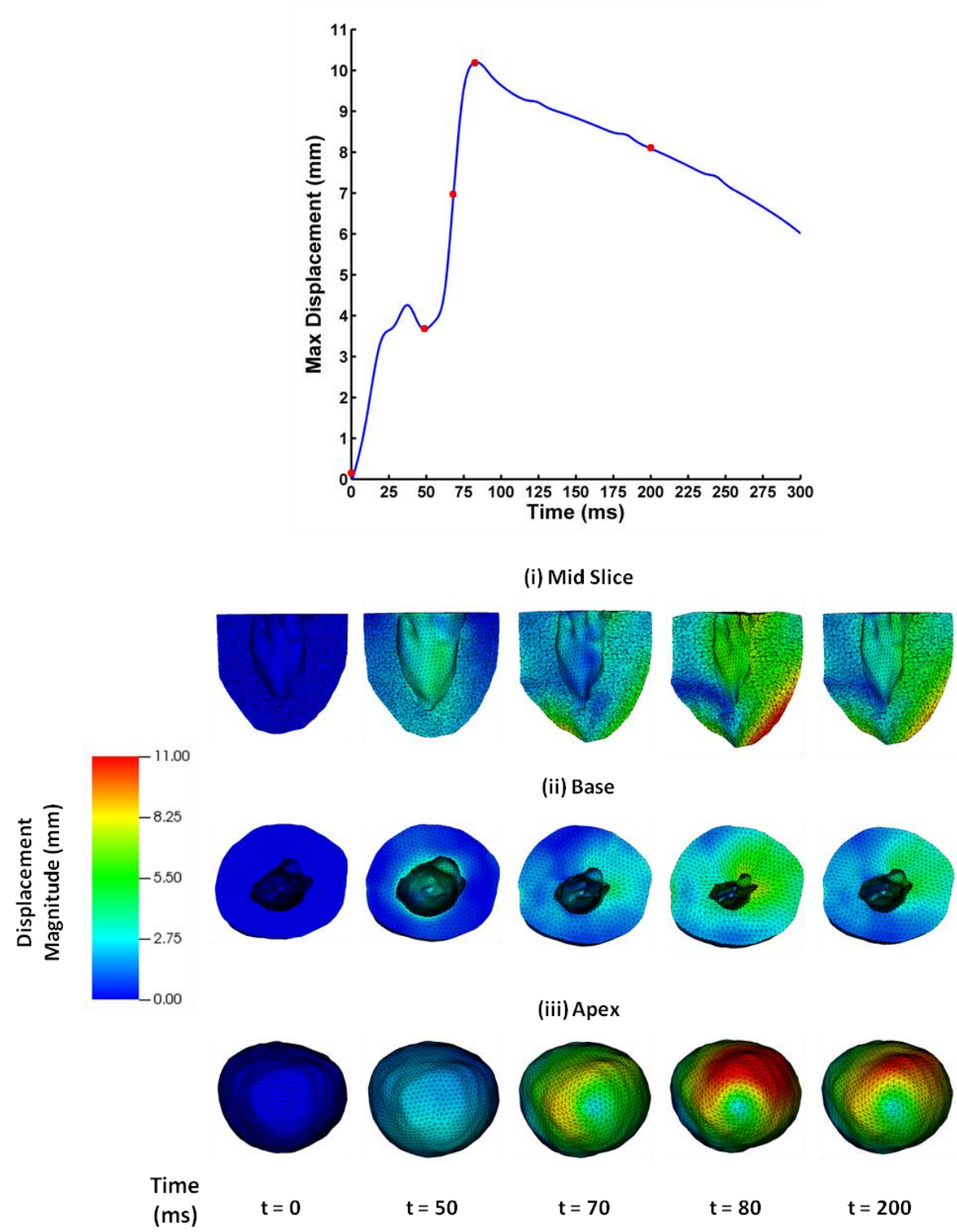


**Figure 6.20 Distribution of LV displacement**

**Profile of max displacement (mm) over time and the overall pattern of displacement across the mid slice (i), base (ii) and apex (iii) of the LV for time points along the profile.**

## Development and distribution of active tension

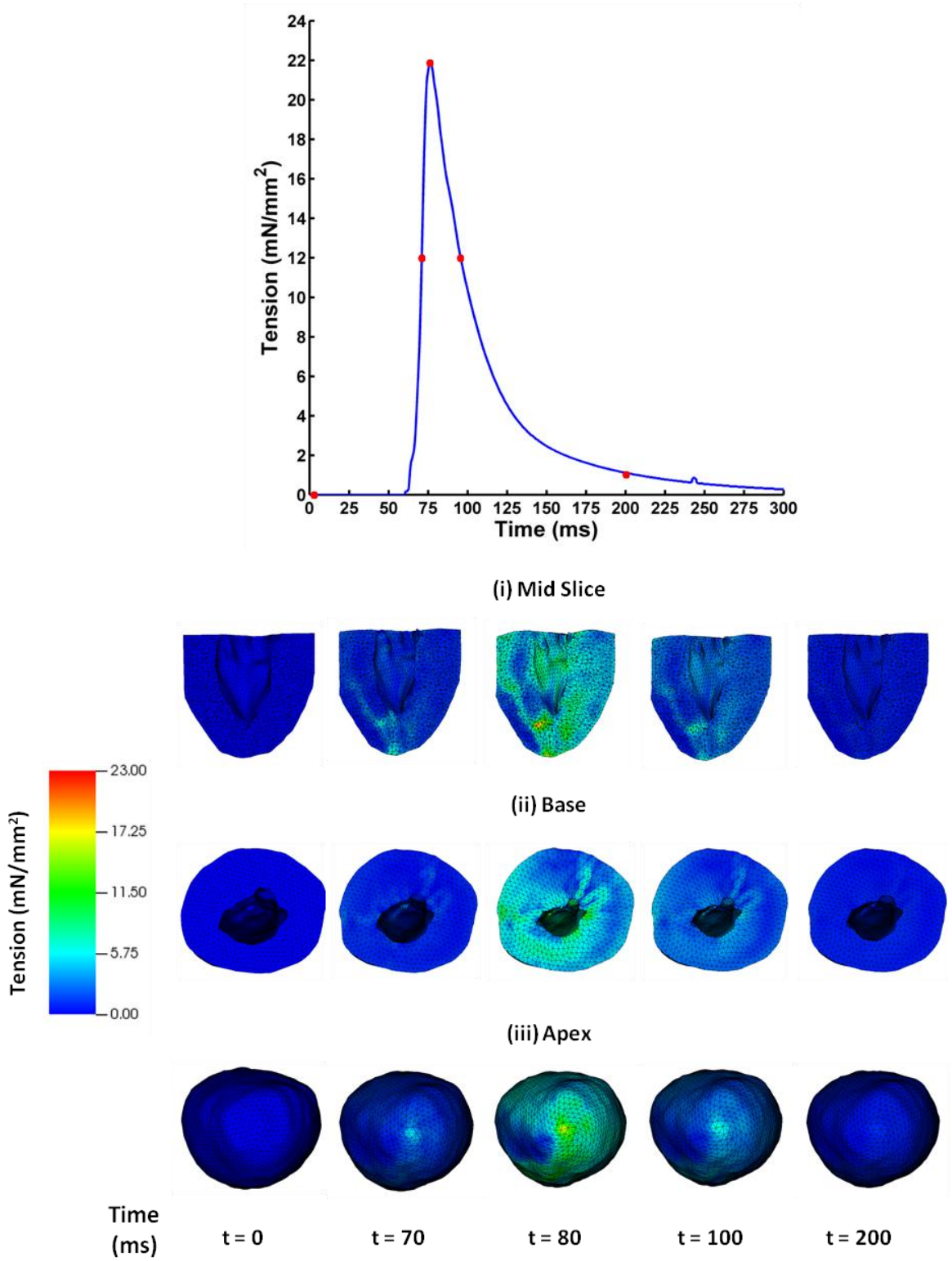


**Figure 6.21 LV active tension development**

**Profile of max tension (mN/mm$^2$) over time and the overall pattern of tension across the mid slice (i), base (ii) and apex (iii) of the LV for time points along the profile.**

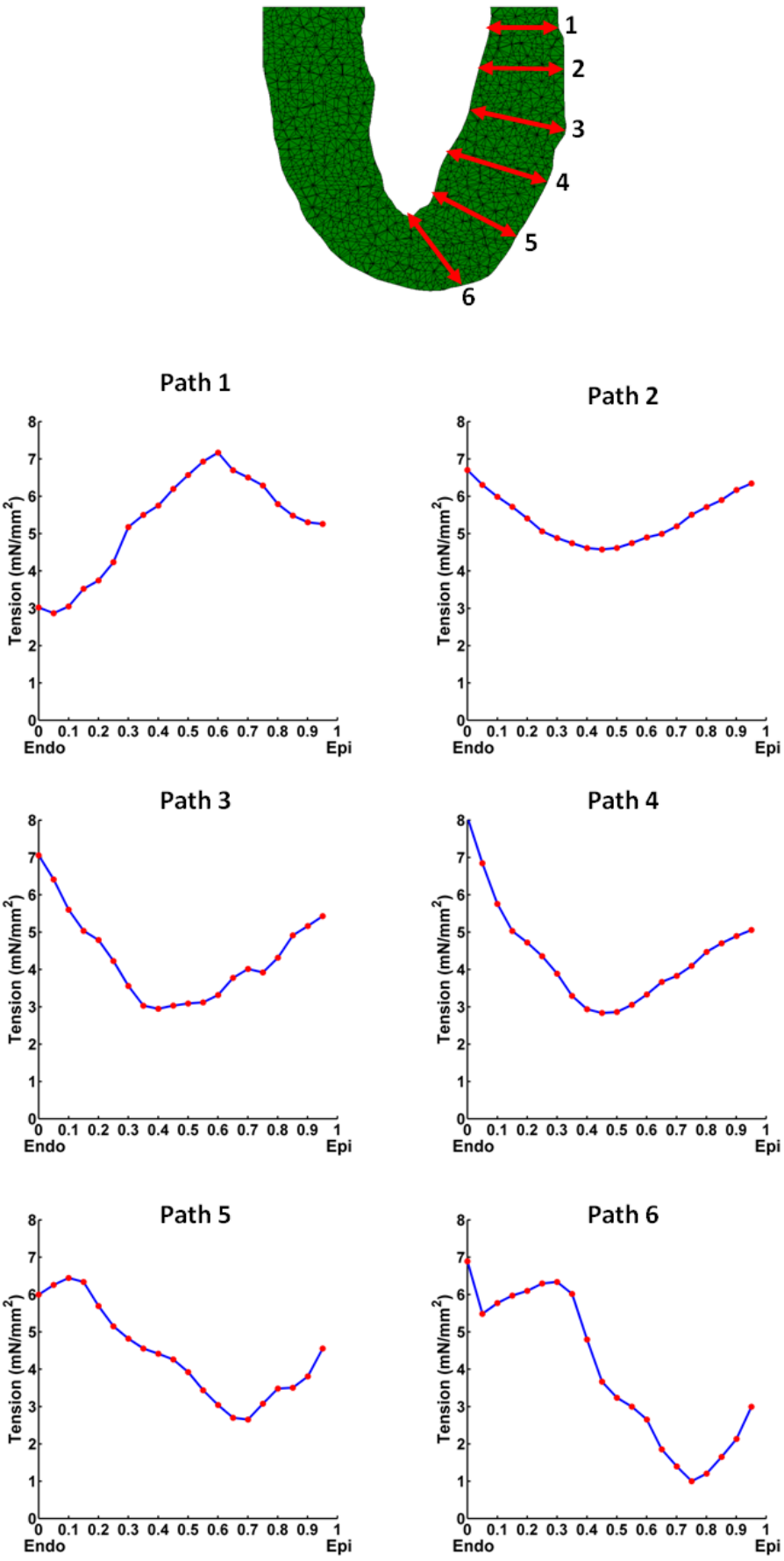


**Figure 6.22 Transmural profile of tension at peak contraction**

**Transmural tension profiles considering six paths from the base to the apex of the LV, where tension is in mN/mm$^2$.**

# Discussion

Whole heart modelling of electrical and mechanical activity has an important role to play in our understanding of the normal function of the heart and the investigation of various physiological paradigms within heart failure. In this study, a realistic three-dimensional computational model of the rabbit left ventricle was developed to simulate both passive and active mechanical properties. The model was able to incorporate DT-MRI based anatomy, along with an orthotropic, invariant-based hyperelastic model of passive elasticity of the heart (Holzapfel and Ogden, 2009). In addition, fluid-structure interactions were incorporated through the finite-element immersed boundary method and the generation of active tension through a model of excitation-contraction coupling (Niederer et al., 2006). Using this model, regional distributions of displacement and active tension were quantified, in addition to transmural distributions of active tension. The main aim of this study was to develop and characterise the model in order to facilitate input of further information from the optical mapping studies in the future.

## General Observations

In general, displacement was homogenously distributed throughout the LV wall, however, there was some discontinuities present in certain regions of the displacement fields (Figure 6.20). When these regions were assessed against nodal distributions, there was some irregularities in the distribution of the nodes. As described previously, fibre helix angle is derived from the intramural distance at each node based on the Rule-based method. This may be the reason for the observed discontinuities. Displacement is highly dependent on the fibre angle distribution and has been shown to have a large impact on stress distributions inside the left ventricular wall (Wang et al., 2013).

Similar to displacement, active tension was relatively homogenously distributed throughout the LV wall (Figure 6.21). Similar to the displacement, there was a region of discontinuity, which may have occurred as a consequence of the effect on displacement. Mean values of active tension were comparable to experimental studies considering isolated cardiac muscle tissue (Allen et al., 1988; Kentish, 1991; Janssen and de Tombe, 1997).

In general, due to the limitation of published data on a number of the derived model parameters it can be difficult to fully characterise the performance of the model. However, in this study the model shows good qualitative agreement with other models currently in the literature, in terms of the transmural distribution of tension across the ventricular wall (Wang et al., 2013; Gao et al., 2014; Guccione et al., 1995; Vetter and McCulloch, 2000). An important consideration in designing any model is to capture enough detail at a particular level of complexity to offer mechanistic insight that compliments the experimental work. In this study, further development of the model is needed in order to fully characterise and validate the use of the model in a meaningful context, such as the calculation of pressure and volume within the LV cavity against pressure-volume measurements currently available experimentally.

It is important to note that the anatomical model of the LV geometry was reconstructed using cardiac DT-MRI data. The geometry of the LV used in this study is not as regular as in other models, which use an idealised approach (Guccione et al., 1995; Nash and Hunter, 2000). Therefore, although this anatomical model represents a more realistic LV geometry, this in turn can introduce irregular distributions of displacement and active tension across the LV. To construct the fibre and sheet orientation within the rabbit LV geometry a rule-based approach was used. This idealised approach is not able to recapitulate fully the true muscle structure inherent in the rabbit LV. In this model, the effects of residual stresses and strains on the LV were not included in the calculations, which may have potential to alter the resultant displacement and active tension. To determine the material property parameters for the constitutive model, experimental data from swine hearts was used. In future, derivation of the material properties using rabbit hearts made available through the optical mapping experiments would be carried out. One of the key limitations of the present model is the absence of the RV, which if incorporated would help to both generate a more complete physiological model and aid in the correlation with the experimental optical mapping data.

## Future directions

In the future, by imposing the experimentally observed activation sequences on the model, the intention would be to gain both electrical and mechanical

information from the simulations. In addition, by coupling the current model with a biophysically detailed mathematical model of myocyte electrophysiology it would be able to incorporate individual ion channels, exchangers and pumps. Incorporating muscle fibre and sheet orientation as measured from DT-MRI or alternative imaging methods would allow us to develop a more realistic tissue structure for both electrical conduction and mechanical contraction.

## Conclusions

In this study, a computational model was developed to describe the passive and active mechanical properties of the rabbit left ventricle. The model was able to incorporate an invariant-based hyperelastic model of the passive elastic response of the LV and a detailed description of excitation-contraction coupling and active force generation, in addition to incorporating fluid-structure interactions through the finite-element immersed boundary framework. Cardiac anatomy was derived from DT-MRI scans of rabbit hearts, using a Rule-based approach to reconstruct fibre and sheet orientation.

Despite the development of the model being in the early stages, it was able to successfully induce pressure loading and initiate contraction with fluid flow and generation of active tension in agreement with previous published models. Future studies will use the information on electrical activity to improve the physiological relevance of the model and to study the mechanical consequences of different patterns of ventricular activation.

# Chapter 7: General Discussion

The general aims of this thesis were to develop a novel method of panoramic optical mapping using a single camera and to study epicardial electrophysiology in isolated Langendorff-perfused rabbit hearts.

## Panoramic optical mapping

The work presented in this chapter gives a detailed account of the protocol developed for the robust selection, filtering and analysis of optical data. The primary aim of this chapter was to test the viability of using this protocol with the panoramic optical mapping system for mapping epicardial electrical activity in the isolated rabbit hearts, by investigating time and heart-dependent differences. The results obtained serve as a foundation for subsequent studies utilising this system. The initial experimental work entailed an investigation of the interaction between activation sequence and action potential duration during RA pacing in these hearts.

The protocol for selection, filtering and analysis of optical data was able to reproducibly delineate, filter and analyse optical signals based on a multi-faceted criteria approach.

The time-dependent feature of the experimental results indicated that, despite progressive decrease in SNR (partially restored by further bolus injections of Di-4-ANEPPS), there were no significant changes in optical AP or ECG morphology. In addition, there were no significant alterations in the overall pattern of electrical events. The experiments were stable over a 2-hour window; all subsequent studies were kept within this timescale, with supplementary dye loading at ~60-minute intervals.

The coupling between activation and repolarisation generated a negative APD gradient along the activation path, where earlier activation times corresponded with longer action potential durations and later activation times corresponded with shorter action potentials durations. This inverse relationship was consistent with values reported in previous experimental studies using RA pacing or during SR (Toyoshima and Burgess, 1978; Hanson et al., 2009; Myles et al., 2010; Osaka

et al., 1987; Yue et al., 2005). The strong association between the activation sequence and the APD supports the idea of electrotonic current flow as the main determinant of the spatial and temporal pattern of APD. Moreover, it suggests that the distinct intrinsic repolarisation characteristics of isolated myocytes between apex-base and LV-RV play a lesser role in the overall pattern of APD across the epicardial surface. Subsequently, this association implies that through the modulation of APD by the activation sequence, dispersion in repolarisation would be predominately dictated by the current activation sequence.

## Effects of hypothermia on ventricular activation and repolarisation

The aim of this study was to examine the changes in features of epicardial electrophysiology as the temperature of a heart is reduced below physiological values. This manoeuvre was chosen to mimic the temperatures experienced during various levels of hypothermia, a condition known to promote arrhythmias. The facility for panoramic optical mapping allowed the extent of changes in conduction timing and pattern of ventricular activation to be assessed.

At both hypothermic temperatures, there was an increase in APD and slowing in CV; however, only at 17°C was there an observed significant increase in the dispersion of APD. This discrepancy could be due to the magnitude of the effect of hypothermia on intercellular uncoupling at 31°C compared to 17°C, where the effect is significantly enhanced. These findings were consistent with the increased occurrence of VT/VF in these heart preparations at 17°C, where there was the presence of spatially discordant alternans. Enhanced dispersion in APD in conjunction with slowed conduction velocity is a major substrate in the development of re-entrant arrhythmias. This discrepancy in APD dispersion between 31°C and 17°C may also offer an explanation for the low incidence of arrhythmias in the clinical setting during therapeutic hypothermia.

This study indicates that cooling of the heart preparation results in a number of profound physiological changes in electrophysiology, where these changes are significantly more pronounced during severe hypothermia, leading to the likely increased susceptibility to arrhythmias at this temperature.

## Effects of different pacing conditions on epicardial electrophysiology in normal and chronic MI hearts

The aim of this study was to investigate the effects of different modes of pacing on the activation and repolarisation sequence, and distribution of APD across the epicardial surface using the panoramic optical mapping system. Specifically, comparing single ventricular pacing and simultaneous and sequential bi-ventricular (BiV) pacing against RA pacing within both the normal (control) rabbit heart and a rabbit model of chronic MI.

In this study, the inverse relationship between APD and activation time that was pronounced during RA pacing tended to become more flattened during ventricular pacing. When comparing spatial differences in APD times across pacing regimes, there was a clear gradient from the longest APD times at the mid-ventricular and apex regions to the shortest APD times at the base. This APD gradient was maintained across all forms of pacing. This is consistent with previous literature describing differences in isolated myocyte electrophysiology across the ventricle (Salata et al., 1996; Cheng et al., 1999) and suggests that the intrinsic repolarisation characteristics of the cells becomes the dominant feature in the distribution of APD times across the epicardial surface during acute ventricular pacing. In interpreting these findings it is important to consider the time period over which stimulation is applied. In a previous study within rabbit hearts, the same loss of inverse relationship between APD and activation time occurred when reverting from RA pacing to ventricular pacing for a short period (~5 minutes) (Costard-Jäckle et al., 1989). However, the same study shows that after an extended period of the same pacing (~120 minutes) there is a return of a strong inverse relationship, seen as a slow adaptation in APD to the change in activation sequence. This observation contradicts some of the current literature, which suggests that the spatial and temporal distribution of APD within the myocardium is the result of an effectively instantaneous interplay between intrinsic cellular properties and electrotonic interactions. An APD adapting to extended periods of pacing will result in a completely altered spatial distribution in APD throughout the myocardium. Electrotonic interactions are a passive electrical phenomenon, which occurs over a short time course (<1s) in comparison to the long time course (over hours) of the changes seen in APD by Costard-Jäckle et al. This suggests that an alternative mechanism is involved in

modulating APD via the activation sequence over an extended time interval. The key question is how the direction of the activation sequence triggers possible changes in ion channel expression and activity of gap junctional proteins, thereby modulating APD. One possible mechanism is through mechano-electrical feedback effects. Specifically, the stretch-induced changes in $Ca^{2+}$ flux (Allen and Kentish, 1985; Kentish and Wrzosek, 1998), handling (Gamble et al., 1992; White et al., 1993) and sensitivity (Allen and Kurihara, 1982), which would be altered in relation to a change in activation sequence. Therefore, the changes observed in APD are likely a result of the complex interaction of a number of signalling pathways, due to the triggering of mechano-electrical feedback effects in response to changes in activation sequence.

The MI group displayed a significant increase in the range of APD across the LV during RA pacing when compared to the control group. This increase in the range of APD suggests that there was heterogeneous regional changes in APD on the epicardial surface. A number of studies have identified prolongation of APD after an MI, in either isolated myocytes (McIntosh et al., 2000; Beuckelmann et al., 1993) or intact myocardium (Yan et al., 2001; Akar and Rosenbaum, 2003; Poelzing et al., 2005). The data presented show both shortening and prolongation in APD in a non-uniform distribution across the epicardium.

Consequently, there was a significant increase in the dispersion of repolarisation across the LV during RA pacing. Given the absence of any significant changes in the activation sequence due to remodelling within the non-infarcted myocardium, it is therefore likely that the increase in dispersion of repolarisation was directly linked to the elevated range of APD.

An inverse relationship emerged between APD and activation time during RA pacing. The slope of this relationship in the LV was comparable to the control group, with negligible differences. During all of the ventricular forms of pacing, there was a diminished relationship between APD and activation time with a poor correlation between the two parameters, equivalent to the control group.

Similar to the pattern seen during RA pacing, there were no significant differences in the distribution and range of activation times across the epicardial

surface when comparing the MI group to the control group for ventricular pacing regimes.

The MI group exhibited a significant increase in the range of APD across the LV for all forms of ventricular pacing when compared to the control group. However, no significant differences were found when comparing the range of APD across the RV.

Despite significant remodelling within the non-infarcted myocardium, there were no significant effects on conduction based on the observed activation times. However, heterogeneous changes in APD across the epicardium were observed, consistent with previous reports of MI-induced effects on APD. The reason for the non-uniform changes in APD is likely a combination of the degree of remodelling in different regions of the myocardium and the regional differences in intrinsic ionic current densities.

## Development of a 3D model of active and passive properties of rabbit LV

The aim of this study was to develop a realistic 3D computational model of the rabbit left ventricle, simulating both passive and active mechanical properties of the heart. Using this model, it could be possible to infer further information from the experimental optical mapping studies.

The model incorporated DT-MRI based anatomy, along with an orthotropic, invariant-based hyperelastic model of passive elasticity of the heart (Holzapfel and Ogden, 2009). In addition, fluid-structure interactions were modelled with the finite-element immersed boundary method and the generation of active tension through a model of excitation-contraction coupling (Niederer et al., 2006). Using this model, regional distributions of displacement and active tension were quanitified, in addition to transmural distributions of active tension.

Due to the limitation of published data for a number of key derived model parameters it proved impossible to characterise the performance of the model quantitatively. However, the model shows good qualitative agreement with

other models reported in the literature (Wang et al., 2013; Gao et al., 2014; Guccione et al., 1995; Vetter and McCulloch, 2000)

It is also important to note that the anatomical model of the LV geometry was reconstructed using cardiac DT-MRI data. The geometry of the LV used in this study is not as regular as in other models, which use an idealised approach (Guccione et al., 1995; Nash and Hunter, 2000). Therefore, although this anatomical model represents a more realistic LV geometry, this introduced irregular distributions of displacement and active tension across the LV. To construct the fibre and sheet orientation within the rabbit LV geometry a rule-based approach was used. This idealised approach is not able to fully recapitulate the true muscle structure inherit in the rabbit LV. In this model, the effects of residual stresses and strains on the LV were not included, which may alter the resultant displacement and active tension. The material property parameters for the constitutive model were derived from experimental data from swine hearts. Future work would derive the material properties using rabbit hearts made available through the optical mapping experiments presented in this thesis.

# References


Abraham, W. (2002) Cardiac resynchronization therapy: a review of clinical trials and criteria for identifying the appropriate patient. *Reviews in cardiovascular medicine*. 4S30–7.

Abraham, W. T. & Hayes, D. L. (2003) Cardiac resynchronization therapy for heart failure. *Circulation*. 108 (21), 2596–2603.

Aguado-Sierra, J. et al. (2011) Patient-specific modeling of dyssynchronous heart failure: a case study. *Progress in Biophysics and Molecular Biology*. 107 (1), 147–155.

Ai, X. et al. (2005) Ca2+/calmodulin-dependent protein kinase modulates cardiac ryanodine receptor phosphorylation and sarcoplasmic reticulum Ca2+ leak in heart failure. *Circulation research*. 97 (12), 1314–1322.

Akar, F. G. & Rosenbaum, D. S. (2003) Transmural electrophysiological heterogeneities underlying arrhythmogenesis in heart failure. *Circulation research*. 93 (7), 638–645.

Allan, A. et al. (2011) Myocardial strain estimated from standard cine MRI closely represents strain estimated from dedicated strain-encoded MRI. *Conference proceedings : ... Annual International Conference of the IEEE Engineering in Medicine and Biology Society. IEEE Engineering in Medicine and Biology Society. Annual Conference*. [Online] 20112650–2653.

Allen, D. et al. (1988) The effects of changes in muscle length during diastole on the calcium transient in ferret ventricular muscle. *The Journal of Physiology*. 406 (1), 359–370.

Allen, D. & Kentish, J. (1985) The cellular basis of the length-tension relation in cardiac muscle. *Journal of molecular and cellular cardiology*. 17 (9), 821–840.

Allen, D. & Kurihara, S. (1982) The effects of muscle length on intracellular calcium transients in mammalian cardiac muscle. *The Journal of Physiology*. 327 (1), 79–94.

Allingham, J. S. et al. (2005) The structural basis of blebbistatin inhibition and specificity for myosin II. *Nature structural & molecular biology*. 12 (4), 378–379.

Amini, A. et al. (1998) Coupled B-snake grids and constrained thin-plate splines for analysis of 2-D tissue deformations from tagged MRI. *Medical Imaging, IEEE Transactions on*. 17 (3), 344–356.

Amini, A. et al. (2001) Tag surface reconstruction and tracking of myocardial beads from SPAMM-MRI with parametric B-spline surfaces. *Medical Imaging, IEEE Transactions on*. 20 (2), 94–103.

Arge, E. & Langtangen, H. P. (1997) *Modern software tools for scientific computing*. Birkhauser.

Aronson, R. S. (1981) Afterpotentials and triggered activity in hypertrophied myocardium from rats with renal hypertension. *Circulation Research*. 48 (5), 720–727.

Arrich, J. et al. (2007) Clinical application of mild therapeutic hypothermia after cardiac arrest*. *Critical care medicine*. 35 (4), 1041–1047.

Baartscheer, A. et al. (2003) Increased Na+/H+-exchange activity is the cause of increased [Na+] i and underlies disturbed calcium handling in the rabbit pressure and volume overload heart failure model. *Cardiovascular research*. 57 (4), 1015–1024.

Baartscheer, A. et al. (2003) SR calcium handling and calcium after-transients in a rabbit model of heart failure. *Cardiovascular research*. 58 (1), 99–108.

Bachtel, A. D. et al. (2011) A novel approach to dual excitation ratiometric optical mapping of cardiac action potentials with di-4-ANEPPS using pulsed LED excitation. *Biomedical Engineering, IEEE Transactions on*. 58 (7), 2120–2126.

De Baker, J. M. et al. (1990) Ventricular tachyrdia in the infarcted, Langendorff-perfused human heart: Role of the arrangement of surviving cardiac fibers. *Journal of the American College of Cardiology*. 15 (7), 1594–1607.

Baker, L. C. et al. (2004) Effects of mechanical uncouplers, diacetyl monoxime, and cytochalasin-D on the electrophysiology of perfused mouse hearts. *American Journal of Physiology-Heart and Circulatory Physiology*. 287 (4), H1771. [online]. Available from: http://ajpheart.physiology.org/content/287/4/H1771.full.pdf.

Balay, S. et al. (2011) *PETSc Users Manual Revision 3.2*.

Banville, I. & Gray, R. A. (2002) Effect of action potential duration and conduction velocity restitution and their spatial dispersion on alternans and the stability of arrhythmias. *Journal of cardiovascular electrophysiology*. 13 (11), 1141–1149.

Barbieri, M. et al. (1994) Electrophysiological basis for the enhanced cardiac arrhythmogenic effect of isoprenaline in aged spontaneously hypertensive rats. *Journal of molecular and cellular cardiology*. 26 (7), 849–860.

Bax, J. J. et al. (2004) Echocardiographic evaluation of cardiac resynchronization therapy: ready for routine clinical use?: A critical appraisal. *Journal of the American College of Cardiology*. 44 (1), 1–9.

Bay, H. et al. (2008) Speeded-up robust features (SURF). *Computer vision and image understanding*. 110 (3), 346–359.

Beckett, P. (1970) The isolated perfused heart preparation: two suggested improvements. *Journal of Pharmacy and Pharmacology*. 22 (11), 818–822.

Bernard, S. A. et al. (2002) Treatment of comatose survivors of out-of-hospital cardiac arrest with induced hypothermia. *New England Journal of Medicine*. 346 (8), 557–563.

Bers, D. et al. (1989) Intracellular Ca2+ transients during rapid cooling contractures in guinea-pig ventricular myocytes. *The Journal of physiology*. 417 (1), 537–553.

Bers, D. M. (2002) Cardiac excitation-contraction coupling. *Nature*. 415 (6868), 198–205.

Beuckelmann, D. et al. (1992) Intracellular calcium handling in isolated ventricular myocytes from patients with terminal heart failure. *Circulation*. 85 (3), 1046–1055.

Beuckelmann, D. & Erdmann, E. (1992) Ca (2+)-currents and intracellular [Ca2+] i-transients in single ventricular myocytes isolated from terminally failing human myocardium. *Basic research in cardiology*. 87235.

Beuckelmann, D. J. et al. (1993) Alterations of K+ currents in isolated human ventricular myocytes from patients with terminal heart failure. *Circulation research*. 73 (2), 379–385.

Bigelow, W. et al. (1950) General hypothermia for experimental intracardiac surgery: the use of electrophrenic respirations, an artificial pacemaker for cardiac standstill, and radio-frequency rewarming in general hypothermia. *Annals of surgery*. 132 (3), 531.

Bishop, M. J. et al. (2009) 'Comparison of rule-based and DTMRI-derived fibre architecture in a whole rat ventricular computational model', in *Functional Imaging and Modeling of the Heart*. Springer. pp. 87–96.

Bishop, M. J. et al. (2010) Development of an anatomically detailed MRI-derived rabbit ventricular model and assessment of its impact on simulations of electrophysiological function. *American Journal of Physiology-Heart and Circulatory Physiology*. 298 (2), H699–H718.

Bishop, M. J. et al. (2007) Photon scattering effects in optical mapping of propagation and arrhythmogenesis in the heart. *Journal of electrocardiology*. 40 (6 Suppl), S75.

Bjørnstad, H. et al. (1995) Diltiazem does not increase ventricular fibrillation threshold during hypothermia. *Acta anaesthesiologica scandinavica*. 39 (5), 659–665.

Bjørnstad, H. et al. (1994) Prevention of some hypothermia induced electromechanical changes by calcium channel blockade. *Cardiovascular research*. 28 (1), 55–60.

Blanchard, E. M. et al. (1990) The effects of 2,3-butanedione monoxime on initial heat, tension, and aequorin light output of ferret papillary muscles. *Pflügers Archiv : European journal of physiology*. 416 (1-2), 219–221.

Van Bommel, R. et al. (2010) Effects of cardiac resynchronisation therapy in patients with heart failure having a narrow QRS Complex enrolled in PROSPECT. *Heart*. 96 (14), 1107–1113.

Botting, J. H. et al. (1985) Arrhythmias associated with myocardial ischaemia and infarction. *Molecular aspects of medicine*. 8 (4), 307–422.

Bourgeois, E. B. et al. (2011) Simultaneous optical mapping of transmembrane potential and wall motion in isolated, perfused whole hearts. *Journal of Biomedical Optics*. 16096020.

Bovendeerd, P. et al. (1992) Dependence of local left ventricular wall mechanics on myocardial fiber orientation: a model study. *Journal of biomechanics*. 25 (10), 1129–1140.

Brack, K. E. et al. (2013) The mechanical uncoupler blebbistatin is associated with significant electrophysiological effects in the isolated rabbit heart. *Experimental physiology*. [Online] 98 (5), 1009–1027.

Bristow, M. R. (2000) $\beta$-Adrenergic receptor blockade in chronic heart failure. *Circulation*. 101 (5), 558–569.

Bristow, M. R. et al. (2004) Cardiac-resynchronization therapy with or without an implantable defibrillator in advanced chronic heart failure. *New England Journal of Medicine*. 350 (21), 2140–2150.

Bryant, S. M. et al. (1997) Regional differences in electrical and mechanical properties of myocytes from guinea-pig hearts with mild left ventricular hypertrophy. *Cardiovascular research*. 35 (2), 315–323.

Burton, F. L. et al. (2000) Ventricular fibrillation threshold and local dispersion of refractoriness in isolated rabbit hearts with left ventricular dysfunction. *Basic research in cardiology*. 95 (5), 359–367.

Carmeliet, E. & Vereecke, J. (2002) 'Ionic currents and action potentials in cardiac cells', in *Cardiac Cellular Electrophysiology*. Springer. pp. 95–177.

Cazeau, S. et al. (2001) Effects of multisite biventricular pacing in patients with heart failure and intraventricular conduction delay. *New England Journal of Medicine*. 344 (12), 873–880.

Chauhan, V. S. et al. (2006) Increased ventricular repolarization heterogeneity in patients with ventricular arrhythmia vulnerability and cardiomyopathy: a human in vivo study. *American Journal of Physiology-Heart and Circulatory Physiology*. 290 (1), H79–H86.

Cheng, J. et al. (1999) Heterogeneous distribution of the two components of delayed rectifier K+ current: a potential mechanism of the proarrhythmic effects of methanesulfonanilideclass III agents. *Cardiovascular research*. 43 (1), 135–147.

Cheung, W. & Hamarneh, G. (2007) 'N-sift: N-dimensional scale invariant feature transform for matching medical images', in *Biomedical Imaging: From Nano to Macro, 2007. ISBI 2007. 4th IEEE International Symposium on*. 2007 pp. 720–723.

Chou, C.-C. et al. (2007) Remodelling of action potential and intracellular calcium cycling dynamics during subacute myocardial infarction promotes ventricular arrhythmias in Langendorff-perfused rabbit hearts. *The Journal of physiology*. 580 (3), 895–906.

CIBC (2015)

Clark, A. L. et al. (2008) The prevalence and incidence of left bundle branch block in ambulant patients with chronic heart failure. *European journal of heart failure*. 10 (7), 696–702.

Cleland, J. G. et al. (2006) Longer-term effects of cardiac resynchronization therapy on mortality in heart failure [the CArdiac REsynchronization-Heart Failure (CARE-HF) trial extension phase]. *European Heart Journal*. 27 (16), 1928–1932.

Cleland, J. G. et al. (1999) Sudden death in heart failure: vascular or electrical? *European journal of heart failure*. 1 (1), 41–45.

Cleland, J. G. et al. (2005) The effect of cardiac resynchronization on morbidity and mortality in heart failure. *New England Journal of Medicine*. 352 (15), 1539–1549.

Cohen, L. et al. (1968) Light scattering and birefringence changes during nerve activity. *Nature*. 218438–441.

Cohen, L. B. & Salzberg, B. M. (1978) *Optical measurement of membrane potential*. Springer.

Cooper, J. A. (1987) Effects of cytochalasin and phalloidin on actin. *The Journal of cell biology*. 105 (4), 1473–1478.

Coromilas, J. et al. (2002) Effects of Pinacidil on Electrophysiological Properties of Epicardial Border Zone of Healing Canine Infarcts Possible Effects of KATP Channel Activation. *Circulation*. 105 (19), 2309–2317.

Costa, K. et al. (1996) A three-dimensional finite element method for large elastic deformations of ventricular myocardium: I—Cylindrical and spherical polar coordinates. *Journal of biomechanical engineering*. 118 (4), 452–463.

Costa, K. D. et al. (2001) Modelling cardiac mechanical properties in three dimensions. *Philosophical Transactions of the Royal Society of London A: Mathematical, Physical and Engineering Sciences*. 359 (1783), 1233–1250.

Costa, K. D. et al. (1997) Three-dimensional residual strain in midanterior canine left ventricle. *American Journal of Physiology-Heart and Circulatory Physiology*. 273 (4), H1968.

Costard-Jäckle, A. et al. (1989) Slow and long-lasting modulation of myocardial repolarization produced by ectopic activation in isolated rabbit hearts. Evidence for cardiac“ memory”. *Circulation*. 80 (5), 1412–1420.

Cotran, R. S. et al. (1999) *Robbins pathologic basis of disease*.

Coulombe, A. et al. (1990) Effect of 2,3-butanedione 2-monoxime on slow inward and transient outward currents in rat ventricular myocytes. *Journal of molecular and cellular cardiology*. 22 (8), 921–932.

Cowie, M. et al. (2000) Survival of patients with a new diagnosis of heart failure: a population based study. *Heart*. 83 (5), 505–510.

Cowie, M. et al. (1997) The epidemiology of heart failure. *European heart journal*. 18 (2), 208–225.

Cranefield, P. F. & Hoffman, B. F. (1958) Propagated repolarization in heart muscle. *The Journal of general physiology*. 41 (4), 633–649.

Crum, W. et al. (2004) Non-rigid image registration: theory and practice. *British journal of radiology*. 77 (suppl 2), S140–S153.

Cubbon, R. M. & Witte, K. K. A. (2009) Cardiac resynchronisation therapy for chronic heart failure and conduction delay. *BMJ*. 338.

Demer, L. L. & Yin, F. (1983) Passive biaxial mechanical properties of isolated canine myocardium. *The Journal of physiology*. 339 (1), 615–630.

Demiray, H. (1976) Stresses in ventricular wall. *Journal of Applied Mechanics*. 43194.

Dhein, S. et al. (1999) Effects of the gap junction uncoupler palmitoleic acid on the activation and repolarization wavefronts in isolated rabbit hearts. *British journal of pharmacology*. 128 (7), 1375–1384.

Dhein, S. et al. (2005) *Practical methods in cardiovascular research*. Springer Verlag.

Di Diego, J. M. et al. (1996) I (to) and action potential notch are smaller in left vs. right canine ventricular epicardium. *American Journal of Physiology-Heart and Circulatory Physiology*. 271 (2), H548–H561.

Dokos, S. et al. (2002) Shear properties of passive ventricular myocardium. *American Journal of Physiology-Heart and Circulatory Physiology*. 283 (6), H2650. [online]. Available from: http://ajpheart.physiology.org/content/283/6/H2650.full.pdf.

Döring, H. J. et al. (1988) *The Isolated Perfused Warm-blood Heart According to Langendorff*. Biomesstechnik-Verlag March.

Efimov, I. R. et al. (2004) Optical imaging of the heart. *Circulation research*. 95 (1), 21–33.

Efimov, I. R. et al. (1994) Optical mapping of repolarization and refractoriness from intact hearts. *Circulation*. 90 (3), 1469–1480.

Egorov, Y. V. et al. (2012) Hypothermia-induced spatially discordant action potential duration alternans and arrhythmogenesis in nonhibernating versus hibernating mammals. *American Journal of Physiology-Heart and Circulatory Physiology*. 303 (8), H1035–H1046.

Engdahl, J. et al. (2002) The epidemiology of out-of-hospital "sudden"cardiac arrest. *Resuscitation*. 52 (3), 235–245.

Entcheva, E. & Bien, H. (2006) Macroscopic optical mapping of excitation in cardiac cell networks with ultra-high spatiotemporal resolution. *Progress in biophysics and molecular biology*. 92 (2), 232–257.

Eriksson, T. et al. (2013) Influence of myocardial fiber/sheet orientations on left ventricular mechanical contraction. *Mathematics and Mechanics of Solids*. 1081286513485779.

Erlebacher, J. A. et al. (1984) Early dilation of the infarcted segment in acute transmural myocardial infarction: role of infarct expansion in acute left ventricular enlargement. *Journal of the American College of Cardiology*. 4 (2), 201–208.

Falgout, R. & Yang, U. (2002) hypre: A library of high performance preconditioners. *Computational Science—ICCS 2002*. 632–641.

Fast, V. (2005) Recording action potentials using voltage-sensitive dyes. *Practical methods in cardiovascular research*. 233–255.

Fedorov, V. V. et al. (2007) Application of blebbistatin as an excitation-contraction uncoupler for electrophysiologic study of rat and rabbit hearts. *Heart Rhythm*. 4 (5), 619–626.

Fedorov, V. V. et al. (2008) Electrophysiological mechanisms of antiarrhythmic protection during hypothermia in winter hibernating versus nonhibernating mammals. *Heart Rhythm*. 5 (11), 1587–1596.

Fedorov, V. V. et al. (2005) Hibernator< i> Citellus undulatus</i> maintains safe cardiac conduction and is protected against tachyarrhythmias during extreme hypothermia: Possible role of Cx43 and Cx45 up-regulation. *Heart Rhythm*. 2 (9), 966–975.

Flather, M. D. et al. (2000) Long-term ACE-inhibitor therapy in patients with heart failure or left-ventricular dysfunction: a systematic overview of data from individual patients. *The Lancet*. 355 (9215), 1575–1581.

Fleet, W. F. et al. (1994) Marked activation delay caused by ischemia initiated after regional K+ elevation in in situ pig hearts. *Circulation*. 90 (6), 3009–3017.

Foley, P. W. et al. (2011) Cardiac resynchronisation therapy in patients with heart failure and a normal QRS duration: the RESPOND study. *Heart*. 97 (13), 1041–1047.

Franz, M. R. et al. (1987) Monophasic action potential mapping in human subjects with normal electrocardiograms: direct evidence for the genesis of the T wave. *Circulation*. 75 (2), 379–386.

Furukawa, Y. et al. (2000) Anisotropic conduction prolongs ventricular repolarization and increases its spatial gradient in the intact canine heart. *Japanese circulation journal*. 64 (4), 287–294.

Gambassi, G. et al. (1994) Temperature modulates calcium homeostasis and ventricular arrhythmias in myocardial preparations. *Cardiovascular research*. 28 (3), 391–399.

Gamble, J. et al. (1992) Myocardial stretch alters twitch characteristics and Ca2+ loading of sarcoplasmic reticulum in rat ventricular muscle. *Cardiovascular research*. 26 (9), 865–870.

Gao, H. et al. (2014) Dynamic finite-strain modelling of the human left ventricle in health and disease using an immersed boundary-finite element method. *IMA Journal of Applied Mathematics*. hxu029.

Gatta, C. et al. (2011) 'Non-rigid multi-modal registration of coronary arteries using SIFTflow', in *Pattern Recognition and Image Analysis*. Springer. pp. 159–166.

Gehi, A. et al. (2005) Primary prophylaxis with the implantable cardioverter-defibrillator: the need for improved risk stratification. *JAMA*. 294 (8), 958–960.

Gilbert, S. H. et al. (2009) 'A quantitative comparison of the myocardial fibre orientation in the rabbit as determined by histology and by diffusion tensor-MRI', in *Functional Imaging and Modeling of the Heart*. Springer. pp. 49–57.

Glukhov, A. V. et al. (2012) 'Cardiac electrical alternans and ventricular fibrillation during hypothermia in non-hibernating versus hibernating animals: Role of propagation velocity and dispersion of repolarization', in *Living in a Seasonal World*. Springer. pp. 293–303.

Greenberg, H. et al. (2004) Analysis of mortality events in the multicenter automatic defibrillator implantation trial (MADIT-II). *Journal of the American College of Cardiology*. 43 (8), 1459–1465.

Greenstein, J. L. et al. (2000) Role of the calcium-independent transient outward current Ito1 in shaping action potential morphology and duration. *Circulation Research*. 87 (11), 1026–1033.

Griffith, B. (2015) *IBAMR: An adaptive and distributed-memory parallel implementation of the immersed boundary method*. [online]. Available from: http://code.google.com/p/ibamr/.

Griffith, B. E. (2009) An accurate and efficient method for the incompressible Navier-Stokes equations using the projection method as a preconditioner. *Journal of Computational Physics*. 228 (20), 7565–7595.

Griffith, B. E. et al. (2007) An adaptive, formally second order accurate version of the immersed boundary method. *Journal of Computational Physics*. 223 (1), 10–49.

Griffith, B. E. (2012) Immersed boundary model of aortic heart valve dynamics with physiological driving and loading conditions. *International Journal for Numerical Methods in Biomedical Engineering*. 28 (3), 317–345.

Griffith, B. E. et al. (2010) Parallel and adaptive simulation of cardiac fluid dynamics. *Advanced computational infrastructures for parallel and distributed adaptive applications*. 105.

Griffith, B. E. & Luo, X. (2012) Hybrid finite difference/finite element version of the immersed boundary method. *Submitted, preprint available from http://www. cims. nyu. edu/\~ griffith*.

Grinvald, A. & Hildesheim, R. (2004) VSDI: a new era in functional imaging of cortical dynamics. *Nature Reviews Neuroscience*. 5 (11), 874–885.

Group, M.-H. S. & others (1999) Effect of metoprolol CR/XL in chronic heart failure: metoprolol CR/XL randomised intervention trial in-congestive heart failure (MERIT-HF). *The Lancet*. 353 (9169), 2001–2007.

Guccione, J. et al. (1991) Passive material properties of intact ventricular myocardium determined from a cylindrical model. *Journal of biomechanical engineering*. 113 (1), 42.

Guccione, J. M. et al. (1995) Finite element stress analysis of left ventricular mechanics in the beating dog heart. *Journal of biomechanics*. 28 (10), 1167–1177.

Güttler, K. et al. (1981) The mechanical atrioventricular time of isolated hearts as a correlate of the atrioventricular conduction time. *Advances in myocardiology*. 3153–158.

Gwathmey, J. K. et al. (1987) Abnormal intracellular calcium handling in myocardium from patients with end-stage heart failure. *Circulation research*. 61 (1), 70–76.

Ter Haar Romeny, B. M. (1999) 'Scale-space theory for multiscale geometric image analysis', in *CVPR99 IEEE International Conference on Computer Vision and Pattern Recognition*. 1999

Hanson, B. et al. (2009) Interaction of activation-repolarization coupling and restitution properties in humans. *Circulation. Arrhythmia and electrophysiology*. [Online] 2 (2), 162–170.

HARRIS, A. S. (1950) Delayed development of ventricular ectopic rhythms following experimental coronary occlusion. *Circulation*. 1 (6), 1318–1328.

Harris, A. S. et al. (1954) Excitatory factors in ventricular tachycardia resulting from myocardial ischemia. Potassium a major excitant. *Science*. 119 (3085), 200–203.

Hayashi, H. et al. (2003) Effects of cytochalasin D on electrical restitution and the dynamics of ventricular fibrillation in isolated rabbit heart. *Journal of cardiovascular electrophysiology*. 14 (10), 1077–1084.

Henriquez, C. S. et al. (2004) Three-dimensional propagation in mathematical models: integrative model of the mouse heart. *Cardiac Electrophysiology from Cell to Bedside*. 4.

Hillege, H. L. et al. (2006) Renal function as a predictor of outcome in a broad spectrum of patients with heart failure. *Circulation*. 113 (5), 671–678.

Hobbs, F. R. et al. (2007) Prognosis of all-cause heart failure and borderline left ventricular systolic dysfunction: 5 year mortality follow-up of the Echocardiographic Heart of England Screening Study (ECHOES). *European heart journal*.

Holzapfel, G. A. et al. (2000) A new constitutive framework for arterial wall mechanics and a comparative study of material models. *Journal of elasticity*. 61 (1), 1–48.

Holzapfel, G. A. & Ogden, R. W. (2003) *Biomechanics of soft tissue in cardiovascular systems*. Springer Verlag.

Holzapfel, G. A. & Ogden, R. W. (2009) Constitutive modelling of passive myocardium: a structurally based framework for material characterization. *Philosophical Transactions of the Royal Society A: Mathematical, Physical and Engineering Sciences*. 367 (1902), 3445–3475. [online]. Available from: http://rsta.royalsocietypublishing.org/content/367/1902/3445.full.pdf.

Horn, B. K. & Schunck, B. G. (1981) Determining optical flow. *Artificial intelligence*. 17 (1), 185–203.

Hornung, R. D. et al. (2006) Managing complex data and geometry in parallel structured AMR applications. *Engineering with Computers*. 22 (3), 181–195.

Hornung, R. D. & Kohn, S. R. (2002) Managing application complexity in the SAMRAI object-oriented framework. *Concurrency and Computation: Practice and Experience*. 14 (5), 347–368.

Horowitz, A. et al. (1988) Structural three-dimensional constitutive law for the passive myocardium. *Journal of biomechanical engineering*. 110 (3), 200–207.

Houser, S. R. et al. (2000) Abnormalities of calcium cycling in the hypertrophied and failing heart. *Journal of molecular and cellular cardiology*. 32 (9), 1595–1607.

Hsieh, Y. C. et al. (2009) Therapeutic hypothermia (30 degrees C) enhances arrhythmogenic substrates, including spatially discordant alternans, and facilitates pacing-induced ventricular fibrillation in isolated rabbit hearts. *Circulation journal: official journal of the Japanese Circulation Society*. 73 (12), 2214.

Hsieh, Y.-C. et al. (2011) Short-duration therapeutic hypothermia causes prompt connexin43 gap junction remodeling in isolated rabbit hearts. *Circulation journal: official journal of the Japanese Circulation Society*. 75 (7), 1706.

Huang, J. et al. (1999) Spatio-temporal tracking of myocardial deformations with a 4-D B-spline model from tagged MRI. *Medical Imaging, IEEE Transactions on*. 18 (10), 957–972.

Humphrey, J. et al. (1990) Determination of a constitutive relation for passive myocardium: II. Parameter estimation. *Journal of biomechanical engineering*. 112 (3), 340–346.

Hunter, P. et al. (1997) Computational electromechanics of the heart. *Computational biology of the heart*. 12347–407.

Hunter, P. et al. (1998) Modelling the mechanical properties of cardiac muscle. *Progress in biophysics and molecular biology*. 69 (2-3), 289–331.

Hunter, P. J. et al. (2001) Integrative models of the heart: achievements and limitations. *Philosophical Transactions of the Royal Society of London A: Mathematical, Physical and Engineering Sciences*. 359 (1783), 1049–1054.

Hunter, P. J. et al. (2003) Modeling total heart function. *Annual review of biomedical engineering*. 5147–177.

Huyghe, J. M. et al. (1992) Porous medium finite element model of the beating left ventricle. *American Journal of Physiology-Heart and Circulatory Physiology*. 262 (4), H1256–H1267.

Ino, F. et al. (2005) A data distributed parallel algorithm for nonrigid image registration. *Parallel Computing*. 31 (1), 19–43.

Jalife, J. et al. (1998) A fungal metabolite that eliminates motion artifacts. *Journal of cardiovascular electrophysiology*. 9 (12), 1358–1362.

Janse, M. J. (2004) Electrophysiological changes in heart failure and their relationship to arrhythmogenesis. *Cardiovascular research*. 61 (2), 208–217.

Janse, M. J. et al. (1980) Flow of" injury" current and patterns of excitation during early ventricular arrhythmias in acute regional myocardial ischemia in isolated porcine and canine hearts. Evidence for two different arrhythmogenic mechanisms. *Circulation Research*. 47 (2), 151–165.

Janssen, P. & de Tombe, P. P. (1997) Uncontrolled sarcomere shortening increases intracellular Ca2+ transient in rat cardiac trabeculae. *American Journal of Physiology-Heart and Circulatory Physiology*. 272 (4), H1892–H1897.

Joyner, R. (1986) Modulation of repolarization by electrotonic interactions. *Japanese heart journal*. 27167–183.

Joyner, R. W. et al. (1991) Cellular mechanisms of delayed recovery of excitability in ventricular tissue. *American Journal of Physiology-Heart and Circulatory Physiology*. 260 (1), H225–H233.

Kääb, S. et al. (1996) Ionic mechanism of action potential prolongation in ventricular myocytes from dogs with pacing-induced heart failure. *Circulation research*. 78 (2), 262–273.

Kaplinsky, E. et al. (1979) Role of endocardial activation in malignant ventricular arrhythmias associated with acute ischemia. *Journal of electrocardiology*. 12 (3), 299–306.

Kaplinsky, E. et al. (1979) Two periods of early ventricular arrhythmia in the canine acute myocardial infarction model. *Circulation*. 60 (2), 397–403.

Kass, D. (2002) Ventricular dyssynchrony and mechanisms of resynchronization therapy. *European Heart Journal Supplements*. 4 (suppl D), D23.

Kentish, J. C. (1991) Combined inhibitory actions of acidosis and phosphate on maximum force production in rat skinned cardiac muscle. *Pflügers Archiv : European journal of physiology*. 419 (3-4), 310–318.

Kentish, J. C. & Wrzosek, A. (1998) Changes in force and cytosolic Ca2+ concentration after length changes in isolated rat ventricular trabeculae. *The Journal of physiology*. 506 (2), 431–444.

Kerckhoffs, R. C. et al. (2007) Coupling of a 3D finite element model of cardiac ventricular mechanics to lumped systems models of the systemic and pulmonic circulation. *Annals of biomedical engineering*. 35 (1), 1–18.

Kerckhoffs, R. C. et al. (2009) Effects of biventricular pacing and scar size in a computational model of the failing heart with left bundle branch block. *Medical image analysis*. 13 (2), 362–369.

Kerwin, W. S. & Prince, J. L. (1998) Cardiac material markers from tagged MR images. *Medical image analysis*. 2 (4), 339–353.

Kettlewell, S. et al. (2004) The electrophysiological and mechanical effects of 2, 3-butane-dione monoxime and cytochalasin-D in the Langendorff perfused rabbit heart. *Experimental physiology*. 89 (2), 163–172.

Khan, N. K. et al. (2007) Prevalence of ECG abnormalities in an international survey of patients with suspected or confirmed heart failure at death or discharge. *European journal of heart failure*. 9 (5), 491–501.

Kirk, B. S. et al. (2006) A C++ library for parallel adaptive mesh refinement/coarsening simulations. *Engineering with Computers*. 22 (3), 237–254.

Knisley, S. B. et al. (2000) Ratiometry of transmembrane voltage-sensitive fluorescent dye emission in hearts. *American Journal of Physiology-Heart and Circulatory Physiology*. 279 (3), H1421–H1433.

Kohl, P. & Sachs, F. (2001) Mechanoelectric feedback in cardiac cells. *Philosophical Transactions of the Royal Society of London A: Mathematical, Physical and Engineering Sciences*. 359 (1783), 1173–1185.

Kolega, J. (2004) Phototoxicity and photoinactivation of blebbistatin in UV and visible light. *Biochemical and biophysical research communications*. 320 (3), 1020–1025.

Kong, W. et al. (2003) Emission ratiometry for simultaneous calcium and action potential measurements with coloaded dyes in rabbit hearts: reduction of motion and drift. *Journal of cardiovascular electrophysiology*. 14 (1), 76–82.

Kongstad, O. et al. (2002) Global and local dispersion of ventricular repolarization: endocardial monophasic action potential mapping in swine and humans by using an electro-anatomical mapping system. *Journal of electrocardiology*. 35 (2), 159–167.

Kovacs, S. J. et al. (2001) Modelling cardiac fluid dynamics and diastolic function. *Philosophical Transactions of the Royal Society of London A: Mathematical, Physical and Engineering Sciences*. 359 (1783), 1299–1314.

Krebs, M. E. et al. (1998) Short-Term Rapid Ventricular Pacing Prolongs Ventricular Refractoriness in Patients. *Journal of cardiovascular electrophysiology*. 9 (10), 1036–1042.

Kuijpers, N. H. et al. (2012) Modeling cardiac electromechanics and mechanoelectrical coupling in dyssynchronous and failing hearts. *Journal of cardiovascular translational research*. 5 (2), 159–169.

Kuo, C.-S. et al. (1983) Characteristics and possible mechanism of ventricular arrhythmia dependent on the dispersion of action potential durations. *Circulation*. 67 (6), 1356–1367.

Lacroix, D. et al. (1999) Factors affecting epicardial dispersion of repolarization: a mapping study in the isolated porcine heart. *Cardiovascular research*. 41 (3), 563–574.

Lakowicz, J. R. (2007) *Principles of fluorescence spectroscopy*. Springer Science \& Business Media.

Langendorff, O. (1895) Untersuchungen am überlebenden Säugetierherzen. *Pflüger's Arch Ges Physiol*. 291–331.

Laurita, K. R. et al. (1996) Modulation of ventricular repolarization by a premature stimulus role of epicardial dispersion of repolarization kinetics demonstrated by optical mapping of the intact guinea pig heart. *Circulation Research*. 79 (3), 493–503.

Lee, B. H. et al. (2004) Effect of ischemic preconditioning based on different epicardial branching patterns of the left coronary artery in the rabbit heart. *Investigative Surgery*. 17 (2), 71–79.

Lee, M. H. et al. (2001) Effects of diacetyl monoxime and cytochalasin D on ventricular fibrillation in swine right ventricles. *American journal of physiology. Heart and circulatory physiology*. 280 (6), H2689–96.

LeGrice, I. J. et al. (1995) Laminar structure of the heart: ventricular myocyte arrangement and connective tissue architecture in the dog. *American Journal of Physiology-Heart and Circulatory Physiology*. 269 (2), H571–H582.

Li, G.-R. et al. (2002) Transmural action potential and ionic current remodeling in ventricles of failing canine hearts. *American Journal of Physiology-Heart and Circulatory Physiology*. 283 (3), H1031–H1041.

Liang, Y. et al. (2005) QT dispersion failed to estimate the global dispersion of ventricular repolarization measured using monophasic action potential mapping technique in swine and patients. *Journal of electrocardiology*. 38 (1), 19–27.

Lichtman, J. W. & Conchello, J.-A. (2005) Fluorescence microscopy. *Nature methods*. 2 (12), 910–919.

Linde, C. et al. (2010) Cardiac resynchronization therapy in asymptomatic or mildly symptomatic heart failure patients in relation to etiology: results from the REVERSE (REsynchronization reVErses Remodeling in Systolic Left vEntricular Dysfunction) study. *Journal of the American College of Cardiology*. 56 (22), 1826–1831.

Linde, C. et al. (2002) Long-term benefits of biventricular pacing in congestive heart failure: results from the MUltisite STimulation in cardiomyopathy (MUSTIC) study. *Journal of the American College of Cardiology*. 40 (1), 111–118.

Linde, C. et al. (2008) Randomized trial of cardiac resynchronization in mildly symptomatic heart failure patients and in asymptomatic patients with left ventricular dysfunction and previous heart failure symptoms. *Journal of the American College of Cardiology*. 52 (23), 1834–1843.

Litwin, S. E. et al. (2000) Dyssynchronous Ca2+ sparks in myocytes from infarcted hearts. *Circulation Research*. 87 (11), 1040–1047.

Liu, B. et al. (1991) Temperature effects on the Na and Ca currents in rat and hedgehog ventricular muscle. *Cryobiology*. 28 (1), 96–104.

Liu, Y. et al. (1993) Effects of diacetyl monoxime on the electrical properties of sheep and guinea pig ventricular muscle. *Cardiovascular research*. 27 (11), 1991–1997.

Loew, L. M. (2011) 'Design and use of organic voltage sensitive dyes', in *Membrane Potential Imaging in the Nervous System*. Springer. pp. 13–23.

Loew, L. M. (2001) Mechanisms and principles of voltage-sensitive fluorescence. *Optical Mapping of Cardiac Excitation and Arrhythmias, edited by Rosenbaum DS and Jalife J. Armonk, NY: Futura*. 33–46.

Loew, L. M. (1996) Potentiometric dyes: imaging electrical activity of cell membranes. *Pure and applied chemistry*. 68 (7), 1405–1409.

Lou, Q. et al. (2012) The role of dynamic instability and wavelength in arrhythmia maintenance as revealed by panoramic imaging with blebbistatin vs. 2, 3-butanedione monoxime. *American Journal of Physiology-Heart and Circulatory Physiology*. 302 (1), H262–H269.

Lowe, D. G. (1999) 'Object recognition from local scale-invariant features', in *Proceedings of the Seventh IEEE International Conference on Computer Vision*. [Online]. 1999 Ieee. pp. 1150–1157 vol.2.

Di Luozzo, G. & Griepp, R. B. (2012) 'Cerebral protection for aortic arch surgery: deep hypothermia', in *Seminars in thoracic and cardiovascular surgery*. 2012 pp. 127–130.

Main, M. et al. (1998) Regional differences in action potential characteristics and membrane currents of guinea-pig left ventricular myocytes. *Experimental physiology*. 83 (06), 747–761.

Mallet, M. (2002) Pathophysiology of accidental hypothermia. *Qjm*. 95 (12), 775–785.

Marshall, C. et al. (2002) Determinants of cardiac Na+/Ca2+ exchanger temperature dependence: NH2-terminal transmembrane segments. *American Journal of Physiology-Cell Physiology*. 283 (2), C512–C520.

McCormick, M. et al. (2011) Modelling left ventricular function under assist device support. *International Journal for Numerical Methods in Biomedical Engineering*. 27 (7), 1073–1095.

McInerney, T. & Terzopoulos, D. (1995) A dynamic finite element surface model for segmentation and tracking in multidimensional medical images with application to cardiac 4D image analysis. *Computerized Medical Imaging and Graphics*. 19 (1), 69–83.

McIntosh, M. et al. (2000) Heterogeneous changes in action potential and intracellular Ca2+ in left ventricular myocyte sub-types from rabbits with heart failure. *Cardiovascular research*. 45 (2), 397–409.

McMurray, J. J. et al. (2003) Effects of candesartan in patients with chronic heart failure and reduced left-ventricular systolic function taking angiotensin-converting-enzyme inhibitors: the CHARM-Added trial. *The Lancet*. 362 (9386), 767–771.

McMurray, J. J. & Pfeffer, M. A. (2005) Heart failure . *The Lancet* . [Online] 365 (9474), 1877 – 1889. [online]. Available from: http://www.sciencedirect.com/science/article/pii/S0140673605666214.

McMurray, J. J. & Stewart, S. (2000) Epidemiology, aetiology, and prognosis of heart failure. *Heart*. 83 (5), 596–602.

McQueen, D. M. & Peskin, C. S. (2002) 'Heart simulation by an immersed boundary method with formal second-order accuracy and reduced numerical viscosity', in *Mechanics for a New Mellennium*. Springer. pp. 429–444.

McQueen, D. & Peskin, C. (1997) Shared-memory parallel vector implementation of the immersed boundary method for the computation of blood flow in the beating mammalian heart. *The Journal of Supercomputing*. 11 (3), 213–236.

Min, G. et al. (2014) Effects of Different Ventricular Pacing Modes on Ventricular Repolarisation in Patients Undergoing Cardiac Resynchronisation Therapy: A single-centre study. *Heart, Lung and Circulation*.

Misier, A. R. R. et al. (1995) Dispersion of "refractoriness" in noninfarcted myocardium of patients with ventricular tachycardia or ventricular fibrillation after myocardial infarction. *Circulation*. 91 (10), 2566–2572.

Moe, A. E. et al. (2005) Improvements in LED-based fluorescence analysis systems. *Sensors and Actuators B: Chemical*. 111230–241.

Moe, G. W. & Armstrong, P. (1999) Pacing-induced heart failure: a model to study the mechanism of disease progression and novel therapy in heart failure. *Cardiovascular research*. 42 (3), 591–599.

Morad, M. & Salama, G. (1979) Optical probes of membrane potential in heart muscle. *The Journal of physiology*. 292 (1), 267–295.

Moradi, M. et al. (2006) 'Deformable registration using scale space keypoints', in *Medical Imaging*. 2006 p. 61442G–61442G.

Mortensen, E. et al. (1993) Changes in ventricular fibrillation threshold during acute hypothermia. A model for future studies. *Journal of basic and clinical physiology and pharmacology*. 4 (4), 313–320.

Myerburg, R. J. & Castellanos, A. (2006) Emerging paradigms of the epidemiology and demographics of sudden cardiac arrest. *Heart Rhythm*. 3 (2), 235–239.

Myles, R. C. et al. (2010) Effect of activation sequence on transmural patterns of repolarization and action potential duration in rabbit ventricular myocardium. *American Journal of Physiology-Heart and Circulatory Physiology*. 299 (6), H1812–H1822.

Nash, M. P. & Hunter, P. J. (2000) Computational mechanics of the heart. *Journal of elasticity and the physical science of solids*. 61 (1-3), 113–141.

Nerbonne, J. M. & Kass, R. S. (2005) Molecular physiology of cardiac repolarization. *Physiological reviews*. 85 (4), 1205–1253.

Ng, A. G. et al. (2002) Depressed inotropic response to increased preload in rabbit hearts with left-ventricular dysfunction induced by chronic myocardial infarction. *Pflügers Archiv European Journal of Physiology*. 444 (4), 513–522.

Ng, G. A. et al. (1998) Non-uniform prolongation of intracellular Ca2+ transients recorded from the epicardial surface of isolated hearts from rabbits with heart failure. *Cardiovascular research*. 37 (2), 489–502.

Nickerson, D. et al. (2001) A model of cardiac cellular electromechanics. *Philosophical Transactions of the Royal Society of London. Series A: Mathematical, Physical and Engineering Sciences*. 359 (1783), 1159–1172.

Niederer, S. et al. (2006) A quantitative analysis of cardiac myocyte relaxation: a simulation study. *Biophysical journal*. 90 (5), 1697–1722.

Niederer, S. et al. (2009) The importance of model parameters and boundary conditions in whole organ models of cardiac contraction. *Functional Imaging and Modeling of the Heart*. 348–356.

Niederer, S. A. et al. (2011) Length-dependent tension in the failing heart and the efficacy of cardiac resynchronization therapy. *Cardiovascular research*. 89 (2), 336–343.

Nielsen, P. et al. (1991) Mathematical model of geometry and fibrous structure of the heart. *American Journal of Physiology-Heart and Circulatory Physiology*. 260 (4), H1365–H1378.

Nisbet, A. M. et al. (2014) Acidosis slows electrical conduction through the atrio-ventricular node. *Frontiers in physiology*. 5.

Nisbet, A. M. (2008) *The electrophysiology of the atrioventricular node in normal and failing rabbit hearts*.

Nordsletten, D. et al. (2011) Fluid-solid coupling for the investigation of diastolic and systolic human left ventricular function. *International Journal for Numerical Methods in Biomedical Engineering*. 27 (7), 1017–1039.

Novak, V. P. et al. (1994) Regional mechanical properties of passive myocardium. *Journal of biomechanics*. 27 (4), 403–412.

Nuss, H. B. et al. (1999) Cellular basis of ventricular arrhythmias and abnormal automaticity in heart failure. *American Journal of Physiology-Heart and Circulatory Physiology*. 277 (1), H80–H91.

O'Rourke, B. et al. (1999) Mechanisms of altered excitation-contraction coupling in canine tachycardia-induced heart failure, I experimental studies. *Circulation research*. 84 (5), 562–570.

Omens, J. H. & Fung, Y. C. (1990) Residual strain in rat left ventricle. *Circulation research*. 66 (1), 37–45.

Osaka, T. et al. (1987) Effects of activation sequence and anisotropic cellular geometry on the repolarization phase of action potential of dog ventricular muscles. *Circulation*. 76

(1), 226–236.

Packer, M. (1985) Sudden unexpected death in patients with congestive heart failure: a second frontier. *Circulation*. 72 (4), 681–685.

Padrini, R. et al. (1992) Effects of pinacidil on guinea-pig isolated perfused heart with particular reference to the proarrhythmic effect. *British journal of pharmacology*. 105 (3), 715–719.

Parker, I. (2002) Photonics for biologists. *Methods in enzymology*. 360345–382.

Patrick, M. J. et al. (2007) Enhanced aqueous solubility of long wavelength voltage-sensitive dyes by covalent attachment of polyethylene glycol. *Organic \& biomolecular chemistry*. 5 (20), 3347–3353.

Peskin, C. S. (1972) Flow patterns around heart valves: a numerical method. *Journal of computational physics*. 10 (2), 252–271.

Peskin, C. S. (1997) 'Fluid dynamics of the heart and its valves', in *APS Meeting Abstracts*. 1997

Peskin, C. S. (2002) The immersed boundary method. *Acta numerica*. 11 (1), 479–517.

Peters, N. et al. (1993) Reduced content of connexin43 gap junctions in ventricular myocardium from hypertrophied and ischemic human hearts. *Circulation*. 88 (3), 864–875.

Petersen, S. et al. (2002) Coronary heart disease statistics: heart failure supplement 2002 edition. *University of Oxford*.

Pfeffer, M. A. et al. (1992) Effect of captopril on mortality and morbidity in patients with left ventricular dysfunction after myocardial infarction: results of the Survival and Ventricular Enlargement Trial. *New England journal of medicine*. 327 (10), 669–677.

Pfeffer, M. A. & Braunwald, E. (1990) Ventricular remodeling after myocardial infarction. Experimental observations and clinical implications. *Circulation*. 81 (4), 1161–1172.

Pham, Q. et al. (2001) 'A FEM-based deformable model for the 3D segmentation and tracking of the heart in cardiac MRI', in *Image and Signal Processing and Analysis, 2001. ISPA 2001. Proceedings of the 2nd International Symposium on*. 2001 pp. 250–254.

Piktel, J. S. et al. (2011) Enhanced dispersion of repolarization explains increased arrhythmogenesis in severe versus therapeutic hypothermia. *Circulation: Arrhythmia and Electrophysiology*. 4 (1), 79–86.

Pitt, B. et al. (2000) Effect of losartan compared with captopril on mortality in patients with symptomatic heart failure: randomised trial—the Losartan Heart Failure Survival Study ELITE II. *The Lancet*. 355 (9215), 1582–1587.

Pitt, B. et al. (1999) The effect of spironolactone on morbidity and mortality in patients with severe heart failure. *New England Journal of Medicine*. 341 (10), 709–717.

Pocock, G. et al. (2013) *Human physiology*. Oxford university press.

Pocock, G. & Richards, C. (2004) Human physiology, the basis of medicine 2nd Ed. *Recherche*. 6702.

Podesser, B. et al. (1997) Epicardial branches of the coronary arteries and their distribution in the rabbit heart: the rabbit heart as a model of regional ischemia. *The Anatomical Record*. 247 (4), 521–527.

Poelzing, S. et al. (2005) Transmural conduction is not a two-way street. *Journal of cardiovascular electrophysiology*. 16 (4), 455–455.

Pogwizd, S. M. et al. (2001) Arrhythmogenesis and Contractile Dysfunction in Heart Failure Roles of Sodium-Calcium Exchange, Inward Rectifier Potassium Current, and Residual $\beta$-Adrenergic Responsiveness. *Circulation research*. 88 (11), 1159–1167.

Pogwizd, S. M. & Corr, P. (1987) Electrophysiologic mechanisms underlying arrhythmias due to reperfusion of ischemic myocardium. *Circulation*. 76 (2), 404–426.

Pogwizd, S. M. & Corr, P. B. (1987) Reentrant and nonreentrant mechanisms contribute to arrhythmogenesis during early myocardial ischemia: results using three-dimensional mapping. *Circulation Research*. 61 (3), 352–371.

Polderman, K. H. & Herold, I. (2009) Therapeutic hypothermia and controlled normothermia in the intensive care unit: Practical considerations, side effects, and cooling methods*. *Critical care medicine*. 37 (3), 1101–1120.

Potse, M. et al. (2006) A comparison of monodomain and bidomain reaction-diffusion models for action potential propagation in the human heart. *Biomedical Engineering, IEEE Transactions on*. 53 (12), 2425–2435.

Pye, M. P. et al. (1996) Comparison of in vivo and in vitro haemodynamic function in experimental heart failure: use of echocardiography. *Cardiovascular research*. 31 (6), 873–881.

Pye, M. P. & Cobbe, S. M. (1996) Arrhythmogenesis in experimental models of heart failure: the role of increased load. *Cardiovascular research*. 32 (2), 248–257.

Pye, M. P. & Cobbe, S. M. (1992) Mechanisms of ventricular arrhythmias in cardiac failure and hypertrophy. *Cardiovascular research*. 26 (8), 740–750.

Qu, F. et al. (2007) Three-dimensional panoramic imaging of cardiac arrhythmias in rabbit heart. *Journal of biomedical optics*. 12 (4), 044019–044019.

Rachev, A. (1997) Theoretical study of the effect of stress-dependent remodeling on arterial geometry under hypertensive conditions. *Journal of biomechanics*. 30 (8), 819–827.

Rao, R. K. et al. (2007) Reduced ventricular volumes and improved systolic function with cardiac resynchronization therapy a randomized trial comparing simultaneous biventricular pacing, sequential biventricular pacing, and left ventricular pacing.

*Circulation*. 115 (16), 2136–2144.

Reuler, J. B. (1978) Hypothermia: pathophysiology, clinical settings, and management. *Annals of internal medicine*. 89 (4), 519–527.

Riccio, M. L. et al. (1999) Electrical restitution and spatiotemporal organization during ventricular fibrillation. *Circulation research*. 84 (8), 955–963.

Richard, S. et al. (1998) Ca2+ currents in compensated hypertrophy and heart failure. *Cardiovascular research*. 37 (2), 300–311.

Rodriguez, E. K. et al. (1994) Stress-dependent finite growth in soft elastic tissues. *Journal of biomechanics*. 27 (4), 455–467.

Rodriguez, M. & Nygren, A. (2012) 'Application of scale-space descriptors for the reliable detection of keypoints for image registration in optical mapping studies in whole heart preparations', in *Engineering in Medicine and Biology Society (EMBC), 2012 Annual International Conference of the IEEE*. 2012 pp. 3171–3174.

Rodriguez, M. & Nygren, A. (2015) Motion Estimation in Cardiac Fluorescence Imaging With Scale-Space Landmarks and Optical Flow: A Comparative Study. *Biomedical Engineering, IEEE Transactions on*. 62 (2), 774–782.

Rohde, G. K. et al. (2005) Correction of motion artifact in cardiac optical mapping using image registration. *Biomedical Engineering, IEEE Transactions on*. 52 (2), 338–341.

Rohr, S. & Kucera, J. P. (1998) Optical recording system based on a fiber optic image conduit: assessment of microscopic activation patterns in cardiac tissue. *Biophysical journal*. 75 (2), 1062–1075.

Rosenbaum, D. (2001) Optical mapping of cardiac excitation and arrhythmias: a primer. *Optical mapping of cardiac excitation and arrhythmias*. 2–7.

Rosenbaum, M. B. et al. (1982) Electrotonic modulation of the T wave and cardiac memory. *The American journal of cardiology*. 50 (2), 213–222.

Rozanski, G. J. et al. (1997) Electrophysiology of rabbit ventricular myocytes following sustained rapid ventricular pacing. *Journal of molecular and cellular cardiology*. 29 (2), 721–732.

Ruan, Y. et al. (2009) Sodium channel mutations and arrhythmias. *Nature Reviews Cardiology*. 6 (5), 337–348.

Rueckert, D. et al. (1999) Nonrigid registration using free-form deformations: application to breast MR images. *Medical Imaging, IEEE Transactions on*. 18 (8), 712–721.

Sakamoto, T. et al. (2005) Blebbistatin, a myosin II inhibitor, is photoinactivated by blue light. *Biochemistry*. 44 (2), 584–588.

Salama, G. et al. (1998) Hypoxia and hypothermia enhance spatial heterogeneities of repolarization in guinea pig hearts. *Journal of cardiovascular electrophysiology*. 9 (2), 164–183.

Salama, G. & Choi, B.-R. (2000) Images of action potential propagation in heart. *Physiology*. 15 (1), 33–41.

Salata, J. J. et al. (1996) IK of rabbit ventricle is composed of two currents: evidence for IKs. *American Journal of Physiology-Heart and Circulatory Physiology*. 271 (6), H2477–H2489.

Sampson, K. J. & Henriquez, C. S. (2005) Electrotonic influences on action potential duration dispersion in small hearts: a simulation study. *American Journal of Physiology-Heart and Circulatory Physiology*. 289 (1), H350–H360.

Sands, G. B. et al. (2005) Automated imaging of extended tissue volumes using confocal microscopy. *Microscopy research and technique*. 67 (5), 227–239.

Schaffer, P. et al. (1994) Di-4-ANEPPS causes photodynamic damage to isolated cardiomyocytes. *Pflügers Archiv : European journal of physiology*. 426 (6), 548–551.

SCHERLAG, B. J. et al. (1974) Characterization and localization of ventricular arrhythmias resulting from myocardial ischemia and infarction. *Circulation Research*. 35 (3), 372–383.

Schmid, H. et al. (2008) Myocardial material parameter estimation. *Biomechanics and modeling in mechanobiology*. 7 (3), 161–173.

Schmid, H. et al. (2006) Myocardial material parameter estimation—a comparative study for simple shear. *Journal of biomechanical engineering*. 128 (5), 742–750.

Schmidt, U. et al. (1998) Contribution of abnormal sarcoplasmic reticulum ATPase activity to systolic and diastolic dysfunction in human heart failure. *Journal of molecular and cellular cardiology*. 30 (10), 1929–1937.

Schröder, F. et al. (1998) Increased availability and open probability of single L-type calcium channels from failing compared with nonfailing human ventricle. *Circulation*. 98 (10), 969–976.

Seo, K. et al. (2010) Structural heterogeneity in the ventricular wall plays a significant role in the initiation of stretch-induced arrhythmias in perfused rabbit right ventricular tissues and whole heart preparations. *Circulation research*. 106 (1), 176–184.

Shvilkin, A. et al. (1998) Evolution and resolution of long-term cardiac memory. *Circulation*. 97 (18), 1810–1817.

Smaill, B. & Hunter, P. (1991) 'Structure and function of the diastolic heart: material properties of passive myocardium', in *Theory of Heart*. Springer. pp. 1–29.

Sprung, J. et al. (1995) Effects of hypothermia, potassium, and verapamil on the action potential characteristics of canine cardiac Purkinje fibers. *Anesthesiology*. 82 (3), 713–722.

Sprung, J. et al. (1994) Hypothermia modifies anesthetic effect on contractile force and Ca2+ transients in cardiac Purkinje fibers. *American Journal of Physiology-Heart and Circulatory Physiology*. 36 (2), H725.

Stevens, C. et al. (2003) Ventricular mechanics in diastole: material parameter sensitivity. *Journal of biomechanics*. 36 (5), 737–748.

Straight, A. F. et al. (2003) Dissecting temporal and spatial control of cytokinesis with a myosin II Inhibitor. *Science*. 299 (5613), 1743–1747.

Streeter Jr, D. D. et al. (1969) Fiber orientation in the canine left ventricle during diastole and systole. *Circulation research*. 24 (3), 339–347.

Suleiman, M. & Chapman, R. (1990) Effect of temperature on the rise in intracellular sodium caused by calcium depletion in ferret ventricular muscle and the mechanism of the alleviation of the calcium paradox by hypothermia. *Circulation research*. 67 (5), 1238–1246.

Sutton, M. G. S. J. et al. (2003) Effect of cardiac resynchronization therapy on left ventricular size and function in chronic heart failure. *Circulation*. 107 (15), 1985–1990.

Svrcek, M. et al. (2009) 'Characteristics of motion artifacts in cardiac optical mapping studies', in *Engineering in Medicine and Biology Society, 2009. EMBC 2009. Annual International Conference of the IEEE*. 2009 pp. 3240–3243.

Svrcek, M. et al. (2009) 'Using image registration to reconstruct spatiotemporal electrical activity in cardiac optical mapping studies', in *Computers in Cardiology, 2009*. 2009 pp. 521–524.

Swedberg, K. & Kjekshus, J. (1988) Effects of enalapril on mortality in severe congestive heart failure: results of the Cooperative North Scandinavian Enalapril Survival Study (CONSENSUS). *The American journal of cardiology*. 62 (2), 60A–66A.

Swift, L. M. et al. (2012) Properties of blebbistatin for cardiac optical mapping and other imaging applications. *Pflügers Archiv European Journal of Physiology*. 1–10.

Tasaki, I. et al. (1968) Changes in fluorescence, turbidity, and birefringence associated with nerve excitation. *Proceedings of the National Academy of Sciences of the United States of America*. 61 (3), 883.

Toyoshima, H. & Burgess, M. (1978) Electrotonic interaction during canine ventricular repolarization. *Circulation research*. 43 (3), 348–356.

Trayanova, N. et al. (2002) Computer simulations of cardiac defibrillation: a look inside the heart. *Computing and Visualization in Science*. 4 (4), 259–270.

Trayanova, N. et al. (2006) What have we learned from mathematical models of defibrillation and postshock arrhythmogenesis? Application of bidomain simulations. *Heart rhythm : the official journal of the Heart Rhythm Society*. 3 (10), 1232–1235.

Tveita, T. (2000) Myocardial effects of hypothermia and rewarming. *CARDIOVASCULAR ENGINEERING*. 5 (3), 179–187.

Uchida, T. et al. (1999) Mechanism of acceleration of functional reentry in the ventricle effects of ATP-sensitive potassium channel opener. *Circulation*. 99 (5), 704–712.

Uretsky, B. F. et al. (2000) Acute coronary findings at autopsy in heart failure patients with sudden death results from the assessment of treatment with lisinopril and survival (ATLAS) trial. *Circulation*. 102 (6), 611–616.

Usyk, T. et al. (2000) Effect of laminar orthotropic myofiber architecture on regional stress and strain in the canine left ventricle. *Journal of elasticity and the physical science of solids*. 61 (1-3), 143–164.

Vassalle, M. (1966) Analysis of cardiac pacemaker potential using a“ voltage clamp” technique. *American Journal of Physiology-Legacy Content*. 210 (6), 1335–1341.

Veress, A. I. et al. (2005) Measurement of strain in the left ventricle during diastole with cine-MRI and deformable image registration. *TRANSACTIONS-AMERICAN SOCIETY OF MECHANICAL ENGINEERS JOURNAL OF BIOMECHANICAL ENGINEERING*. 127 (7), 1195.

Vermeulen, J. T. et al. (1994) Triggered activity and automaticity in ventricular trabeculae of failing human and rabbit hearts. *Cardiovascular research*. 28 (10), 1547–1554.

Verrecchia, F. & Hervé, J. C. (1997) Reversible blockade of gap junctional communication by 2,3-butanedione monoxime in rat cardiac myocytes. *The American journal of physiology*. 272 (3 Pt 1), C875–85.

Vetter, F. J. & McCulloch, A. D. (1998) Three-dimensional analysis of regional cardiac function: a model of rabbit ventricular anatomy. *Progress in biophysics and molecular biology*. 69 (2-3), 157–183.

Vetter, F. J. & McCulloch, A. D. (2000) Three-dimensional stress and strain in passive rabbit left ventricle: a model study. *Annals of Biomedical Engineering*. 28 (7), 781–792.

Volders, P. G. et al. (1999) Repolarizing K+ currents ITO1 and IKs are larger in right than left canine ventricular midmyocardium. *Circulation*. 99 (2), 206–210.

Vossoughi, J. et al. (1980) Compressibility of the myocardial tissue. *Advances in bioengineering Mow VC*. 45–48.

Vrtovec, B. et al. (2003) Prolonged QTc interval and high B-type natriuretic peptide levels together predict mortality in patients with advanced heart failure. *Circulation*. 107 (13), 1764–1769.

Walker, N. et al. (2004) 'Epicardial activation in isolated rabbit hearts with chronic myocardial infarction.', in *BIOPHYSICAL JOURNAL*. 2004 p. 15A–15A.

Walker, N. L. et al. (2007) Mapping of epicardial activation in a rabbit model of chronic myocardial infarction. *Journal of cardiovascular electrophysiology*. 18 (8), 862–868.

Walton, R. D. et al. (2013) Electrophysiological and structural determinants of electrotonic modulation of repolarization by the activation sequence. *Frontiers in physiology*. 4.

Walton, R. D. & Bernus, O. (2009) 'Electrotonic effects on action potential duration in perfused rat hearts', in *Engineering in Medicine and Biology Society, 2009. EMBC 2009. Annual International Conference of the IEEE*. 2009 pp. 4190–4193.

Wang, H. M. et al. (2013) Structure-based finite strain modelling of the human left ventricle in diastole. *International journal for numerical methods in biomedical engineering*. [Online] 29 (1), 83–103.

Warren, S. E. et al. (1988) Time course of left ventricular dilation after myocardial infarction: influence of infarct-related artery and success of coronary thrombolysis. *Journal of the American College of Cardiology*. 11 (1), 12–19.

Watanabe, H. et al. (2004) Multiphysics simulation of left ventricular filling dynamics using fluid-structure interaction finite element method. *Biophysical journal*. 87 (3), 2074–2085.

Weidmann, S. (1951) Effect of current flow on the membrane potential of cardiac muscle. *The Journal of physiology*. 115 (2), 227–236.

Wenk, J. F. et al. (2011) A novel method for quantifying the in-vivo mechanical effect of material injected into a myocardial infarction. *The Annals of thoracic surgery*. 92 (3), 935–941.

Westergaard, P. et al. (2008) 'Non-linear image registration for correction of motion artifacts during optical imaging of human hearts', in *Electrical and Computer Engineering, 2008. CCECE 2008. Canadian Conference on*. 2008 pp. 001729–001732.

Wettwer, E. et al. (1994) Transient outward current in human ventricular myocytes of subepicardial and subendocardial origin. *Circulation Research*. 75 (3), 473–482.

White, E. et al. (1993) The effects of increasing cell length on auxotonic contractions; membrane potential and intracellular calcium transients in single guinea-pig ventricular myocytes. *Experimental Physiology*. 78 (1), 65–78.

White, H. D. et al. (1987) Left ventricular end-systolic volume as the major determinant of survival after recovery from myocardial infarction. *Circulation*. 76 (1), 44–51.

Wiegerinck, R. F. et al. (2008) Transmural dispersion of refractoriness and conduction velocity is associated with heterogeneously reduced connexin43 in a rabbit model of heart failure. *Heart Rhythm*. 5 (8), 1178–1185.

Witkowski, F. et al. (2001) Optimization of temporal filtering for optical transmembrane potential signals. *Optical Mapping of Cardiac Excitation and Arrhythmias. DS Rosenbaum and J. Jalife, editors. Futura Publishing, Armonk, NY*. 79–92.

Witte, K. K. et al. (2008) Biventricular pacing: Impact on exercise-induced increases in mitral insufficiency in patients with chronic heart failure. *Canadian Journal of Cardiology*. 24 (5), 379–384.

Wu, J. et al. (1998) Cytochalasin D as Excitation-Contraction Uncoupler for Optically Mapping Action Potentials in Wedges of Ventricular Myocardium. *Journal of cardiovascular electrophysiology*. 9 (12), 1336–1347.

Yan, G.-X. et al. (2004) Phase 2 reentry as a trigger to initiate ventricular fibrillation during early acute myocardial ischemia. *Circulation*. 110 (9), 1036–1041.

Yan, G.-X. et al. (2001) Ventricular hypertrophy amplifies transmural repolarization dispersion and induces early afterdepolarization. *American Journal of Physiology-Heart and Circulatory Physiology*. 281 (5), H1968–H1975.

Yin, F. C. P. et al. (1987) Quantification of the mechanical properties of noncontracting canine myocardium under simultaneous biaxial loading. *Journal of biomechanics*. 20 (6), 577–589.

Young, J. B. et al. (2003) Combined cardiac resynchronization and implantable cardioversion defibrillation in advanced chronic heart failure: the MIRACLE ICD Trial. *Jama*. 289 (20), 2685–2694.

Yu, H. et al. (1999) Transient outward current, Ito1, is altered in cardiac memory. *Circulation*. 99 (14), 1898–1905.

Yuan, S. et al. (2001) Global repolarization sequence of the ventricular endocardium: monophasic action potential mapping in swine and humans. *Pacing and clinical electrophysiology : PACE*. 24 (10), 1479–1488.

Yue, A. M. et al. (2005) Global dynamic coupling of activation and repolarization in the human ventricle. *Circulation*. 112 (17), 2592–2601.

Zubair, I. et al. (1994) Effects of activation sequence on the spatial distribution of repolarization properties. *Journal of electrocardiology*. 27 (2), 115–127.